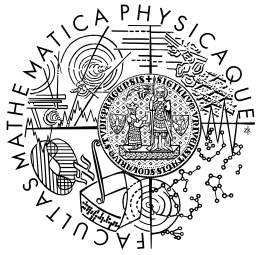

FACULTY
OF MATHEMATICS
AND PHYSICS
Charles University

DOCTORAL THESIS

Mgr. Šimon Midlik

Quantum fluid dynamics and quantum turbulence probed using micro- and nano-resonators

Department of Low-Temperature Physics

Supervisor of the doctoral thesis:	doc. RNDr. David Schmoranzer, Ph.D.
Study programme:	Physics of Condensed Matter and Materials Research
Study branch:	Physics

Prague 2023

I declare that I carried out this doctoral thesis independently, and only with the cited sources, literature and other professional sources. It has not been used to obtain another or the same degree.

I understand that my work relates to the rights and obligations under the Act No. 121/2000 Sb., the Copyright Act, as amended, in particular the fact that the Charles University has the right to conclude a license agreement on the use of this work as a school work pursuant to Section 60 subsection 1 of the Copyright Act.

In ..... date ....

Author's signature

First, I would like to thank all of my parents, friends, and partners, for a lot of emotional and personal support. Next, I would like to thank all my colleagues and collaborators for the well-spent time during the endless measurements. The most thanks belong to my supervisor David Schmoranzer for his advising, good leadership, and a lot of past knowledge. I want to thank him for the time spent with all the corrections and for the great collaboration on the joint projects. Further, I would like to thank my colleagues from the Laboratory of Superfluidity in Prague, for the inspiration and help with the experiments, namely Ladislav Skrbek and Emil Varga and younger students Filip Novotný, Maximilian Goleňa, and Marek Talíř, working on the projects together. During my Ph.D., thanks to a European Microkelvin Platform, I was allowed to visit some of the top European ultra-low-temperature laboratories in Grenoble, Lancaster, and Helsinki. For these beautiful collaborations, I want to thank Andrew Fefferman, Eddy Collin, Sebastien Triqueneaux, James Buttherworth, Ilya Golokolenov, and Viktor Tsepelin, Theo Noble, Roch Schanen, Sergey Kafanov, and Vladimir Eltsov, Jere Mäkinen and Timo Kamppinen. My last thanks go to my good friend and great human Jozef.

Title: Quantum fluid dynamics and quantum turbulence probed using micro- and nano-resonators

Author: Mgr. Šimon Midlik

Department: Department of Low-Temperature Physics

Supervisor: doc. RNDr. David Schmoranzer, Ph.D., Department of Low-Temperature Physics

Abstract: In this Thesis, we present an extensive study of the dynamics of quantum fluids employing the detectors in the form of mechanical resonating structures with characteristic dimensions below 1 mm. We operate the devices in normal and superfluid liquid phases of both helium isotopes scanning the wide range of temperatures between 2.17 K and ≈ 150 μK. We show, that the detectors in the form of quartz tuning forks and superconducting vibrating wires are suitable probes in both hydrodynamic and ballistic regimes of superfluids, described by the two-fluid model. Not only can these devices be used to trigger the turbulent transition in quantum fluids by their driven motion, they can also operate as detectors of externally generated turbulence. The observation of the initial instability is reported in mechanically and thermally driven oscillatory flows. Its origin in either normal or superfluid component is identified and described in terms of suitable dimensionless parameters, solving previous discrepancies regarding critical velocities in oscillatory counterflow experiments. Additionally, in steady thermal counterflow, a microwire is characterised as a local probe of quantized vorticity and compared to second sound measurements. Finally, we discuss the properties and potential of the MEMS and NEMS devices, advancing from much smaller dimensions, fabricated via custom cleanroom processes and we report the manufacture of our own device. Such detectors are able to probe the quantum fluids on the scale of a single quantized vortex, studying its detailed dynamics and should lead to more information about the energy dissipation in zero temperature limit.

Keywords: superfluid helium quantum turbulence MEMS/NEMS oscillatory flow

Contents

Preface

This thesis aims to report and discuss cryogenic experiments conducted by the author, with the goal to enrich current knowledge of turbulent flows in quantum fluids. Superfluid helium (^{4}He and ^{3}He isotopes) are one of the best laboratory-accessible quantum fluid systems, although temperatures of the order of units of Kelvin (for ^{4}He) or even millikelvin (for ^{3}He) are required. As a payoff for the higher complexity of the technical realization of the quantum flows, they offer a plethora of fascinating physical effects, having no analogy in any classical fluids, e.g. quantization of circulation leading to the existence of quantized vortices. One of the most interesting tasks in the research of superfluids is the study of flow instabilities and the development of complex turbulent flows representing the phenomena of quantum turbulence (QT) [1–4] or A.1. Despite many distinguishing differences between quantum and classical turbulence, QT may be used, under specific conditions, as a model system of classical turbulence. The study of turbulence in quantum fluids can, therefore, lead to a better understanding even of its classical counterpart.

Studying the drag forces acting on submerged mechanical resonators represents one of the most expanded techniques of QT research. In this configuration, turbulence can be both generated and detected by the devices of various shapes, e.g. tuning forks [5, 6] or A.2, vibrating wires [7–10] or A.2, moving grids [11, 12], levitating spheres [13–15]. The recent expansion of accessibility of highly equipped cleanroom facilities allowed the boom of custom MEMS and NEMS (micro/nano electro-mechanical systems) device manufacture. The great advantage of the local character of these detectors can be effectively used to probe externally driven flows and is a necessary condition for the studies of systems with spatially non-homogeneous turbulence [16–20] or A.3. Scaledown of resonator dimensions opens the way to significantly higher sensitivity for the devices used for the detection. With the ability to reach nano-metric scales, it is now possible to probe quantum liquids at the level of coherence length (in the case of ^{3}He). Customization of the used geometry further allows to effectively trap single quantized vortices, now in both isotopes of superfluid helium, with the device and study their mutual interaction. Experimental observations of single vortex dynamics should lead to a better understanding of fundamental questions of energy dissipation in a pure superfluid regime where a viscous dissipation channel is absent [21–26].

Manufacture of such local detectors stands on lithography processes allowing very precise etching and layer coating procedures. Typical devices are created from thin Si_3N_4 membranes or monocrystal Si wafers and covered with superconducting layers (aluminum, niobium, ...) used for movement induction [27–29] or A.6. Even devices based only on superconducting metal have been reported re-

cently [30]. The geometry of the MEMS/NEMS may be easily varied, e.g. doubly clamped cantilevers or goal-post-shaped wires. The device position may lead to a well-tuned distance from the substrate or other device, employing the grids of devices [31], or alternatively, it can probe the bulk, standing in an open window.

In the first chapter 1, we present the theoretical background essential to this Thesis and discuss the recent author‘s contribution to the understanding of quantum turbulence. We further refer to more detailed works suitable for further reading. The second chapter 2 is dedicated to the description of the turbulent instability onset in oscillatory flows of He II, based on our experimental observations. We discuss the turbulent transition occurring in either of the He II components and show that the cross-over between the two is possible in a single experimental setup. In the third chapter 3, we show the measurements of the local detection of externally driven turbulent flow in He II employing vibrating wire resonators. We are trying to approach the theoretical understanding of the processes, affecting the resonant frequency and amplitude of a weakly driven oscillator exposed to a turbulent thermal counterflow at temperatures above 1 K. In the final chapter 4, we discuss the general use of the MEMS and NEMS structures for the detection of quantum turbulence and characterize the damping due to acoustic emission in ^{3}He , which may limit the detection ability of the probe. In the end, we present the fabrication process of custom-made MEMS devices manufactured by the author and characterize their properties at 20 mK temperatures. In the end, we present the data showing a stably attached single quantized vortex to a similar device in ^{3}He -B and study the additional losses caused by the vortex. A list of the most relevant publications, with the author's contribution, is attached in Appendix A.

Chapter 1

Theoretical background

1.1 Quantum fluids

The study of classical fluid dynamics represents one of the most important research fields with applications in everyday life. Under extreme conditions, such as low temperatures or high pressures, fluids can behave under special quantum restrictions, similar to many quantum phenomena in solid bodies. Fluids, whose macroscopic behaviour cannot be described entirely by classical models, e.g. Navier-Stokes equations [32], are generally called quantum fluids. The idea of quantum fluids was introduced following the discovery of superfluidity in ^{4}He (independently by Kapitza [33] and Allen & Misener [34]), resulting from rapid cryogenic development at the beginning of the twentieth century. Nowadays, the most frequently studied quantum fluids are superfluid phases of liquid helium and ultracold atomic gases. In this work, we restrict our interest to the former ones, especially to the superfluid ^{4}He .

1.1.1 Superfluid helium isotopes

Upon lowering the temperature towards absolute zero, helium remains liquid (if high pressure is not applied) unlike all other substances, which freeze to their solid state. It is due to the imbalance of the ground state motion energy of the helium atoms acting against weak van der Waals forces, trying to bind the atoms together. This allows the existence of liquid phases experiencing quantum behaviour on a macroscopic scale. In this new liquid phase of ^{4}He , existing below 2.17 K, several non-classical phenomena were observed, e.g. ability to flow through very small pores without the viscosity, formation of a thin superfluid film, the fountain effect or thermo-mechanical effect and led to the recognition of this phase as the superfluid ^{4}He also denoted as He II. The full phase diagram of ^{4}He is displayed in Fig 1.1. The phase transition line between two helium liquid phases (normal liquid He I and superfluid He II) is called the λ transition line. This name comes from the shape of the heat capacity evolution across the transition.

The superfluid phase was later experimentally discovered also in much rarer helium isotope ^{3}He in 1972 [35, 36]. The main technical obstacle connected with ^{3}He superfluidity is the three orders of magnitude lower superfluid transition temperature being of units of millikelvin. The different physical properties of

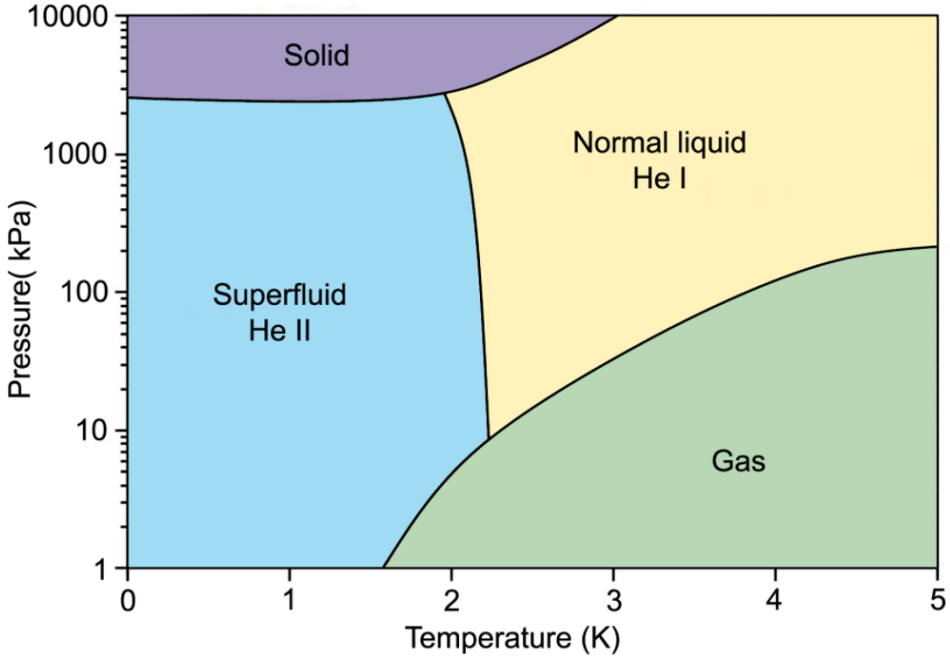

Figure 1.1: Phase diagram of ^{4}He . It can exist in two liquid phases, either classical normal liquid denoted He I or in superfluid phase - He II, which consist of normal and superfluid component. Second order phase transition between the two, happening at around 2 K, is called superfluid or lambda transition.

these superfluids originate from the bosonic nature of ^{4}He vs the fermionic nature of ^{3}He and require different theoretical approaches.

Superfluidity of ^{4}He was first connected with Bose-Einstein condensation in 1938 by London [37] and the same idea was further used in works of Tizsa [38] introducing the first two-fluid model of He II. However, this approach was criticized by Landau, for omitting the atomic interactions, presenting his own model build on the ideal gas of elementary excitations [39, 40]. As a result, both approaches were shown to be complementary. Superfluid, as a quantum mechanical ground state, consists of cca. 10% of the condensate, as measured experimentally by neutron scattering [41]. The lower portion of the particles in the atomic ground state comes from their interactions.

The issue with ^{3}He superfluidity description through the mere idea of the Bose-Einstein condensation is evident due to its fermionic nature. However, in analogy to the Cooper pairing of the electrons in the theory of superconductivity, a similar process works for the ^{3}He atoms. Having an atomic spin of one-half, ^{3}He atom pairs created below the transition temperature form a triplet state (unlike singlet pairing of electrons in superconductors), with possible spin projection S_z=0,±1. In addition, pair of atoms orbiting around a common centre has an orbital spin $\boldsymbol{L}$=1. Based on the properties of the spin-orbital space and external parameters - pressure and magnetic field, we may observe three different bulk phases. The first one, with all possible spin projections, is called superfluid-B phase or ^{3}He -B. At higher pressures, concerning a zero magnetic field for now,

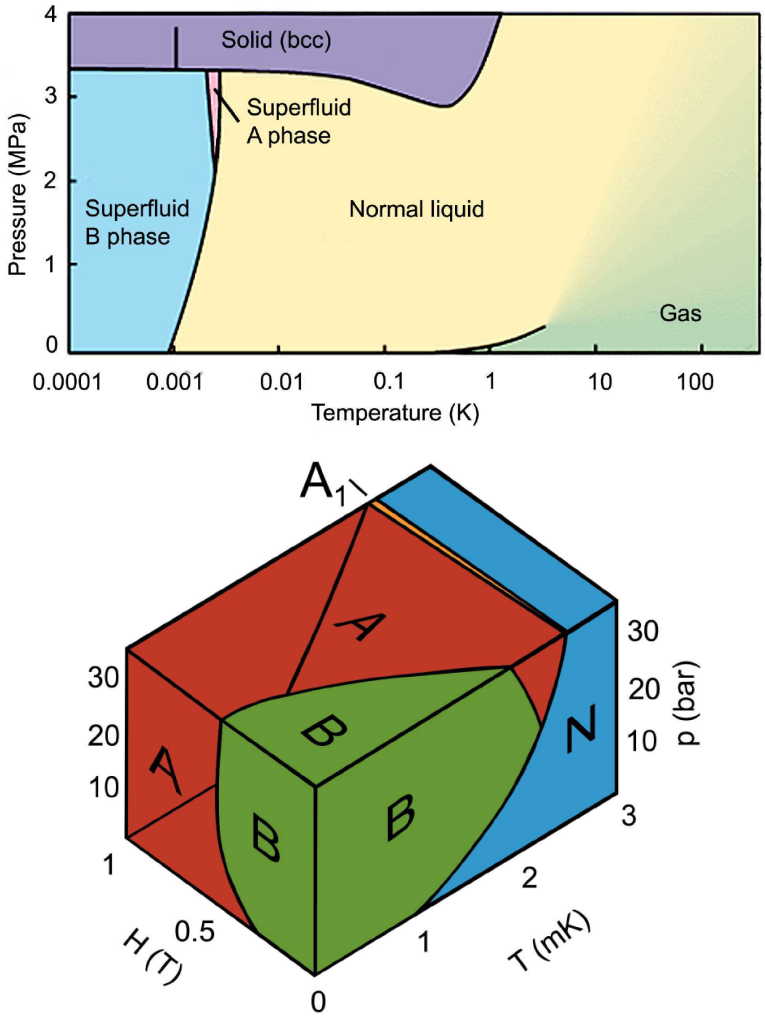

Figure 1.2: Top: Phase diagram of ^{3}He in zero magnetic field. Superfluid transition occurs from 1 mK to 3 mK in dependence on the pressure. Two different superfluid phases, ^{3}He -A and ^{3}He -B, exist in bulk at zero field. Bottom: 3D phase diagram of ^{3}He showing also magnetic field dependence. At higher fields, ^{3}He -A phase is more preferable, and a new bulk phase ^{3}He -A1 can exist.

see the phase diagram in Figure 1.2, superfluid-A phase or ^{3}He -A exists, not containing any S_z=0 component. When higher magnetic field is applied the area covered by in ^{3}He -A grows rapidly. Finally, in a non-zero magnetic field we can observe ^{3}He -A1 phase, similar to A phase, but consisting of only S_z=1 ($|\uparrow\uparrow\rangle$) spin projection component. The full 3D phase diagram of ^{3}He superfluid phases as a function of pressure, temperature, and magnetic field is shown in Figure 1.2. Additional superfluid ^{3}He phases, e.g. polar phase, exist under special topological restrictions [42, 43], but a closer description of these is beyond the scope of this Thesis.

1.1.2 Two-fluid model - hydrodynamic regime

Superfluid phases of both helium isotopes can be described by the two-fluid model. We can, therefore, describe the He II as a mixture of two inter-penetrating fluid components. The first one is a classical-like normal component independently acting as a viscous fluid in accordance with the Navier-Stokes equations [32]. This holds, in the high-temperature regime, between the λ transition and ≈ 0.7 K, where normal component can be described by its hydrodynamical properties. In the following, we discuss this hydrodynamic limit of the two-fluid regime.

The second component is called superfluid component and is responsible for the originally observed peculiar behaviour of He II. The superfluid component is a practical realization of compressible ideal fluid which may be described by Euler's equations [32]. It lacks any viscosity and does not possess or transfer any entropy, as it represents the macroscopic quantum mechanical ground state of the fluid. The normal component is therefore responsible for the whole entropy and heat transfer. He II has, for these reasons, an extremely high thermal conductivity, which strongly suppresses bulk boiling as all excessive heat is effectively transferred to the surface and lost due to evaporation.

Two-fluid nature of He II is further allowing the existence of flows that have no equivalence in classical fluids. One can easily mechanically generate the mean flow of whole fluid, resulting in the co-flow [44] of the components. Alternatively, the flow of the normal fluid may be blocked by the porous plug, which does not affect the flow of inviscid superfluid component, resulting in the pure superflow [45]. Finally, a flow of the two components in opposite directions, so-called counterflow [46], may be generated either mechanically or thermally.

As purely independent flows of the components are possible, we have to introduce separate densities ρ_n, ρ_s and velocity fields $\boldsymbol{v}_n$, $\boldsymbol{v}_s$, for the components of the two-fluid model. The total density of He II ρ is only weakly dependent on the temperature [47] and its value equals the sum of the single component densities:

$$\rho = \rho_n + \rho_s. \tag{1.1}$$

Due to the discussed properties of the two components, it is obvious that the ratio, or better say density, of the normal component must be decreasing with the temperature. The local ratio of ρ_n and ρ_s is then, in the general approximation neglecting the pressure dependence, defining the temperature of He II and vice versa. The first measurement of the normal component and superfluid component densities as a function of temperature, proving this idea, was performed by Andronikashvili [48] in 1946. In his experiment, a set of closely packed torsional disks on a string were used as a fully-submerged oscillator. The spacing was made small enough, smaller than the viscous penetration depth, to force the oscillation of the normal component between the discs together with the whole body. The changes in the oscillator period led to the determination of the temperature dependence of the normal and superfluid density ratios as displayed in Figure 1.3.

Further, in analogy to classical fluids, we should be able to build a set of equations of motion governing the macroscopic behaviour of the fluid system proposed by the two-fluid model. As stated above, it should be based on the Navier-Stokes-like equation for normal component and Euler-like equation for the

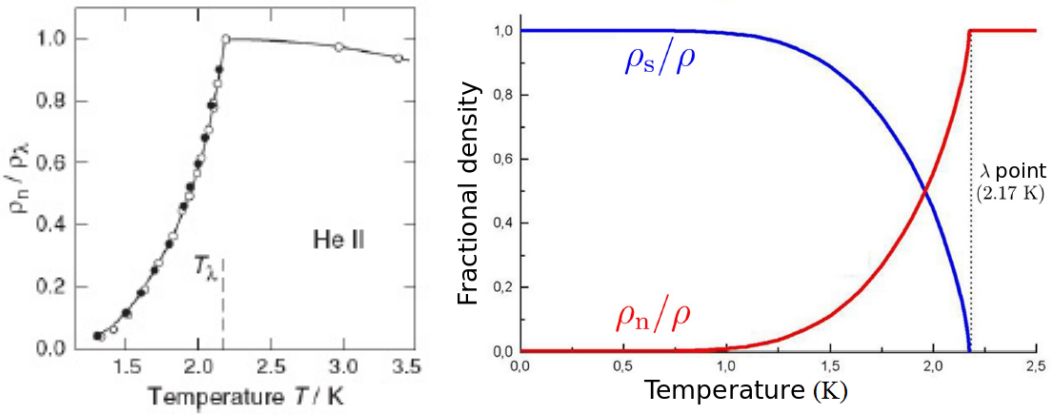

Figure 1.3: Left: Normal component density measurement performed by Andronikashvili [48]. Right: Temperature dependence of normal (red) and superfluid (blue) component density in a He II.

superfluid component. First, the mass and entropy flow inside the fluid should be described by the equations of continuity. For the system of our two fluids, we get:

$$\frac{\partial(\rho_n + \rho_s)}{\partial t} + \nabla(\rho_n \mathbf{v}_n + \rho_s \mathbf{v}_s) = 0, \tag{1.2}$$

for the conservation of the total mass, also stating that the exchange of the mass between the components is not forbidden. And:

$$\frac{\partial(\rho S)}{\partial t} + \nabla(\rho S \mathbf{v}_n) = 0, \tag{1.3}$$

assuming only the non-dissipative flows. Here, S denotes the specific entropy. Finally, assuming the incompressible flows, we can write the following equations of motion, called HVBK equations (named after Hall, Vinen, Bekarevich and Khalatnikov [49–51]):

$$\frac{\partial \mathbf{v}_n}{\partial t} + (\mathbf{v}_n \cdot \nabla)\mathbf{v}_n = -\frac{1}{\rho}\nabla P - \frac{\rho_s}{\rho_n} S \nabla T + \nu \triangle \mathbf{v}_n + \frac{\rho_s}{\rho}\mathbf{F}, \tag{1.4}$$

$$\frac{\partial \mathbf{v}_s}{\partial t} + (\mathbf{v}_s \cdot \nabla)\mathbf{v}_s = -\frac{1}{\rho}\nabla P + S \nabla T + \mathbf{T} - \frac{\rho_n}{\rho}\mathbf{F}, \tag{1.5}$$

where ν stands for the kinematic viscosity of the normal component, P for pressure, T for temperature and $\boldsymbol{T}$ for the vortex tension. We can further define the vector difference of the component velocities as, so-called, counterflow velocity $\boldsymbol{v}_{ns} = \boldsymbol{v}_n$ - $\boldsymbol{v}_s$. Finally, $\boldsymbol{F}$ represents the mutual friction force, which is responsible for the coupling of the motion of the two He II components. However, this force is nonzero only in the presence of rotational flow in the superfluid component, possible only due to quantized vortices, which will be closer described in the following chapters.

When describing the superfluid ^{3}He , the same two-fluid model having normal and superfluid components can be applied. However, the main difference to He II picture is the viscosity of the normal component. While normal component of

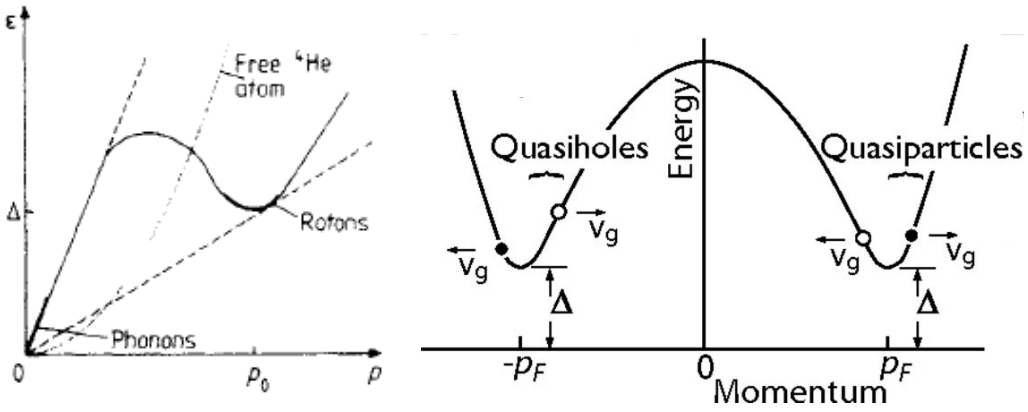

Figure 1.4: Left: Dispersion of thermal excitations in He II. Two branches of linear phonons and parabolic rotons, with energy gap Δ, are present. Under critical Landau velocity (highlighted by dashed line), roton minimum gets below zero energy line and excitation generation beaks the superfluidity. Right: Dispersion of thermal excitations in superfluid ^{3}He . Superfluidity is connected with the existence of an energy gap Δ in the spectrum, which might be anisotropic. The fermionic nature of the excitations leads to the necessity of distinguishing quasiparticles and quasiholes based on the direction of the momentum and the group velocity.

^{4}He possesses one of the lowest viscosities, three orders of magnitude lower than the water, the viscosity of the normal ^{3}He is closer to that of the honey. For this reason, in most of the experiments performed close below critical temperature T_C, the normal component is considered to be static and only the flow of superfluid component can be studied. However, the situation changes, if superfluid ^{3}He is cooled further, below approx. 0.2 T_C, where normal component can be no longer described as a continuum. For the He II it happens below ≈0.7 K. In this case, we have to consider normal component to behave rather like a ballistic gas of thermal excitations surrounded by "superfluid vacuum" and we can discuss the two-fluid model in its ballistic limit.

1.1.3 Two-fluid model - ballistic regime

At low enough temperatures, where the normal component density is too low for it to be described by the hydrodynamic model, we have to consider a different picture. The presented ballistic model for normal component is based on the original phenomenological description of He II made by Landau [39, 40]. However it is important to understand, that Landau's model does not restrict to a ballistic regime and can lead to approximately correct normal and superfluid component density in two-fluid regime in accordance with Fig 1.3.

At first, Landau intuitively correctly postulated the dispersion law, see Fig 1.4, for the introduced thermal excitations, as was later proven by neutron scattering experiments [52–54]. In his ideas, an ideal gas of these excitations represented the weakly interacting atoms of the normal fluid. We can find many analogical approaches in solid body physics, trying to describe interacting systems of the

electrons [55]. Based on the shape of the dispersion curve, two types of excitations may be discussed. First, at the low-energy part of the spectrum, we can see a linear dependence of the energy E with the momentum of the excitation $\boldsymbol{p} = h\boldsymbol{k}$, with h being the Plank constant and $\boldsymbol{k}$ the wave vector. This part of the spectrum, in analogy with linear excitations in solids (considering only longitudinal modes as dealing with the liquid), represents phonons, having the following dispersion relation:

$$\epsilon = u_1 p, \tag{1.6}$$

defining the speed of sound u_1.

The second type of the thermal excitations, having an effective mass μ, is called rotons and occupy parabolic part 1.7 of the dispersion around the energy minimum at p_0 momentum.

$$\epsilon = \Delta + \frac{(p - p_0)^2}{\mu}. \tag{1.7}$$

The right branch of the roton spectrum, with the group velocity in the direction of the momentum, can be denoted as R^+, while the left branch, having the group velocity direction opposite to the momentum direction, being called R^-. The energy Δ of the excitations with the momentum $\mathbf{p}_0$ gives the roton energy gap necessary for its generation in He II flow. This leads to the existence of a critical "Landau" velocity given as $v_L = \epsilon(p_0)/p_0$, being of the order of 60 m/s, at which thermal excitations can be created spontaneously. However, typically in experiments a different type of perturbation of the superfluid (quantized vortices, which will be further discussed later) onsets at much lower velocities.

The population of the energy spectra of thermal excitations N_{phonon} and N_{roton} is naturally strongly dependent on the temperature:

$$N_{phonon} \sim (k_B T)^3, \tag{1.8}$$

$$N_{roton} \sim (k_B T)^{\frac{3}{2}} e^{-\frac{\Delta}{k_B T}}, \tag{1.9}$$

with k_B, being Boltzmann constant.

The dispersion law in ^{3}He differs from that of ^{4}He , due to its fermionic nature. It is missing the phonon part, see Figure 1.7, which results in the existence of the energy gap Δ in the energy spectrum. Moreover, the energy gap might be anisotropic across the $\boldsymbol{k}$-vector sphere. It is not the case for the ^{3}He -B, but in ^{3}He -A phase energy gap disappears at the "south and north" poles, see Figure 1.5, having consequences regarding the anisotropy and the temperature dependence of the excitation population in these phases. In ^{3}He , we have to account for the fermionic nature of the thermal excitations. Based on the momentum of the excitation, we can divide them into quasiparticles having momentum larger than the Fermi momentum $|\mathbf{p}| > \mathbf{p}_F$ in the same direction as the group velocity and into quasiholes with $|\mathbf{p}| < \mathbf{p}_F$ with opposite direction of the momentum and the group velocity. The energy of the excitation is given as [56]:

$$E_{\mathbf{p}} = \sqrt{\Big(\frac{p^2}{2m^*} - \epsilon_F\Big)^2 + \Delta^2}, \tag{1.10}$$

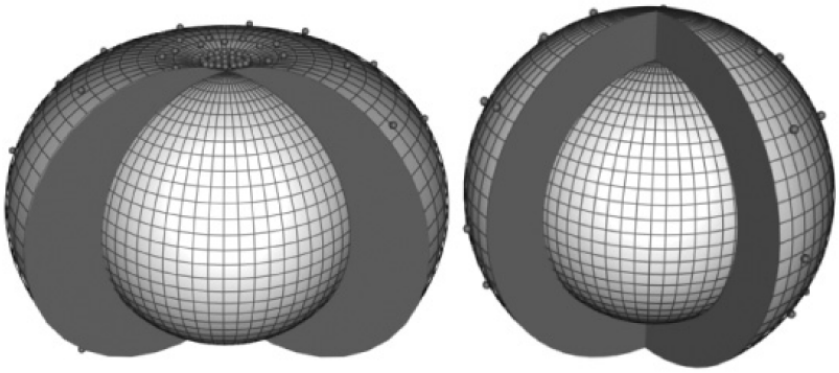

Figure 1.5: Superfluid ^{3}He energy gap visualization in the k-space. Left: Anisotropic gap in ^{3}He -A phase vanishing at the poles. Right: Fully isotropic energy gap in ^{3}He -B phase.

with m^* being effective mass of the excitation and ϵ_F Fermi energy. The existence of the isotropic energy gap leads to the exponential temperature dependence of the excitation population in ^{3}He -B phase:

$$N_{excit} \sim e^{-\frac{\Delta}{k_B T}}, \tag{1.11}$$

The nature of the excitation spectrum further allows effects, which do not exist in He II, such as screening of the excitations by the superfluid flow in the form of Andreev reflection [57, 58].

Temperature dependence of the thermal excitation population can be effectively used for the thermometry in the superfluids, especially in ^{3}He having exponential dependence, via measurement of the damping forces acting on a solid resonator due to ballistic collisions [5]. In the recent work of Lancaster group [59], employing a nano-metric resonating cantilever in He II, they experimentally showed the cross-over between the hydrodynamic behaviour in the two-fluid regime and ballistic behaviour with mainly roton contribution at higher temperatures and mere phonon contribution at the lowest temperatures, down to the units of millikelvins, in accordance with Equations 1.8 1.9.

1.1.4 Quantized Vortices

In previous, we have introduced, in closer detail, the description of normal component of superfluid helium. Let's further concentrate on the behaviour of superfluid component of He II. As discussed above, superfluid component can be identified with the macroscopical quantum mechanical ground state. It is therefore advantageous to introduce the macroscopic wave function $\Psi(\mathbf{r}, t)$, as originally done by Tizsa:

$$\Psi(\mathbf{r}, t) = \sqrt{\rho_s(\mathbf{r}, t)} e^{i\Phi(\mathbf{r}, t)}, \tag{1.12}$$

with superfluid density $\rho_s(\mathbf{r}, t)$ and macroscopic phase $\Phi(\mathbf{r}, t)$, both as a function of time and spatial coordinate.

Using this description, we can obtain the superfluid velocity $\mathbf{v}_s(\mathbf{r},t)$, as a fraction of superfluid mass flux $\mathbf{J}(\mathbf{r},t)$ and superfluid density, in following form:

$$\mathbf{v}_s(\mathbf{r},t) = \frac{-i\hbar}{2m_4\rho_s(\mathbf{r},t)}\Big[\Psi^*(\mathbf{r},t)\nabla\Psi(\mathbf{r},t) - \Psi(\mathbf{r},t)\nabla\Psi^*(\mathbf{r},t)\Big] = \frac{\hbar}{m_4}\nabla\Phi(\mathbf{r},t) \quad (1.13)$$

with m_4 being a mass of helium atom. This equation should prescribe the existence of only potential flows of superfluid component making rotation of superfluid velocity $\nabla \times \mathbf{v}_s$ identically zero.

It is, nonetheless, possible to arrive with the rotational flow of the superfluid component if a multiply connected region of superfluid is considered. Having this assumption in mind, we can discuss the circulation of superfluid component Γ, defined as the closed loop integral of superfluid velocity:

$$\Gamma = \oint_L \mathbf{v}_s(\mathbf{r},t)\mathbf{dl} = \frac{\hbar}{m_4}\oint_L \nabla\Phi(\mathbf{r},t)\mathbf{dl}, \quad (1.14)$$

using 1.13. Considering the properties of the macroscopic wave function, being uniquely defined in space and time, the change of its phase after passing around any closed loop must be equal to the integer value of 2π. As a result, applying it to 1.14 leads to the condition for quantization of circulation in superfluid component in He II 1.15 by integer number of circulation quanta $\kappa \approx 10^{-7}$ m^2/s.

$$\Gamma = n\frac{\hbar}{m_4} = n\kappa, \quad (1.15)$$

The rotational flow may be therefore realized in superfluid component, but only in the form of superfluid circulating around a non-superfluid singularity, as multiply connected region is required and possessing integer number or circulation quanta. Described structures are called quantized vortices and in He II take the form of line topological defects of superfluid, which represent the vortex core. The energy of the unit length of quantized vortex ϵ_v is then given as kinetic energy of the superfluid component circulating around the core, having the radius a_0, see 1.16. However, with the subatomic core size, of the order of Å, it cannot be interpreted simply as normal component. It is rather defined by the coherence length of the macroscopic wavefunction. The spatial distribution of superfluid density and superfluid velocity away from the vortex axis is shown in Fig. 1.6.

$$\epsilon_v = \int_{a_0}^{b} \pi\rho_s v_s^2 r dr = \frac{n^2\rho_s\kappa^2}{4\pi}\ln\frac{b}{a_0}. \quad (1.16)$$

Single quantized vortex energy ϵ_v also weakly depends on the interaction with the container walls or with other vortices in the volume, being in distance b. From the equation 1.16 further follows, that in He II only singly quantized vortices exist as they are energetically favourable. This is, however, not true in superfluid ^{3}He , where e.g. half-quantizes vortices or other exotic types of superfluid defects are possible [56]. As vortex cores represent topological defects in both discussed superfluids, there are additional important restrictions, defining their dynamical behaviour. It is not allowed for the quantized vortex to start or end inside the bulk superfluid. The only possible configurations are such, that place vortex ends on the free liquid surface or present solid surface (of the container or of the submerged

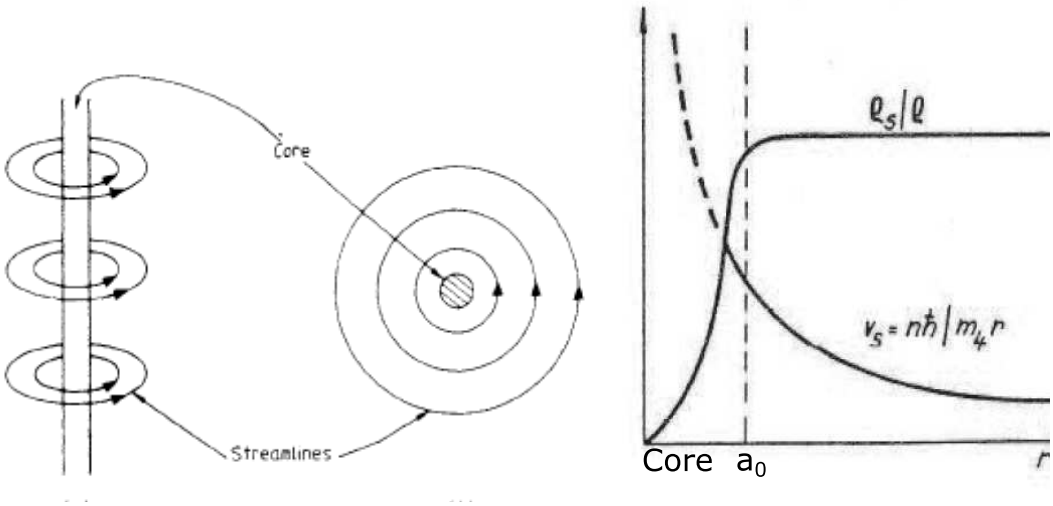

Figure 1.6: Left: Scatch of the quantized vortex with hollow core and superfluid component circulation around it. Circulation must be quantized by $\kappa \approx 10^{-7}$ m^2/s. Right: The structure of quantized vortex with ρ_s and $\boldsymbol{v}_s$ spatial dependencies. The dashed line represents the core's dimension.

body) or in the form of a closed loop propagating in the bulk [60]. Another option, also supported by the continuity of the superfluid phase, is a quantized circulation around fully submerged bodies, e.g., nanometric cantilevers [59], substituting the vortex core.

Similar restrictions hold for the superfluid ^{3}He , with circulation quanta being $\kappa_{He3} = \hbar/2m_3 \approx 6.6\times10^{-8}$ m^2/s, as Cooper pair consists of two atoms with the mass m_3, but with more complex nature of the possible vortex structures. Especially, in the case of ^{3}He -A phase various vortex structures are possible, such as "continual unlocked vortices" having a "soft" core, without the full suppression of the order parameter (superfluid wave function), "locked vortices", 2D "vortex sheets" or "singular vortices" with the "hard" core (representing the singularity of the A-phase order parameter), being the closest relative in ^{3}He -A to He II quantized vortices. Recently, also theoretically predicted half-quantum vortices have been experimentally confirmed [61]. A more detailed description of these vortices is far beyond the scope of this work but can be found in [62].

All possible vortex structures in ^{3}He -B have a "hard" core. However, the coherence length is much larger than in the case of He II, being of order tens of nm depending on the pressure. Quantized vortices in ^{3}He -B are therefore macroscopic objects, with the core being "filled" by normal component or possibly other superfluid phases, unlike the hollow core of vortices in He II and can also be connected with the vortex mass [63].

1.2 Turbulent flows in quantum fluids

Regarding fluid mechanics research, the study of turbulent flows contains some of the most important problems with applications in everyday life e.g., aerodynamics and acting drag forces, fluid transfer, energy transport in the fluid, large-scale flows in oceans or atmosphere, and many others. In fact, most of the real flows in nature are turbulent. However, there is still no rigorous definition of turbulence and it is rather described by its characteristic features, namely chaotic pressure and velocity changes, stochastic behaviour, diffusive flows and the presence of rotational flows and vortex structures. In contrast with turbulent flows, we discuss laminar or strictly potential flows. Describing the transition between the two and characterizing the initial instability occurrence is one of the most important tasks to understand fluid behaviour. For the first time, it was studied for the pipe flows in 1883 by Osborne Reynolds[64]. After the initial instability, upon raising the flow velocity, a developed turbulent flow is built up, typically containing vortex structures on a wide range of length scales and connected with excess drag (on submerged body) or dissipation (in the fluid). As He II may consist of two components with very different properties, let's first discuss the turbulent flows of each separately.

1.2.1 Classical turbulence

Discussing the normal component of He II, as an incompressible viscous fluid, we can simply use all classical models known for fluid mechanics [32]. The flow of normal component must obey the Navier-Stokes equations, which for the steady pipe flows or steady flows past the body introduce a single critical parameter, called Reynolds number (Re). This parameter depends on both the properties of the body or pipe, given by its characteristic dimension D; and the properties of the fluid, given by the flow velocity V and its kinematic viscosity ν. Its value distinguishes between previously discussed flow regimes and prescribes the instability onset as giving a ratio of inertial and viscous forces. The critical flow parameter for classical fluid may of course differ, depending on the flow geometry. For example, it may be the Keulegan-Carpenter number (K_C) in the case of oscillatory flow past a smooth body [65]. Although, the presence of sharp corners or rough surface of the body leads again to Re, being the critical parameter also in the oscillatory flow, with characteristic dimension represented by viscous penetration depth $\delta = \sqrt{2\nu/\omega}$, dependent on angular frequency ω. When discussing normal component of He II, this critical parameter should be referred to as Donnelly number (Dn) A.2.

When the critical value of the flow governing parameter is reached, the transition from originally laminar flow starts and the first individual vortex structures start to occur. In the case of a flow past the body the typical critical value of this parameter is of the order of unity. In channel flows it is of the order of 10^3. When increasing the flow intensity past this transition, fully turbulent flow containing many vortex structures of different sizes will gradually develop having all discussed characteristic properties of the turbulence.

The developed turbulent flow of classical fluid may be further understood describing the energy $E(k)$ distribution, as a function of wavenumber k, in the

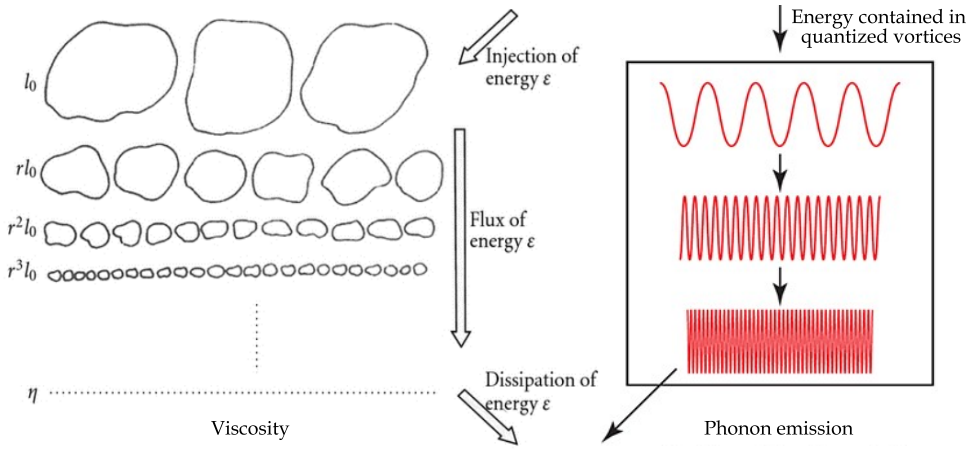

Figure 1.7: Left: Classical process of energy transfer in viscous fluid. Kinetic energy is injected and stored at large scales and then transferred via dissipationless Richardson cascade process towards Kolmogorov length scale η_K, where viscous dissipation operate. Right: Viscous dissipation process is not present in inviscid superfluid component. The energy stored in quantized vortices, which may at large scales imitate the Richardson cascade, must be dissipated via different processes, e.g., propagation of the discrete cascade of Kelvin waves on single vortices leading to dissipation over phonon emission at high frequencies.

flow, looking at different length scales. The energy is inserted into the flow typically at the large scales - energy-containing scale, and than transferred via the Richardson cascade process [66], to a small scales, where it can be dissipated, see Figure 1.7. The rate of energy dissipation ϵ, in steady state equal to energy injection, is given by the vorticity, $\omega = \nabla \times \boldsymbol{v}$ as:

$$\epsilon = -\frac{dE}{dt} = \nu \langle \omega^2 \rangle. \tag{1.17}$$

The length scale, small enough that the viscous forces overcome the inertia of the eddies and the dissipation can take place, is called the Kolmogorov's length scale:

$$\eta_K = \left(\frac{\nu^3}{\epsilon} \right)^{\frac{1}{4}}. \tag{1.18}$$

There is no significant energy dissipation during the cascade decomposition of the eddies towards Kolmogorov's scale and for each step of the cascade $l_n / l_{n+1} = const.$ holds [67], where l_i denotes length scale of each step of Richardson cascade. It was Kolmogorov who first introduced a detailed theory of turbulence [68, 69], including the description of energy distribution in the non-dissipative range, also called inertial range, of the energy spectra:

$$E(k) = C \epsilon^{2/3} k^{-5/3}, \tag{1.19}$$

with C being a universal Kolmogorov constant of the order of unity.

When the turbulence generation mechanism is switched off, we can observe its temporal decay. Solving for the time evolution of the total turbulent energy E

$= \int E(k)dk$. In the first stage of the decay, the energy-containing scale increases and eventually saturates, reaching the limiting scale of the vessel dimension D. Now, using Kolmogorov's shape of inertial range 1.19, occupying most of the energy spectrum and 1.17, we can get the decay of vorticity in the following form [70, 71]:

$$\omega(t) = \frac{D(3C)^{3/2}}{2\pi\sqrt{\nu}}(t + t_0)^{-3/2}, \tag{1.20}$$

with t_0 representing the virtual decay start, being the origin time of infinitely intense turbulence decay. Further detailed description of classical turbulent flows can be found in various textbooks [66, 72].

1.2.2 Quantum vortex dynamics

The turbulent flow, strictly in superfluid component is much different to the classical case due to quantum restrictions. The only possible rotational flow is allowed in the form of quantized vortices 1.1.4. The most natural way to create the quantized vortices is to induce a rotation to the superfluid by the external source. Many experiments with the rotating He II vessels have been performed to verify that superfluid component can mimic the solid body rotation by creating the triangular mesh of straight, parallel to the axis of rotation, vortex lines [73], see Figure 1.8. This has an analogy in superconductors of the second type with a mesh of quantized magnetic flux vortices. The critical angular velocity Ω_c for the creation of single quantized vortex in the vessel of radius R is then given by Feynman criterion [74]:

$$\Omega_c = \frac{\kappa}{2\pi R^2} ln\Big(\frac{R}{a_0}\Big), \tag{1.21}$$

Further speeding of the rotation then results in the creation of the quantized vortex mesh with the density (number of vortices per unit area) equal to $2\Omega/\kappa$.

The creation of a quantized vortex in the flow of the superfluid is connected with the instability, typically due to a critical flow velocity. The seeding perturbations, which are constantly created by thermal fluctuations, may persist in the fast flow and lead to vortex creation. Such a vortex generation mechanism, without the existence of an already stable seeding vortex, represents the intrinsic vortex nucleation. In the case of He II, vortex loops may nucleate at critical Feynman velocity [76] (where the vortex nucleation is energetically favourable) of the order of tens of m/s. The vortex nucleation is favourable around sharp corners in the case of flow past a body, where the velocity is enhanced [32]. The vortex loops may also intrinsically nucleate around fast ions flying through the superflluid [77–79] due to quantum tunnelling, at Landau critical velocity [40, 80] (representing a limit of superfluidity as discussed in 1.1.3), being also of the order of tens of m/s. However, much smaller critical velocities are typically observed, because intrinsic nucleation in He II is rarely a case in real experiments, as preparation of remnant-vortex-free state is a non-trivial task [81, 82].

The first vortices are nucleated already during the superfluid transition. It is partially governed by the Kibble-Zurek type mechanism[83], but more importantly due to conventional hydrodynamic mechanisms [84]. Additionally, a small number of quantized vortices might be generated in the vessel by natural radioactivity, due to ionization of the liquid [85], or from the rotation velocity of

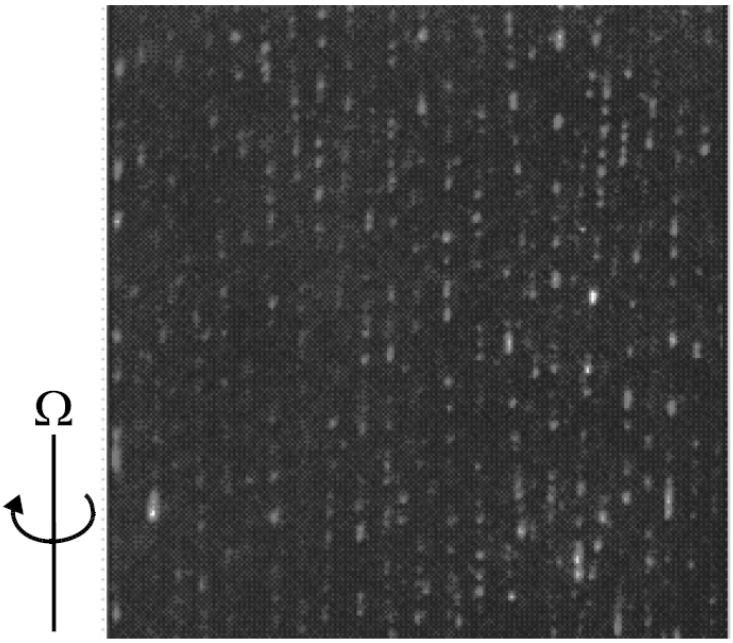

Figure 1.8: Direct visualization of the uniform mesh of quantized vortices as occur in rotating vessel [75] at velocity Ω.

the Earth. With respect to the quantized vortex core size in He II, all real surfaces must be considered very rough, having a great number of possible pinning sites. It is, therefore, extremely difficult to remove remnant vortices, which are pinned to all submerged surfaces and prepare conditions for intrinsic nucleation in the flow. However, it does not limit the study of intrinsic nucleation by the flying ions happening in the bulk.

This is not true if we consider the nucleation of the quantized vortices in ^{3}He -B. Due to the much larger coherence length - core size, the statement about the impossibility to create a smooth surface does not hold. However, again because of the larger core size, the critical velocity for the intrinsic nucleation is much smaller.

If we consider the preexisting seeding loops, we may discuss an extrinsic vortex generation, where the energy is transferred to existing vortices, which then grow, rather than new vortices are being nucleated. Therefore, the possible mechanisms of such generation of quantized vortices are much different to previously mentioned. The typical critical velocities for extrinsic generation of quantized vortices in the flow of He II are the order of magnitude lower in the range of cm/s. In the case of oscillatory flows a frequency scaling of such critical velocity $v_c \approx \sqrt{\kappa 2\pi f}$ was further confirmed in many experimental works [86, 87] or A.2. One of the typical processes which are responsible for the vortex stretching and sub-sequent emission of the vortex loops is the Donnelly-Glaberson instability [88–90], resulting from induction of the helical wave perturbances (Kelvin waves) on quantized vortex due to parallel passing flow.

When quantized vortices are generated in greater number, they start to interact and create a chaotic bundle forming a developed turbulent flow in superfluid

component. The same can be obtained when abruptly stopping the vessel rotation. When vortices in the bundle get close to each other, they may reconnect and exchange their segments. A single vortex may even reconnect within itself and create a free vortex loop, which then may travel through the superfluid bulk. A localized bundle of quantized vortices, therefore, emits free vortex loops. The velocity of such loop depends inversely on its radius and is induced by the interaction of its opposite segments having anti-parallel circulation. Interaction of the two parallel vortices with the same direction of the circulation results in joined rotation of the quantized vortices around their common centre. If the vortex gets to the vicinity of the solid wall, it will further interact with the mirror vortex behind the boundary, having opposite directions of circulation. More details on the dynamics of the quantized vortices in He II can be found in [2, 60].

In order to define the intensity of the turbulence in superfluid component, we can use the quantity L, vortex line density, giving the total length of the vortex cores per unit volume. Another important quantity, defined as the inverse square root of vortex line density describes the important length scale of superfluid turbulence called intervortex spacing $l = 1/\sqrt{L}$, giving the mean distance between the vortex lines. The development of the random vortex bundle is described by Vinen's equation [91]:

$$\frac{\partial L}{\partial t} = \alpha\chi_1 v_{ns} L^{\frac{3}{2}} - \frac{\chi_2\kappa}{2\pi} L^2. \tag{1.22}$$

Here, the first term describes the generation of the quantized vortices by loop growth in thermal counterflow. This is a rather specific mechanism and does not apply at low temperatures in a ballistic regime. The second term describes the decay of quantized vortices, happening upon the vortex collision and annihilation of opposite segments in the bundle. Dimensionless constants χ_1 and χ_2 are of order unity and α describes the interaction between He II components (will be further discussed later). The temporal decay of this type of turbulent flow, resulting from turning the first term of 1.22 off, is different to what we introduced for the classical turbulence 1.20. The decrease of the vortex line density governed by vortex annihilation in the bundle should evolve inversely with time [2, 92] as:

$$L(t) = \left[\frac{1}{L_0} + \frac{\chi_2\kappa}{2\pi} t\right]^{-1}, \tag{1.23}$$

with L_0 denoting the initial vortex line density of the steady-state turbulence.

The question remains, how can the energy of the single quantized vortex be dissipated in the absence of viscosity and if a collision with other vortices is improbable? This may happen, when helical wave perturbance - Kelvin wave, defined by wavenumber k, is induced on the vortex line propagating along it. The energy of the wave is then propagated towards higher frequencies in a non-linear cascade-like process as theoretically predicted [21–25] (this may be considered as an analogy to Richardson cascade in classical turbulence), see Figure 1.7. At high enough frequencies the energy may then be dissipated over emission of thermal excitations [93] in He II or excitation of core bound states [94] in ^{3}He -B. The experimental verification of the Kelvin wave cascade existing on quantized vortex in superfluid ^{4}He is still missing but recent measurements in Helsinki with rotation-modulated wave-turbulence in superfluid ^{3}He are pointing towards this phenomenon [95]. Additionally, our new experiments in collaboration with the

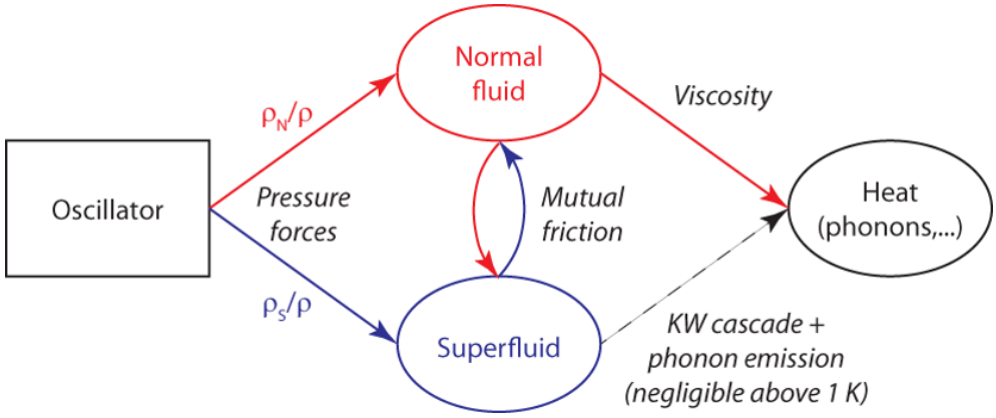

Figure 1.9: Schematic picture of possible energy flow in superfluid helium. Energy input may be realized, for example, by moving oscillating object, thermally driven flow or other, into one or both components. The mutual exchange of the energy between the components is then mediated by mutual friction force, which may operate in one direction only. Final loss of the energy can then be directed to either of the dissipation channels (i) viscous dissipation in normal component dominating at temperatures above 1 K and not existing in zero-temperature limit (ii) energy transfer in Kelvin wave cascade terminated by phonon emission.

Helsinki ultra-low-temperature group, with a single quantized vortex trapped on a small resonating device, see 4.4, seem to be leading to similar results, which will be published soon.

1.2.3 Mutual friction force

Now, that we have introduced the turbulent behaviour of both components separately, let's discuss the more realistic situation, switching the interaction between the components on. As mentioned before 1.1.2, there is a force $\boldsymbol{F}$ coupling the motion of the two components, see Equations 1.4 1.5, called mutual friction force. It originates from the scattering of normal component on the quantized vortex core and is acting to align the flow of the components to be parallel. It was first studied in thermal counterflow experiments [91, 96–99] introducing it in the following approximate form, dependent on a cube of the counterflow velocity $\boldsymbol{v}_{ns}$ and the temperature-dependent Gorter-Mellink parameter A.

$$F_{GM} = A\rho_s\rho_n(v_s - v_n)^2(v_s - v_n). \tag{1.24}$$

The geometry of the straight aligned vortex lines, existing under the rotation, is however, more straightforward for the study of this phenomenon, as was later done by Hall and Vinen [49, 100]. In their experiments with the helium vessel rotating at angular velocity Ω, they arrived at:

$$F_{VH} = -B\frac{\rho_n\rho_s}{\rho}\hat{\Omega} \times \Big(\Omega \times (\overline{v}_s - \overline{v}_n)\Big) - B'\frac{\rho_n\rho_s}{\rho}\hat{\Omega} \times (\overline{v}_s - \overline{v}_n), \tag{1.25}$$

using a coarse-grained averaging of the fluid velocities over regions exceeding the mean inter-vortex distance. The tabulated values of experimentally determined

mutual friction parameters B and B' may be found in [47]. Finally, $\hat{\Omega} = \Omega/\Omega$ represents the unity vector in the direction of the rotation. When investigating dissipative phenomena only, the prescription of mutual friction force may be further simplified, using experimentally shown vortex line density dependence on the velocity, when generated in the thermal counterflow [46], and ignoring the second term in 1.25, which represents inertial forces and thus does not lead to dissipation of energy, to a form [74, 101]:

$$F_L = -B\kappa\frac{\rho_s\rho_n}{2\rho}Lv_{ns}. \tag{1.26}$$

The existence of the coupling between He II components has important consequences for the dynamics of the energy flow in the fluid. In the two-fluid regime, mutual friction allows both-way energy transfer between the components, as schematically shown in Figure 1.9. It acts on the quantized vortices in order to polarize the vortex bundle into large-scale eddies following the vortex structures in the normal component and even form a Richardson cascade-like system. It can be therefore expected, that at finite temperatures, the dominant dissipative channel will be represented by the viscous drag in the normal component. Turbulent energy stored in the superfluid component, in the form of quantized vortices, can be transferred via mutual friction onto the normal component. However, the flow of energy and dissipation via Kelvin wave cascade on the single vortices is not disallowed and will dominate at low temperatures in the absence of normal component continuum.

1.3 Quantum turbulence

Now, that we have introduced flow regimes and their peculiarities in both components of the superfluid separately, together with the mutual interaction between the two, we can discuss the quantum turbulence phenomena. It should be understood as any turbulent motion in the quantum fluid and can consist of beforehand mentioned turbulent structures. We will follow the recently published phenomenological description of quantum turbulence A.1, with the experimental contribution of the Thesis author, see A and bring forward the most important ideas.

First, we have to introduce all relevant length scales. Starting from the largest, we have a limiting dimension of the vessel size D, where no larger structures may exist. The energy input is realized at the scale M, which may differ significantly regarding the turbulence driving mechanism. The dissipation in normal component happens at Kolmogorov viscous scale η_K. If $M < \eta_K$ no turbulent flow may develop in normal component. We can further introduce a new length scale denoted quantum length scale l_Q defined as:

$$l_Q = \left(\frac{\kappa^3}{\epsilon}\right)^{\frac{1}{4}}. \tag{1.27}$$

It is an analogy to classical Kolmogorov scale 1.18, where circulation quantum κ takes place of the viscosity ν, having the same dimension and even similar values regarding the two-fluid regime of He II. The quantum length scale is comparable to the inter-vortex distance and marks the onset of the quantum character of the flow, where quantization of circulation becomes essential. It may be understood as a cut-off length for any classical-like description of the flow and its presence implies that no quantum flow may be fully described by a classical analogy. This implies, that the full component coupling via mutual friction below the quantum length scale is not possible. Finally, we have a smallest length scale l^*, where dissipation processes on single vortices, as described in 1.2.2, takes place.

At finite temperatures, the developed turbulent flow of He II driven at reasonably large scales, $M \gg l_Q$, consists of both large-scale eddies in normal component; and vortex bundle in superfluid component. In this case, the mutual friction force causes the vortex bundle to polarize and form large vortex structures imitating the normal component eddies. These structures can then follow the Richardson cascade process resulting in the same Kolmogorov shape of the inertial range of the energy spectra 1.19 in both components. At all scales above l_Q, the system may be in first approximation described as a single quasi-classical fluid possessing effective viscosity ν_{eff}, dependent on the temperature and the energy dissipation is given as $\epsilon = \nu_{eff}(\kappa L)^2$. At high temperatures, dissipation happens dominantly by the viscous channel at η_K and the energy in superfluid component is transferred to this channel via dissipative mutual friction force. Energy dissipation by single vortices is not important here as the Kelvin waves are heavily damped by mutual friction. We call this turbulent system a quasi-classical or Kolmogorov turbulence. Finally, the decay of the vortex line density in this system is similar to the classical case [71], see equation 1.20:

$$L(t) = \frac{D(3C)^{\frac{3}{2}}}{2\pi\kappa\sqrt{\nu_{eff}}}(t + t_0)^{-\frac{3}{2}}. \tag{1.28}$$

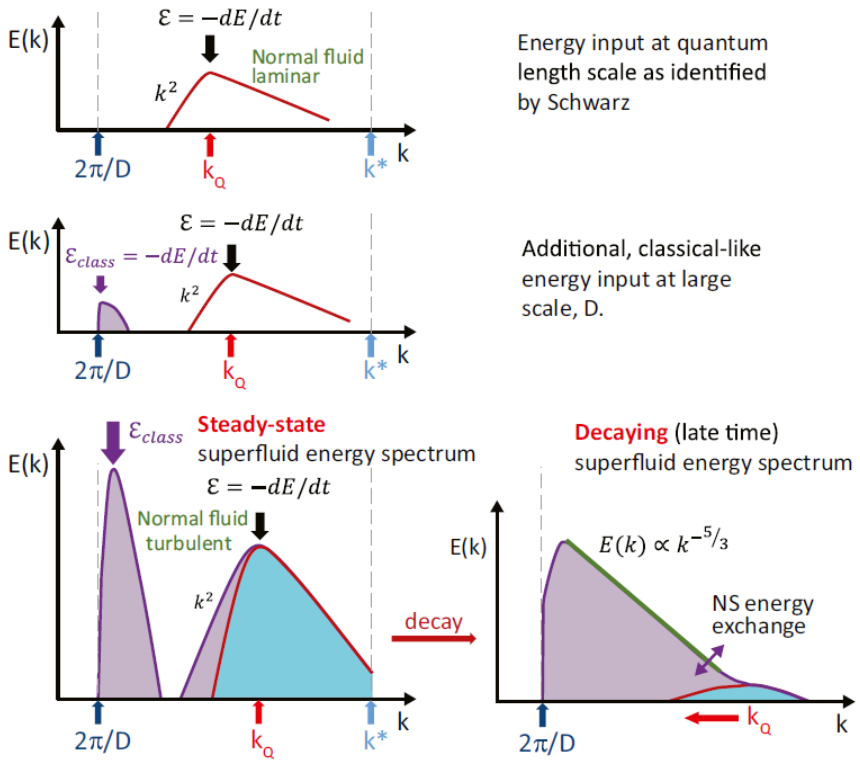

Figure 1.10: Schematic log-log view of the energy spectra of the steady-state of thermal counterflow, in the channel, with increasing intensity (from top to bottom), having energy input ultimately at two different length scales, quantum length scale and size of the channel D. The quantum length scale is represented by k-vektor $k_Q = 2\pi/l_Q$ and energy spectrum termination scale by $k^* = 2\pi/l^*$. Inertial range with Kolmogorov scaling $k^{-5/3}$ develops during the temporal decay initially of Vinen type $L \propto t^{-1}$ and changing to Kolmogorov type $L \propto t^{-3/2}$ for later times upon this process.

However, the picture changes dramatically, if the turbulent flow is driven at small scales of the order or smaller than l_Q, e.g., by a small quartz tuning fork with prong cross-section of (75x90) μm^2 or using ultrasound. For this case driving mechanism operate at scales already smaller than η_K (as $\nu \approx \kappa$) and classical turbulent flow in normal component cannot develop in the first place. The temporal decay of such a system will be much different from the previous, as the main dissipation mechanism would be a local decay governed by the annihilation of the vortex lines, leading to $L(t) \propto t^{-1}$ as described in 1.2.2 by equation 1.23. However, the viscous dissipation channel is still operational, at these temperatures and dominates, when the density of the tangle decreases significantly. The experimental realization of such decay is shown in Figure 1.12. This type of turbulent system is then called ultra-quantum or Vinen type of quantum turbulence. We can again introduce the effective viscosity for this turbulent fluid, where $\epsilon = \nu'(\kappa L)^2$, but now describing only turbulent superfluid component consisting of the vortex bundle given as:

$$\nu' = \frac{\chi_2 \rho_s \kappa}{8\pi^2 \rho} \ln\left(\frac{l}{a_0}\right). \tag{1.29}$$

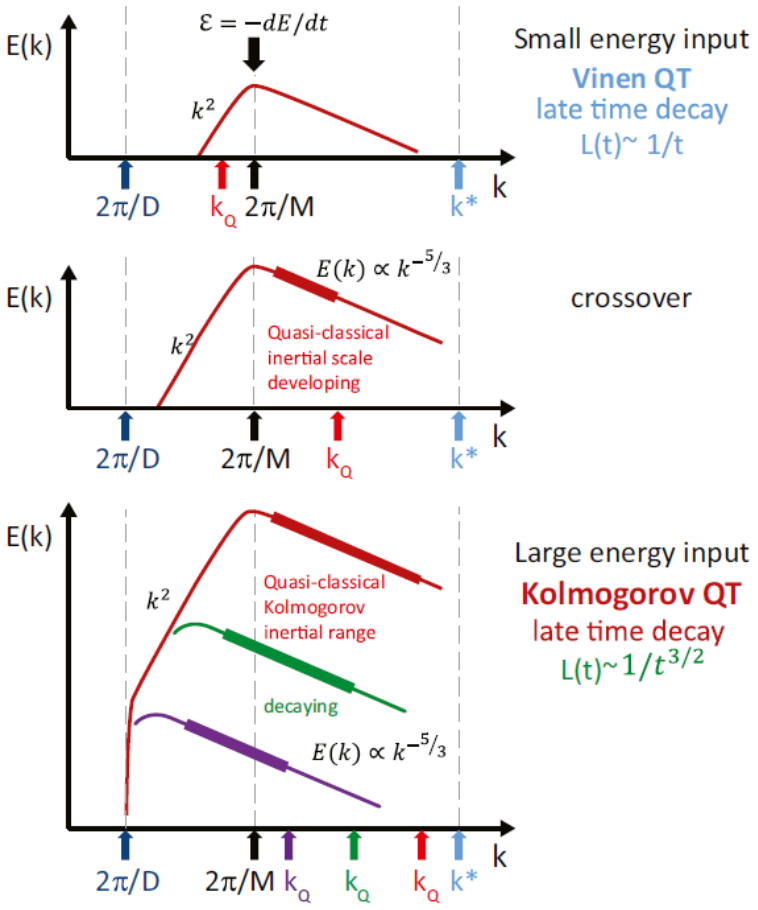

Figure 1.11: Schematic log-log view of the energy spectra of quantum turbulence in zero-temperature limit. The turbulent regime depends on the interplay between energy input scale M and quantum length scale, represented by k_Q, dependent on energy input. For small energy input, we will observe Vinen type of quantum turbulence. Upon rising the energy input, quasi-classical turbulence of Kolmogorov type develops. During the decay, energy flow decreases together with k_Q.

Both ν_{eff} and ν' can be obtained from the experimental realization of the temporal decay of the corresponding type of turbulent flow. Discussion on the two presented forms of quantum turbulence may be found also in [102–104].

It is further possible, to have an energy input on more scales of the spectrum simultaneously. This situation may be realized, e.g. in channel thermal counterflow, having an energy input at the level of l_Q in superfluid component via reconnection-based mechanism [105, 106] and energy input at the scale of order channel size D via instability in normal component flow. The energy spectrum of the steady state of such a case is illustrated in Figure 1.10. The classical spectrum is, however, missing the Kolmogorov inertial range 1.19 as this energy is also transferred by mutual friction to the creation of the polarized quantized vortex structures and the coupling is not perfect [107]. Upon switching the driving mechanism off, the initial Vinen-like decay $L(t) \propto t^{-1}$ occurs as vortex bundle annihilation of energy stored around quantum length scale dominates. During

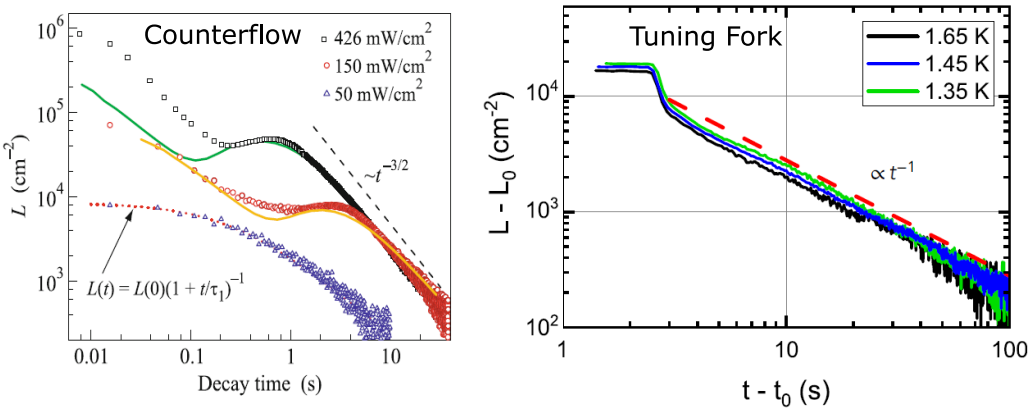

Figure 1.12: Left: Temporal decay of thermal counterflow in the channel. Initially Vinen type $L \propto t^{-1}$ of decay transforms over short vortex line density increase (a "bump") to Kolmogorov type $L \propto t^{-3/2}$. At the smallest drive, 50 mW/cm^2 only Vinen type is observed as normal component does not experience flow instability, and energy input at large scales is therefore missing. Further description can be found in the text. Right: Temporal decay of mechanically driven turbulence at small scales $\approx l_Q$ around small oscillating quartz tuning fork. The decay is of Vinen type at all times. Meaning of L_0 and t_0 can be found in the main text.

this time, quasi-classical cascade develops building the inertial energy range. As the Richardson cascade develops towards smaller scales, energy input from normal component into quantized vortices causes a temporal rise of L resulting in the "bump" in the decay [108, 109]. Afterwards, flow has a quasi-classical energy spectrum and Kolmogorov-like decay $L(t) \propto t^{-3/2}$ follows until the late times. Experimental realization of such temporal decay is shown in Figure 1.12

Finally, one may expect that getting rid of normal component, cooling the system to a zero-temperature limit, should result in mere ultra-quantum turbulence. However, this is not necessarily true. The resulting type of the turbulent flow in this regime depends on the generation intensity affecting the ϵ and therefore the value of quantum length scale l_Q and on the scale at which the flow is driven M. It is the interplay between these two scales, which resolves if quasi-classical or ultra-quantum turbulent regime operate as schematically shown in Figure 1.11. In the case that $M < l_Q$ there is no possible effect leading to the creation of quasi-classical form and the turbulence is always of Vinen type. This may be obtained when driving the flow at a low enough scale (M is small) or with low enough energy input (l_Q is big). However, if the opposite case, M being larger than l_Q, quasi-classical inertial range will develop over the polarization of the bundle of quantized vortices resulting in Kolmogorov type of turbulence. The final dissipation channel here, in the absence of viscosity, must be the phonon emission from single vortices at scales below l^*.

1.4 Quantum turbulence detection

Let's now discuss the experimental techniques, which allow us to directly or indirectly visualize above described flows of quantum fluids. These techniques work well as verification tools for the presented theoretical models. For the direct visualization of the turbulent superflows, similarly to classical visualization methods, we may use "Eulerian" particle image velocimetry (PIV) or "Lagrangian" particle tracking velocimetry (PTV) techniques. The difference with a classical case is in the suitability of the tracker particles (tracers). With liquid helium having a density of about seven times lower than water, there is a limit on the mass of the tracers [110, 111]. In He II, micrometer-sized frozen particles of hydrogen or deuterium are broadly being used [112–115] or alternatively an excimers He^*_2, being neutral helium triplet molecules [116, 117] with the size of several Å. The necessity of the optical access for this method, as tracers are typically illuminated by the laser sheet and tracked by the high-speed camera, represents a technical issue if very-low temperatures (below 1.2 K) are being aimed for. Having the particles interacting with both fluid components, being pulled by normal component and trapped by quantized vortices at the same time, and affecting the flow itself, special care must be taken when interpreting the results. Despite these limitations, very important results are being obtained by the visualization of the superfluid flow. One of many such results is the first direct visualization of the regular vortex mesh (1.2.2) in rotating vessel [75], see Figure 1.8.

Creating helium ions, using a radioactive source or sharp emission tip and their fine manipulation by electric field can be also effectively used to probe turbulence in superfluid component. Knowing the interaction cross-section vortex line density may be measured, as done originally by Milliken and co-authors [118, 119]. In their experiments, they were able to measure the free decay of the vortex bundle or characterize vortex bundle in the channel counterflow. This technique is still being regularly used in Manchester group [104, 120, 121].

In ^{3}He , we can benefit from an extremely powerful detection method of nuclear magnetic resonance (NMR), thanks to the magnetic properties of the superfluid. In analogy to spin systems in solid bodies and biomolecular systems, we can extract very detailed information about the superfluid ^{3}He structure from the relaxation of its spin system. This technique is very suitable for the study of different superfluid phases as they differ by the texture of the spin-orbital space. Even detection of the different phase existing inside the core of the quantized vortex is possible as shown in [122]. More information on the usability of the NMR for superfluid ^{3}He research might be found in [123–125].

Finally, we will mention the second sound attenuation technique, allowing the measurement of vortex line density in superfluid component of He II and the use of small mechanical resonators able to probe turbulent flows in both He II components as well as in superfluid ^{3}He . These mechanical devices allow detection of the turbulence generated by the probe itself in the means of energy loss or alternatively detection of externally driven turbulent flows via their mutual interaction. We will pay detailed attention to these two techniques in the following sections, as they represent the vast majority of detection tools used for the analysis of the studied flows presented in this Thesis.

1.4.1 Second sound attenuation

The hydrodynamic properties of He II in the two fluid regime, as described in 1.1.2, allow the existence of a number of non-classical wave modes. For the detection of quantized vortices, we can use a wave mode called second sound, whose existence was experimentally confirmed by Peshkov [126]. It can be described as a counter-oscillation of normal and superfluid components against each other. The standing wave can be therefore understood as local oscillations of density ratio of the components ρ_s/ρ_n or alternatively a spatial temperature or entropy wave. However, the total density ρ distribution is not affected unlike in the case of the first sound. Being based on the oscillatory flow of the normal component, second sound can be advantageously used to detect the quantized vortices due to scattering on their cores. The presence of the vortices in the probed volume can therefore result in attenuation of the second sound wave.

The mutual interaction of second sound with quantized vortex matrix was originally studied in rotating cryostat experiments [49, 100], finding the geometrical dependence on the angle Θ between sound propagation direction and vortex lines. The attenuation was found maximal in the perpendicular case, but being zero if second sound propagated in parallel to the vortex cores, having $\sin^2(\Theta)$ dependence. Assuming a fully random isotropic and homogeneous vortex tangle, we can arrive at the following formula to obtain the vortex line density in the experiment:

$$L \cong \frac{6\pi\Delta f}{\kappa B}\Big(\frac{A}{A_0} - 1\Big), \tag{1.30}$$

where measurement of calibration peak in the non-vortex state (omitting now the presence of remnant vortices), having amplitude A_0 and width (FWHM) Δf, is necessary. When driving the turbulence, generating vortex lines, the measured amplitude of second sound standing wave A will decrease. The mutual friction parameter B and circulation quantum κ are described in previous sections. A more detailed description of this detection technique can be found in [127]. In Figure 1.13, we show the typical series of the measured second sound peaks in gradually intensifying turbulent flow in superfluid component of He II.

Taking the described properties of the second sound wave, it may be practically driven either mechanically or thermally. In the case of the thermal generation, by sine-shaped heat pulses, there is an issue with the average DC heat input, which might affect the studied flow. However, small localized detectors with limited heat input are being developed [128]. It is, however, technically more advantageous to use mechanical apparatus based on electrically driven oscillations of the "superleak" - a porous wall allowing for the passage of only superfluid component. Pair of such detectors can be used in closed-volume geometry, e.g. in the flow channel, one acting as a transducer and the second as a receiver. A model picture of one such decomposed detector unit based on the movable gold-coated porous membrane stretched on the brass electrode is shown in Figure 1.14.

The second sound attenuation technique is well established for the study of approximately homogeneous isotropic turbulent bundles, occurring for example in channel counterflow experiments. The sensitivity of the wave mode depends on its spatial distribution being highest in the anti-nodes, where the velocity of the components oscillation peaks. Therefore probing more low-frequency modes

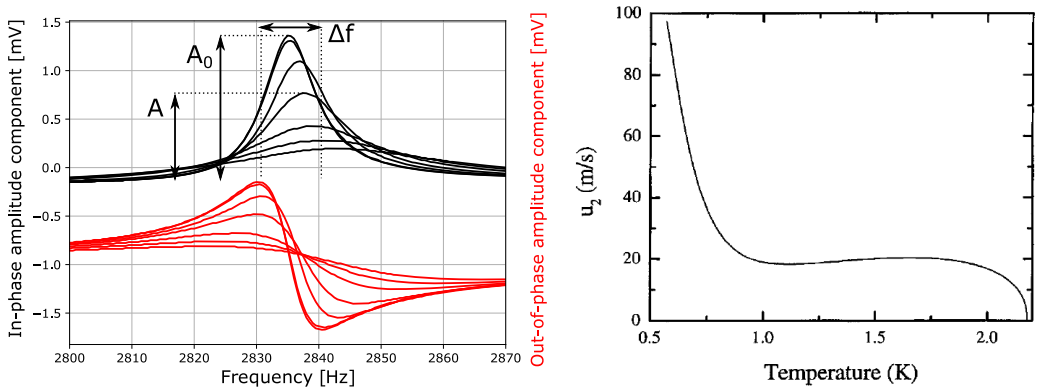

Figure 1.13: Left: Overview of second sound resonance attenuation. Series of in-phase (black) and quadrature (red) signal components are being attenuated as amount of quantized vortices in volume rise. A_0 denotes the original amplitude in non-vortex state. Right: Temperature dependence of second sound velocity in He II.

may lead to a better understanding of the quantized vortex distribution, as suggested in [46, 127], and the use of high-frequency modes give the average value of vortex line density in probed volume. Although, extra care must be taken when interpreting the results if dealing with strongly non-homogeneous vortex bundles. One can try to model both the spatial distribution of the bundle and the spatial distribution of the detection mode used to find appropriate quantitative results, but it would be a non-trivial task. This is being attempted for the case of spherically symmetric thermal counterflow [20], which should contain a strongly non-homogeneous vortex structure [16, 17, 19], existing around a point-like heater. However, even under these conditions, if we assume that relative vortex distribution is not changing much as the turbulence is driven harder or if we use a "dense" enough detection mode (high-frequency mode with many anti-nodes), the qualitative picture of the vortex line density expressed by changes of resonance quality factor can be approximately correct.

Another technical issue, connected with second sound attenuation technique, is the temperature dependence of the sound propagation velocity u_2, which causes changes of resonant frequency if the helium sample is overheated by the turbulence generation mechanism. It may be overcome, if overheating is not too severe, by PID algorithm stabilizing the quadrature signal component, as done in A.4 or by post-processing based on calibration peaks as described in [127]. The temperature dependence of second sound velocity in He II was systematically measured by Peshkov [129], see also Figure 1.13 and can be found tabulated in [47].

1.4.2 Local mechanical probes

Since the presentation of the original idea of the existence of quantized vortices various mechanical resonators (in the form of disks, spheres, grids, tuning forks, reeds, double paddles, wires... A.2) are being used to probe the turbulent flows of quantum fluids. The first experiments in He II have been conducted by Vinen [7] employing resonating string stretched through the centre of the experimental cell.

Figure 1.14: Photo (left) and scheme (right) of capacitive second sound sensor consisting of brass electrode and gold-plated porous membrane.

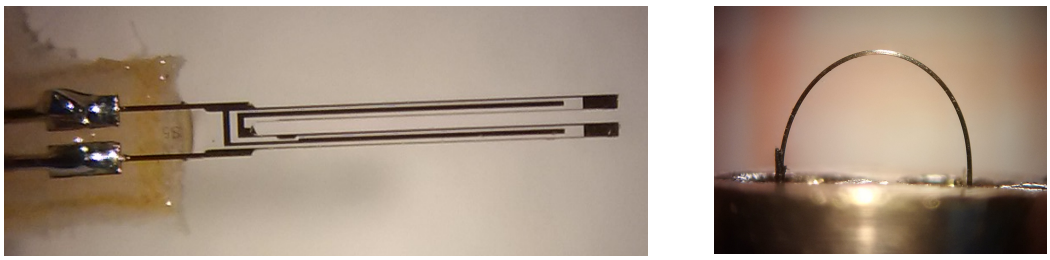

Figure 1.15: Left: Custom-made quartz tuning fork with spacing of the prongs of 90 μm. Right: Vibrating wire resonator with leg spacing of 3 mm. The loop is made of NbTi 60 μm thick wire.

In this experiment, it was possible to fully or partially trap a single quantized vortex along the string and measure its precession due to the Magnus force induced by the superfluid flow. As a result, Vinen was able to measure the value of the circulation quantum κ. Similar experimental setups are still being used for example to study the boundary conditions for the vortex movement across the boundary at very low temperatures [130].

Another type of heavily studied mechanical resonators used to study superfluids is levitating spheres [13, 15, 85, 86, 131–133]. The great advantage of this geometry is its theoretical simplicity for the hydrodynamical models and full isolation from other surfaces, which may propagate extra remnant vortices or additional heat onto the device. Such resonators are typically levitated in the superfluid bulk via the use of the magnetic forces acting on light superconducting or charged ferromagnetic spheres.

Arguably, the most used mechanical resonators to study not only the turbulent flows in superfluids but working as great probes of the properties of the fluid (such as temperature, pressure, viscosity) [5] are quartz tuning forks [6, 134–139], see Figure 1.15. They are manufactured in mass as they are widely used as a frequency standard in watches. The customization of the device fabrication allows for the dimensions of order tens of micrometers. Having a crystalline structure further leads to relatively high values of quality factors $Q \approx 10^5$ of the resonance, which is important for the device sensitivity. Oscillation motion is being driven by the alternating voltage $U(\omega)$ using the piezoelectric properties of the quartz and the motion of the prongs induce current $I(\omega)$ proportional to its amplitude. Obtaining the fork constant $a_f = \sqrt{4\pi m_e f f \Delta_f I/U}$ [5] by the calibration measurement in a vacuum, we get the connection between electrical and

mechanical properties, force F and velocity v, see equation 1.31. The calibration must be done still in the linear regime, where Δ_f denotes the with (FWHM) of the Lorenzian resonance peak and m_eff gives the effective mass of the fork A.2.

$$F(\omega) = \frac{a_f U(\omega)}{2}, v(\omega) = \frac{a_f}{I(\omega)}. \tag{1.31}$$

Last but not least, we will mention the vibrating wire resonators, being superconducting wire half-loops with leg spacing D, see Figure 1.15, which are very typically used for very-low temperature thermometry in ^{3}He experiments, measuring the thermal excitation gas density. However, their use is definitely not restricted to the above and numerous experiments with quantum turbulence generated or detected by these probes are being performed [8–10, 140–143]. The typical driving geometry is using a magneto-motive induction. The device, placed in the magnetic field $\boldsymbol{B}$ is driven by Lorentz force F, when alternating current $I(\omega)$ is supplied and its movement induces Faraday voltage $U(\omega)$. Again, we can connect electrical to mechanical properties by equations 1.32, holding as presented here for the typical case, where the magnetic field is parallel with the wire legs and if we account for the first resonant mode shape, for more details see A.2. More detailed discussion on mechanical resonators use at low temperatures may be found in [144].

$$F(\omega) = 0.69BDI(\omega), v(\omega) = \frac{U(\omega)}{0.69BD}. \tag{1.32}$$

Both quartz tuning forks and superconducting vibrating wires may be effectively used at a high enough drive for the generation of quantum turbulence eventually driving turbulent flow in both components in the case of He II. This self-generated turbulence might then be studied by the device itself, as energy input to the flow must equal dissipation measured on the device. The laminar to turbulent flow transition may be simply characterized by the change of resonant peak shape, going from Lorenzian, displaying linear dependence of measured peak velocity on driving force to a "distorted" one tending to a quadratic behaviour of *F(v)*. Under more detailed analysis A.2 including also changes of resonant frequency, a closer description of the laminar to turbulent transition may be obtained. For example, the existence of multiple critical velocities in the oscillatory flow of the tuning fork in He II was shown [6], connected with the multiplication of vortex loops pinned on the device surface leading to effective mass enhancement, next the start of loop emission with the onset of extra drag and finally build-up of large scale turbulent wake.

The big advantage of mechanical resonators when used as quantum turbulence probes is their local character, allowing for the study of any vortex structure. Although, the mutual interaction with the fluid may be very complex and is typically leading to a puzzling interpretation. It is anyway a great tool to study the self-generated turbulence and critical flow phenomena in superfluid. Mechanical resonators might be further used to probe the externally driven turbulence. Devices in the form of wire loops were used in past, to study the vortex emission at very low temperatures with the device working as a time of flight collision detector [82, 145, 146]. We believe, that the potential for the detection of externally driven turbulent flow has not yet been fully exploited and in the following, we present our results reaching towards this goal in the two-fluid regime also.

Figure 1.16: Illustrative photos of chosen mechanical resonators of micro- and nano-metric dimensions fabricated with use of lithography and other cleanroom processes. For more details see [27, 31, 149].

Device properties and their interaction with the fluid is further limiting the accessible sensitivity caused by the parasitic dissipation, which may be caused, e.g., by the intrinsic material or resistive losses or excessive damping [147]. These might be overcome by nowadays well-accessible customization of the device geometry and the material choice. Using lithography and clean room processes allows down-scaling of the device dimensions to micro-metric or even nano-metric range and it become a fairly routine procedure. At these scales, we may already reach the order of the coherent length of ^{3}He -B or study detailed dynamics of the single trapped quantized vortex [148]. In Figure 1.16, we show some of the different types of existing devices. More generally used manufacture procedures and device geometries may be found in [27–31, 149] or A.6.

Chapter 2

Onset of quantum turbulence

We have already discussed the peculiarities of the developed turbulent flow of quantum fluids resulting from their two-fluid nature. It is though, equally important to address the initial onset of the flow instabilities which also possess complex behaviour. At low velocities, the interaction between the He II components is weak, as only a small amount of remnant quantized vortices is present, and we can consider the components as independent. Following the two-fluid model, we have to account for the possible origin of the instability in either of the components and develop an analytical approach allowing their identification. It is, however, not a trivial task as the mutual friction force typically initiates the transition also in the other component soon after the initial instability occurs. At higher drives, we then deal with the combination of the developed turbulent flow in both components, if present, as described in 1.3.

We have introduced the available detection methods 1.4, which are sensitive to excess damping originating from either He II component, such as submerged mechanical resonators 1.4.2 or those that can display only the presence of quantized vortices in superfluid component, such as the second sound attenuation 1.4.1. A well-designed combination of these techniques can, therefore, offer complementary information on the fluid system under turbulent transition. The most straightforward approach, to identify transition with either of components, is to seek for the critical parameter governing the transition as it is expected to differ for the classical instability in normal component and instability leading to vortex creation in superfluid component, as discussed below.

In this work, we experimentally address behaviour of He II in the temperature regime of continuous normal component above 1 K. Due to technical difficulties connected with the realization of stationary steady flows in He II, we concentrate on the study of the steady oscillatory motion of the fluid realized by moving objects or by the application of alternating heat pulses. We are able to accurately identify the origin of the instabilities and show a temperature-controlled crossover between the two mentioned types of instability in both experimental setups.

2.1 Normal fluid instability

To closely describe the hydrodynamic behaviour of normal component and introduce the governing critical parameter, we will follow the summary offered in the attached publication A.2, see A. All performed experiments are considered in

high-Stokes-number (or high-frequency) limit of oscillatory flow, defined for the body of the characteristic dimension D as $\mathrm{St} = D^2/(\pi\delta^2) \gg 1$. For the submerged body oscillating at frequency ω, we consider normal component, with kinematic viscosity ν and density ρ_n, to create the Stokes boundary layer of temperature-dependent thickness $\delta_n = \sqrt{2\nu/\rho_n\omega}$. The same quantity can be analogically introduced for the case of oscillating He II driven by the heat impulses.

The hydrodynamic behavior of normal component is described by Navier-Stokes equations, which are in their dimensionless form governed by a single flow parameter. The exact form of the dimensionless parameter further depends on the surface roughness or presence of the sharp corners. For the hydrodynamically smooth body, e.g., smooth cylinder representing clean vibrating wire, it is the Keulegan-Carpenter number $\mathrm{K_C} = 2\pi v_n/(\omega D)$, with v_n being characteristic flow velocity. On the other hand, if surface imperfections are present, flow character is described merely by the value of the boundary-layer-based Reynolds number, called Donnelly number in the context of the two-fluid model, reflecting and honoring the work of Russell James Donnelly:

$$\mathrm{Dn} = \delta_\mathrm{n} \mathrm{v_n}/\nu. \tag{2.1}$$

Upon exceeding the flow velocity of normal component beyond $v_{n,cr}$ leading to the critical value of Dn it will experience first instabilities towards turbulent regime. The specific critical value can differ for different flow geometries, in direct analogy to different critical Re for the flow past cylinder, being of order unity and for the pipe flow, being $\approx 10^3$.

However, to describe scaling of viscous drag forces at low velocities, in the laminar regime, Dn may be used regardless of the body geometry (even if having a smooth surface). In this regime, only viscous drag is offered by the normal fluid. The drag forces F_D may be well described by means of the dimensionless drag coefficient:

$$C_D^n = \frac{2F_D}{A\rho_n V_n^2}, \tag{2.2}$$

using peak velocity V_n and oscillators cross-sectional area A perpendicular to the flow direction. The laminar drag then obeys the universal scaling $C_D^n = \Phi/\mathrm{Dn}$, for all types of bodies, with Φ being purely a geometrical parameter. Any instability can then be associated with deviation from this scaling law.

2.2 Superfluid instability

In superfluid component, we deal with the quantum-restricted flow, and the turbulent transition is connected with the start of excessive generation of quantized vortices. Although an ideal low-velocity regime should be described by purely potential flow, it is mostly the case that remnant vortex loops are already present. They are pinned to all surfaces and exist in bulk stabilized by the Earth‘s rotation. The instability is, therefore, typically not connected with the generation of the first quantized vortices in the fluid sample but rather with the start of the free vortex production into the bulk, originating from the seeding loops on the body's surface. As Schmoranzer et. al [6] showed, the multiplication of vortex loops on the surface of the oscillator may happen prior to free vortex loop production.

The generation of the free vortex loops from the oscillating body or from the channel surface in the case of oscillatory counterflow is governed by vortex self-reconnection due to Donnelly-Glaberson type of instability [89]. This transition may be associated with the existence of the critical flow velocity $v_{s,cr}$ of superfluid component, working here as the critical flow parameter. The value of the critical velocity obeys universal scaling, given by equation 2.3, as shown in experiments employing small 100 μm sized magnetically levitating oscillating spheres [14, 86].

$$v_{s,cr} \approx \sqrt{\frac{\kappa\omega}{\beta}} \tag{2.3}$$

The numerical factor β, dependent on the mutual friction parameters, is of order unity and its value decreases slightly with the rising temperature. The value of the critical velocity, therefore, varies by about 10% in temperature region above 1 K. For these reasons, it is convenient to introduce a reduced dimensionless peak superfluid velocity as:

$$\hat{V}_s = \frac{V_s}{\sqrt{\kappa\omega/\beta}}, \tag{2.4}$$

which represents the true critical flow parameter.

In analogy, with classical case, we may introduce a dimensionless superfluid drag coefficient C_D^s, describing the drag forces acting in superfluid component as:

$$C_D^s = \frac{2F_D\beta}{A\rho_s\kappa\omega\hat{V}_s{}^2}. \tag{2.5}$$

In the sub-critical regime, we should again expect the universal laminar drag (with origin in normal component) scaling, expressed as $C_D^s = \phi/\hat{V}_s$, with Φ and ϕ relation given by equation (8) in A.2, see A.

It is important to emphasize, that in experiments employing turbulence driven by oscillating bodies, we consider an oscillatory coflow having $V_n = V_s$, while in the case of oscillatory thermal counterflow it does not hold.

2.3 Turbulent onset in oscillatory coflow

In the first experiments, we present measurements of drag evolution of three mechanical resonators fully submerged in He II, scanning the temperature region above ≈ 1.3 K. We have employed two different quarts tuning forks, commercially made and custom-made, and one superconducting vibrating wire, each measured separately in dedicated cooldown. The tuning forks were driven using their piezo-electric properties and the vibrating wire was driven magneto-motivelly, in accordance with the description offered in 1.4.2. Used devices are similar to those in Figure 1.15. Agilent A33220 signal generator was used as a source of driving voltage/current and induced signal was measured with a phase-sensitive Stanford Research SR830 lock-in amplifier measuring both in-phase and quadrature signal components. In the case of tuning forks, an induced current is processed using an I/V converter and lock-in is reading voltage signal from all oscillators. Measured electrical quantities may be translated to mechanical ones using relations given by equations 1.31 and 1.32.

Specific dimensions of the used tuning forks are listed in the table 2.1. The corresponding resonant frequency of the fundamental mode for a commercial tuning fork is 32 kHz, while for a custom-made tuning fork, we have used both fundamental and first overtone modes resonating at 6.5 kHz and 40 kHz, respectively.

Table 2.1: Listed dimensions of the two used quartz tuning forks.

Type	prong length	prong width	prong thickness	prongs spacing
commercial	2.17 mm	210 μm	100 μm	120 μm
custom	3.5 mm	90 μm	75 μm	90 μm

In Figure 2.1, we show the characteristic behaviour of quartz tuning forks as the motion velocity is increased. Each individual point is a result of the full frequency sweep across the resonance at a given drive and obtained peak quantities are plotted. In the left panels, we show the velocity dependence of the clasicall drag coefficient defined analogically to 2.2, using whole fluid density ρ (instead ρ_n) and peak velocity of the device V_p representing correctly V_n, as we are dealing with coflow. Temperature dependence of the laminar regime is clearly showing that superfluid component is not contributing to the drag significantly at these velocities. However, after the turbulent transition, showing as signature deviation from the linear dependence, the total drag collapses towards a single, temperature-independent, value of the drag coefficient. This manifests that the turbulent flow develops in both He II components which are coupled together and the system behaves as a single fluid. This is in good agreement with the model introduced above.

The correct parameter showing the behaviour of normal component only is one given by equation 2.2 and is plotted in the right panels of Figure 2.1 as a function of Donnelly number. The results show very good agreement with the presented scaling law and agree almost perfectly with approximate predictions for values of Φ (plotted as blue dashed lines), made based on theory for rectangular beams [150], ignoring the surface roughness. The normal flow instability can be well identified from this picture, as a first deviation from the obtained scaling.

The very same measurements have been performed also with the vibrating wire resonator, allowing the study of a similar system in a different geometry. The loop is made from a single filament NbTi wire of diameter of 40 μm having a leg spacing of $\approx$ 2 mm. The stationary magnetic field of (170$\pm$10) mT (room temperature value, which should drop by $\approx$ 23% upon cooling) is generated by the pair of NdFeB permanent magnets. The theoretical prediction for the value of the scaling factor Φ for the smooth cylinder may be done exactly, following [32] and is in reasonable agreement (regarding geometrical uncertainties) with the measured data. The same original analysis, as for the tuning forks, is performed and shown in Figure 2.2, obtaining the expected behavior. The significant difference, compared to quartz tuning forks, is the evident temperature dependence of the deviation point from the laminar scaling law when plotted as a function of the Donnelly number which will be discussed in more detail later.

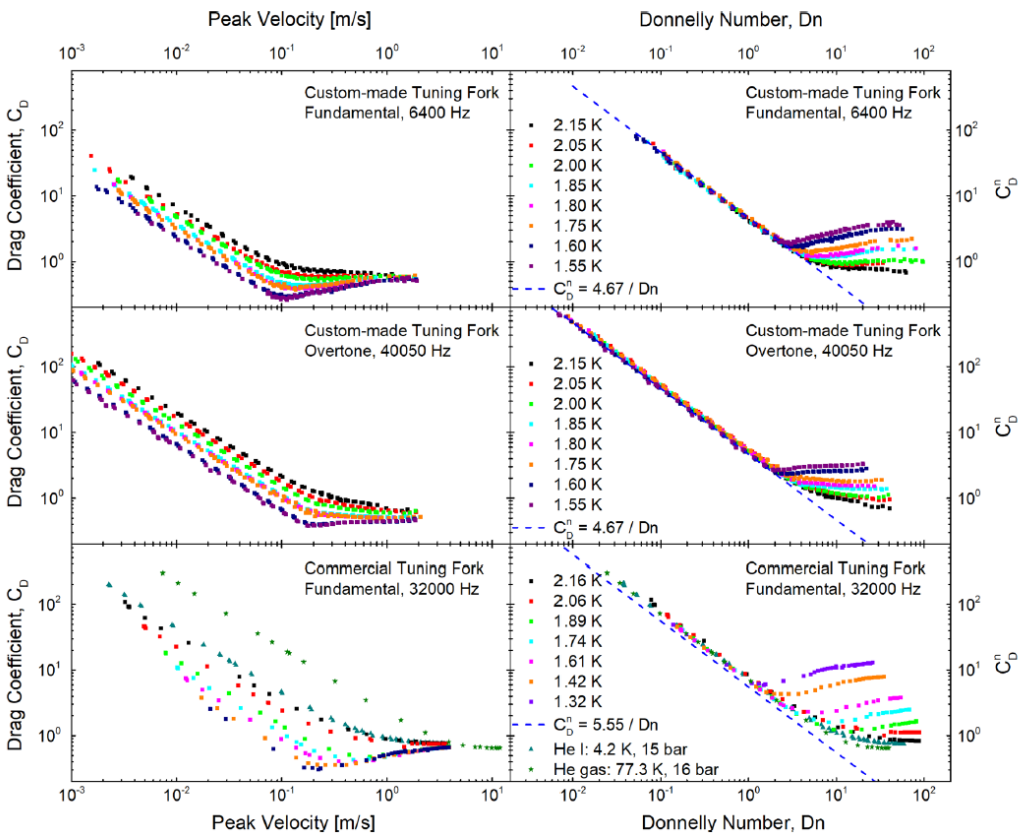

Figure 2.1: Left: Drag coefficient of the whole fluid as a function of measured peak velocity. Right: Normal component drag coefficient as a function of Donnelly number. Blue dashed lines are representing the universal scaling of laminar drag predicted based on ideas in [150]. The values of the resonant mode independent scaling factor Φ are printed. The data are presented for two quartz tuning forks using fundamental or first overtone resonant modes in a wide range of temperatures.

2.4 Turbulent onset in oscillatory counterflow

In the second experiment, described in more detail in A.3, see A, we study the turbulent transition in high amplitude second sound standing wave, which might be understood, regarding its properties described in 1.4.1, as the oscillatory counterflow. As was shown in the original work of Kotsubo and Swift [151, 152], second sound wave may generate quantized vortices, when driven hard enough, that the peak counterflow velocity locally exceeds the critical value.

In our experiment, see schematics in Figure 2.3, we employ two perpendicular second sound waves, propagating inside a closed brass channel (second sound resonator), with the length of 3.2 cm and square (1x1) cm^2 cross-section. The first standing wave is driven thermally, along the channel, using a resistive heater as the driving unit and biased (constant current of 1 μA) Ge/GaAs sensitive semiconductor thermometer [153] for the detection of the temperature wave. This mode is able to initialize the vortex production and we refer to it as "longitudinal" or "generation" mode. The second wave is generated mechanically, between the

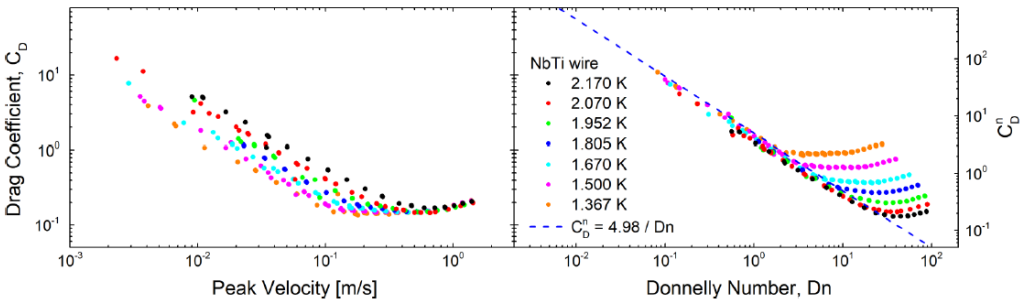

Figure 2.2: Left: Drag coefficient of the whole fluid as a function of peak velocity and Right: normal component drag coefficient as a function of Donnelly number, measured with the vibrating wire resonator. The Blue dashed line represents the universal scaling of the laminar drag on a smooth cylinder derived according to [32].

pair of capacitive sensors described in 1.4.1, see also Figure 1.14, in the center of the channel. This mode is used for the detection of generated vortex line density and we refer to it as "transversal" or "detection" mode.

The longitudinal wave mode is driven via the application of alternating voltage $U = U_0 \cos(\omega t)$ to the 50 Ω manganine wire heater by the Agilent A33220 signal generator. The generated heat pulses $Q \propto U^2$ result in the heat flux $\dot{Q} = \dot{Q}_{dc} + \dot{Q}_{ac}$ having a net DC component and AC thermal wave component at double frequency of the voltage source 2ω.

$$\dot{Q} = \frac{U_0^2}{2R} \left[1 + \cos(2\omega t)\right]. \tag{2.6}$$

We, therefore, have to keep in mind the parasitic steady counterflow being generated due to a DC heat component. The thermometer signal at a frequency of the AC heat wave 2ω was measured with Stanford SR830 lock-in amplifier.

In order to identify the transition into the turbulent state, we can analyze both of the second sound modes. Let us start with the "longitudinal" mode, which might be used for the self-detection of the generated vortices as it gets attenuated in their presence also. This results in the following driving power series of full frequency sweeps, illustrated in Figure 2.4. At low drives, no quantized vortices are generated and the resonance has a Lorenzian shape. It is good to understand that measured signal amplitude is directly connected with the peak velocity of the fluid oscillations, for details see A.3. Knowing this, it is then straightforward, that the peak amplitude cannot exceed some critical value, meaning that the critical velocity is reached, where most of the accessible energy is injected into the formation of the vortex bundle. This behaviour is clearly demonstrated in Figure 2.4 as resonance peaks for higher drives change, having a "cut-off-top" shape. This was observed at three different temperatures exciting the first three resonant modes of the "longitudinal" second sound wave. However, it may seem, that the amplitude saturation value is even decreasing with the further rise of the drive. This was not observed in previous experiments [151, 152] with mechanically driven "generation" mode and is connected with additional parasitic vortex line density having origin in net DC heat input.

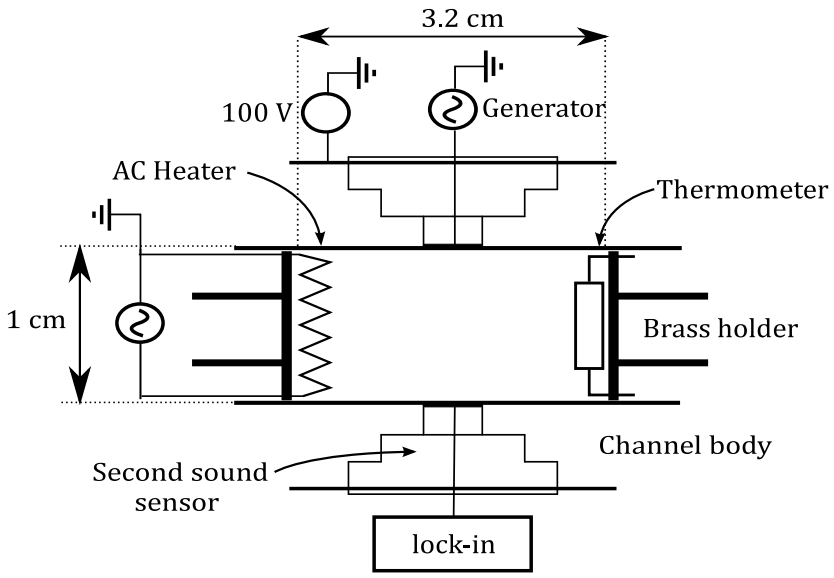

Figure 2.3: Schematic of the experimental cell arrangement. The longitudinal second sound wave is generated thermally via the heater, along the resonator, and probed by the sensitive resistance thermometer at the opposite end. The transversal second sound signal is driven perpendicularly in the middle of the resonator, between the two capacitive sensors.

Additionally, in our setup, we can verify the vortex production with the "transverse" mode. It is done in a usual way, measuring the onset of the attenuation of the "detection" mode propagating simultaneously in the centre of the channel. As may be seen in A.3 (Figure 3), it exactly agrees with the amplitude saturation of the first resonant mode of the "longitudinal" wave and directly proves the generation of the quantized vortices. This is, however, not true if a second resonant longitudinal mode is employed, regarding the measurable saturation of its amplitude. It is clearly showing, that the vortex generation is well localized in the anti-nodes of the "generation" wave, where the flow velocity is maximal.

From the simultaneous measurements of "transversal" mode during the power series of "longitudinal" mode, we can identify the critical heat power and associate it with critical counterflow velocity, as done in A.3. It is finally necessary to emphasize, that above characterized transition is again not the observation of pure initial instability, but rather an onset of the additional excessive vortex production in oscillatory counterflow from already preexisting vortex loops generated at lower velocities by present DC counterflow.

2.5 Interplay of normal and superfluid component instabilities

In order to address the origin of the initial instabilities described previously, in more detail, we need to present the obtained data in a convenient form. First, let us discuss the instability onset in oscillating coflow experiments. As we presented above, the superfluid component instability should be governed by well-defined

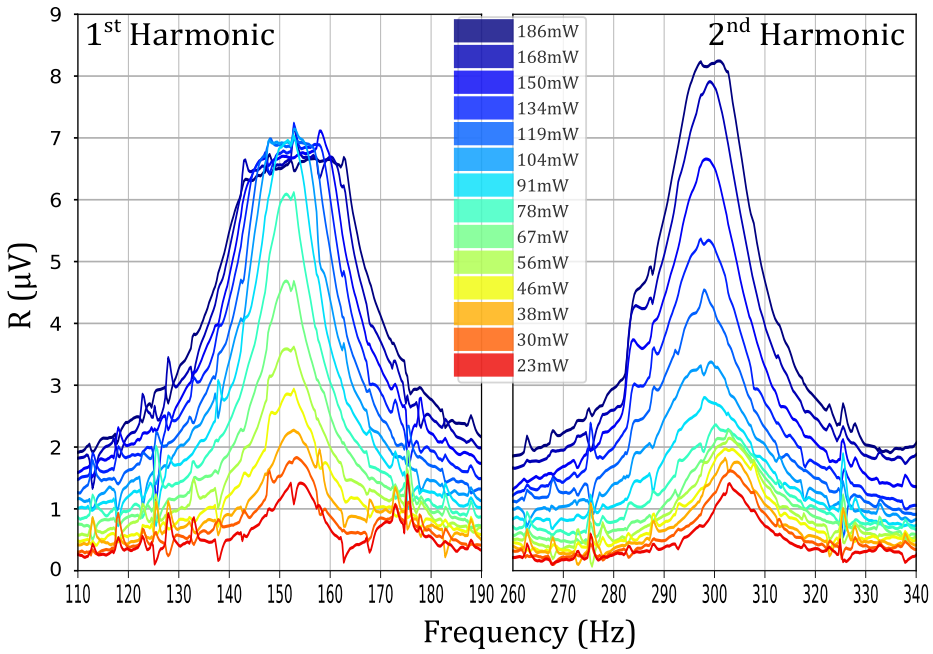

Figure 2.4: Driving power series of full frequency sweeps of longitudinal second sound wave. First two resonant modes are shown, measured at 1.65 K. Signal values represent the full voltage amplitude measured across the biased thermometer. Plotted frequencies agree with the supplied ac voltage and represent the half frequency of resulting heat pulses. Two distinct resonance shapes are present, depending on the power. At low drives, we observe a non-dissipative flow having a Lorenzian peak shape. At higher drives, signal amplitude saturates and cut-off-top peak shape is observed, meaning the production of quantized vortices.

nearly temperature-independent critical velocity $v_{s,cr}$, at which deviation from the universal linear drag dependence $C_D^s = \phi/\hat{V}_s$ occur. Analogously for instability in normal component, we expect a deviation from $C_D^n = \Phi/\mathrm{Dn}$ laminar drag at a well-defined critical value of the Donnelly number.

For this reason, it is advantageous to introduce scaled non-linear drag contributions 1 - $\phi/(C_D^s \hat{V}_s)$ and 1 - $\Phi/(C_D^n \mathrm{Dn})$ for superfluid and normal component, respectively. These quantities are close to zero for laminar drag and exhibit a steep rise at turbulent transition onset. In Figure 2.5, we plot these quantities as a function of the corresponding parameter for the data measured with three described mechanical resonators.

It is evident, that all devices are behaving in a different manner, deducing from the relative spread of shown critical parameters and the rate of the nonlinearity onset. The instability presence is identified by the crossing of the dotted horizontal line, representing the safe estimate for experimental noise levels, being set as 5% for the tuning forks and 10% for the vibrating wire.

In the case of the custom-made tuning fork, see top panels in Figure 2.5, we can identify the instability onset with the transition in normal component observing a small spread for critical $\mathrm{Dn_{cr}} \approx 2.5$ at all temperatures, see the left panel. On the other hand, the critical velocity value is clearly temperature dependent, showing a higher spread than Dn.

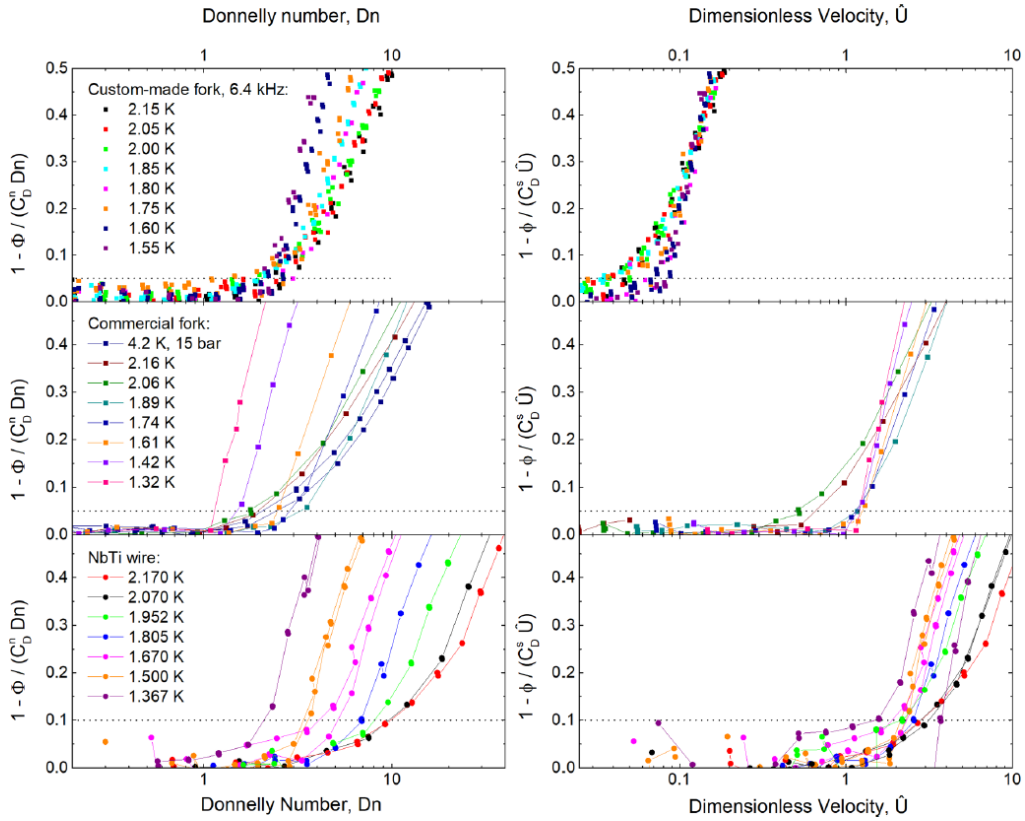

Figure 2.5: Nonlinear drag contribution for three studied mechanical resonators showing the origin of the initial instability. Left: Drag normalized for the normal component as a function of Donnelly number. Right: Drag normalized for superfluid component as a function of dimensionless velocity.

The commercial tuning fork, shown in the middle panels, exhibits a crossover, as for low temperatures well defined critical dimensionless velocity exists $\hat{V}_{cr}$=1.2, pointing to initial transition in superfluid component, but for the two highest temperatures it does not hold and $\mathrm{Dn_{cr}}$ of a similar value of 2.5 is the governing parameter. The same value of $\mathrm{Dn_{cr}}$ is observed, when measuring in normal helium at 4.2 K, where only classical instability is considerable, strengthening our argumentation.

Finally, the vibrating wire, shown in the bottom panels, is exhibiting behavior similar to the commercial tuning fork. The wide spread in critical Dn and much sharper transition in velocity is obvious, except for the two highest temperatures, where $\mathrm{Dn_{cr}} \approx 9$ is observed. The difference in this value has its origin in the device geometry, as velocity flow around sharp edges of tuning forks is likely to be enhanced, resulting in higher than measured real peak flow velocity.

Our experiments with mechanically driven oscillatory coflow have shown, that the instability in either of the components of He II can initialize the turbulent transition of the whole fluid. Further, there is a possible crossover in a single experiment, depending on device geometry, between the superfluid and classical transition, which is tunable by the temperature of the system.

We will now continue, with the discussion of the instability onset in oscilla-

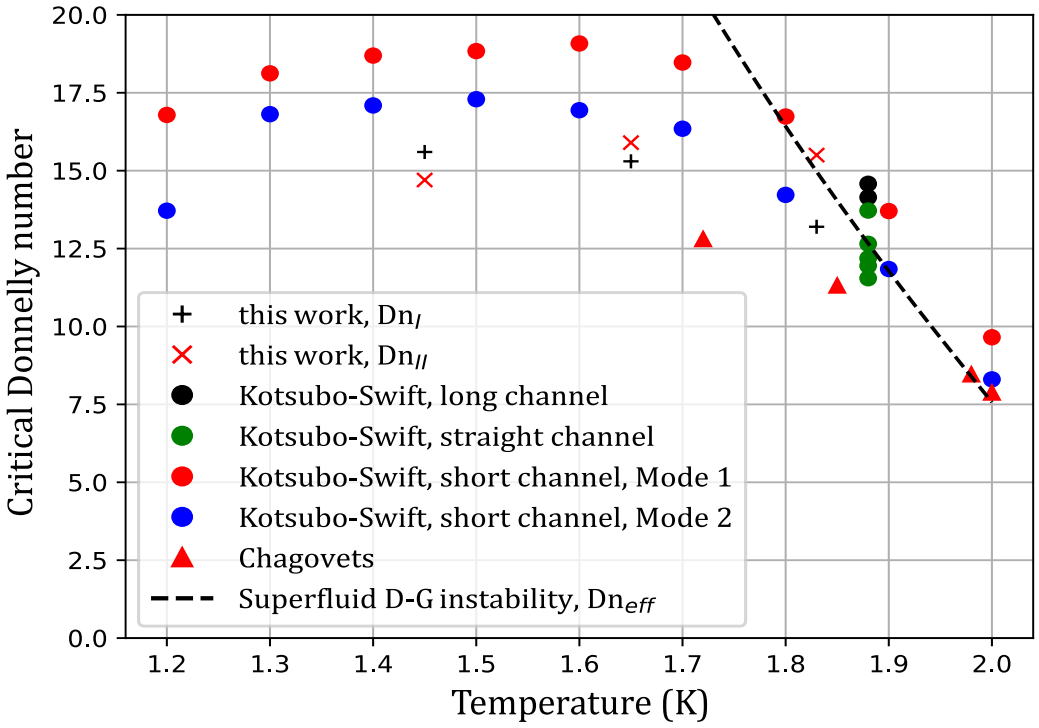

Figure 2.6: Critical Donnelly number observed for oscillatory counterflow in various experiments A.3 [151, 152, 154] as a function of temperature. The Black dashed line follows the effective Donnelly number introduced by equation 2.7, representing the correct governing parameter for the onset of turbulent transition in superfluid component.

tory counterflow, although, special care must be taken, as velocity amplitudes of normal and superfluid components are not equal, as it was in the previous experiment. We, therefore, need to introduce a common dimensionless parameter, allowing us to distinguish the two turbulent transition mechanisms. Classical hydrodynamic instability occurring at critical normal component velocity $v_{n,cr}$ is governed by the Donnelly number as introduced by equation 2.1. The generation of quantized vortices, on the other hand, happens above the critical velocity of superfluid component $v_{s,cr}$. However, this critical velocity may be converted into means of effective critical Donnelly number:

$$\mathrm{Dn}_{cr,eff} = \frac{\delta_n v_{s,cr} \rho_s}{\rho_n \nu}. \tag{2.7}$$

using zero net mass flow condition $v_n = v_s \rho_s / \rho_n$, holding for the counterflow. The physical meaning of this parameter is the Donnelly number of normal component flow, exactly when the critical superfluid velocity is reached and Donnelly-Glaberson instability is initiated in the superfluid component. Substituting for the true universally constant critical parameter $\hat{v}_s$, given by equation 2.3, and considering the frequency dependence of the viscous boundary layer size δ_n, we find that the value of $\mathrm{Dn}_{\mathrm{cr,eff}}$ is independent of frequency, but strongly temperature dependent. This may be seen in Figure 2.6, being plotted as a black dashed line.

In Figure 2.6, we show the temperature dependence of the critical Donnelly number in the oscillatory counterflow, as provided from our experiment A.3 and reconstructed from the previous experiments of Kotsubo and Swift [151, 152] and Chagovets [154]. Specific details can be found in A.3. It is clearly seen, that in the low-temperature regime, a well-defined constant value of critical $\mathrm{Dn}_{\mathrm{cr}} \approx 17$ is followed, in all experiments involving turbulence generated in oscillatory counterflow driven at various frequencies. However, for temperatures above ≈ 1.8 K results follow the $\mathrm{Dn}_{\mathrm{cr,eff}}$, representing the correct critical parameter for transition in superfluid component.

These results show, that the crossover from classical to superfluid instability exists in this type of flow as well, but has the opposite temperature character than one observed in coflow, with classical transition preferred at lower temperatures. The reason for this phenomenon is the inequality of the component velocities in counterflow, where having a smaller density of either component leads to a much higher flow velocity.

Chapter 3

Local detection of quantum turbulence in two fluid regime

Detection of the self-generated turbulent flow in the vicinity of oscillating structures plays a very important role for a better understanding of the turbulent transition in quantum fluids and its further development towards fully turbulent flow. However, we also need to be able to characterize the properties of externally driven flows. There is a number of probes that can address this goal, e.g., employment of second sound [46, 127], tracking of ions or excimers [117], and hot wire anemometry [155], although, all have their disadvantages as described in 1.4. The main issue, typically, is the interpretation and accessible information, when used for the study of highly non-homogeneous turbulence, which became a rather hot topic lately [16–20] or A.3. The need for good and reliable local probes of quantum turbulence emerged, seeking a deeper understanding of turbulent flows in new geometries (oscillatory counterflow, cylindrically or spherically symmetric counterflow).

The use of second sound attenuation is providing a great tool for scanning the average density of quantized vortex lines, although, interpretation relies on consideration of homogeneity and isotropy. It is true, that approaches towards local probes exist [128], but have a limiting sensitivity. However, the employment of mechanical probes proposes a very straightforward option thanks to its very local character and fast development of processes allowing further miniaturization. The devices in the form of superconducting vibrating wire loops [82, 145, 146] have proved their usability at temperatures close to and below 1 K, where the contribution of normal component is negligible. We try to study these devices further A.4, in the hydrodynamic limit of He II, and offer an understanding of their mutual interaction with the quantum turbulence in a wide range of flow intensity.

3.1 Experimental apparatus and method

Our experimental setup included two conventional thermal counterflow channels [46] of square cross-section. The first channel, denoted "long", had 7 mm × 7 mm in cross-section and a length of 167.5 mm. This channel included two vibrating wire resonators, L_2 and L_3, and two conventional second sound attenuation units probing the same volume, as illustrated in the sketch, see Figure 3.1. The addi-

tion of second sound sensors is giving us the ability to independently calibrate our sensors against vortex line density, under rather well-understood properties of thermal counterflow [46, 107–109]. The real situation with mechanical probes is, however, more complex, as they are able to sense both components of He II, providing additional information about the flow. The second channel, denoted "short", with a cross-section of 4 mm × 4 mm and length of 40 mm included only the two of the vibrating wire resonators, M_1 and M_2 (for geometrical reasons, we could not add a second sound unit) and was allowing for the production of much denser vortex bundles, as the counterflow velocity v_{ns} at temperature T for given heater power $\dot{Q}$ depends on the channel area A as:

$$v_{ns} = \frac{\dot{Q}}{AsT\rho_s}, \tag{3.1}$$

where s and ρ_s have the same meaning as in 1.1.2. Both channels had additional Ge/GaAs thermometer installed inside, to probe the real temperature as affected by a small gradient in the thermally driven flow.

All four mechanical devices studied in our experiments were of the same form of superconducting wire loops, as described in 1.4.2, made from the $d = 60$ um in diameter thick single core NbTi wire. It was first stripped from the layers of varnish insulation (mechanical abrasion and chemical etching) and of Cu matrix (etched in 67% HNO_3) to obtain bare superconducting half-loop with leg spacing of ≈ 3 mm. The variations in the exact loop shape result in the difference of the resonant frequencies, ranging between 5300 Hz and 7300 Hz. The position of the wires in custom-made holders, see Figure 3.2, was secured with 2850FT Stycast gluing and was made such that the top of the loop is close, ± 1 mm, to the centre of the channel. Resonators were placed in static magnetic field B of the order of 100 mT, generated by FeNdB magnets, necessary to induce movement. The real value of the magnetic field can be obtained based on calibration to the universal laminar drag, described in A.2, see A.4.

In the experiments, counterflow was generated in a slow pulse sequence using driving powers up to 500 mW. At each power two repetitions of heater-ON and heater-OFF states were set, each step of a length of ≈ 100 s, while the response of all detectors was measured. It is essential that all detectors are driven in a laminar regime and do not contribute to the vortex generation. In Figure 3.3, we show the illustrative time evolution of the scaled resonant amplitude signals of each detector type, as the counterflow pulses with rising drive intensity are applied. At some critical power, turbulence starts to be generated as second sound amplitude begins to decrease. The same occurs for vibrating wires, but only at higher heater power, showing their limited sensitivity. Together with the resonant amplitude, we track the resonant frequency evolution of the mechanical probes, which increases with the applied flow. The resonance is tracked using the PID stabilization algorithm holding zero value of quadrature signal.

The attenuation of the second sound amplitude may be used to evaluate generated vortex line density L, following equation 1.30 and used for calibration of mechanical resonator response. In our measurements, we have verified the expected counterflow velocity evolution of L [46], above the critical counterflow velocity $v_{ns,cr}$ of the order of cm/s:

$$L = \gamma^2({v_{ns}}^2 - {v_{ns,cr}}^2) \tag{3.2}$$

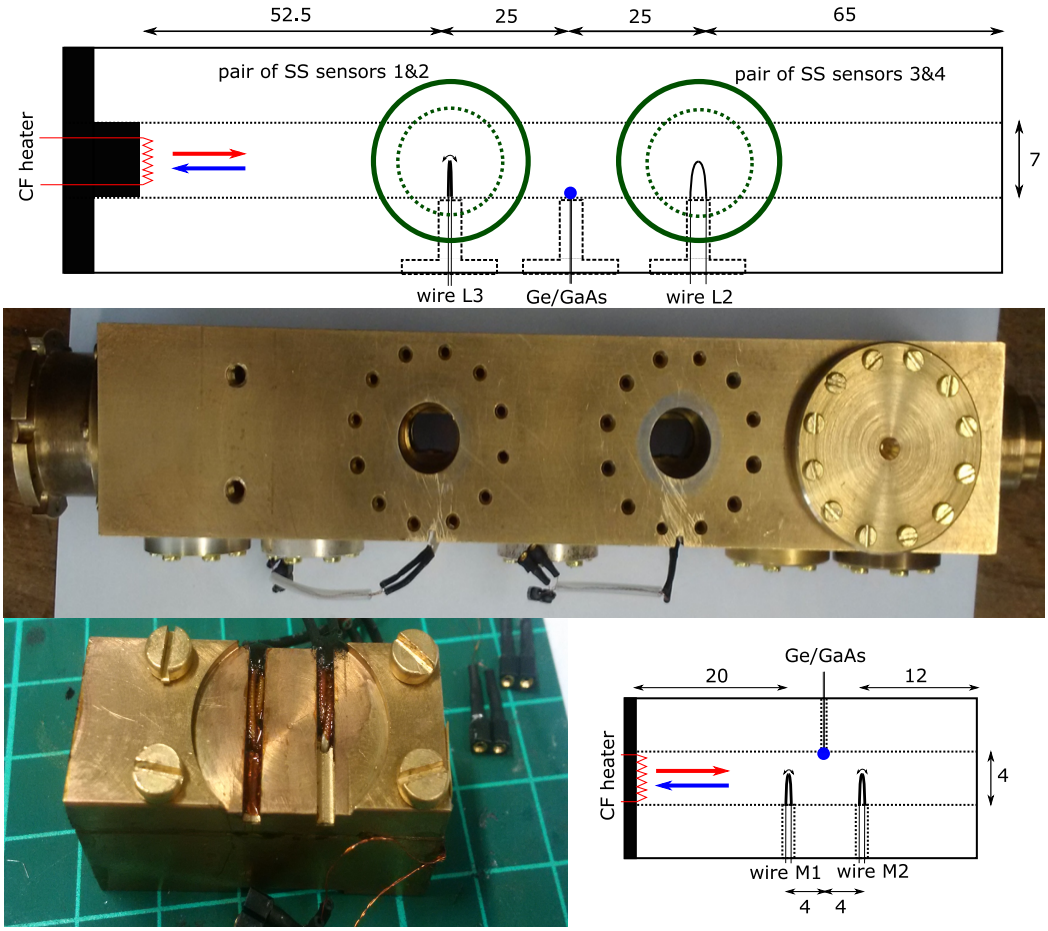

Figure 3.1: Top: Schematics and photographs of the "long" semi-closed counterflow channel, showing the open ports for the second sound sensors. Scheme includes all the relevant dimensions in mm. Position of the second sound sensors is such, that the exact volume occupied by vibrating wire sensor is probed. In the centre, between the sets of probes, Ge/GaAs thermometer is placed. Bottom: Photograph and scheme of the "short" channel with same notation. Second sound sensors are not included for geometrical reasons.

and evaluated the values of the γ coefficients in the whole range of probed temperatures, between 1.45 K and 2.05 K. Our obtained values correspond well with those reported in previous works with thermal counterflow [46]. The exact values can be found in A.4, in Table 1. We consider the same $\gamma(T)$ in both channels, as it should not be affected by the change in the cross-sectional area in the desired range of dimensions.

Finally, we can convert measured changes of the mechanical device resonant frequency and amplitude, upon exposure to the turbulent flow, to the hydrodynamic quantities. We can connect the observed shifts of the resonant frequency to the change of the probe effective mass Δm_{eff}, neglecting any change of the stiffness, as argued in A.4, by:

$$\Delta m_{eff} = m_{eff}\Big(\frac{f_0^2}{f^2} - 1\Big), \tag{3.3}$$

where f_0 denotes original resonant frequency and f the changed resonant fre-

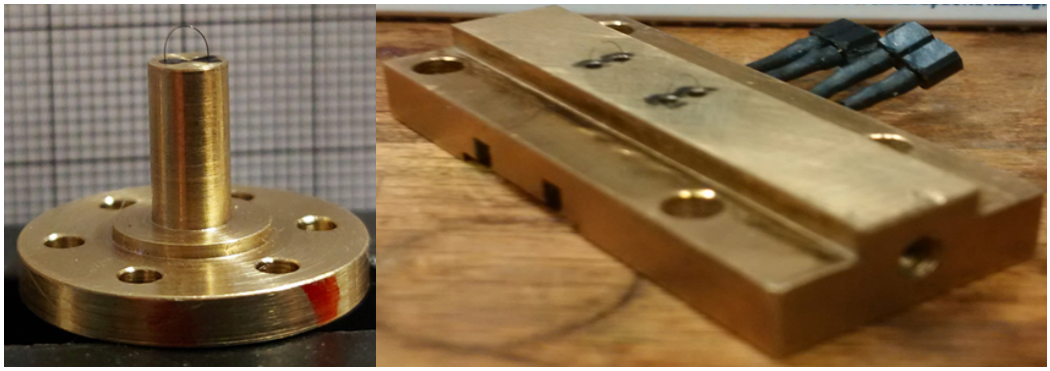

Figure 3.2: Photographs of the vibrating wire detectors installed on custom holders compatible with the "long" channel (left) and the "narrow" channel (right).

quency after the flow application. The effective mass m_{eff} of the oscillating structure submerged in He II, without any external flow, may be expressed as A.2:

$$m_{eff} = \xi m + \beta \rho V + \beta' S \rho_n \delta_n. \tag{3.4}$$

The first term describes the vacuum effective mass originating from the velocity profile of the resonant mode. The second term represents the backflow of both normal and superfluid components, proportional to the probe volume V. Finally, the third term, dependent on the surface area S, gives the additional mass of the normal fluid in the viscous boundary layer, having a temperature-dependant thickness δ_n (as defined in 2.1), moving together with the oscillator. The geometrical constants β and β' are of order unity.

In a similar way, we convert the observed amplitude decrease, from original A_0 to A in the flow, to the means of additional damping due to the turbulent flow of He II components. This can be best expressed as the inverse quality factor:

$$Q_{cf}^{-1} = \frac{\Delta f_0}{f_0}\Big(\frac{A_0}{A} - 1\Big), \tag{3.5}$$

with Δf_0 being the resonant linewidth (FWHM) in the absence of the flow.

In Figure 3.4, we show the calibration of the additional damping $Q_{QT}^{-1} = Q_{cf}^{-1}$ - Q_{th}^{-1} to the value of vortex line density, exhibiting the linear dependence in both channels. The additional contribution of parasitic effects, resulting from the temperature rise in the channel of order $\approx$ 10 mK maximum (as measured by an in-channel thermometer and predicted by the theory, see A.4), was subtracted from the data. The origin of the thermal effect Q_{th}^{-1} is in the change of the viscous drag, scaling with $\sqrt{\rho_n(T)\eta(T)}$, but was shown to be the order of magnitude smaller than the total observed response.

Data measured in "short" channel, reaching much higher tangle densities, show two distinct regimes. At lower L, linear dependence prefactor $c = Q_{QT}^{-1}/L$ depends systematically on temperature, and scales approximately with ρ_s. In contrast, above $L \approx 10^{10}$ data collapse to a single dependence, hinting at the coupling of the two components. The limited sensitivity, compared to second sound attenuation technique, well visible from Figure 3.3, seems to be connected with the characteristic device dimension, being the wire diameter of 60 μm, as it roughly coincides with the mean inter-vortex spacing l at the detectable threshold

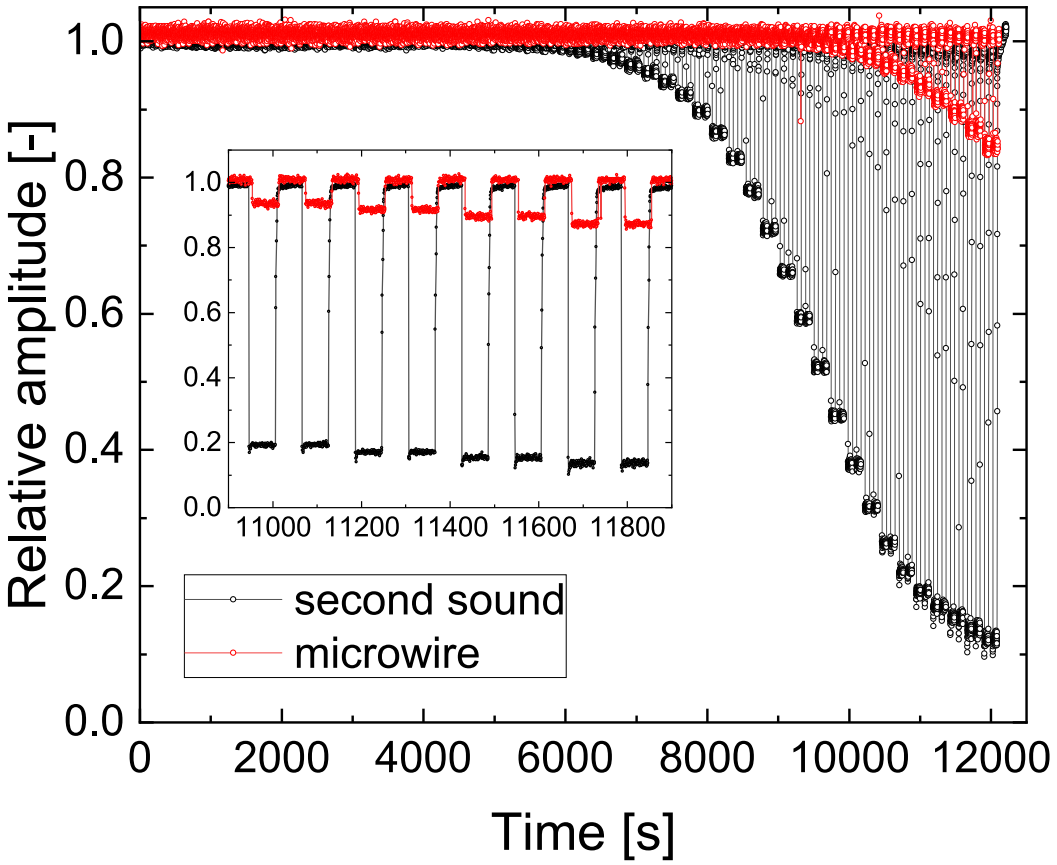

Figure 3.3: Measured time series of second sound and vibrating wire amplitude at 1.65 K as the heater power is gradually stepped up. The heater is switched on/off twice at each given power. The microwire is visibly less sensitive than the second sound technique, as expected for a local, but fairly large, mechanical probe.

L. This, together with the well-defined linear dependence of excess damping on the vortex line density offers additional information about the possible mechanism of the device interaction with the flow, which must be connected to the direct or mediated interaction with the quantized vortices.

3.2 The origin of the device response

In order to seek the origin of the measured change of the mechanical probe response, when turbulent counterflow is driven, we have to further analyze observed changes in its resonant frequency and amplitude. The additional damping may be addressed by the introduction of the effective viscosity of the turbulent flow providing the excess damping force. However, the change of the resonant frequency, which, in our experiments, always rise upon flow induction (meaning the decrease of the effective mass), is most likely connected with the boundary layer. This is deducted from the fact, that neither vacuum effective mass nor oscillatory back-flow contribution to effective mass, described by Equation 3.4, should be affected by the presence of externally applied stationary flow. In further text, we introduce these approaches, which are fully discussed in A.4.

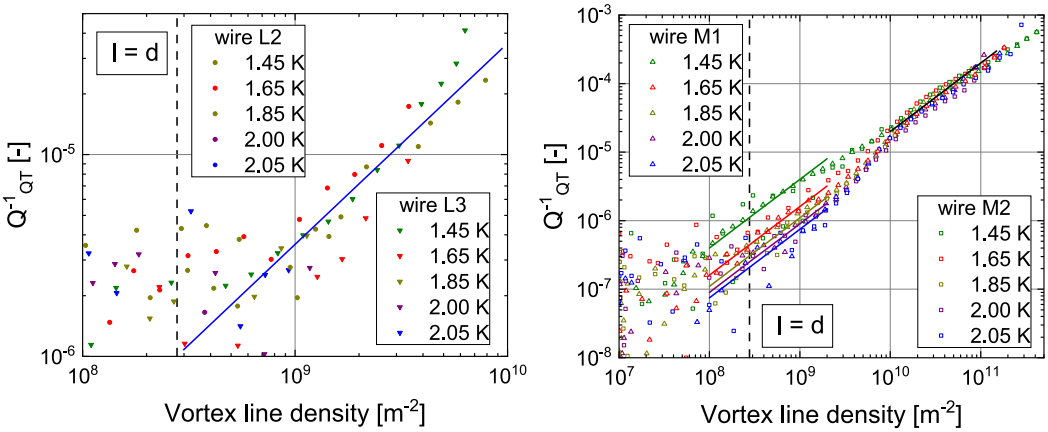

Figure 3.4: Left: Calibration of the vibrating wire additional damping against the vortex line density L in the "long" channel. The solid blue line shows a linear relationship observed in the upper decade of L. Right: Microwire additional damping as a function of vortex line density L, deduced from the observed γ factors, in the "short" channel. The solid lines depict linear relationships $Q_{QT}^{-1} = c\,L$. Two distinct regimes are observed, with temperature-dependent damping at low L and temperature-independent regime at L above 10^{10}. The mean inter-vortex distance $l = L^{-1/2}$ is equal to the wire diameter at $L = 2.78 \times 10^8$ m^{-2}, see the vertical dashed lines in both graphs.

3.2.1 Effective viscosity based boundary layer

It is important to realize, that the nature of such effective dynamic viscosity $\eta_{eff,QT}$ is conceptually not equivalent with the ν_{eff}, described in 1.3, being based on turbulent energy dissipation of the coupled turbulent flow in He II, which is driven externally. In our case, we have to describe the extra dissipation of the driven device kinetic energy due to the interaction with turbulent flow. The necessary condition for such a scenario to be applicable is the sufficient density of the vortex bundle. It is needed, that the vortex spacing is smaller than the boundary layer thickness in order for quantized vortices to be able to mimic the viscous-like momentum exchange in fluid layers around the body. The thickness of this boundary layer, connected with $\eta_{eff,QT}$, can be estimated based on A.2, Equation (9), leading to:

$$\delta_{eff,QT} = \frac{Q_{QT}^{-1}\rho_w d}{4\rho}, \tag{3.6}$$

where ρ_w= 6550 kgm^{-3} denotes the density of the wire material. All of the values of $\delta_{eff,QT}$ obtained from the measured Q_{QT}^{-1} are below 1 μm. This would require a value of vortex line density higher than 10^{12} m^{-2} to obtain an inter-vortex spacing in the desired range. Therefore, we cannot in our experiments consider the viscous-like interaction with the vortex bundle, but rather ballistic interactions of the individual quantized vortices affecting the boundary layer. These events occur randomly and sporadically, but our measuring scheme is rather providing the mean value of $\langle L \rangle$ in the boundary layer, as lock-in is averaging over many device oscillation periods. We can discuss the possible effect of these vortices on the normal fluid boundary layer further.

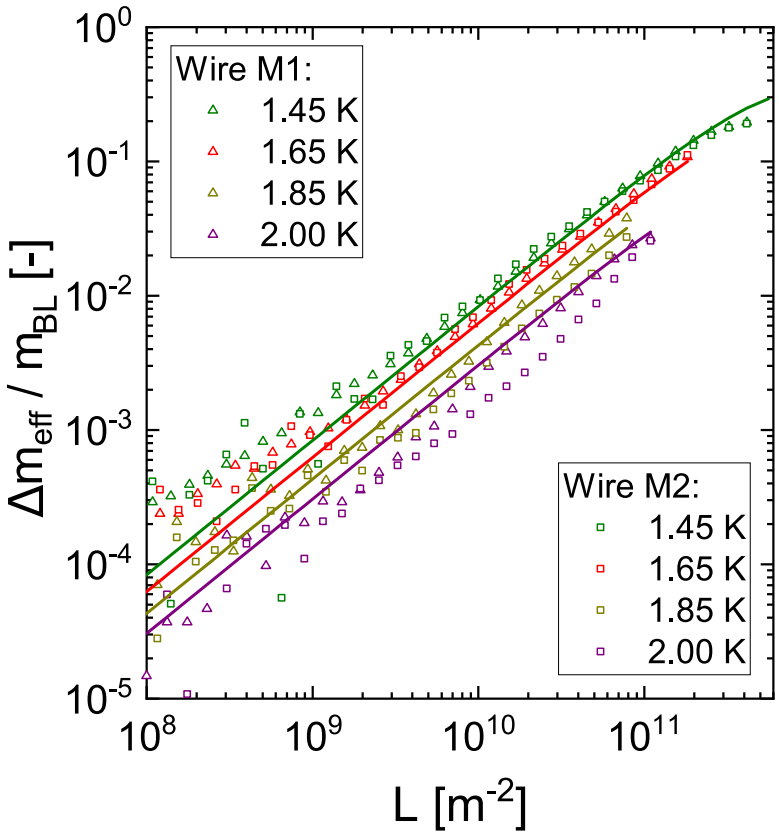

Figure 3.5: Change in effective mass normalized by the mass of the Stokes boundary layer as a function of L, measured in "short channel". The solid lines are calculated using the correction factor ξ_1, given by Equation 3.13, representing the change of the boundary layer affected by the mean mutual friction force. It is showing remarkable agreement with the data.

3.2.2 Boundary layer with mean mutual friction

Having only a limited amount of the quantized vortices in the close vicinity of the resonator, we may still consider a boundary layer to be affected by the mutual friction force. Here, we consider only the modification of an oscillatory Stokes-like boundary layer and omit the Blasius-like boundary layer due to stationary flow, as it should not be experimentally probed at used frequencies. However, the interaction of these two might be very complex and is not well understood yet.

Evaluating the full mass of the Stokes boundary layer:

$$m_{bl} = \frac{\pi^2}{2}\rho_n D\delta_n \left(d + \delta_n\right), \tag{3.7}$$

we can plot the measured mass decrease Δm_{eff}, given by Equation 3.3, normalized as a fraction of m_{bl}, as a function of L, see Figure 3.5. The mass decrease observed from the frequency change measurement indeed represents a fraction of the boundary layer, comparable with m_{bl} at high counterflow velocity.

When trying to describe the oscillatory boundary layer, affected by the mutual friction force, in thermal counterflow, we need to solve Stoke's second problem [32] for the two-fluid system of He II. The flow past a circular cylinder in a high-frequency limit may be approximated by planar elements. The equations of

motion must originate from the HVBK Equations 1.4 1.5, but we can consider the pressure and temperature gradients and the vortex tension to be negligible, arriving at:

$$\rho_n \frac{\partial v_n}{\partial t} = -\frac{\rho_n \rho_s}{2\rho} B\kappa L v_{ns} + \eta \Delta v_n, \tag{3.8}$$

$$\rho_s \frac{\partial v_s}{\partial t} = +\frac{\rho_n \rho_s}{2\rho} B\kappa L v_{ns}, \tag{3.9}$$

using the expression of the mutual friction given by equation 1.26. The solution for the flow around an in-plane oscillating planar infinite boundary can be considered in the form:

$$v_n = v_{n0} + v_{n1} e^{i(kz-\omega t)}, \tag{3.10}$$

$$v_s = v_{s0} + v_{s1} e^{i(kz-\omega t)} \tag{3.11}$$

with the z representing the perpendicular space coordinate being zero at the position of plane. We consider both velocities to oscillate in the same direction as the plane with the no-slip boundary condition for the normal component only. The superfluid component motion is induced by the mutual friction force as described by Equation 3.9.

As discussed above, we consider the mean value $\langle L \rangle$ of vortex line density in the boundary layer, as decomposed from $L = \langle L \rangle + \tilde{L}$, and neglect the fluctuating term. As a result, considering only terms oscillating at the drive frequency ω, we get the following condition for the wavenumber k:

$$(k\delta_n)^2 = 2i \, \frac{(2\rho\omega)^2 + \rho_n \rho (B\kappa \langle L \rangle)^2 + 2i\rho\rho_s \omega B\kappa \langle L \rangle}{(2\rho\omega)^2 + (\rho_n B\kappa \langle L \rangle)^2}. \tag{3.12}$$

We can estimate the mean relaxation time for the action of mutual friction by the term $\tau_{mf} \equiv 2/(\mathrm{B}\ \kappa \langle L \rangle)$, being of the order of ms for our experimental values of L. It agrees with the idea that the mutual friction is sufficiently fast to affect the boundary layer behaviour measured during ≈ 100 ms (given by lock-in time constant), but cannot fully follow the oscillations of the device with period ≈ 30 μs.

Following the solution for purely classical problem, see chapter §24 in [32] and one yielded in our case when further modifying Equation 3.12 as done in A.4, we arrive at the comparison for the resulting boundary layer thickness δ_n and acting viscous stress forces σ_n. This approach, in the linear approximation, predicts the correction to the classical solutions originating from the mean-field effect of the mutual friction force in externally driven stationary counterflow:

$$\delta_{n,mf} = \delta_n \xi_1 \quad ; \quad \xi_1 \approx 1 - \frac{\rho_s}{\rho} \frac{B\kappa L}{4\omega}. \tag{3.13}$$

$$\sigma_{n,mf} = \sigma_n \xi_2 \quad ; \quad \xi_2 \approx 1 + \frac{\rho_s}{\rho} \frac{B\kappa L}{4\omega}. \tag{3.14}$$

The resulting agreement with the experimental data of effective mass decrease, shown in Figure 3.5, is strongly supporting this scenario. However, the measured values of additional damping Q_{QT}^{-1}. see Figure 3.6, are systematically higher than the ones predicted but scale correctly with the temperature i.e., with ρ_s. It shows, that the described effect significantly contributes to the additional damping, but

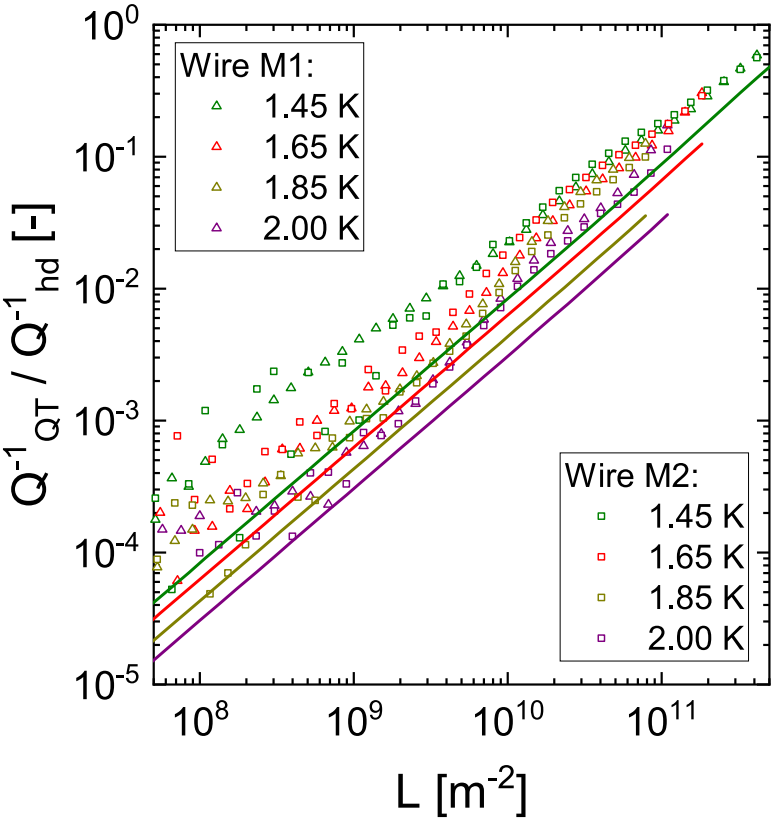

Figure 3.6: Ratio of extra drag due to quantum turbulence, Q_{QT}^{-1}, to the hydrodynamic viscous drag in zero counterflow, Q_{hd}^{-1} as function of L, measured in "short"channel. The solid lines are obtained using the correction ξ_2 to a classical hydrodynamic solution of Stoke's boundary layer. The data show higher damping than predicted and additional effects must be considered.

other mechanisms with a similar effect might be present in the flow. We can imagine the direct momentum transfer during the events of the ballistic collision of the device with the vortex loops. This will lead to an increase in the measured damping, but should not affect the boundary layer significantly.

Our experiments clearly show the potential of the mechanical oscillating probes for the local study of turbulent flows in quantum fluids, even in the hydrodynamic regime of the two-fluid model, but further experiments are needed to fully describe their interaction with the flow. The steps towards higher sensitivity devices should be taken through size reduction. The smaller devices reaching the nanometric dimensions should provide much higher sensitivity to the effects governed by the direct momentum transfer during the collisions with the vortex loops, operating at all temperatures, thanks to their very low total mass. Finally, such devices also allow the measurement of the dynamics of single quantized vortex, which can be stably trapped on the surface of the probe [148].

Chapter 4

Use of micro-scaled mechanical resonators

The physical oscillating probes have already shown their big potential for the study of quantum fluids at a large range of temperatures reaching even below millikelvin. The recent rise of accessibility of clean-room facilities is allowing fast development and simplifies the customization of the device for its specific use. The employment of optical or electron lithography processes makes designs with nanometric (order of hundreds of nm) critical dimensions reachable and a plethora of etching and deposition techniques bring freedom in material and device geometry choices. This is proven by the existence of many devices being used in various experimental works, including studying quantum liquids properties [5, 59, 156], the dynamical behaviour of quantum turbulence at the smallest scales [148], studies of mechanical quantum states [157], and many others. We aim for the study of superfluid helium isotopes at the level of single quantized vortex dynamics in zero-temperature limit. To reach this goal, we present the manufacturing process and characterization measurements of such new device A.6, produced by the author of the thesis, and discuss the limiting effects complicating the detection with the required sensitivity.

4.1 General damping of mechanical resonators

In this Thesis, we are proposing the mechanical resonating devices to be used, under various experimental conditions, as detectors of quantum turbulence. In order to employ such a device, at first, the parasitic damping effects, other than those under study, must be understood and characterized. Discussing the dissipation experienced by the device of micro- or nano- dimensions Ref. [147] presents a good overview. We can categorize the damping forces into two main groups based on their origin: intrinsic and extrinsic dissipation.

In the case of intrinsic dissipation, only the properties of the device itself must be considered. The origin of the main contribution to the damping may differ for the specific device properties. It can be governed by, e.g., the defects of the single crystal lattice, the effects on the grain boundaries in polycrystals, the internal residual stresses or other effects in multi-material devices, the existence of the two-level energy systems or the surface effects especially important for low dimensional devices. The characterization of these effects can be performed

experimentally by vacuum measurements at the lowest possible temperatures over the full intended range of amplitudes or velocities to be used in the experiments.

The extrinsic losses can be important even in the absence of the measured media, depending on the driving mechanism. The most typical effects in the electrically driven devices are the resistive losses, which can be suppressed by the use of the superconducting materials or the magneto-motive losses due to eddy currents scaling as $Q^{-1} \propto B^2$. Further additional losses might be caused by the phonon propagation through the mechanical clamps of the device in the experiment.

Finally, we can discuss the dissipation originating from the studied media. Some part of this dissipation is typically at the centre of the interest for the experiment, but we have to be able to distinguish its contribution to the total measured damping. We have already, in previous chapters, broadly discussed the excessive dissipation resulting from the turbulent instability and its development, which is governed by the flow velocity. This can be ruled out by the device operation in the laminar regime well below the critical condition. In this case, depending on the temperature, damping is offered by the hydrodynamic or the ballistic effects in normal component. The transition between the two regimes, reaching even temperature-independent region at the very lowest temperatures, was demonstrated in Ref. [59], using a nano-metric doubly-clamped cantilever. The damping in the ballistic regime depends on the population and energy of the thermal excitations as discussed in 1.1.3. In the hydrodynamic regime, not only damping but also an effective mass of the device is affected, as described by Equation 3.4. For the body oscillating in the high-frequency limit ($D \gg \delta_n$), we can express the additional viscous hydrodynamic damping in the means of the resonant width Δf^{visc} as [5]:

$$\Delta f^{visc} = C \frac{S}{2\xi m} \sqrt{\frac{\rho_n \eta f_0}{\pi}} \left(\frac{f_H}{f_0} \right)^2, \tag{4.1}$$

with f_H being a hydrodynamically shifted resonant frequency, f_0 the original resonant frequency in vacuum, and C being a purely geometrical constant of order unity, which should be universal for the given device, despite the fluid properties. Viscous hydrodynamic damping is, therefore, dependent on the frequency as $\propto \sqrt{f}$ and on the temperature via the $\sqrt{\rho_n \eta}$ term. Experimentally obtaining the value of the geometrical factor C allows for the device to be used as a good thermometer or viscometer [5].

Last, but not least, we will discuss in more detail the dissipation due to generation of acoustic waves, which can then propagate in the fluid media. The acoustic emission can be a limiting factor for the detectors, especially ones, operating at high frequencies. Therefore, it is very important to be able to predict its contribution in the planned device geometry. The theoretical models describing the acoustic emission by the resonators of different geometries are presented in Ref. [158]. The experimental verification of the model for the quartz tuning forks in ^{4}He was provided in Refs. [135, 159], where the tuning fork is described as a linear quadrupole of point sources with effective strength based on the mode-dependent velocity distribution, see Equation 4.2. In the next chapter, we show and discuss our recent data, see A.5, of the acoustic emission by the quartz tuning forks in normal and superfluid ^{3}He and compare them with the results from ^{4}He

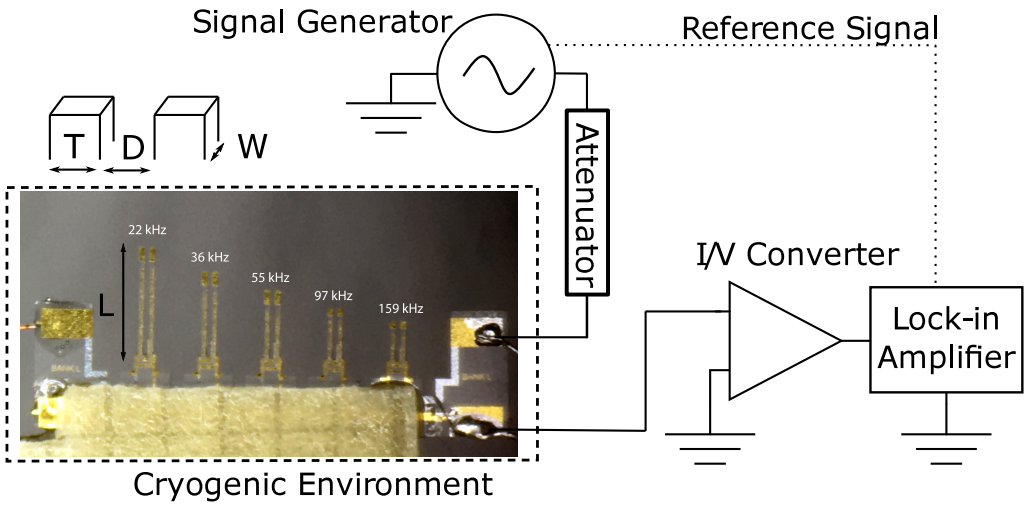

Figure 4.1: Photograph of the tuning fork array together with the scheme of the piezoelectric drive and read-out circuit.

.

4.1.1 Acoustic emission in quantum fluids

In our experimental setup, we have employed an array of five custom-made quartz tuning forks L_1,...,L_5. They were mounted in an experimental cell, being part of a "wet" dilution refrigerator with a Cu nuclear demagnetization stage, in Lancaster [160]. All dimensions of the tuning forks in the array, except for the prong length $\mathbf{L}_f$, were the same, namely: prong width $T_f = 90$ μm, thickness $W_f = 75$ μm and prong spacing $D_f = 90$ μm. The prong lengths were chosen in a range from 0.9 mm to 1.9 mm to approximately uniformly cover the range of resonant frequencies between 20 kHz and 600 kHz using the fundamental and the first overtone resonant modes.

// In Figure 4.1, we show the picture of the tuning fork array and measurement schematics. Driving and read-out methods are the same as described in 1.4.2. All resonant frequencies were measured in a dedicated cell at the end of a dipstick at cold 4.2 K vacuum, together with the resonant widths characterizing the intrinsic (and other parasitic) damping, are listed in Table 4.1. It seems that the flexural modes of the shared base are very important for the clamping losses, as the vacuum width for the L_2 and L_4 tuning forks are an order of magnitude larger than the others.

In Figure 4.2, we show the measured values of the resonant widths as a function of the frequency, where vacuum widths have been already subtracted. Therefore, the presented data are representing only dissipation by hydrodynamic/ballistic and acoustic emission losses. Each point is a result of the full resonant peak measurement. The data were taken at five different temperatures between 1.5 K and 12 mK in normal ^{3}He and at ≈ 0.16 T_C in superfluid ^{3}He -B. The temperature was measured via additional vibrating wire resonators. The dashed lines are representing the fits of the hydrodynamic contribution, performed based on the model given by Equation 4.1, using only the values at frequencies below 100 kHz, where it dominates the dissipation. From the measured hydrodynamic frequen-

Table 4.1: Vacuum properties of fundamental and overtone resonant modes of used tuning forks measured at 4.2 K. The last column shows the product of the angular frequency, ω, and the estimated relaxation time τ in superfluid ^{3}He -B at $\approx 0.16\ T_C$. In normal ^{3}He $\omega\tau$ remains below 0.04 even for the highest frequency at all investigated temperatures.

Fork-mode	Frequency Hz	Width Hz	$\omega\tau$ (T=0.16T_C)
L1-fund	22,403	0.05	56.1
L2-fund	35,770	5.15	89.7
L3-fund	55,276	0.29	139
L4-fund	97,055	3.58	243
L5-fund	159,316	0.55	399
L1-over	138,689	0.44	348
L2-over	220,110	32	552
L3-over	337,514	3.90	846
L4-over	579,000	159	1450

cies F_H, known fork dimensions, and tabulated properties of the liquid, we can evaluate the value of the geometrical constant C=0.65, with variation less than 3% at all temperatures and for all forks separately, which is in good agreement with the previous works [135, 159]. In the case of superfluid data, we consider only constant ballistic contribution, as described in [159], equal to the value of the first point.

After the subtraction of these contributions, we can analyze the dissipation by the acoustic emission only. For this purpose, we use the same theoretical model as derived and applied for the ^{4}He [135, 158]:

$$\Delta f^{3D} = C_{3D}\frac{\rho}{c}\frac{W_f^2 L_{eff}^2}{\xi m}\frac{f_H^4}{f_0^2}\times\sum_{\substack{m=0,\\ even}}^{\infty}(2m{+}1)\left[j_m\left(\frac{\pi f_H(2T_f+D_f)}{c}\right)-j_m\left(\frac{\pi f_H D_f}{c}\right)\right]^2 \tag{4.2}$$

based on the spherical Bessel functions j_m. It again depends on the single geometrical constant C_{3D} of order unity and c denotes the applicable sound velocity. The effective length of the acoustic source $L_{eff} = \mu_{eff} L_f$ is however, unlike the effective mass ξm, resonant mode dependent. The values of the prefactors $\mu_{eff} = 0.3915$ for the fundamental resonance and $\mu_{eff} = 0.2169$ for the first overtone, can be derived based on A.2. It is, therefore, necessary to evaluate the datasets from the fundamental and the overtone modes separately. In the case of the overtone mode, due to its geometry, it would be more correct to consider two separate quadrupole sources with opposite directions, shifted by a half-length along the prong, to the maxima of the velocity. Regarding our results, see further, the used approximation is well applicable. For the normal ^{3}He data it is only the overtone mode measurements, which may be used, as at the lower frequencies viscous dissipation dominates, and acoustic emission is practically absent.

Performed fits of the acoustic emission contribution, based on Equation 4.2 including only fitting parameter C_{3D}, show the good agreement of the data with the model. It is shown by the dotted lines in Figure 4.2, representing the total

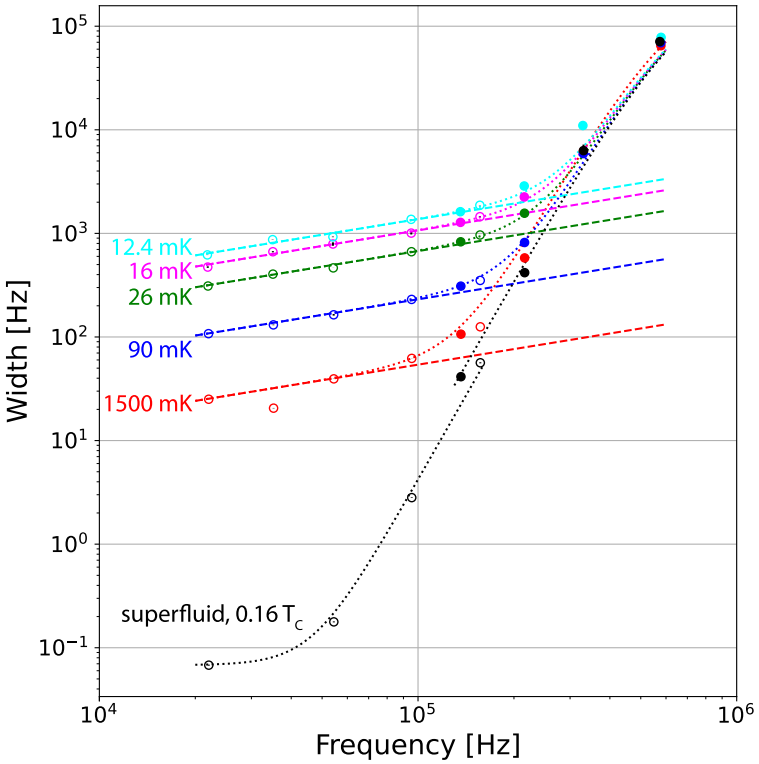

Figure 4.2: Total resonance widths (minus vacuum values) as a function of tuning fork frequency measured at five temperatures in normal ^{3}He and one temperature in superfluid ^{3}He -B. Empty and filled circles represent fundamental and overtone resonant modes, respectively. Dashed lines correspond to the viscous drag contribution using the fitted value of the geometrical parameter $C = 0.65$. The dotted lines represent fits of total resonance width as a sum of viscous drag and acoustic emission contributions. Regarding ^{3}He -B data, we obtained different geometrical coefficients for acoustic emission by fundamental $C_{3D}^{fund} = 3.3$ and overtone $C_{3D}^{ovt} = 8.5$ resonant modes.

dissipation as a sum of the fitted widths, giving hydrodynamic/ballistic plus acoustic losses. We have observed following values of the geometrical parameter: $C_{3D}^{ovt} = 8.5$ for the overtone mode data and $C_{3D}^{fund} = 3.3$ for the fundamental mode data, measured at 0.16 T_C in ^{3}He -B. These values are in good agreement with the experimental results observed in superfluid ^{4}He [135] (we note that agreement is met only after the correction for the newly derived value of $\mu_{eff} = 0.2169$ is used as in Ref [135] where the overtone data are treated using $\mu_{eff} = 0.3915$).

Our results, together with the previous works [135, 159] confirm the validity of the same acoustic emission model for the bulk of both normal and superfluid phases of ^{4}He and ^{3}He . The fact, that a single model holds in the whole range of temperatures of both quantum liquids is pointing towards the same mechanism of wave emission of the first sound in normal ^{3}He and in liquid phases of ^{4}He and longitudinal zero sound in superfluid ^{3}He -B. In Table 4.1, we evaluate the product of the frequency ω and fluid relaxation time τ, which determines the

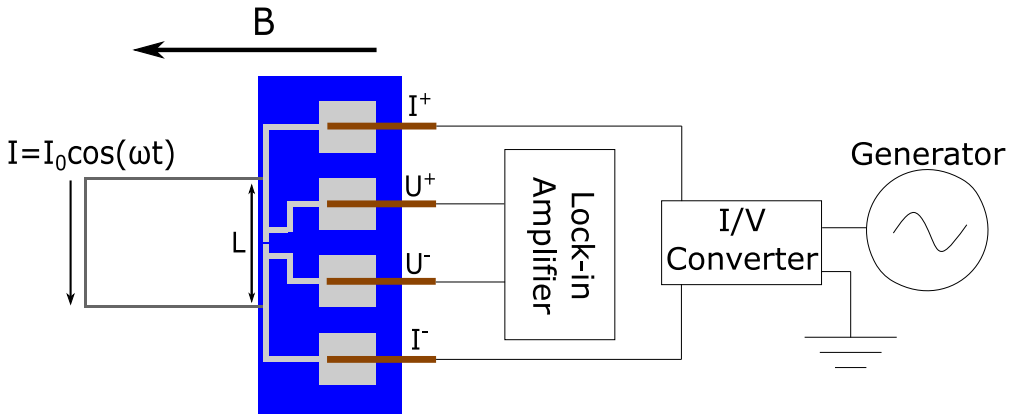

Figure 4.3: Driving circuit for custom fabricated MEMS device. The aluminum layer (grey) was deposited over the chip body (blue) creating electrical pads and leads (300 nm thick) and over a single crystal Si goal-post-shaped device (120 nm thick). The low-temperature connection was realized by gluing superconducting NbTi leads (brown) to the pads, using silver epoxy.

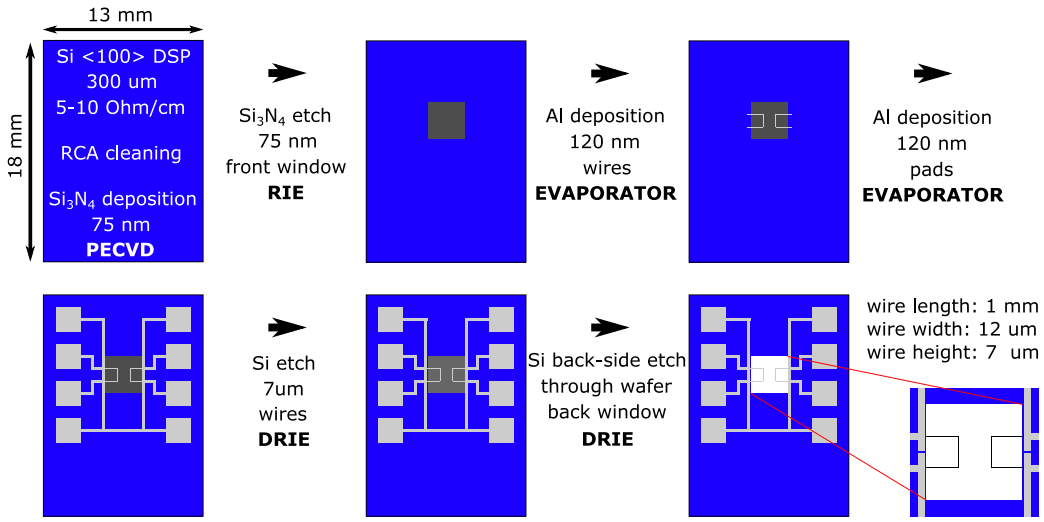

Figure 4.4: Schematic of the step-by-step workflow of MEMS fabrication process, see text for more details.

collisionless limit $\omega\tau \gg 1$, see [56]. The relaxation time τ represents the thermalization of individual quasiparticles to an equilibrium temperature or to the walls of the cell. In this limit, Landau zero sound mode [161], being described as asymmetric deformations of the Fermi sphere, is preferable. In our experiments, the collisionless limit is reached only at the very lowest temperature.

Finally, the acoustic model for the tuning fork geometry, in a long wavelength approximation, predicts a very steep $\propto f^6$ dependence of the dissipation, which strongly limits the devices operating at high frequencies. Analogous models, predicting a lower power dependence, describing the wire or cantilever geometry can be found in [158]. However, it is clear that acoustic emission must be considered when designing mechanical resonating devices for detection purposes in quantum liquids.

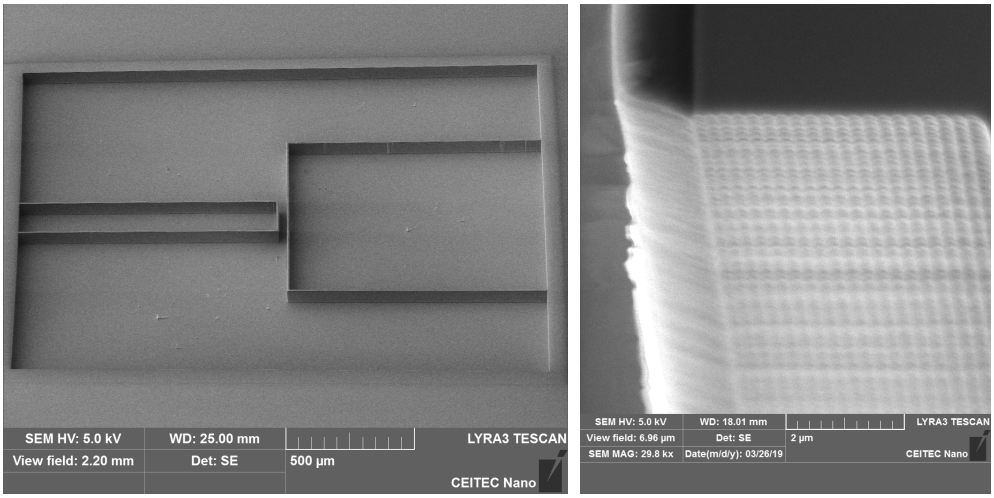

Figure 4.5: Left: SEM picture of wire structure made by smooth Bosh DRIE process. Right: SEM picture showing the resulting surface roughness of the MEMS, having scallops of the order of 10 nm deep as a result of cyclical smooth Bosh process. The sample is rotated by 90deg to visualize the scallops. The layer on the top of the device (e.i. left in the picture) is remaining photoresist.

4.2 Custom MEMS fabrication

We have designed and manufactured single crystal silicon chips containing two goal-post-shaped vibrating wire resonators, similar to those referred in [27], freely standing in the open window. Oppositely standing MEMS (Micro-Electro-Mechanical System) devices can differ in dimensions, being of the order of 10 μm in cross-sectional dimensions and of the order of mm in length of the goal-post and spacing between the devices is tuned between 1 mm and 30 μm. This design should allow the pinning of the single quantized vortices between the two devices, securing the vortex geometry. Used device shape leads to the resonant frequencies below 10 kHz. Aluminum film of 120 nm thickness, superconducting below $\approx$ 1 K, is covering the device and allows its magneto-motive drive and electric readout, see 1.4.2. The conversion of electrical to mechanical quantities slightly differs in this geometry and is given as:

$$F(\omega) = L_{MEMS}BI(\omega), v(\omega) = \frac{U(\omega)}{L_{MEMS}B}. \tag{4.3}$$

with L_MEMS being the length of the device crossbar. The measuring scheme is illustrated in Figure 4.3. The single crystal nature of our MEMS leads to a relatively high-quality factor Q, representing very low intrinsic damping losses.

We have built our devices starting from RCA cleaned 300μm thick double side polished single crystal 4 inch silicon wafers with <100> orientation and 5-10 Ohm/cm resistivity. The fabrication process is based on multiple optical lithography steps from both sides of the chip. Here, we introduce the step-by-step fabrication process, which is illustrated in Figure 4.4. In the first step, using the PECVD process, a 7 nm thick Si_3N_4 layer was deposited on both sides of the wafer. From the top, windows were opened in the Si_3N_4 with the use of reactive ion etching by CHF_3 gas. In the second step, 120 nm of aluminum was deposited by an evaporator, directly on silicon in the pre-opened window, having the shape

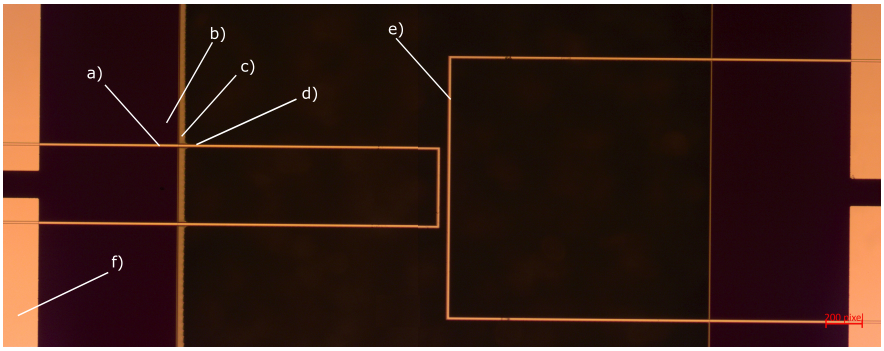

Figure 4.6: Optical microscope image of the final devices in the opened window of the H3 chip. Devices are separated by a gap of 30μm on this chip. a) 120 nm aluminum layer on top of the substrate, b) substrate, still covered with 75 nm of Si_3N_4, c) thin Si ledge, as a result of wall screening effect during deep back-side etching, d) Si wire, with 120 nm of aluminum layer on top, freely standing in the open window e) the oppositely standing wire separated by a gap of 30μ. f) 300 nm thick aluminum leads.

of final wire devices. Next, aluminum electrodes and leads with a thickness of 300 nm were deposited and connected (having an overlap) to the layer from the previous step. Si_3N_4 layer under the pads works as a buffer for the mechanical strain caused by electrical contacts.

The wafer was then cut to single chips (it included chips with various configurations of the device dimensions) using a laser or mechanical saw and further fabrication processes continued on each chip separately. In the following step, the silicon device structures were created by the Si etch around the aluminum wire coating, using a design enlarged by 1 μm to each side. It was done by the smooth Bosch process using the deep reactive ion etching (DRIE), having a height of ≈ 7 μm. The result after this step is illustrated on SEM picture in Figure 4.5, as executed on the testing chip (with much higher etching depth and not including the aluminum layer yet).

In the final step, devices were covered by the protective photoresist, filling the whole window, and released by a deep DRIE etch from the back side. This etch of the window in Si of a similar size was stopped at the moment of the device's appearance. The protective photoresist was then cleaned by liquid chemical solvent and photoresist residuals were removed in O_2 plasma. Exact details of each fabrication step, including photoresist type and lithography specifics, can be found in A.6. The pictures of resulting devices are shown in Figure 4.6 as done by optical microscope and in Figure 4.7 by scanning electron microscope (SEM).

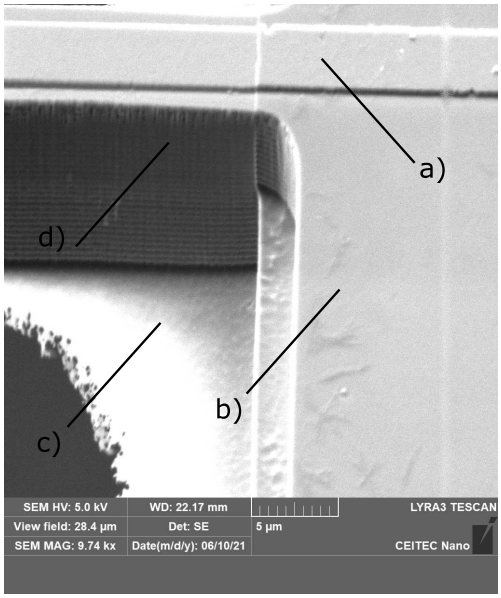

Figure 4.7: SEM image of the base of the silicon wire showing its structure. Pointers a)->d) correspond with the Figure 4.6.

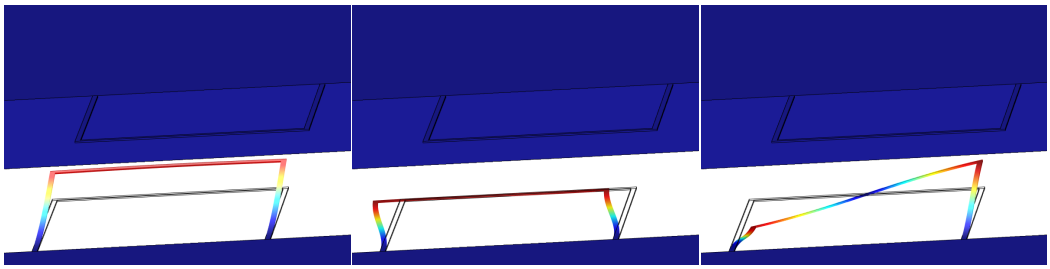

Figure 4.8: Visualization of the first three resonant modes of our MEMS devices, produced by finite element method model using the geometry of the whole chip.

4.3 Vacuum properties

In the first set, we have been able to prepare three working devices placed on two chips. One of the chips had only one of the devices working electrically, but both still physically present. In Table 4.2, we list the characteristic dimensions of all used MEMS devices. In Figure 4.8, we show the models of the first three resonant modes as a result of finite element method calculations using the geometry of the whole chip. We have accounted for the anisotropic elasticity of <100> Si, using following elastic constants [162], c_{11} = 165.7 GPa, c_{12} = 63.9 GPa, c_{44} = 79.6 GPa. These models can be used to predict the resonant frequencies of the individual devices modes and we list the values of the first fundamental mode in Table 4.2.

Initial experiments were performed in vacuum at room temperature, using a glass desiccator connected to a rotary pump, in order to find the resonant frequency of the devices and compare them with the values predicted by the model. The results agree well with the calculations, see Table 4.2. Both chips have been later mounted in the ^{4}He cell on the "wet" helium bath dilution refrigerator, with the base temperature of $\approx$ 20 mK, in Prague. In order to characterize devices

further, especially the intrinsic damping, we performed vacuum measurements at the base temperature. The MEMS were operated in an electrical scheme visualized in Figure 4.3, using Agilent A33220 signal generator and phase-sensitive Stanford Research SR830 lock-in amplifier, measuring the induced voltage. The driving current could be adjusted by the resistance of the I/V Converter and a static magnetic field was generated by the superconducting magnet. In the case of all here presented data, constant values of the magnetic field $B = 504$ mT and I/V resistance $R = 1$ MΩ were used.

Table 4.2: Listed dimensions and resonant frequencies of four used MEMS devices denoted by chip name (A->H) and position of wire on the chip (1->2). In this table, L_{MEMS} denotes the crossbar length, h the leg length, w the width, t the thickness, and d_{MEMS} the spacing between the two wires on the chip. The frequencies f_{calc} were calculated from the design geometry using the finite element method model. The vacuum frequencies f_{300K} and f_{20mK} were measured in a desiccator at room temperature and in a dilution refrigerator cell at the base temperature (20 mK), respectively. We note that the uncertainty in the thickness t of up to 0.5 μm due to uneven etching is sufficient to explain the discrepancies in the resonant frequencies. The intrinsic quality factor of the MEMS resonators Q, are evaluated from low-temperature measurements at a relatively high magnetic field $B = 504$ mT. It should be noted that higher Q factors are obtained in lower magnetic fields, see text.

Name	L_{MEMS} (μm)	h (μm)	w (μm)	t (μm)	d_{MEMS} (μm)	f_{calc} (kHz)	f_{300K} (kHz)	f_{20mK} (kHz)	Q-factor
G1–1	1000	1000	22	6.8	1080	4.80	4.88	4.91	1.5×10^5
G1–2	1000	900	22	6.8	1080	5.72	5.50	5.54	1.8×10^5
H3–2	300	1000	12	7.3	30	7.08	7.62	7.67	0.8×10^5

In Figures 4.9 4.10 4.11, we show the current drive series of the full frequency dependence sweeps of the MEMS resonances. At the highest drive currents, we start to operate in a non-linear Duffing regime, which is most profound for the G1-2 device, see Figure 4.10. The transition to this regime is typical for these devices and is described in more detail in Ref. [27]. We further evaluate the vacuum quality factors Q of order 10^5, see Table 4.2, estimated based on the fractions of resonant frequency and resonance width (FWHM) $Q = f_{res}/\Delta f$. For this purpose, we consider only the linear resonances at low drives. The main contributions, which should be considered for the observed dissipation are intrinsic, magneto-motive losses. We report the values of $Q \approx 4\times10^5$, for the G1 devices driven at smaller fields ≈ 10 mT. Concerning the resistive losses, we should be able to operate the MEMS in both normal and superconducting states of the driving aluminum layer. The state of the layer can be tuned by the temperature or more easily by the magnetic field. However, even in normal state of aluminum, having a resistance of the order of tens of Ω, the resulting power, in the range of used driving currents, should not exceed picowatt. Our results, therefore, show the good potential for the further use of manufactured devices as quantum turbulence detectors. More information on the following analysis of the temperature and the magnetic field dependence of device characteristics in

vacuum can be found in the Master Thesis of Maximilián Goleňa from Prague. His work also discusses the preliminary data from the device response in isotopically clean superfluid ^{4}He at temperatures below 1 K.

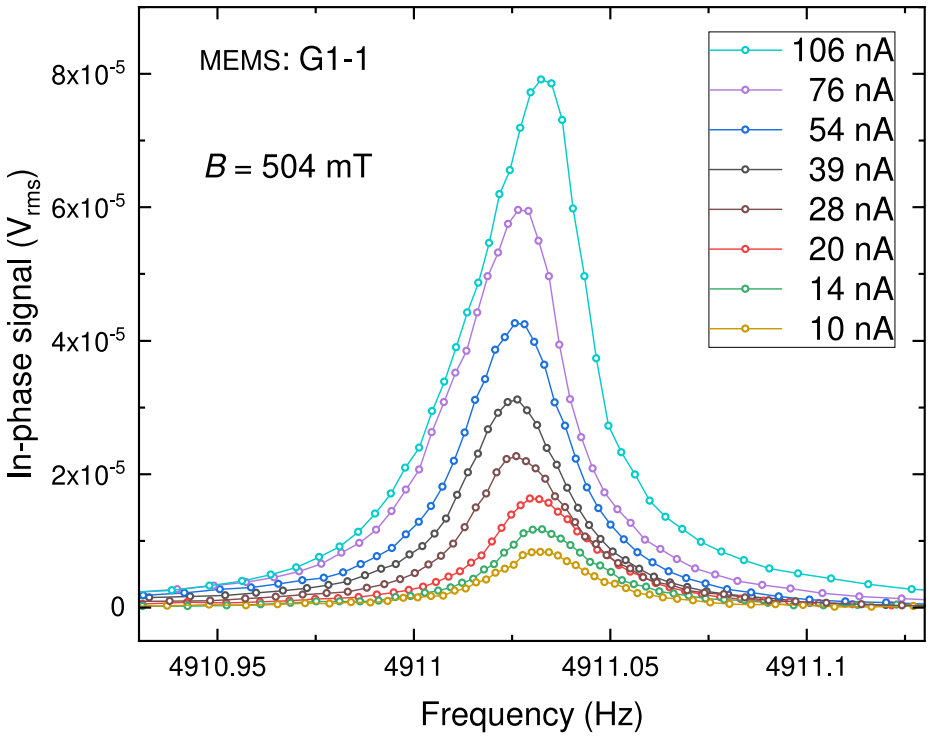

Figure 4.9: Drive series, between 10 nA and 106 nA, of the full resonant sweeps measured for MEMS device G1–1 in vacuum at 20 mK.

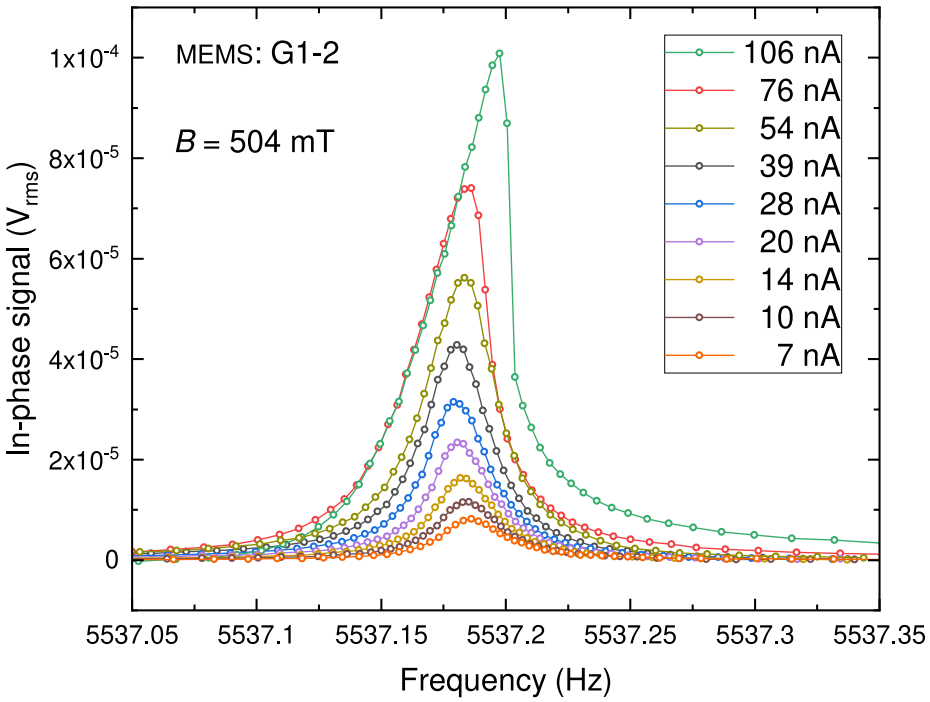

Figure 4.10: Drive series, between 7 nA and 106 nA, of the full resonant sweeps measured for MEMS device G1–2 in vacuum at 20 mK. The device is showing Duffing-type non-linearity at highest used drive.

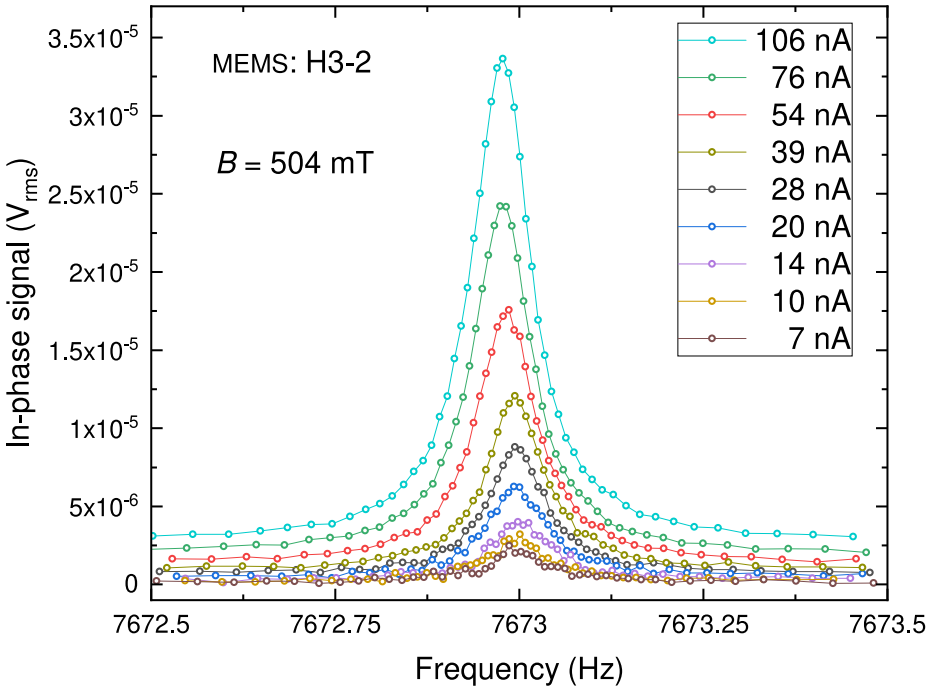

Figure 4.11: Drive series, between 7 nA and 106 nA, of the full resonant sweeps measured for MEMS device H3–2 in vacuum at 20 mK. Lower amplitude compared to the devices on G1 chip is caused by the smaller cross-bar length, as it affects the electro-mechanical properties given by Equation 4.3.

4.4 Detection of single quantized vortices in ^{3}He

In our last experiment, we performed measurements employing NEMS device, having similar geometry to the ones discussed above, submerged in ^{3}He-B on a rotating dilution refrigerator with a copper nuclear demagnetization stage at Aalto University in Helsinki. This experiment was conducted in collaboration with the ultra-low-temperature group led by Vladimir Eltsov. The used goal-post-shaped NEMS, manufactured by Timo Kamppinen, based on a single layer of aluminum in open window geometry is described in Ref. [30], having the following dimensions: cross-bar length = 160 μm, leg length = 50 μm, bar width = 20 μm, bar thickness = 250 nm. It was driven, at the resonant frequency of about 15 kHz, via magneto-motive technique, according to Equations 4.3, in magnetic field $B = 93$ mT.

In Figure 4.12, we show the typical force-velocity dependence of the device, operated at 0.15 T_C at the pressure of 19 bar. We plot the peak velocity of the NEMS, obtained from the full frequency sweeps, divided by driving force, to better visualize different observed regimes, as a function of the driving force, which is in a steady state equal to the sum of the drag forces. The real flow velocity values near the device are most probably higher than measured, due to the flow enhancement around the sharp edges. We can identify three distinct regimes of device operation. At the lowest velocities, NEMS velocity behaves linearly with force as expected for losses dominated by drag from ballistic quasi-particles. At higher velocities, damping due to thermal excitations is weakened by the screening effect of Andreev reflection [57, 58]. The thermal excitations may be reflected in the flow field generated around the oscillating NEMS, effectively decreasing their population sensed by the device. The same behavior was observed and explained in Ref [143]. Finally, at the highest velocities, above the critical velocity ≈ 7 mms^{-1}, we enter the "pair-breaking" regime [139, 143], where the superfluidity of ^{3}He starts to be suppressed. It is connected with a strong excess dissipation and NEMS velocity is saturating, see inset in Figure 4.12. In this regime, the detection ability of the device is limited by this dissipation mechanism and resonances are strongly non-linear, resembling frequency softening.

The unique geometry of the Helsinki apparatus is allowing for cryostat rotation leading to the generation of a uniform matrix of vertical quantized vortices. The NEMS is oriented in the experiment in such a way, that the device legs are aligned with the vortex grid (the axis of rotation is vertical), thus cross-bar being perpendicular (horizontal), with NEMS pointing down. In this geometry, we have been able to prepare a device state, with a single quantized vortex stably pinned to it. It is done by an "abrupt" change (on a timescale of order 10 s) of the steady rotation angular velocity, causing the vortex grid to travel towards the cell edges and eventually decay in case of zero rotation velocity or to reorganize spatially in other cases [163]. During this process, vortices passing the NEMS can interact with it and get trapped, see Figure 4.13. These events can be detected as a change in the device signal driven at a constant resonant frequency $\approx$ 15kHz, as vortex trapping causes a frequency shift of order 1 Hz. In an illustrative vortex trapping event shown in Figure 4.13, we distinguish between a vortex-free state, having original signal values visualized by solid lines, and a vortex-trapped state, with shifted signal values visualized by the dashed lines. Right after the rotation

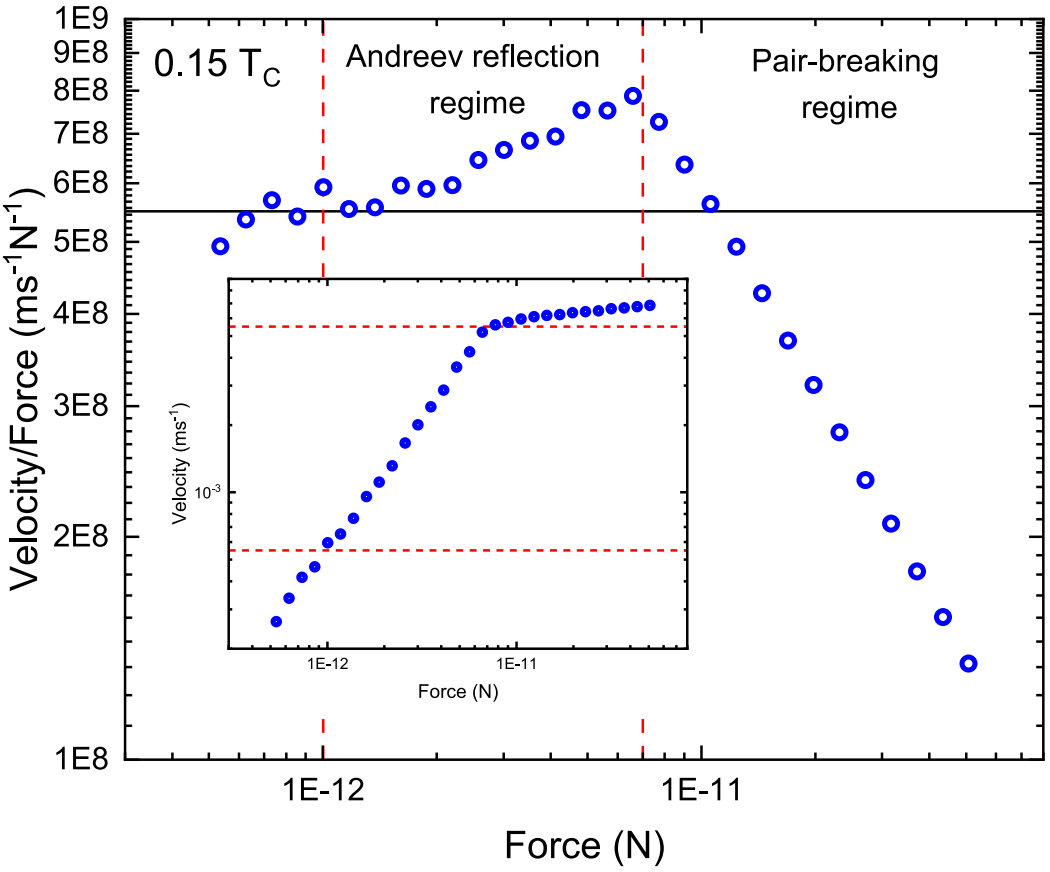

Figure 4.12: NEMS peak velocity, divided by driving force for visualization of the linear regime at low drives (black horizontal line), as a function of driving force, measured at 0.15 T_C. The red dashed lines bound different regimes. At the lowest velocities (i.e., lowest drives), NEMS velocity behaves linearly with force. At higher velocities, damping due to thermal excitations is weaker than linear caused by the screening effect of Andreev reflection. At the critical velocity, of the order of 7 mms^{-1} (see inset), the pair-breaking regime is reached, limiting further increases in velocity due to very effective dissipation. In the inset, corresponding force-velocity dependence is shown.

is stopped, a complex interaction of the device with a number of vortices in the system is observed, happening for $\approx$ 600 s, in this specific case. After this time, the signal changes are less frequent and more stable as there are fewer vortices remaining in the system. In the end, the vortex state is rather rare at zero or low rotation velocities, but if created then very stable. In the presented event, there is a vortex being trapped to the device after 1700 s from the rotation stopping and this state then persists for the whole experimental run of the order of days. When the vortex is trapped on the device after the vortex mesh decay is finished, it is very stable, and the device properties affected by the vortex, containing information about the single quantized vortex dynamics, may be studied. Vortices are much easier to trap at higher final rotation velocities and the signal levels are highly reproducible for multiple vortex trapping events.

In Figure 4.14, we show the difference in the drag experienced by the NEMS in vortex-free and pinned-vortex states, as measured at 0.15 T_C. At low velocities, there is no difference in the drag coefficient, and only the frequency of the

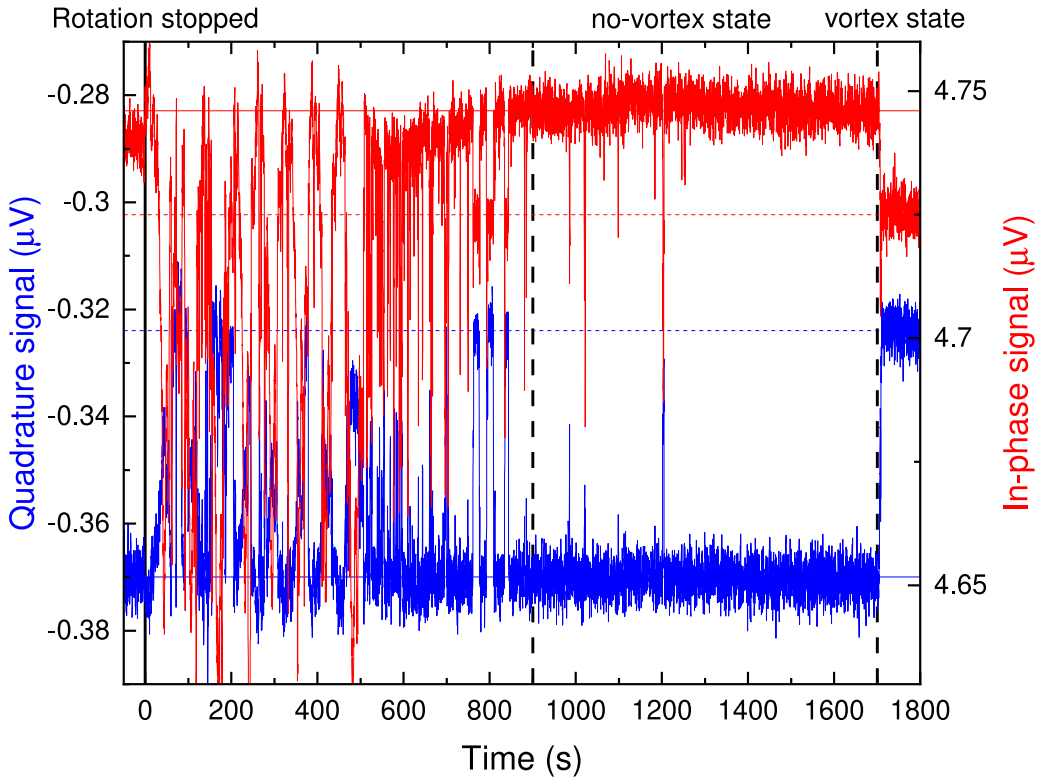

Figure 4.13: Time trace of the NEMS device response, measuring both signal components, after the abrupt stop of the cryostat rotation. After initial complex interaction with many vortices in the system, two device states are observed, based on values of signal components. Solid lines are representing the NEMS response without the vortex and dashed lines represent the state with the trapped vortex.

device is affected by the vortex, as discussed above. The quantized vortex is starting to contribute to the NEMS dissipation only above some critical velocity $\approx$3.7 mms^{-1}, where the two plotted data sets start to deviate. The additional drag should be directly connected to the dissipation mechanism of the vortex in a zero temperature limit, as discussed in 1.3. Unfortunately, we have a limited window of velocities where it can be studied further as the "pair-breaking" regime sets soon after. It is also possible that the vortex shifts the velocity at which the pair-breaking mechanism comes into effect.

Similar experiments on trapped vortices should lead to the observation of the Kelvin wave excitations on the trapped vortex, obtaining their spectrum and verifying the expected scaling of frequencies. The experimental work and analysis is ongoing [164] at the moment of writing of this Thesis and the details will be published elsewhere.

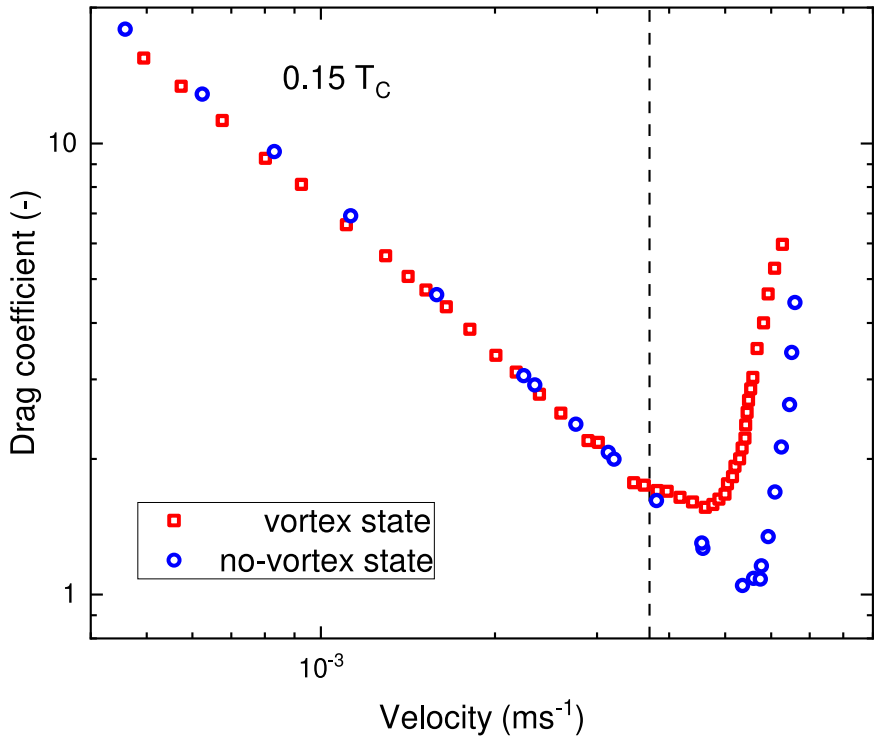

Figure 4.14: The difference in the drag experienced by the NEMS with trapped quantized vortex and without the vortex. The vortex is clearly causing additional damping above the critical velocity ≈3.7 mms^{-1}. The real critical velocity is however different, as flow enhancement around the sharp corners of the NEMS must be considered. The steep increase of the drag at the highest velocities is connected with the pair-breaking regime.

Conclusion

This Thesis brings together the main results of the Author, accumulated during his Ph.D. studies, working in the Laboratory of Superfluidity at the Department of Low-Temperature Physics, Faculty of Mathematics and Physics, Charles University. Over the past four years, numerous experiments employing mechanical resonating structures as tools for the study of the turbulent flows of quantum fluids have been performed, leading to the findings summarized below.

In general, the experimental work of the Author, especially measurements of the turbulent flows of superfluid ^{4}He in a wide range of temperatures, has contributed to a better understanding of the phenomenon of quantum turbulence 1.3. Based on the experimental data, properties of the turbulent flows in hydrodynamic and zero temperature limit were discussed on the phenomenological level. Two distinct types of turbulent flow can exist at all temperatures in He II, having different dynamical properties and coupling character of the possible turbulent structures – classical vortices and quantized vortices. We can distinguish the quasi-classical or Kolmogorov type of quantum turbulence with the coupled motion of normal and superfluid components and the ultra-quantum or Vinen type of quantum turbulence consisting of a chaotic bundle of quantized vortices. Further, new quantum lengthscale l_Q was introduced, marking the onset of the quantum character of the flow, where quantization of circulation becomes essential. It may be understood as a cut-off length for any classical-like description of the flow and its presence implies that no quantum flow may be fully described by a classical analogy.

In Chapter 2, we have addressed the onset of quantum turbulence in oscillatory flows of He II, i.e., in mechanically driven coflow and mechanically or thermally driven counterflow. Two types of instability can be considered in He II, being classical hydrodynamic instability in normal component or quantum instability connected with the production of quantized vortices in superfluid component. The origin of the initial transition can be identified through the analysis of the critical flow parameters. We showed that temperature-controlled cross-over between the two mentioned types of instability can exist in a single experiment, for both coflow and counterflow, however, having an inverse temperature trend in these two flow types. Among other, this approach helped to explain previously observed critical velocities in oscillatory counterflow and offers a unified framework for future discussion of flow instabilities.

The mechanical resonators in the form of superconducting vibrating wires have been also used, as local detectors of externally driven turbulent flows, as discussed in Chapter 3. Experiments have been conducted probing the hydrodynamic regime of He II, above 1 K, with complex interaction of its components. We measured the changes in resonant frequency and amplitude of the oscillator,

driven strictly in the laminar regime, upon application of the turbulent thermal counterflow. The changes in the device response can be connected with the change of its effective mass and excess damping and show the linear dependence with the vortex line density. Obtained decrease of the effective mass represents the fraction of Stokes boundary layer and can be explained by the properties of the boundary layer affected by mean mutual friction. However, this effect does not explain the whole measured excess damping and other mechanisms are present, e.g. direct momentum transfer during the device-vortex collisions.

In the final Chapter 4, we have discussed the general dissipation mechanisms of the resonators submerged in quantum fluids and closely characterized the losses due to acoustic emission, measured in ^{3}He , which can limit the detection potential of the device. Additionally, we report the fabrication process of the custom MEMS, following the trend of miniaturization of the devices leading to much higher sensitivity. Our devices have been characterized in vacuum at 20 mK and show potential for further study of quantum turbulence at the level of single quantized vortices. This goal was, nonetheless, achieved in experiments based on collaboration with the Helsinki ultra-low-temperature group. We have shown, that we can stably attach a single quantized vortex to a MEMS device, from the decaying turbulence in rotating vessel in ^{3}He -B, and measure additional losses caused by the vortex. Further experiments with the deeper analysis are still ongoing and will be presented elsewhere.

As a result, we have proven the potential of the employment of the mechanical resonating structures for the study of turbulent flows in quantum liquids. Devices of the custom dimensions and geometries can be developed for the specific experiments and can probe the superfluids at all temperatures with the great resolution and sensitivity. The use of such devices can lead to a better understanding of the properties of fully developed turbulent flow, but also of the initial instability onset. Finally, the MEMS and NEMS devices can be used to tackle the questions of single vortex dynamics, having unmatched spatial resolution amongst the available detection techniques.

Bibliography

[1] C.E. Swanson R.J. Donnelly. Quantum turbulence. *J Fluid Mech*, 173: 387—-429, 1986.

[2] C.F. Barenghi, R.J. Donnely, and W.F. Vinen. *Quantized Vortex Dynamics and Superfluid Turbulence*. Springer, 2001.

[3] L. Skrbek and K.R. Sreenivasan. Developed quantum turbulence and its decay. *Phys Fluids*, 24:011301—-011347, 2012.

[4] M. Tsubota, K. Fujimoto, and S. Yui. Numerical studies of quantum turbulence. *J. Low Temp. Phys.*, 188(5-6):119–189, 2017.

[5] R. Blaauwgeers, M. Blažková, M. Človečko, V.B. Eltsov, R. de Graaf, J.J. Hosio, M. Krusius, D. Schmoranzer, W. Schoepe, L. Skrbek, P. Skyba, R.E. Solntsev, and D.E. Zmeev. Quartz tuning fork: Thermometer, pressure- and viscometer for helium liquids. *J. Low Temp. Phys.*, 146(537), 2007.

[6] D. Schmoranzer, M. J. Jackson, V. Tsepelin, M. Poole, A. J. Woods, M. Človečko, and L. Skrbek. Multiple critical velocities in oscillatory flow of superfluid 4He due to quartz tuning forks. *Phys. Rev. B*, 94(214503), 2016.

[7] W. F. Vinen. The detection of single quanta of circulation in liquid helium II. *Proc. Roy. Soc. London., Series A*, 181:1524, 1961.

[8] M. Morishita, T. Kuroda, A. Sawada, and T. Satoh. Mean free path effects in superfluid 4He. *J. Low Temp. Phys.*, 76:387—-415, 1989.

[9] D.I. Bradley. Repetitive single vortex-loop creation by a vibrating wire in superfluid 3He-B. *Phys. Rev. Lett.*, 84(6):1252–1255, 1999.

[10] D.I. Bradley, D.O. Clubb, S.N. Fisher, A.M. Guénault, R.P. Haley, C.J. Matthews, G.R. Pickett, and K.L. Zaki. Turbulence generated by vibrating wire resonators in superfluid 4He at low temperatures. *J. Low Temp. Phys.*, 138:493—-498, 2005.

[11] D.I. Bradley, S.N. Fisher, A.M. Guénault, R.P. Haley, M. Holmes, S. O'Sullivan, G.R. Pickett, and V. Tsepelin. Grid turbulence in superfluid He-3-B at low temperatures. *J. Low Temp. Phys.*, 150:364–372, 2008.

[12] P. Švančara and M. La Mantia. Flows of liquid He-4 due to oscillating grids. *J. Fluid Mech.*, 832:578–599, 2017.

[13] J. Jäger, B. Schuderer, and W. Schoepe. Turbulent and laminar drag of superfluid helium on an oscillating microsphere. *Phys. Rev. Lett.*, 74(566), 1995.

[14] R. Hänninen and W. Schoepe. Statistics of intermittent switching between potential flow and turbulence around an oscillating sphere in superfluid He-4 below 0.5 k. *J. Low Temp. Phys.*, 158(410), 2010.

[15] M. Arrayás, F. Bettsworth, R.P. Haley, R. Schanen, J.L. Trueba, C. Uriarte, V.V. Zavjalov, and D.E. Zmeev. Progress on levitating a sphere in cryogenic fluids. *J. Low Temp. Phys.*, 2023.

[16] E. Varga. Peculiarities of spherically symmetric counterflow. *J. Low Temp. Phys.*, 196:28–34, 2019.

[17] Y.A Sergeev and C.F. Barenghi. Turbulent radial thermal counterflow in the framework of the HVBK model. *Eur. Phys. Lett.*, 128, 2019.

[18] E. Rickinson, C.F. Barenghi, Y.A. Sergeev, and A.W. Baggaley. Superfluid turbulence driven by cylindrically symmetric thermal counterflow. *Phys. Rev. B.*, 101, 2020.

[19] S. Inui and M. Tsubota. Spherically symmetric formation of localized vortex tangle around a heat source in superfluid He-4. *Phys. Rev. B.*, 101, 2020.

[20] Z.L Xie, Y.H. Huang, F. Novotny, Š. Midlik, D. Schmoranzer, and L. Skrbek. Spherical thermal counterflow of He II. *J. Low Temp. Phys.*, 208: 426–434, 2022.

[21] D. Kivotides, J.C. Vassilicos, D.C. Samuels, and C.F. Barenghi. Kelvin waves cascade in superfluid turbulence. *Phys. Rev. Lett.*, 86:3080–3083, 2001.

[22] W.F. Vinen, M. Tsubota, and A. Mitani. Kelvin-wave cascade on a vortex in superfluid 4He at a very low temperature. *Phys. Rev. Lett.*, 91(135301), 2003.

[23] E. Kozik and B. Svistunov. Kelvin-wave cascade and decay of superfluid turbulence. *Phys. Rev. Lett.*, 92, 2004.

[24] V.S. L'vov and S. Nazarenko. Spectrum of Kelvin-wave turbulence in superfluids. *JETP Lett.*, 91:428—-434, 2010.

[25] A.W. Baggaley and C.F. Barenghi. Spectrum of turbulent Kelvin-waves cascade in superfluid helium. *Phys. Rev. B.*, 83, 2011.

[26] V.B. Eltsov and V.S. L'vov. Amplitude of waves in the Kelvin-wave cascade. *JEPT Lett.*, 111, 2020.

[27] E. Collin, L. Filleau, T. Fournier, Y. M. Bunkov, and H. Godfrin. Silicon vibrating wires at low temperatures. *J. Low Temp. Phys.*, 150:739—-790, 2008.

[28] M. Defoort, K. J. Lulla, C. Blanc, H. Ftouni, O. Bourgeois, and E. Collin. Stressed silicon nitride nanomechanical resonators at helium temperatures. *J. Low Temp. Phys.*, 171:731–736, 2013.

[29] D.I. Bradley, R. George, A.M. Guénault, R.P. Haley, S. Kafanov, M.T. Noble, Yu. A. Pashkin, G.R. Pickett, M. Poole, J. R. Prance, M. Sarsby, R. Schanen, V. Tsepelin, T. Wilcox, and D.E. Zmeev. Operating nanobeams in a quantum fluid. *Scientific Reports*, 7(4876), 2017.

[30] T. Kamppinen and V.B. Eltsov. Nanomechanical resonators for cryogenic research. *J. Low Temp. Phys.*, 196:283–292, 2019.

[31] I. Golokolenov, B. Alperin, B. Fernandez, A. Fefferman, and E. Collin. Fully suspended nano-beams for quantum fluids. 210:550–561, 2023.

[32] L.D. Landau and E.M. Lifshitz. *Fluid Mechanics*. Pergamon Press, 1987.

[33] P. Kapitza. Viscosity of liquid helium below the λ-point. *Nature*, 141:74, 1938.

[34] J. Allen and A. Misener. Flow of liquid helium II. *Nature*, 141:75, 1938.

[35] D.D. Osheroff, R.C. Richardson, and D.M. Lee. Evidence for a new phase of solid He3. *Phys. Rev. Lett.*, 28:885, 1972.

[36] D.D. Osheroff, W.J. Gully, R.C. Richardson, and D.M. Lee. New magnetic phenomena in liquid He3 below 3 mk. *Phys. Rev. Lett.*, 29:920, 1972.

[37] F. London. The λ-phenomenon of liquid helium and the Bose-Einstein degeneracy. *Nature*, 141:643, 1938.

[38] L. Tizsa. Transport phenomena in helium II. *Nature*, 141:913, 1938.

[39] L.D. Landau. The theory of superfuidity of helium II. *J. Phys. USSR*, 5: 71–100, 1941.

[40] L.D. Landau. On the theory of superfluidity of helium II. *J. Phys. USSR*, 11:91, 1947.

[41] V. F. Sears, E. C. Svensson, P. Martel, and A. D. B. Woods. Neutron-scattering determination of the momentum distribution and the condensate fraction in liquid ^{4}He. *Phys. Rev. Lett.*, 49:279–282, 1982.

[42] V.V. Dmitriev, A.A. Senin, A.A. Soldatov, and A.N. Yudin. Polar phase of superfluid 3He in anisotropic aerogel. *Phys. Rev. Lett.*, 115(165304), 2015.

[43] L.V. Levitin, B. Yager, L. Sumner, B. Cowan, A.J. Casey, J. Saunders, N. Zhelev, R.G. Bennett, and J.M. Parpia. Evidence for a spatially modulated superfluid phase of 3He under confinement. *Phys. Rev. Lett.*, 122 (085301), 2019.

[44] S. Babuin, E. Varga, L. Skrbek, E. Lévêque, and P.E. Roche. Effective viscosity in quantum turbulence: a steady-state approach. *Europhys. Lett.*, 106(24006), 2014.

[45] S. Babuin, M. Stammeier, E. Varga, M. Rotter, and L. Skrbek. Quantum turbulence of bellows-driven 4He superflow: Steady state. *Phys. Rev. B*, 86 (134515), 2012.

[46] E. Varga, S. Babuin, and L. Skrbek. Second-sound studies of coflow and counterflow of superfluid 4He in channels. *Phys. Fluids*, 27(065101), 2015.

[47] R. J. Donnelly and C. F. Barenghi. The observed properties of liquid helium at the saturated vapor pressure. *J. Phys. Chem. Ref. Data*, 27, 1998.

[48] E.L. Andronikashvili. *Fiz. Zh.*, 10(201), 1946.

[49] H.E. Hall and W.F. Vinen. The rotation of liquid helium II II. the theory of mutual friction in uniformly rotating helium II. *Proc. Roy. Soc. A*, 238: 215, 1956.

[50] H. E. Hall. *Phil. Mag. Supp.*, 9, 1960.

[51] I.L. Bekharievich and I.M. Khalatnikov. *JETP*, 13, 1961.

[52] H. Palevsky, K. Otnes, and K. E. Larsson. Excitations of rotons in helium-II by cold neutrons. *Phys. Rev.*, 112:11–18, 1958.

[53] J.L. Yarnell, G.P. Arnold, P.J. Bendt, and E.C. Kerr. Excitations in liquid helium - neutron scattering measurements. *Phys. Rev.*, 113:1379–1386, 1959.

[54] D.G. Henshaw and A.D.B. Woods. Modes of atomic motions in liquid helium by inelastic scattering of neutrons. *Phys. Rev.*, 121, 1961.

[55] N.W. Ashcroft and N.D. Mermin. *Solid State Physics*. College Edition, 1976.

[56] D. Vollhardt and P. Wolfle. *The superfluid phases of helium 3*. Taylor & Francis, 1990.

[57] J.J. Hosio, V.B. Eltsov, R. de Graaf, M. Krusius, J. Mäkinen, and D. Schmoranzer. Propagation of thermal excitations in a cluster of vortices in superfluid He-3-B. *Phys. Rev. B*, 84(224501), 2011.

[58] Y.A. Sergeev, C.F. Barenghi, S.N. Fisher, V. Tsepelin, and N. Suramlishvili. Scattering length of Andreev reflection from quantized vortices in He-3-B. *Phys. Rev. B*, 91(134507), 2015.

[59] A.M. Guénault, A. Guthrie, R.P. Haley, S. Kafanov, Yu.A. Pashkin, G.R. Pickett, M. Poole, R. Schanen, V. Tsepelin, D.E. Zmeev, E. Collin, O. Maillet, and R. Gazizulin. Probing superfluid 4He with high-frequency nanomechanical resonators down to millikelvin temperatures. *Phys. Rev. B*, 100 (020506(R)), 2019.

[60] W.F. Vinen and L. Skrbek. Quantum turbulence generated by oscillating structures. *Proc. Natl. Acad. Sci. (USA)*, 111(4699), 2014.

[61] S. Autti, V.V. Dmitriev, J.T. Mäkinen, A.A. Soldatov, G.E. Volovik, A.N. Yudin, V.V. Zavjalov, and V.B. Eltsov. Observation of half-quantum vortices in topological superfluid 3He. *Phys. Rev. Lett.*, 117(255301), 2016.

[62] J.T. Mäkinen, V.V. Dmitriev, J. Nissinen, J. Rysti, G.E. Volovik, A.N. Yudin, K. Zhang, and V.B. Eltsov. Half-quantum vortices and walls bounded by strings in the polar-distorted phases of topological superfluid 3He. *Nature Com.*, 10(237), 2019.

[63] M.A. Silaev. Spectrum of bound fermion states on vortices in 3He-B. *JEPT Lett.*, 90:391—-397, 2009.

[64] O. Reynolds. An experimental investigation of the circumstances which determine whether the motion of water shall be direct or sinuous, and of the law of resistance in parallel channels. *Phil. Trans. Royal Soc. London*, 174, 1883.

[65] G.H. Keulegan and L.H. Carpenter. Forces on cylinders and plates in an oscillating fluid. *J. Res. Natl. Bureau Standards*, 60(423), 1958.

[66] S. B. Pope. *Turbulent Flows*. Cambridge University Press, 2000.

[67] L.F. Richardson. *Weather Prediction by Numerical Process*. Cambridge University Press, 1922.

[68] A.N. Kolmogorov. The local structure of turbulence in incompressible viscous fluid for very large Reynolds numbers. *Dokl. Akad. Nauk. SSSR*, 30: 299–303, 1941.

[69] A.N. Kolmogorov. A refinement of previous hypotheses concerning the local structure of turbulence in a viscous incompressible fluid at high Reynolds number. *J. Fluid Mech.*, 13:82–85, 1962.

[70] S.R. Stalp, L. Skrbek, and R.J. Donnelly. Decay of grid turbulence in a finite channel. *Phys. Rev. Lett.*, 82:4831, 1999.

[71] L. Skrbek and K.R. Sreenivasan. *How similar is quantum turbulence to classical turbulence? in Ten Chapters in Turbulence, ed. by P.A. Davidson, Y. Kaneda, K.R. Sreenivasan*. Cambridge University Press, 2013.

[72] U. Frisch. *Turbulence: The Legacy of A. N. Kolmogorov*. Cambridge University Press, 1995.

[73] D.V. Osborne. The rotation of liquid helium II. *Proc. Phys. Soc. A*, 63: 909, 1950.

[74] R.J. Donnelly. *Quantized Vortices In Helium II*. Cambridge University Press, 1991.

[75] G.P. Bewley, D. Lathrop, and K. Sreenivasan. Visualization of quantized vortices. *Nature*, 441:588, 2006.

[76] R.P. Feynman. *Progress in Low Temperature Physics, edited by C. J. Gorter, vol. 1, Chapter 2*. North-Holland Publications, Amsterdam, 1955.

[77] G. W. Rayfield and F. Reif. Quantized vortex rings in superfluid helium. *Phys. Rev.*, 136(A1194), 1964.

[78] C.M. Muirhead, W.F. Vinen, and R.J. Donnelly. *Philos. Trans. Roy. Soc. London A*, 311:433, 1984.

[79] P.C. Hendry, N.S. Lawson, P.V.E. McClintock, C.D.H. Williams, and R.M. Bowley. Macroscopic quantum tunneling of vortices in he II. *Phys. Rev. Lett.*, 60, 1988.

[80] D.R. Allum, P.V.E. McClintock, A. Phillips, and R.M. Bowley. The breakdown of superfluidity in liquid 4He: an experimental test of Landau's theory. 1977.

[81] N. Hashimoto, R. Goto, H. Yano, K. Obara, O. Ishikawa, and T. Hata. Control of turbulence in boundary layers of superfluid 4He by filtering out remanent vortices. *Phys. Rev. B*, 76(020504(R)), 2007.

[82] R. Goto, S. Fujiyama, H. Yano, Y. Nago, N. Hashimoto, K. Obara, O. Ishikawa, M. Tsubota, and T. Hata. Turbulence in boundary flow of superfluid 4He triggered by free vortex rings. *Phys. Rev. Lett.*, 100(045301), 2008.

[83] W.H. Zurek. Cosmological experiments in superfluid helium? *Nature*, 317, 1985.

[84] M.E. Dodd, P.C. Hendry, N.S. Lawson, P.V.E. McClintock, and C.D.H. Williams. Nonappearance of vortices in fast mechanical expansions of liquid 4He through the Lambda transition. *Phys. Rev. Lett.*, 81(17):3703–3706, 1998.

[85] M. Niemetz and W. Schoepe. Stability of laminar and turbulent flow of superfluid 4He at mK temperatures around an oscillating microsphere. *J. Low Temp. Phys.*, 135:447—469, 2004.

[86] R. Hänninen and W. Schoepe. Universal critical velocity for the onset of turbulence of oscillatory superfluid flow. *J. Low Temp. Phys.*, 153:189—-196, 2008.

[87] R. Hänninen and W. Schoepe. Dynamical scaling of the critical velocity for the onset of turbulence in oscillatory superflows. *J. Low Temp. Phys.*, 164: 1—4, 2011.

[88] D.K. Cheng, M.W. Cromar, and R.J. Donnelly. Influence of an axial heat current on negative-ion trapping in rotating helium II. *Phys. Rev. Lett.*, 31: 433, 1973.

[89] W.I. Glaberson, W.W. Johnson, and R.M. Ostermeier. Instability of a vortex array in He II. *Phys. Rev. Lett.*, 33:1197, 1974.

[90] R.M. Ostermeier and W.I. Glaberson. Instability of vortex lines in the presence of axial normal fluid flow. *J. Low Temp. Phys.*, 21:191—-196, 1975.

[91] W.F. Vinen. Mutual friction in a heat current in liquid helium II. III. Theory of the mutual friction. *Proc. R. Soc. Lond. A*, 242:493, 1957.

[92] S. Babuin, E. Varga, W.F. Vinen, and L. Skrbek. Quantum turbulence of bellows-driven 4He superflow: Decay. *Phys. Rev. B*, 92(184503), 2015.

[93] W.F. Vinen. Decay of superfluid turbulence at a very low temperature: The radiation of sound from a Kelvin wave on a quantized vortex. *Phys. Rev. B*, 64(134520), 2001.

[94] M.A. Silaev. Universal mechanism of dissipation in Fermi superfluids at ultralow temperatures. *Phys. Rev. Lett.*, 108(045303), 2012.

[95] J.T. Mäkinen, S. Autti, P.J. Heikkinen, J.J. Hosio, R. Hänninen, V.S. L'vov, P.M. Walmsley, V.V. Zavjalov, and V.B. Eltsov. Rotating quantum wave turbulence. *Nature Physics*, 2023.

[96] C.J. Gorter and J.H. Mellink. On the irreversible processes in liquid helium II. *Physica*, 15:285–304, 1949.

[97] W.F. Vinen. Mutual friction in a heat current in liquid helium II I. Experiments on steady heat currents. *Proc. R. Soc. Lond. A*, 240:114, 1957.

[98] W.F. Vinen. Mutual friction in a heat current in liquid helium II. II. Experiments on transient effects. *Proc. R. Soc. Lond. A*, 240:128, 1957.

[99] W.F. Vinen. Mutual friction in a heat current in liquid helium II. IV. Critical heat currents in wide channels. *Proc. R. Soc. Lond. A*, 243:400, 1958.

[100] H. E. Hall and W. F. Vinen. The rotation of liquid helium II I. Experiments on the propagation of second sound in uniformly rotating helium II. *Proc. Roy. Soc. A*, 238:204, 1956.

[101] E. Varga and L. Skrbek. Thermal counterflow of superfluid 4He: Temperature gradient in the bulk and in the vicinity of the heater. *Phys. Rev. B*, 100(054518), 2019.

[102] P.M. Walmsley and A.I. Golov. Quantum and quasiclassical types of superfluid turbulence. *Phys. Rev. Lett.*, 100(245301), 2008.

[103] D.E. Zmeev, P.M. Walmsley, A.I. Golov, P.V.E. McClintock, S.N. Fisher, and W.F. Vinen. Dissipation of quasiclassical turbulence in superfluid He 4. *Phys. Rev. Lett.*, 115, 2015.

[104] P.M. Walmsley and A.I. Golov. Coexistence of quantum and classical flows in quantum turbulence in the T=0 limit. *Phys. Rev. Lett.*, 118(134501), 2017.

[105] K.W. Schwarz. Theory of turbulence in superfluid 4He. *Phys. Rev. Lett.*, 38(551), 1977.

[106] K.W. Schwarz. Three-dimensional vortex dynamics in superfluid 4He. Homogeneous superfluid turbulence. *Phys. Rev. B*, 38(2398), 1988.

[107] J. Gao, E. Varga, W. Guo, and W.F. Vinen. Energy spectrum of thermal counterflow turbulence in superfluid helium-4. *Phys. Rev. B*, 96(094511), 2017.

[108] J. Gao, W. Guo, V.S. L'vov, A. Pomyalov, L. Skrbek, E. Varga, and W.F. Vinen. Decay of counterflow turbulence in superfluid 4He. *JETP Lett.*, 103 (648), 2016.

[109] E. Varga and L. Skrbek. Dynamics of the density of quantized vortex lines in counterflow turbulence: Experimental investigation. *Phys. Rev. B*, 97 (064507), 2018.

[110] G.P. Bewley, D.P. Lathrop, and K.R. Sreenivasan. Particles for tracing turbulent liquid helium. *Exp. Fluids*, 44(887), 2008.

[111] W. Guo, M. La Mantia, D.P. Lathrop, and S.W. Van Sciver. Visualization of two-fluid flows of superfluid helium-4. *Proc. Nat. Acad. Sci.*, 111:4653–4658, 2014.

[112] M.S. Paoletti, M.E. Fisher, K.R. Sreenivasan, and D.P. Lathrop. Velocity statistics distinguish quantum turbulence from classical turbulence. *Phys. Rev. Lett.*, 101(154501), 2008.

[113] T.V. Chagovets and S.V. Van Sciver. A study of thermal counterflow using particle tracking velocimetry. *Phys. Fluids*, 23(107102), 2011.

[114] M. La Mantia, T.V. Chagovets, M. Rotter, and L. Skrbek. Testing the performance of a cryogenic visualization system on thermal counterflow by using hydrogen and deuterium solid tracers. *Rev. Sci. Instrum.*, 83(055109), 2012.

[115] W. Kubo and Y. Tsuji. Lagrange trajectory of small particles in superfluid he II. *J. Low Temp. Phys.*, 187:611—617, 2017.

[116] W. Guo, J.D. Wright, S.B. Cahn, J.A. Nikkel, and D.N. McKinsey. Metastable helium molecules as tracers in superfluid 4He. *Phys. Rev. Lett.*, 102(235301), 2009.

[117] D.E. Zmeev, F. Pakpour, P.M. Walmsley, A.I. Golov, W. Guo, D.N. McKinsey, G.G. Ihas, P.V.E. McClintock, S.N. Fisher, and W.F. Vinen. Excimers He_2^* as tracers of quantum turbulence in 4He in the T = 0 limit. *Phys. Rev. Lett.*, 110(175303), 2013.

[118] F.P. Milliken, K.W. Shwarz, and C.W. Smith. Free decay of superfluid turbulence. *Phys. Rev. Lett.*, 48(1204), 1982.

[119] D.D. Awschalom, F.P. Milliken, and K.W. Schwarz. Properties of superfluid turbulence in a large channel. *Phys. Rev. Lett.*, 53(1372), 1984.

[120] P.M. Walmsley, A.I. Golov, H.E. Hall, A.A. Levchenko, and W. F. Vinen. Dissipation of quantum turbulence in the zero temperature limit. *Phys. Rev. Lett.*, 99(265302), 2007.

[121] P.M. Walmsley, A.I. Golov, H.E. Hall, W.F. Vinen, and A. A. Levchenko. Decay of turbulence generated by spin-down to rest in superfluid He-4. *J. Low Temp. Phys.*, 153:127, 2008.

[122] J.P. Pekola, J.T. Simola, K.K. Nummila, and O.V. Lounasmaa. Persistent-current experiments on superfluid 3He-B and 3He-A. *Phys. Rev. Lett.*, 53 (12), 1984.

[123] O.T. Ikkala, G.E. Volovik andd P.J. Hakonen, Y.M. Bunkov, S.T. Islander, and G.A. Kharodze. NMR in rotating superfluid He-3-B. *JETP Lett.*, 35: 416–420, 1982.

[124] P.J. Hakonen, O.T. Ikkala, S.T. Islander, O.V. Lounasmaa, T.K. Markkula, P. Roubeau, K.M. Saloheimo, G.E. Volovik, E.L. Andronikashvili, D.I. Garibashvili, and J.S. Tsakadze. NMR experiments on rotating superfluid 3He-A: Evidence for vorticity. *Phys. Rev. Lett.*, 48:1838–1841, 1982.

[125] Ü. Parts, J.M. Karimäki, J.H. Koivuniemi, M. Krusius, V.M.H. Ruutu, E.V. Thuneberg, and G.E. Volovik. Phase diagram of vortices in superfluid 3He-A. *Phys. Rev. Lett.*, 75:3320–3323, 1995.

[126] V. Peshkov. *Dokl. Akad. Nauk SSSR*, 45:365, 1944.

[127] E. Varga, M.J. Jackson, D. Schmoranzer, and L. Skrbek. The use of second sound in investigations of quantum turbulence in He II. *J. Low Temp. Phys.*, 197:130—148, 2019.

[128] E. Woillez, J. Valentin, and P.E. Roche. Local measurement of vortex statistics in quantum turbulence. *Europhys. Lett.*, 134(46002), 2021.

[129] V. Peshkov. *Zh Eksp, Teor. Fiz*, 11:1000, 1946.

[130] R.J. Zieve, C.M. Frei, and D.L. Wolfson. Energy loss from a moving vortex in superfluid helium. *Phys. Rev. B*, 86(174504), 2012.

[131] W. Schoepe. Statistics of intermittent switching between potential flow and turbulence around an oscillating sphere in superfluid 4He below 0.5 K. *J. Low Temp. Phys.*, 161:526–535, 2010.

[132] M. Arrayás, J.L. Trueba, C. Uriarte, and D.E. Zmeev. Design of a system for controlling a levitating sphere in superfluid 3He at extremely low temperatures. *Scientific Reports*, 11(20069), 2021.

[133] W. Schoepe. Vortex shedding from a microsphere oscillating in superfluid 4He at mk temperatures and from a laser beam moving in a Bose–Einstein condensate. *J. Low Temp. Phys.*, 210:539—-549, 2023.

[134] M. Blažková, D. Schmoranzer, and L. Skrbek. Transition from laminar to turbulent drag in flow due to a vibrating quartz fork. *Phys. Rev. E*, 75 (025302(R)):539–549, 2007.

[135] D. I. Bradley, M. Človečko, S.N. Fisher, D. Garg, E. Guise, R.P. Haley, O. Kolosov, G.R. Pickett, V. Tsepelin, D. Schmoranzer, and L. Skrbek. Crossover from hydrodynamic to acoustic drag on quartz tuning forks in normal and superfluid 4He. *Phys. Rev. B*, 85(014501), 2012.

[136] G. Sheshin, I. Gritsenko, D. Schmoranzer, and L. Skrbek. Mutual interactions of oscillating quartz tuning forks in superfluid 4He. *Low Temp. Phys.*, 39:823–827, 2013.

[137] D.I. Bradley, M. Človečko, S.N. Fisher, D. Garg, A.M. Guénault, E. Guise, R.P. Haley, G.R. Pickett, M. Poole, and V. Tsepelin. Thermometry in normal liquid 3He using a quartz tuning fork viscometer. *J. Low Temp. Phys.*, 171:750—-756, 2013.

[138] M. Človečko, K. Goliaš, and P. Skyba. Quartz tuning fork as a parametric resonator in high magnetic fields. *J. Low Temp. Phys.*, 201:154—161, 2020.

[139] M.T. Noble, S.L. Ahlstrom, D.I. Bradley, E.A. Guise, R.P. Haley, S. Kafanov, G.R. Pickett, M. Poole, R. Schanen, T. Wilcox, A.J. Woods, D.E. Zmeev, and V. Tsepelin. Producing and imaging quantum turbulence via pair-breaking in superfluid 3He-B. *Phys. Rev. B*, 105(174515), 2022.

[140] N. Hashimoto, A. Handa, M. Nakagawa, K. Obara, H. Yano, O. Ishikawa, and T. Hata. Switching phenomena between laminar and turbulent flows of superfluid 4He generated by a vibrating wire. *J. Low Temp. Phys.*, 148: 299—-303, 2007.

[141] Y. Nago, M. Inui, R. Kado, K. Obara, H. Yano, O. Ishikawa, and T. Hata. Vortex generation induced by low-frequency wire vibration in superfluid 3He-B. *Phys. Rev. B*, 82(224511), 2010.

[142] D.I. Bradley, M.J. Fear, S.N. Fisher, A.M. Guénault, R.P. Haley, C.R. Lawson, G.R. Pickett, R. Schanen, and V. Tsepelin. Anomalous damping of a low frequency vibrating wire in superfluid 3He-B due to vortex shielding. *J. Low Temp. Phys.*, 175:372—378, 2014.

[143] M. Defoort, S. Dufresnes, S.L. Ahlstrom, D.I. Bradley, R.P. Haley, A.M. Guénault, E.A. Guise, G.R. Pickett, M. Poole, A.J. Woods, V. Tsepelin, S.N. Fisher, H. Godfrin, and E. Collin. Probing bogoliubov quasiparticles in superfluid 3He with a 'vibrating-wire like' MEMS device. *J. Low Temp. Phys.*, 183, 2015.

[144] P. Skyba. Notes on measurement methods of mechanical resonators used in low temperature physics. *J. Low Temp. Phys.*, 160:219—239, 2010.

[145] Y. Nago, A. Nishijima, H. Kubo, T. Ogawa, K. Obara, H. Yano, O. Ishikawa, and T. Hata. Vortex emission from quantum turbulence in superfluid 4He. *Phys. Rev. B*, 87(024511), 2013.

[146] Y. Wakasa, S. Oda, Y. Chiba, K. Obara, H. Yano, O. Ishikawa, and T. Hata. Vortex emissions from quantum turbulence generated by vibrating wire in superfluid 4He at finite temperature. *J. Phys.: Conf. Ser.*, 568(012027), 2014.

[147] M. Imboden and P. Mohanty. Dissipation in nanoelectromechanical systems. *Phys. Reports*, 534:89–146, 2014.

[148] A. Guthrie, S. Kafanov, M.T. Noble, Y.A. Pashkin, G.R. Pickett, V. Tsepelin, A.A. Dorofeev, V.A. Krupenin, and D. E. Presnov. Nanoscale real-time detection of quantum vortices at millikelvin temperatures. *Nat. Commun.*, 12(2645), 2021.

[149] M. Človečko, P. Skyba, and F. Vavrek. Study of the nonlinear dynamics of micro-resonators based on a Sn-whisker in vacuum and at mK temperatures. *J. Low Temp. Phys.*, 196(2645):301—307, 2019.

[150] D.R. Brumley, M. Willcox, and J.E. Sader. Oscillation of cylinders of rectangular cross section immersed in fluid. *Phys. Fluids*, 22(052001), 2010.

[151] V. Kotsubo and G.W. Swift. Vortex turbulence generated by second sound in superfluid 4He. *Phys. Rev. Lett.*, 62(2604), 1989.

[152] V. Kotsubo and G.W. Swift. Generation of superfluid vortex turbulence by high-amplitude second sound in 4He. *J. Low Temp. Phys.*, 78(351), 1990.

[153] V.F. Mitin, P.C. McDonald, F. Pavese, N.S. Boltovets, V.V. Kholevchuk, I.Yu. Nemish, V.V. Basanets, V.K. Dugaev, P.V. Sorokin, R.V. Konakova, E.F. Venger, and E.V. Mitin. Ge-on-GaAs film resistance thermometers for cryogenic applications. *Cryogenics*, 47(474), 2007.

[154] T.V. Chagovets. Electric response in superfluid helium. *Physica B*, 488: 62–66, 2016.

[155] D. Durì, Ch. Baudet, J.P. Moro, P.E Roche, and P. Diribarne. Hot-wire anemometry for superfluid turbulent coflows. *Rev. Scient. Inst.*, 86(025007), 2015.

[156] A. Kraus, A.Erbe, and R.H. Blick. Nanomechanical vibrating wire resonator for phonon spectroscopy in liquid helium. *Nanotechnology*, 11:165–168, 2000.

[157] D. Cattiaux, I. Golokolenov, S. Kumar, M. Sillanpää, L. Mercier de Lépinay, R.R. Gazizulin, X. Zhou, A.D. Armour, O. Bourgeois, A. Fefferman, and E. Collin. A macroscopic object passively cooled into its quantum ground state of motion beyond single-mode cooling. *Nat. Commun.*, 12(6182), 2021.

[158] D. Schmoranzer, M. La Mantia, G. Sheshin, I. Gritsenko, A. Zadorozhko, M. Rotter, and L. Skrbek. Acoustic emission by quartz tuning forks and other oscillating structures in cryogenic 4He fluids. *J. Low Temp. Phys.*, 163(229):317—-344, 2011.

[159] A.M. Guénault, R.P. Haley, S. Kafanov, M.T. Noble, G.R. Pickett, M. Poole, R. Schanen, V. Tsepelin, J. Vonka, T. Wilcox, and D.E. Zmeev. Acoustic damping of quartz tuning forks in normal and superfluid 3He. *Phys. Rev. B*, 100(104526), 2019.

[160] D.J. Cousins, S.N. Fisher, A.M. Guénault, R.P. Haley, I.E. Miller, G.R. Pickett, G.N. Plenderleith, P. Skyba, P.Y.A. Thibault, and M.G. Ward. An advanced dilution refrigerator designed for the new Lancaster microkelvin facility. *J. Low Temp. Phys.*, 114:547—-570, 1999.

[161] W.R. Abel, A.C. Anderson, and J.C. Wheatley. Propagation of zero sound in liquid He3 at low temperatures. *Phys. Rev. Lett.*, 32(74), 1966.

[162] M.A. Hopcroft, W.D. Nix, and T.W. Kenny. What is the Young's modulus of silicon? *J. Microelectromech. Systems.*, 19(229), 2010.

[163] V.B. Eltsov, R. de Graaf, P.J. Heikkinen, J.J. Hosio, R. Hänninen, and M. Krusius. Vortex formation and annihilation in rotating superfluid 3He-B at low temperatures. *J. Low. Temp. Phys.*, 161:474—-508, 2010.

[164] private communication V. Eltsov.

Appendix A

Selected publications

A.1 L. Skrbek, D. Schmoranzer, Š. Midlik, K. R. Sreenivasan, Phenomenology of quantum turbulence in superfluid helium, PNAS 118 (2021)

PERSPECTIVE

Phenomenology of quantum turbulence in superfluid helium

Ladislav Skrbek[a,1], David Schmoranzer[a], Šimon Midlik[a], and Katepalli R. Sreenivasan[b,1]

Edited by David A. Weitz, Harvard University, Cambridge, MA, and approved February 22, 2021 (received for review December 4, 2020)

Quantum turbulence—the stochastic motion of quantum fluids such as ^{4}He and ^{3}He-B, which display pure superfluidity at zero temperature and two-fluid behavior at finite but low temperatures—has been a subject of intense experimental, theoretical, and numerical studies over the last half a century. Yet, there does not exist a satisfactory phenomenological framework that captures the rich variety of experimental observations, physical properties, and characteristic features, at the same level of detail as incompressible turbulence in conventional viscous fluids. Here we present such a phenomenology that captures in simple terms many known features and regimes of quantum turbulence, in both the limit of zero temperature and the temperature range of two-fluid behavior.

quantum turbulence | pure superfluid state | two-fluid state | Vinen and Kolmogorov turbulence

Turbulence is ubiquitous in Nature. Although it is an unfinished problem in science, incompressible turbulence in classical viscous fluids described by the Navier–Stokes equations, especially its decay without sustained production, as in the case of homogeneous and isotropic turbulence (HIT), is understood sufficiently well at the phenomenological level. Its properties can be described in surprisingly tangible detail (1). Quantum turbulence (QT) (2, 3) occurs in quantum fluids displaying superfluidity and two-fluid behavior at finite temperatures, such as the liquid phase of ^{4}He below the lambda temperature T_λ or the superfluid B phase of ^{3}He (4). Physical properties of quantum fluids cannot be described entirely by classical physics contained in the Navier–Stokes equations. Most physical properties of He II and ^{3}He-B are understood within the phenomenological two-fluid model, with the following main features. For temperatures $T < T_\lambda \approx 2.2$ K, liquid ^{4}He, called He II, is described as if it is composed of two interpenetrating constituents, the superfluid of density ρ_s and the normal fluid of density ρ_n; for ^{3}He-B the corresponding temperature $T_c \approx (1-3)$ mK, depending on the pressure. The viscous normal fluid consists of a gas of thermal excitations and carries the entire entropy content of the liquid. At relatively "high" temperatures (approximately above 1 K in He II and >200 μK in ^{3}He-B), the mean-free path is small and the thermal excitations can be described hydrodynamically as a fluid with finite viscosity. It coexists with the inviscid superfluid component carrying no entropy. The total density ρ of the liquid is nearly temperature independent and satisfies $\rho = \rho_n + \rho_s$. In the $T \to 0$ limit, helium is entirely a superfluid ($\rho_s/\rho \to 1$ and $\rho_n/\rho \to 0$), while superfluidity vanishes at the high temperatures just stated ($\rho_s/\rho \to 0$ and $\rho_n/\rho \to 1$).

Under isothermal conditions, the two fluids move independently when flow velocities are small. When a certain critical velocity is exceeded, however, thin vortex lines are formed in the superfluid component. Their circulation is not arbitrary as in classical fluids but quantized (5, 6) in units of $\kappa = h/M$ (usually singly), where h is Planck's constant and M is the mass of the superfluid particle (in the He II which is bosonic, $M = m_4$, the mass of the ^{4}He atom, while in the fermionic ^{3}He-B $M = 2m_3$, mass of the Cooper pair, twice the mass of the ^{3}He atom). The interaction of these quantized vortices gives rise to a tangle of quantized vortices, whose dynamics are QT's essential ingredient.

In the experimentally challenging limit of zero temperature with no normal fluid, QT consists only of the dynamical and disordered tangle of quantized vortex lines and can be called pure superfluid turbulence. The quantity characterizing the intensity of superfluid turbulence is the vortex line density, L,

[a]Faculty of Mathematics and Physics, Charles University, 121 16 Prague, Czech Republic; and [b]Department of Physics, Courant Institute of Mathematical Sciences, Tandon School of Engineering, New York University, New York, NY 11201

Author contributions: L.S. and D.S. designed research; D.S. and Š.M. performed research; D.S. and Š.M. analyzed data; and L.S. and K.R.S. wrote the paper.

The authors declare no competing interest.

This article is a PNAS Direct Submission.

[1]To whom correspondence may be addressed. Email: Ladislav.Skrbek@mff.cuni.cz or katepalli.sreenivasan@nyu.edu.

Published March 31, 2021.

which is the length of vortex line per unit volume. There exist two distinctly different and well-defined turbulent regimes called the Vinen (or ultraquantum) turbulence and the Kolmogorov (or quasiclassical) turbulence, the latter having various analogies with that in classical fluids.

At finite temperatures with the two-fluid behavior, QT may or may not involve turbulent motion of the normal fluid. When vortex lines are present in the isothermal flow, the otherwise independent normal and superfluid velocity fields become coupled by mutual friction acting at all relevant length scales, adding more complexity. Still, Vinen and Kolmogorov forms of quantum turbulence exist. We shall discuss them when the normal and superfluids flow counter to each other (called counterflow), for which there is no obvious classical analogue, and when they flow in parallel (coflow).

In this article we offer a systematic phenomenological description of various forms of QT in helium superfluids and compare them with turbulence of viscous fluids. For simplicity, our analysis is focused on three-dimensional (3D) HIT and based on experimental observations but, toward the end, employs models that treat the superfluid component containing the vortex tangle as a continuum possessing an effective "superfluid viscosity." The reason is that, even though the essential information in QT lies at small scales between vortex lines, their coarse graining enables useful views of the continuum type to be valid.

Pure Superfluid Turbulence

We start with the zero-temperature limit. In the frame of the two-fluid model both He II and ^{3}He-B are purely superfluid. As in classical turbulence, we have to consider only one velocity field. However, this velocity field is subject to the quantum mechanical constraint that the vorticity is zero everywhere except within the cores of quantized vortices.

The Model. In classical HIT, the finite size D of the turbulent box bounds the largest scale. The turbulent energy is supplied at some characteristic scale $M \leq D$, which might be the size of a bluff body, the mesh size of the turbulence-generating grid, or D itself. In a steady state, the turbulent kinetic energy, K, and the rate of energy dissipation ε at small scales are related by $\varepsilon = -dK/dt$. Nonlinearity ensures that the energy is dissipated in a different range of scales than the injection range. By the processes of advection and stretching, the energy is thought to undergo the Richardson cascade down the scales until it reaches small scales of dissipation. The characteristic scale around which the turbulent energy eventually dissipates is the Kolmogorov scale $\eta \equiv (\nu^3/\varepsilon)^{1/4}$, where ν is the fluid viscosity; the corresponding Kolmogorov wavenumber $k_\eta = 2\pi/\eta$. One can also define, taking ν and ε as the only relevant variables, a corresponding velocity scale $u \equiv (\nu\varepsilon)^{1/4}$, which characterizes the motion of the scale η; the characteristic Reynolds number $\mathrm{Re}_\eta = u\eta/\nu \equiv 1$. From these considerations, scales smaller than η are not relevant to turbulence dynamics in a classical viscous fluid.

If the energy input at scale M is small enough for the Kolmogorov dissipation length η to be of the order of M, no turbulence can be created. Upon increasing ε, η becomes smaller and crosses M; gradually an "inertial range" of scales develops between M and η. According to our present understanding, the part of the spectrum for $k < M$ acquires a k^2 slope by the equipartition theorem, in agreement with the Birkhoff–Saffman invariant (7, 8). By requiring the spectral energy density $E(k)$ in the inertial range to depend only on the wavenumber k and ε (which is transmitted across the inertial range without dissipation), one arrives at the celebrated Kolmogorov form $E(k) = C\varepsilon^{2/3}k^{-5/3}$, where the constant C is experimentally known to be about 1.62 ± 0.17 (9).

After the cessation of energy input, the energy-containing scale grows with time and could saturate at D at some point. Although η also grows with time, leading to a shorter inertial range, considerable scale separation could persist and the spectrum in the decaying state could retain the same form as above. In this state of decay (10), it is possible to solve for the energy as a function of time. The result is that $\varepsilon \propto t^{-2}$ and the turbulent energy decays as $K \propto t^{-2}$.

In pure superfluid turbulence, there is no viscosity and hence no dissipative scale η. The flow exists down to the smallest scale, which is the size of the vortex core $\xi_4 \approx 0.1$ nm in He II and $\xi_3 \approx 10$ to 60 nm in ^{3}He-B. One can, however, define the superfluid Reynolds number Re_Q by replacing the kinematic viscosity ν by the quantum of circulation κ of the same dimensions, and ask for the length scale ℓ_Q at which $\mathrm{Re}_Q = u_Q\ell_Q/\kappa \equiv 1$, where $u_Q \equiv (\kappa\varepsilon)^{1/4}$.* We call the length ℓ_Q as the quantum length scale† $\ell_Q = (\kappa^3/\varepsilon)^{1/4}$ and define a corresponding wavenumber as $k_Q = 2\pi/\ell_Q$. Physically, ℓ_Q marks the transition between quasiclassical scales for which quantization of circulation plays no role (or the "granularity" of QT does not matter) and the quantum scales for which quantum restrictions are essential.

The Kolmogorov cascade cannot proceed beyond k_Q because its very existence is a purely quantum effect. The transfer of turbulent energy farther down the scales is possible by a different mechanism mediated by the Kelvin wave cascade on individual vortex lines in incompressible flow (12) [although a bottleneck, analogous to the classical case (13), might develop around ℓ_Q (14)]. The dissipation mechanism for $k > k^*$ is the phonon emission by Kelvin waves in He II (15) or the excitation of Caroli–Matricon states in vortex cores in ^{3}He-B (16). For this range, L'vov and Nazarenko (17) derived (neglecting these dissipation mechanisms) the superfluid energy spectrum for $k > k_Q$ to be of the form

$$E(k) = C_{LN}\Lambda\kappa\varepsilon^{1/3}\Psi^{-3/2}k^{-5/3}, \qquad [1]$$

where $\Psi = 4\pi K\Lambda^{-1}\kappa^{-2}$, $K = \int E(k)dk$, the dimensionless number Λ is about 15 for He II and 12 for ^{3}He-B, and $C_{LN} = 0.304$ (18). Beyond k^*, there must be a cross-over to $E(k) \propto 1/k$, which is the form of the spectral energy for straight vortex lines. Length scales smaller than $2\pi/k^*$ are not relevant to

*The quantum length scales in He II (for which $\kappa \cong 0.997 \times 10^{-7}$ m^2/s) and ^{3}He-B (for which $\kappa \cong 0.662 \times 10^{-7}$ m^2/s) are of the same order as the Kolmogorov dissipation scale η in the normal liquid He I just above T_λ; indeed, $\nu \approx \kappa/6$ according to ref. 11. As in unitary Fermi gas [M. Zwierlein, "Quantum transport in strongly interacting fermi gases" in *International Workshop on Quantum Turbulence: Cold Atoms, Heavy Ions, and Neutron Stars, March 18–April 19, Seattle* (2019), vol. 1, p. 1.], this fact links two apparently unrelated physical quantities—the kinematic viscosity, ν, in the normal state and the quantum of circulation, κ, in the superfluid state, bridging classical and quantum-mechanical descriptions of liquid ^{4}He.

†In the literature, the term quantum length scale is often used for the mean distance between vortex lines in the tangle, $\ell = 1/\sqrt{L}$. Although a useful measure of the intensity of QT and density of vortex lines, it does not carry any information on whether or not the normal fluid is turbulent. We will later show that ℓ_Q and ℓ differ by no more than a factor of 2 in He II. We reserve the phrase for ℓ_Q because it is analogous to the dissipation length η and allows useful comparisons to be made of complementary phenomena in classical turbulence and QT.

the dynamical motion of vortex tangles. An alternative approach to calculating the high wavenumber spectrum considers the flow as compressible. Tanogami (19) studied superfluid turbulence in 3D via the Gross–Pitaevskii equation and exploited the analytical method of Onsager's "ideal turbulence" theory. He proposed a quantum energy cascade with k^{-3} scaling beyond the quantum length scale, induced by quantum stresses, which, interestingly, may include the Kelvin wave cascade.

Now, let us examine the evolution of the steady-state superfluid energy spectrum in a box of size D, assuming a sustained energy input at scale M (e.g., by a grid of mesh size M, $\xi_3, \xi_4 \ll M \ll D$) (Fig. 1). Any remnant vorticity (21) (e.g., vortex loops pinned on the grid surface, which is nearly always rough on these scales) becomes unstable by the Glaberson–Donnelly instability (22), leading to a vortex tangle when the critical flow velocity is exceeded. A steady-state superfluid energy spectrum develops after a transient, truncated at k^* by one of the mechanisms described above.

The actual form of the steady-state energy spectrum depends on the interplay between the two important scales, M and ℓ_Q. For small enough ε, $\ell_Q > M$, and so the Richardson cascade cannot operate. Energy is transferred down the scales via a Kelvin wave cascade or quantum stress cascade, until k^* is reached. This is the Vinen (ultraquantum) turbulence, where the vortex tangle is approximately random (Fig. 1, *Top*). The temporal decay of this turbulence, characterized by just one fixed length scale (quantized vortices in the tangle are assumed to be approximately evenly spaced), was first discussed by Vinen (23). On page 504, he wrote, "We shall now suppose that, if two oppositely directed vortex lines approach each other sufficiently closely, they can break up into small vortex rings in the manner suggested by Feynman (6) and eventually degenerate into thermal excitations" and argued that the vortex line density decays according to the equation

$$\frac{dL}{dt} = -\frac{\vartheta_2 \kappa}{2\pi} L^2, \qquad [2]$$

where ϑ_2 is a constant of order unity, leading to $L(t) \propto 1/t$ for late times. This form of the temporal decay of L, once the energy input stops, is the fingerprint of the Vinen turbulence.

Let us now increase ε so that ℓ_Q becomes nominally smaller than M (Fig. 1, *Middle*). Assuming an interaction between scales á la the equipartition theorem, the spectrum to the left of M must acquire the k^2 form, but the situation to the right of M changes by developing an inertial range between M and ℓ_Q, with the energy transfer from the small to the large wavenumbers occurring quasiclassically via the Richardson cascade. With increasing ε, the inertial range of scales increases and contains most of the kinetic energy of superfluid turbulence; see the red spectrum in Fig. 1, *Bottom*. This is the Kolmogorov (quasiclassical) turbulence, containing large vortex structures which can be thought of as composed of vortex-line bundles, achieved by partial polarization of the tangle. At scales sufficiently larger than ℓ_Q, the shape of the energy spectrum is thus Kolmogorov's. How far in k this picture holds depends on the interplay between classical and quantum physics, since the latter starts to intervene when approaching $k_Q = 2\pi/\ell_Q$; thereon, the turbulent motion is discretized and governed by quantum physics, described by the dynamics of individual quantized vortices. The quasiclassical limit is very similar to 3D Navier–Stokes for HIT, where viscous dissipation acting at small scales of order η is replaced by one of the mechanisms discussed above. At scales smaller than ℓ_Q the turbulence is always ultraquantum.

A key point is that for classical turbulence in the unbounded case, there are only two length scales to consider: M and η. In superfluid turbulence, there is an additional important scale, ℓ_Q, which intervenes as described above. Pure superfluid turbulence therefore cannot be considered, in contrast to statements in the literature, a simple "prototype" of turbulence; despite the similarities, it is different and more complex than the classical case. Naturally, however, the quasiclassical part of the picture is the same as that of classical 3D HIT and its temporal decay follows predictions of the spectral decay model (10, 24, 25). It is applicable also for decaying vortex line density, L, since the quasiclassical relation $\varepsilon = \nu_{\text{eff}}(\kappa L)^2$, following from the Navier–Stokes equations, holds (20). Here κL is the quasiclassical vorticity and ν_{eff} denotes the effective kinematic viscosity. We present the experimental evidence for this relationship in *Cross-Over from the Vinen to Kolmogorov Forms*.

We note that this close correspondence of the Kolmogorov-type QT with the classical case suggests the plausibility that the intermittency corrections may be the same for classical 3D HIT and for Kolmogorov pure superfluid turbulence at scales sufficiently larger than ℓ_Q. We will comment more on it later.

Manifestations of Vinen and Kolmogorov Forms of QT. At present, there are no direct spectral measurements of superfluid turbulence at zero temperature (i.e., close enough to zero that the

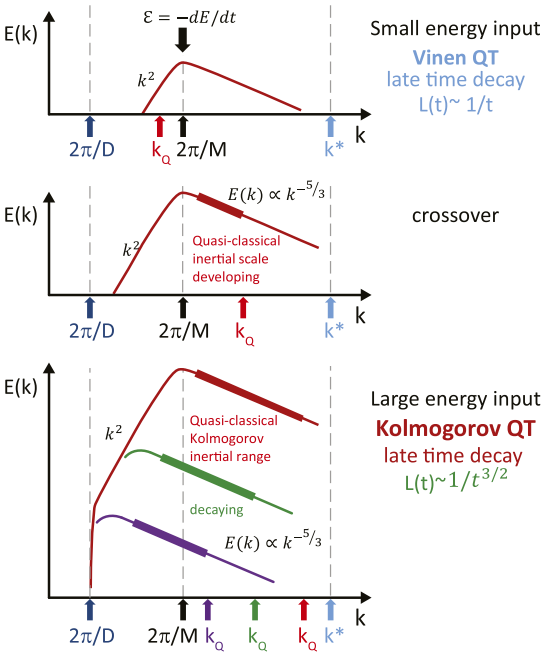

Fig. 1. Schematic in log-log coordinates of the general shapes of 3D energy spectra $E(k)$ plotted versus the wavenumber k of purely superfluid turbulence, assuming that it is forced at the scale M. (*Top*) Vinen turbulence, where ℓ_Q (red arrow) is larger than M. (*Middle*) Crossover from Vinen to Kolmogorov turbulence. With increasing ε, ℓ_Q crosses M. The classical Richardson cascade begins to operate and an inertial range of scales (thick red) develops gradually. (*Bottom*) For large enough ε, a significant extent of the inertial range develops as in steady-state classical 3D HIT (red). After the forcing stops, the decaying spectrum is shown in green and violet for two subsequent times; k_Q values are shown explicitly for each of them. The energy-containing scale grows during decay and eventually saturates at D and the classical decay of the form $L(t) \propto t^{-3/2}$ follows (20). Also, k_Q decreases faster than the energy-containing scale, so the inertial range shrinks with time. The spectra between k_Q and k^* have been drawn with slopes of $-5/3$ to be consistent with Eq. 1.

normal component is essentially nonexistent), so we cannot test the model in detail. Following Vinen (20), we introduce an effective mean-square vorticity in the superfluid component, defined by $\langle\omega^2\rangle_{\rm eff} = (\kappa L)^2$, which allows us to make direct reference to the experimentally measured quantity L. Using the above relation, we obtain the expression $L(t) \propto 1/t^{3/2}$ at late times for Kolmogorov QT when the length-scale saturation occurs; this is the result we shall test repeatedly here. The spectral form of the Vinen turbulence is not known [it could be of the $k^{-5/3}$ form as in Eq. **1** with a bottleneck or of the k^{-3} form of Tanogami (19)].[‡] For the purposes of Fig. 1, we take the manifestation of the Vinen turbulence to be Eq. **2**, according to which (at late times) $L \propto 1/t$. This is the main result we will test here. Our other important exploration concerns the cross-over between the two types of turbulence.

Cross-Over from the Vinen to Kolmogorov Forms. We will illustrate the cross-over in both steady-state and decaying quantum turbulence in ^{3}He-B in the measurements of the Lancaster group (27). QT was generated by oscillating grids and detected using the unique technique of Andreev reflection, which is possible because of the fermionic nature of superfluidity in ^{3}He-B. Briefly, the equilibrium number of quasiparticles (and quasiholes) can be sensed by a vibrating wire resonator. The drag force exerted on the vibrating wire by these ballistically propagating excitations is reduced if the wire is surrounded by a vortex tangle, as some incoming quasiparticles (quasiholes) cannot reach it, being Andreev reflected by energy barriers of the velocity field near the vortex cores.[§] The fractional decrease in damping can then be converted into the vortex line density in the tangle (27).

Two complementary experiments are worthy of attention. In the first one, quantum turbulence is generated by an oscillating grid of fine copper wires spaced $M = 50$ μm apart. By increasing the forcing, more and more energy is supplied to the flow at the scale M, all of which is being dissipated in the steady state. Facing the grid are detectors of quantum turbulence—two vibrating wire resonators—detecting the transition to quantum turbulence above a certain drive level (28). Increasing the oscillation amplitude of the grid results in a higher energy decay rate, ε; consequently, the quantum wavenumber $k_{\rm Q} \propto \varepsilon^{1/4}$ increases. Bradley et al. (29) then investigated the temporal decay of vortex line density originating from various levels of intensity of the steady state; they presented representative results in their figure 2. With increasing ε used to reach the steady state, temporal decay changed its form from $L(t) \propto t^{-1}$ (Vinen QT) to $L(t) \propto t^{-3/2}$ (the Kolmogorov QT in a bounded domain).[¶]

In the second experiment, Bradley et al. (31) measured directly the energy decay rate ε of grid-generated turbulence inside a small box acting as a black body radiator of quasiparticles. The late-time decay changes in character, from $\varepsilon \propto t^{-2}$ to $\varepsilon = \nu_{\rm eff}\kappa^2 L^2 \propto t^{-3}$—consequently the turbulent energy decays as $K \propto t^{-2}$, in agreement with the late decay of turbulent energy in classical 3D HIT in a bounded domain. We emphasize that this experiment provides a direct measurement of the energy released by freely decaying quantum turbulence. It is remarkable that, leaving aside caveats such as homogeneity and isotropy of the turbulence inside the black box radiator, the decay of pure superfluid turbulence was found to be surprisingly similar to the known decay of classical 3D HIT. The results also confirm that the key phenomenological relationship, $\varepsilon = -dK/dt = \nu_{\rm eff}(\kappa L)^2$, first suggested by Vinen (20), is meaningful for the Kolmogorov type of pure superfluid turbulence.

We now consider another indication of the transition from Vinen to Kolmogorov turbulence in pure superfluid, following the scenario of Fig. 1, this time in He II. It is based on the observation of three critical velocities marking cross-overs between different types of flow due to the oscillating quartz tuning fork that resonates at 6.5 kHz, with prongs 3.50 mm long and a 90×75-μm cross-section (32). The first critical velocity of about 2 cm/s is hydrodynamic in origin, related to the formation of a vortical boundary layer, and therefore not directly relevant to turbulence in the bulk liquid.[#]

The second critical velocity can be linked reliably to significant production of quantized vorticity, which then propagates away from the surface of the tuning fork (or similar oscillators such as vibrating wires) and features a rapid increase in the drag force.[‖] The observed drag coefficients are typically 10^{-2} to 10^{-1}, much lower than in classical oscillatory flows, where drag coefficients of order unity are expected for cylinders or tuning forks at sufficiently high Reynolds number (or Keulegan–Carpenter number). This strongly suggests flow patterns significantly different from classical turbulence. No large flow structures resembling the classical wake exist in the superflow above the second critical velocity, which we therefore associate with the Vinen turbulence. It is only above the third critical velocity, about 1.5 m/s, that the drag coefficient starts to rise toward unity, the value typical for classical high Re flows. This is most likely related to a distinct change in the flow pattern, in which the superfluid develops larger polarized structures and starts to mimic the behavior of classical turbulent flows. We are therefore led to conclude that the third critical velocity marks the transition from Vinen- to Kolmogorov-type superfluid QT.

Pure Superfluid Turbulence in He II Driven at Small and Large Scales. Quantitative data on steady-state and decaying pure superfluid He II turbulence have been obtained by Golov and coworkers (34–36). They injected negative ions into the experimental

[‡]Although the energy spectrum beyond $\ell_{\rm Q}$ has not yet been measured, a hint of possible k^{-3} scaling at high k appears in the Andreev reflection data (figure 13 in ref. 26) on the vorticity deduced for grid turbulence in ^{3}He-B.

[§]At very low temperatures below about 0.2 $T_{\rm c}$ the mean-free paths of these excitations—quasiparticles and quasiholes, the constituents of the normal fluid of ^{3}He-B—exceed the size of the turbulent box; hydrodynamic description of the normal fluid is therefore meaningless. The interaction of vortex line defects in the superfluid component of ^{3}He-B with the normal fluid thus must be described in terms of scattering of individual quasiparticles.

[¶]The cross-over corresponds to a steady-state level generated by grid velocity about 5 mm/s, when the grid is forced by about 0.2 μN (30). Multiplying these values gives the absolute energy decay rate in the stationary case. Knowing the size of the grid, we estimate that the decay takes place in a volume of order 5×10^{-8} m^3. With the density of ^{3}He-B ≈ 100 kg/m^3 this gives $\varepsilon \approx 2 \times 10^{-4}$ m^2/s^3, resulting in $\ell_{\rm Q} = 2\pi(\varepsilon/\kappa^3)^{-1/4} \approx M$.

[#]Schmoranzer et al. (32) collected evidence from various complementary experiments employing small objects oscillating in He II in the zero-temperature limit and argued that the first critical velocity, connected mostly to frequency shifts rather than changes in the drag force, is associated with the formation of a number of quantized vortex loops near the surface of the oscillator, possibly forming a thin layer, which affects the coupling to the fluid and thus the hydrodynamic added mass.

[‖]Its magnitude is about 6 cm/s if measured at 6.5 kHz, using the fundamental vibrating mode of the fork, and about 12 cm/s if measured at 39.8 kHz, using the overtone, satisfying the scaling with the square root of oscillating frequency (33).

cell by a sharp field-emission tip and manipulated them by an electric field. This technique can be used for both the generation and detection of quantum turbulence. We focus first on the pure superfluid turbulence generated by impulsive spin-down, in which a rotating cubic-shaped container of He II, 4.5 cm in size, is brought rapidly to rest. For all starting angular velocities ($0.05 \leq \Omega \leq 1.5$ rad/s) (34), observed decays are of the form $L(t) \propto t^{-3/2}$, expected for late decay in classical 3D HIT decaying in the bounded domain—a strong signature of Kolmogorov-type QT.

Let us now consider temporal decay of pure superfluid turbulence with relatively low starting vortex line density, generated using an alternative technique of a jet of charged vortex rings of size about 1 μm, resulting from the injection of negative ions. At late times, two distinctly different power law decays were observed, depending on experimental conditions and the history of preparing the initial vortex tangle. Basically, instances of QT produced after short injection of ions display $L(t) \propto 1/t$ decay, while those generated after sufficiently long injection follow $L(t) \propto t^{-3/2}$ decay law at late times, in agreement again with Kolmogorov's pure superfluid turbulence generated by the rapid spin-down technique.

The phenomenological explanation within our model is as follows. For short charging times, the turbulent energy is supplied to the flow at the scale given by the typical size, 1 μm, of small vortex rings injected to the flow. The situation is basically the same as in Fig. 1, *Top*, with the size of the injected rings playing the role of the mesh size of the grid, *M*. The result is the Vinen turbulence with its typical signature, the $L(t) \propto 1/t$ form of the late decay. On the other hand, if the tangle of the same vortex line density is prepared by long charging times, the injected vortex rings have plenty of time to interact with each other (for more details, see ref. 14 and numerical simulations therein) as well as with the already existing vortex tangle. During the reconnection processes, both smaller and larger vortex loops are created, the former quickly propagating and decaying and the latter eventually creating large energy-containing superfluid eddies. This way, a superfluid energy spectrum is formed whose large scales have a form similar to classical turbulence. This results in the $L(t) \propto t^{-3/2}$ form of the late decay, a typical signature of the Kolmogorov turbulence in contained domains.

Situations intermediate to these two limiting cases are also possible, depending on the duration of charging, for which QT is neither of the Vinen nor of the Kolmogorov type. When charging is stopped, the vortex line density first roughly obeys the Vinen $L(t) \propto 1/t$ type of decay (corresponding to the decay of energy contained in small eddies of the size of order ℓ_Q), displays a cross-over, and enters the $L(t) \propto t^{-3/2}$ regime.

Quantum Turbulence in the Two-Fluid Regime

At finite temperatures, He II and ^{3}He-B behave as two-fluid systems consisting of the inviscid superfluid and viscous normal components having their separate velocity fields. We emphasize that the presence of the normal fluid renders the issue more complex.

The first step in the phenomenological description is to determine which fluid is turbulent. With no vortex lines, the superfluid component under isothermal conditions flows independently of the normal fluid possessing a kinematic viscosity $\nu_n = \mu/\rho_n$, where μ is the dynamical viscosity of the entire liquid. Potential superflow can be superimposed on the normal fluid flow. Although this ideal situation is uncommon, there is experimental evidence in flow of He II around oscillatory objects for classical instabilities in the normal fluid flow before the critical velocity for Glaberson–Donnelly instability is reached in the corresponding superflow (37). If vortex lines are present, they couple the two velocity fields by the action of the mutual friction force, acting at all length scales. This has the serious consequence of creating superfluid energy spectra of shapes drastically different from those at $T \to 0$.

Superfluid Turbulence in Stationary Normal Fluid of ^{3}He-B. This case represents the next logical step in the phenomenological description of QT because of its simplicity. The simplicity arises from the relatively high kinematic viscosity of the normal fluid of ^{3}He-B, which renders the normal fluid effectively stationary. ** Although we formally deal with two velocity fields, the velocity field of the normal fluid only determines the unique and physically significant frame of reference in which the normal fluid is at rest.

Experiments with ^{3}He-B have to be performed at sub-milliKelvin temperatures; to keep the flow so cold, the energy input needs to be very modest, typically of the order a few nanowatts. It is this factor and the high viscosity of the normal fluid that ensure that the normal fluid remains at rest with respect to the experimental container. The vortex lines will thus not move freely but are subject to a friction force as they move; this friction is temperature dependent and becomes larger as $T \to T_c$ (38). We should therefore expect that superfluid turbulence considered in the earlier section in the zero-temperature limit will be modified by the presence of damping: Vortex lines will appear smoother and short Kelvin waves and vortex cusps resulting from reconnections will be quickly damped out. With increasing temperature the damping becomes so strong that above $\approx 0.6 T_c$ quantum turbulence does not exist. Temperature thus plays a similar role here as the inverse Reynolds number in classical turbulence (39).

The energy spectrum of the turbulent superfluid possesses the following special features: 1) There is a maximum size of the turbulent eddy limited by mutual friction (40), and 2) dissipation due to mutual friction occurs at all length scales and 3) modifies the roll-off exponent to −3 at largest scales which, according to predictions of continuum approximation, displays a cross-over to the classical −5/3 (40, 41). Let us emphasize, however, that these results have been obtained theoretically within the continuum approximation, i.e., assuming that all relevant length scales of the problem are sufficiently larger than ℓ and the energy input occurs at large scales. These features are yet to be investigated in detail experimentally.

Quantum Turbulence in He II above ≈1 K. Here He II displays the two-fluid behavior. Isothermal incompressible flow of the normal fluid of He II can be described using the Navier–Stokes equations with density ρ_n and very low kinematic viscosity of order κ, characterized by the analogue of the Reynolds number in classical viscous fluids: the Donnelly number, Dn, which is based on the kinematic viscosity of the normal fluid alone, $\nu_n = \mu/\rho_n$, not on the kinematic viscosity $\nu = \mu/\rho$ of the entire fluid.[††]

**We assume here that the hydrodynamic description of the normal fluid of ^{3}He-B is justified; i.e., the mean-free path of its constituents, viz. quasiparticles and quasiholes, is short; in practice, this means that the temperature is above about 0.3 T_c.

[††]This dimensionless parameter, a "Reynolds number" defined for the normal component of He II only, was named by Schmoranzer et al. (37) as the Donnelly number, based on the latter's early investigations of boundary layer flows of He II.

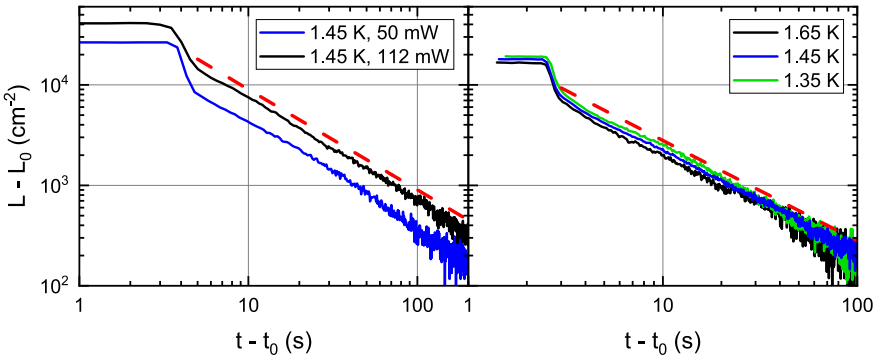

Fig. 2. Temporal decay of vortex line density (*Left*) in spherical counterflow generated by a steady-state central heater and (*Right*) generated mechanically by a vibrating fork. In both panels, t_0 is a virtual origin of time and L_0 denotes the remnant vorticity. Red dashed lines have the slope $1/t$ to guide the eye.

Schmoranzer et al. (37) used this nomenclature for oscillatory flows at high Stokes numbers, but we extend its definition for any quantum flow of superfluid helium and suggest that its meaning is the same for the normal fluid flow as that of the Reynolds number in classical flows. Flow of the superfluid component of He II is potential. In isothermal flow of He II, the normal and superfluid velocity fields are independent but become coupled by the mutual friction force when quantized vortices appear in the superfluid. Additionally, any temperature gradient in He II results in a thermal counterflow of the normal and superfluid components against each other which we shall consider in detail later.

From the fluid-dynamical point of view, the situation in He II differs from that in ^{3}He-B because the normal fluid is much less viscous. Additionally, the mutual friction force (characterized by the dissipative mutual friction parameter α) (42) at temperatures far enough away from T_λ is typically weaker by one to two orders of magnitude than in ^{3}He-B above $\approx 0.3T_c$, considered above. It therefore seems sensible to check whether the physical picture of two nearly independent velocity fields agrees with some experimental observations. We first focus on the isothermal and mechanically driven flows of He II.

It is often stated in the literature that the mechanically driven He II, with both components forced in the same way, results in the so-called coflow and represents Kolmogorov-type QT. This, however, is generally not the case. Experimental evidence on this point comes from a recent Prague experiment. QT is driven mechanically by a small quartz tuning fork with prongs of small (75×90) μm^2 cross-section. Fig. 2, *Right* shows that $L(t) \propto 1/t$, the late temporal decay of the Vinen type, in accordance with Fig. 1, *Top*, where the flow is driven at a scale smaller than or comparable to ℓ_Q.[‡‡] The normal fluid is therefore driven by the fork at scale smaller than η_n, for which the classical phenomenology is hardly applicable. The situation is somewhat as in ^{3}He-B, but without the unique quiescent normal fluid frame; the normal fluid flow is characterized by Dn = 17, which is slightly past the classical instability (37). Mutual friction is weak and does not significantly affect the decay.

It is fair to note that QT generated by an oscillating fork is far from HIT, so the experimental results should be interpreted with care. The nonhomogeneous tangle is expected to undergo a decay process accompanied by vortex diffusion. However, convincing experimental evidence was provided by Milliken et al. (43), who used the technique based on pulses of negative ions propagating through the steady state and decaying vortex tangles generated by ultrasound. The pulses were shaped by gate grids and manipulated by electric field, so that they could be stopped at a chosen position to provide spatial as well as temporal information on the decay. An overall inverse time decay of L was observed, which seemed to preserve its spatial profile, indicating that local decay dominates over diffusive phenomena. Under such an assumption, the nonlinear decay rate $\propto L^2$ would first lead to a rapid homogenization of the tangle, which would further decay as $L(t) \propto t^{-1}$.[§§]

Kolmogorov Quantum Turbulence in Coflowing He II. Consider now QT in coflowing He II at $T > 1$ K. Perhaps surprisingly, it has properties closely similar to those of 3D HIT in classical fluids. In contrast with ^{3}He-B, the normal fluid of He II becomes readily turbulent: There are not one but two turbulent velocity fields, coupled by the mutual friction force, acting at all relevant length scales. We are dealing here with the situation of double turbulence and have to examine both the superfluid and the normal fluid energy spectra.

Let us consider the example of turbulent He II flow driven by a grid at mesh scale $M \gg \ell_Q$. To simplify the problem, let us artificially switch off the mutual friction and assume that the temperature is just below 1.5 K, where $\nu_n \approx \kappa$ (42)—in other words, the Donnelly number is equal to the superfluid Reynolds number. It follows that ℓ_Q in the superfluid is equal to the Kolmogorov dissipation scale η_n in the normal fluid and that the turbulent spectra in the normal fluid and in the superfluid are naturally matched at scales considerably larger than ℓ_Q or η_n. The difference is that while in the normal fluid the Richardson cascade is terminated at this scale, it continues in the superfluid in the form of a Kelvin wave or quantum stress cascade, and the dissipation occurs beyond k^* introduced above. Upon decreasing (increasing) the temperature, due to the steep temperature dependence of $\nu_n(T)$, η_n becomes larger (smaller) than ℓ_Q. By turning on the mutual friction, not much happens at large scales (significantly exceeding η_n or ℓ_Q, whichever is larger), as large eddies of normal and superfluid components are

[‡‡]At $T = 1.35$ and 1.45 K the Kolmogorov dissipation scale in the normal component, η_n, is even larger and, at 1.65 K, about equal to ℓ_Q.

[§§]While this scenario is contrary to the claim that the spatial profile is maintained during decay, it is surprisingly consistent with the raw data in figure 2 of ref. 43, where in the center of the cell, the initially high L drops by a factor of ≈ 4.5 within the first 4 s, while in the border regions a significantly smaller drop by a factor of ≈ 2 is observed. This validates the scenario of predominantly local decay of nonhomogeneous QT, which results in $L(t) \propto t^{-1}$ at late times.

closely matched. Upon approaching smaller and smaller scales, however, the matching cannot be complete, dissipation due to mutual friction starts to operate (the roll-off exponent becomes gradually steeper), and one component starts to act as a source or drain for the other. This results in an increase of intermittency corrections, as predicted by Boue et al. (44) and experimentally confirmed by Varga et al. (45).

Both the superfluid and normal energy spectra in steady-state and decaying Kolmogorov turbulence of He II contain an inertial range of scales. This has been observed in a number of coflow experiments, first by Maurer and Tabeling (46) in the von Kármán flow and by Roche and coworkers (47) in superfluid wind tunnels (48). In these experiments, velocity fluctuations were determined using a Pitot tube, and the characteristic $f^{-5/3}$ frequency dependence of the spectrum was observed; this scaling corresponds to $E(k) \sim k^{-5/3}$, if one uses Taylor's frozen flow hypothesis, and confirms the presence of a Richardson energy cascade as in classical turbulence. Geometrically it means that the turbulence contains, within a tangle of random vortex lines, partially polarized vortex lines, or bundles, with relatively large coarse-grained superfluid vorticity. We also note that the inertial range in the turbulent normal fluid was observed by Guo and coworkers (45) by visualizing grid-generated turbulence using neutral He2* molecules, allowing one to measure transverse velocity structure functions selectively in the normal fluid. This is possible due to the small size of He2* triplet molecules that are effectively part of the normal fluid and do not trap vortex lines above $\approx$1 K (49).

Grid-generated QT in He II, driven at the large-scale M, when both components are turbulent on scales appreciably larger than ℓ_Q, represents a typical example of Kolmogorov QT. Large normal and superfluid scales are closely coupled by mutual friction, which does not cause any appreciable energy loss and, in accordance with Richardson's picture, there is an inertial range characterized by the −5/3 exponent (neglecting intermittency). Matching is not possible once the quantum or Kolmogorov length scale is reached. Mutual friction partly dissipates and partly transfers the turbulent energy from superfluid eddies to normal ones and vice versa, with either fluid serving as the drain or source of energy for the other. Viscous dissipation, together with the coupling by dissipative mutual friction, terminates both normal and superfluid cascades. The Kelvin wave or quantum stress cascades, so important in the zero-temperature limit, do not play a significant role here. Turbulent coflowing He II above about 1 K can thus be treated, at least approximately, as a single-component quasiclassical fluid, characterized by the temperature-dependent effective kinematic viscosity $\nu_{\rm eff}$. Its value can be extracted from the temporal decay, when $L(t)$ displays the universal form of the decay [as observed in many experiments (10, 24, 25, 50–52) and reviewed in ref. 25]:

$$L(t+t_0) = L(\tau) = \frac{3\sqrt{3}D}{2\pi\kappa}\sqrt{\frac{C^3}{\nu_{\rm eff}}}\tau^{-3/2}. \qquad [3]$$

Here t_0 is the virtual origin time marking the instant when L would be infinite if this law of decay were to be valid, and D is the size of the turbulent box (playing the role of saturated energy-containing length scale). This decay is the typical quasiclassical signature (20) of the Kolmogorov QT, allowing us to extract $\nu_{\rm eff}(T)$; see also the more rigorous recent treatment based on independent measurements of decaying turbulence in the superfluid and normal components of He II (52, 53).

Thermal Counterflow of He II. The flow of He II can take various forms because of the existence of two fluid components. One can push the normal fluid and the superfluid components to flow with different average velocities, a situation generally called counterflow. A special case of counterflow is the thermal counterflow, easily achieved in a channel closed at one end and open to the He II bath at the other. Heat flux q supplied at the closed end is carried away by the normal fluid, with the superfluid flowing in the opposite direction so that the net mass flux is zero. The counterflow velocity $u_{\rm ns} = q/(\rho_s \sigma T)$ is established, where σ is the entropy of He II. QT appears in the channel when q exceeds a critical value.

It has been known since early experiments, notably those performed by Tough's group (56), that counterflow turbulence can exist in two forms, referred to as T I and T II. Recently Guo and coworkers (49, 57), using helium excimer molecules as tracers of the normal fluid, revealed that the normal fluid in the T II state is turbulent. In the T I state, where the flow of the normal component is laminar beyond reasonable doubt, the turbulent energy is injected around ℓ_Q by the reconnection-based mechanism first identified by Schwarz (54, 55). The superfluid energy spectrum therefore has the shape as sketched in Fig. 3, *Top*. The shape is the same as in Fig. 1, *Top*. For small enough ε we deal with Vinen turbulence, the decay of which was experimentally confirmed (58) to obey $L(t) \propto t^{-1}$ at late times.

The two forms of QT in He II—Vinen and Kolmogorov—display two distinctly different forms of decay which subsequently allow the definition of two effective kinematic viscosities of turbulent He II. In addition to $\nu_{\rm eff}(T)$ introduced above for Kolmogorov QT, we now follow refs. 36 and 52 and note that the energy per unit mass associated with a random tangle of vortex lines in Vinen QT (i.e., superflow circulating with velocity $\kappa/(2\pi r)$ around vortex lines) is given by $(\rho_s\kappa^2)/(4\pi\rho)\, L \ln(\ell/\xi_4)$, where $\ell = 1/\sqrt{L}$ denotes the mean intervortex distance in the tangle. By differentiating with respect of time and using Eq. **2**, we see that the turbulent energy would then decay as $\varepsilon = \nu' \kappa^2 L^2$, where the quantity

$$\nu' = \frac{\vartheta_2 \rho_s}{8\pi^2\rho}\kappa \ln(\ell/\xi_4) \qquad [4]$$

is the effective kinematic viscosity for the Vinen-type QT.

We thus have two definitions for two effective kinematic viscosities ν' and $\nu_{\rm eff}$, which can be extracted from decaying turbulent He II flow of the Vinen and Kolmogorov forms. Their existence is not a consequence of the two-fluid behavior, since they readily exist in the $T \to 0$ limit as well. And they need not be the same, either. Indeed, while $\nu_{\rm eff}$ is a property of turbulent flow of the entire He II, i.e., of both fluids whose turbulent motions are coupled at large enough scales, ν' is the property of a single fluid flow, namely of the turbulent superfluid component, coupled by the mutual friction force to the normal fluid. This difference—coupling to the normal fluid as well as the factor ρ_s/ρ—should disappear with dropping temperature, as ρ_s approaches ρ and the mutual friction gradually ceases to operate. For reasons such as ill-defined boundary conditions in He II below 1 K, the values of ν' and $\nu_{\rm eff}$ are so far not determined with sufficient accuracy to unequivocally confirm that ν' equals $\nu_{\rm eff}$ at low temperature; however, they both have been found to be of order 0.1κ (51).[¶¶]

[¶¶]Discussion of boundary conditions for turbulent flows of helium superfluids is outside the scope of this paper. In short, there is experimental evidence that both in He II (51) and in ^{3}He B (59) the turbulent flow with dropping temperature decouples from the container reference frame.

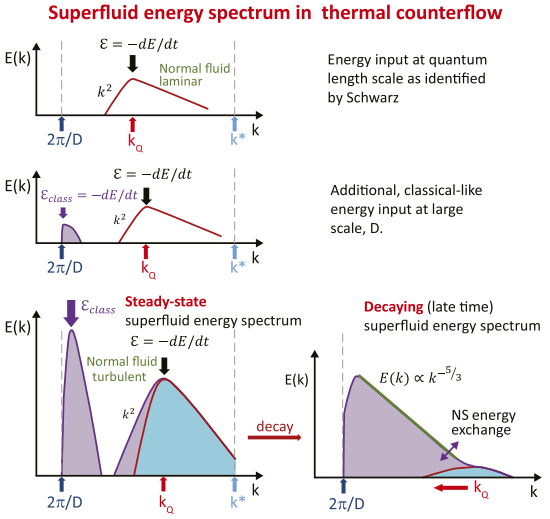

Fig. 3. Schematic view in log-log coordinates of the general shapes of 3D superfluid energy spectra of thermal counterflow turbulence in He II. (*Top*) Vinen turbulence, where the energy input identified by Schwarz (54, 55) occurs at $\ell_Q = 2\pi/k_Q$ (red arrow). The temporal decay is of the form $L(t) \propto 1/t$. (*Middle*) Upon increasing the heat flux, there is additional quasiclassical energy input in the normal component at large scale which, because of mutual friction, occurs in the superfluid component as well. (*Bottom Left*) With increasing heat input, there is energy input at large scale akin to classical turbulence, but the inertial range of the Kolmogorov-type QT, characterized by the −5/3 roll-off exponent, cannot develop, as mutual friction acts on all scales making the roll-off in this range much steeper. There is still a quantum peak because of the energy input at quantum length-scale ℓ_Q, which itself shifts to the right with increasing heat input. (*Bottom Right*) Once the heat flux ceases, the quantum energy peak quickly decays and the energy content at large scales gradually cascades down the scales, forming an inertial range that acquires classical Kolmogorov form. It results in a classical decay of the form $L(t) \propto 1/t^{3/2}$, with growing quantum length-scale ℓ_Q.

At this point, we need to discuss the relation between the quantum length scale, defined as before quasiclassically as $\ell_Q = (\kappa^3/\varepsilon)^{1/4}$, and the mean intervortex distance $\ell = 1/\sqrt{L}$, as this quantity is also often referred to in the literature as quantum length scale. It is easy to show that for Kolmogorov turbulence in He II they are roughly equal. Indeed, assuming the validity of the above quasiclassical relationship $\varepsilon = \nu_{\text{eff}}(\kappa L)^2$ (20), we obtain their ratio to be

$$\frac{\ell_Q}{\ell} = \left(\frac{\kappa}{\nu_{\text{eff}}}\right)^{1/4}. \qquad [5]$$

Available experimental data on $\nu_{\text{eff}}(T)$ (51, 53, 60, 61) suggest that in He II over most of the temperature range ℓ_Q and ℓ differ by less than a factor of 2.

Let us now return to counterflow turbulence. Upon increasing the heat load, there develops an instability of laminar flow that carries the heat away from the heater, and the transition to turbulence occurs in the normal fluid (as in any channel or pipe flow of classical viscous fluid) to which the energy is injected quasiclassically, at the outer scale of order the size of the counterflow channel, D. An inertial range of scales with the classical roll-off exponent of −5/3 cannot be established in the normal fluid. The reason is that mutual friction creates superfluid eddies and couples them with normal eddies and also dissipates the turbulent energy at all scales. This mutual friction mechanism serves as an additional source of energy injection to the superfluid component, at large scales, resulting in the gradual growth of a classical-like peak, as sketched in Fig. 3, *Middle*; the situation for increasing heat input is shown in Fig. 3, *Bottom*. The sketch takes into account that eddies larger than D cannot exist and that steady-state measurements of the structure functions (49, 57) suggest a steeper roll-off exponent of its right-hand side. Of course, the steady energy input into the superfluid component identified by Schwarz (54, 55) operates and results in a quantum peak in the superfluid energy spectrum around ℓ_Q. Its low wavenumber end is again of the k^2 form because of the equipartition theorem (62).

This steady-state, two-peak shape of the superfluid energy spectrum drastically changes during the temporal decay that occurs when heating is switched off. For a short transition time, counterflow is still driven by the excess entropy contained in the channel; for details, see refs. 63 and 64. The quantum peak quickly decays, displaying a decay of the $L \propto 1/t$ type. Simultaneously, over times of the order of the turnover time of large eddies, the energy contained at large scales of both fluids proceeds through the inertial range of scales. From now on, the inertial range is characterized by the classical −5/3 roll-off exponent, as superfluid and normal eddies are coupled at these scales; thus, hardly any significant dissipation occurs, with the situation being similar to that in the coflow (Kolmogorov) QT. As the energy reaches smaller and smaller scales, a larger number of vortex lines are needed for carrying nearly the same energy content. This is displayed as a "bump" in recorded decay curves of $L(t)$. The quasiclassical decay occurs beyond this point, displaying $L(t) \propto t^{-3/2}$ (58, 62).

The dynamics of vortex tangles in thermal counterflow are not fully understood by any means. Their complexity can be illustrated by an experimental study of thermal counterflow in a channel when the turbulence was not allowed to settle to a statistical steady state (64). This was achieved by modulating by a square-wave $\dot{q}$ and a similarly varying counterflow velocity u_{ns}. The turbulent transients thus obtained allowed one to study, by using the phase portrait, the time evolution of both the growth and decay of L. In particular, while the growth of L always followed the same form, independent of the length of the heat pulse, the temporal decay of vortex line density was strongly affected by the history of the turbulent sample (figure 7 in ref. 64). The bump in decaying $L(t)$ was displayed only in decays of dense original tangles, prepared using long heat pulses sufficient for generating large eddies and, with the aid of mutual friction, the classical-like part of the superfluid energy spectrum. The situation is similar to that discussed earlier, when the tangle was generated in the $T \to 0$ limit by the injection pulses of ions (immediately creating small vortex rings) of variable duration (36). In both these cases the decay of $L(t)$ depends on the shape of the superfluid energy spectrum (also on the shape of the energy spectrum in the normal fluid in the case of thermal counterflow, due to coupling by the mutual friction force); these shapes depend on how intensely and on which length scales QT is driven.

Let us add that this phenomenological scenario of thermal counterflow and its decay, complex though it is, derives indirect support from complementary experiments. First, the Prague group investigated in detail the steady-state (65) and temporal decay (66) of pure superflow in square channels, with ends covered by sintered silver superleaks, allowing a net throughflow of the superfluid component only (the normal fluid throughflow was suppressed by submicrometer pores of the sintered silver plugs). While the measurements of L in the steady states of counterflow and

pure superflow display the same value for the same mean counterflow velocity, the temporal decays are distinctly different. The experimentally recorded bump on $L(t)$ decay curves originating from pure superflow is suppressed, either fully or at least significantly. The reason is easily understood: In pure superflow the classical energy input at large scale of order D is inefficient, as there is no net flow of the normal component through the channel.

In the second example, the Prague group utilized an experimental cell of the outside form of a regular dodecahedron containing a spherical sample of He II. The heat, supplied by a small spherical heater in the center, generates a nearly spherical counterflow. Upon exceeding some critical heating level, an inhomogeneous vortex tangle is formed and surrounds the spherical heater. A full account of this experiment will be published elsewhere, but preliminary second sound data display temporal decay of the form $L(t) \propto 1/t$, where $L(t)$ now stands for the spatially averaged vortex line density, detected by a chosen spherical resonant harmonic of second sound, as shown in Fig. 2, *Left*. Assuming local decay, this is a typical signature of Vinen type of quantum turbulence. It is important to emphasize that this decay form follows the steady-state vortex line density values which, in conventional 1D thermal counterflow, would have displayed a complex decay containing a bump and subsequent quasiclassical late decay $\propto t^{-3/2}$. The reason for this distinctive difference is the lack of classical large-scale energy input that in the "conventional" 1D counterflow occurs due to the friction between the normal fluid and solid channel wall. Such an energy input does not exist in spherical counterflow with radial normal fluid flow.

Conclusions

We have presented a unified phenomenological description of various forms of QT in helium superfluids. We believe that all forms of QT observed to date, and their relation to classical turbulence in viscous fluids, are broadly understood at this phenomenological level. In particular, we presented a unified description on the existence of the Vinen and Kolmogorov forms of QT. Their existence is not a consequence of the two-fluid behavior of quantum fluids; they readily exist as two different forms of pure superfluid turbulence in the zero-temperature limit. These two forms emerge as a direct consequence of quantum mechanical constraint on circulation in a superfluid, which results in the existence of a finite quantum length scale. We have discussed a crossover from one form of QT to the other. The very existence of the quantum length scale makes even pure superfluid turbulence more complex than classical turbulence in viscous fluids.

At finite temperature, the presence of the normal fluid, whether turbulent or not, adds more complexity to existing forms of quantum turbulence and their temporal decays. Although the phenomenology presented here is semiquantitative at best, this unified picture captures many experimental facts, known features, and regimes of quantum turbulence accumulated over many years of research of helium superfluids, both in the limit of zero temperature and in the temperature range where they display two-fluid behavior. We therefore believe that our perspective represents a firm basis for fluid-dynamical studies of even more complex turbulent superfluid systems, such as mixtures of Bose–Einstein condensates, heavy atomic nuclei, and neutron stars.

Data Availability. All study data are included in this article.

Acknowledgments

We thank our many colleagues, too numerous to name here, for fruitful collaboration and stimulating discussions over the years. This research is funded by the Czech Science Foundation under Project GAČR 20-00918S. D.S. and S.M. acknowledge support for the experimental work with tuning-fork microresonators under Project GAČR 20-13001Y.

1 U. Frisch, *Turbulence: The Legacy of A. N. Kolmogorov* (Cambridge University Press, 1995).
2 L. Skrbek, K. R. Sreenivasan, Developed quantum turbulence and its decay. *Phys. Fluids* **24**, 011301 (2012).
3 C. F. Barenghi, L. Skrbek, K. R. Sreenivasan, Introduction to quantum turbulence. *Proc. Natl. Acad. Sci. U.S.A.* **111**, 4647 (2014).
4 D. R.Tilley, J. Tilley, *Superfluidity and Superconductivity* (Institute of Physics Publishing, 1986).
5 L. Onsager, In discussion on paper by C. J. Gorter. *Nuovo Cimento* **6** (suppl. 2), 249 (1949).
6 R. P. Feynman, "Application of quantum mechanics to liquid helium" in *Progress in Low Temperature Physics*, C. J. Gorter, Ed. (North Holland, Amsterdam, The Netherlands, 1955), vol. 1, pp. 493–515.
7 G. Birkhoff, Fourier synthesis of homogeneous turbulence. *Commun. Pure Appl. Math.* **7**, 19 (1954).
8 P. G. Saffman, The large-scale structure of homogeneous turbulence. *J. Fluid Mech.* **27**, 581 (1967).
9 K. R. Sreenivasan, On the universality of the Kolmogorov constant. *Phys. Fluids* **7**, 27788 (1995).
10 S. R. Stalp, L. Skrbek, R. J. Donnelly, Decay of grid turbulence in a finite channel. *Phys. Rev. Lett.* **82**, 4831 (1999).
11 V. S. L'vov, L. Skrbek, K. R. Sreenivasan, Viscosity of liquid 4He and quantum of circulation: Are they related?. *Phys. Fluids* **26**, 041703 (2014).
12 B. Svistunov, Superfluid turbulence in the low-temperature limit. *Phys. Rev. B* **52**, 3647 (1995).
13 D. A. Donzis, K. R. Sreenivasan, The bottleneck effect and the Kolmogorov constant in isotropic turbulence. *J. Fluid Mech.* **657**, 171–188 (2010).
14 P. C. diLeoni, P. Mininni, M. E. Brachet, Dual cascade and dissipation mechanisms in helical quantum turbulence. *Phys. Rev. A* **95**, 053636 (2017).
15 W. F. Vinen, Decay of superfluid turbulence at a very low temperature: The radiation of sound from a Kelvin wave on a quantized vortex. *Phys. Rev. B* **64**, 134520 (2001).
16 M. A. Silaev, Universal mechanism of dissipation in Fermi superfluids at ultralow temperatures. *Phys. Rev. Lett.* **108**, 045303 (2012).
17 V. S. L'vov, S. Nazarenko, Spectrum of Kelvin-wave turbulence in superfluids. *JETP Lett.* **91**, 464 (2010).
18 L. Boue *et al.*, Exact solution for the energy spectrum of Kelvin wave turbulence in superfluids. *Phys. Rev. B* **84**, 064516 (2011).
19 T. Tanogami, Theoretical analysis of quantum turbulence using the Onsager "ideal turbulence" theory. arXiv:2009.11057v1 (23 September 2020).
20 W. F. Vinen, Classical character of turbulence in a quantum liquid. *Phys. Rev. B* **61**, 1410 (2000).
21 D. D. Awschalom, K. W. Schwarz, Observation of a remanent vortex-line density in superfluid helium. *Phys. Rev. Lett.* **52**, 49–52 (1984).
22 W. I. Glaberson, W. W. Johnson, R. M. Ostermeier, Instability of a vortex array in He II. *Phys. Rev. Lett.* **33**, 1197 (1974).
23 W. Vinen, Mutual friction in a heat current in liquid helium II. III. Theory of the mutual friction. *Proc. R. Soc. Lond. A* **242**, 493–515 (1957).
24 L. Skrbek, S. Stalp, On the decay of homogeneous isotropic turbulence. *Phys. Fluids* **12**, 1997 (2000).
25 L. Skrbek, K. R. Sreenivasan, "How similar is quantum turbulence to classical turbulence"? in *Ten Chapters of Turbulence*, P. A. Davidson, Y. Kaneda, H. K. Moffatt, K. R. Sreenivasan, Eds. (Cambridge University Press, 2013), chap. 10.
26 V. Tsepelin *et al.*, Visualization of quantum turbulence in superfluid 3He-B: Combined numerical and experimental study of Andreev reflection. *Phys. Rev. B* **96**, 054510 (2017).
27 S. N. Fisher, G. R. Pickett, "Quantum turbulence in superfluid 3He at very low temperatures" in *Progress in Low Temperature Physics XVI*, M. Tsubota, W. P. Halperin, Eds. (Elsevier, 2009), vol. XVI, pp. 147–194.

28 D. I. Bradley *et al.*, Emission of discrete vortex rings by a vibrating grid in superfluid 3He-B: A precursor to quantum turbulence. *Phys. Rev. Lett.* **95**, 035302 (2005).
29 D. I. Bradley *et al.*, Decay of pure quantum turbulence in superfluid ^{3}He-B. *Phys. Rev. Lett.* **96**, 035301 (2006).
30 D. I. Bradley *et al.*, Vortex generation in superfluid He-3 by a vibrating grid. *J. Low Temp. Phys.* **134**, 381 (2004).
31 D. I. Bradley *et al.*, Direct measurement of the energy dissipated by quantum turbulence. *Nat. Phys.* **7**, 473 (2011).
32 D. Schmoranzer *et al.*, Multiple critical velocities in oscillatory flow of superfluid 4He due to quartz tuning forks. *Phys. Rev. B* **94**, 214503 (2016).
33 R. Hanninen, W. Schoepe, Universal onset of quantum turbulence in oscillating flows and crossover to steady flows. *J. Low Temp. Phys.* **158**, 410 (2010).
34 P. M. Walmsley, A. I. Golov, H. E. Hall, A. A. Levchenko, W. F. Vinen, Dissipation of quantum turbulence in the zero temperature limit. *Phys. Rev. Lett.* **99**, 265302 (2007).
35 P. M. Walmsley, A. I. Golov, Quantum and quasiclassical types of superfluid turbulence. *Phys. Rev. Lett.* **100**, 245301 (2008).
36 P. M. Walmsley, A. I. Golov, Coexistence of quantum and classical flows in quantum turbulence in the T=0 limit. *Phys. Rev. Lett.* **118**, 134501 (2017).
37 D. Schmoranzer *et al.*, Dynamical similarity and instabilities in high Stokes number oscillatory flows of superfluid helium. *Phys. Rev. B* **99**, 054511 (2019).
38 T. D. C. Bevan *et al.*, Vortex mutual friction in superfluid He-3. *J. Low Temp. Phys.* **109**, 423 (1997).
39 A. P. Finne *et al.*, Observation of an intrinsic velocity-independent criterion for superfluid turbulence. *Nature* **424**, 1022 (2003).
40 W. F. Vinen, Theory of quantum grid turbulence in superfluid ^{3}He-B. *Phys. Rev. B* **71**, 024513 (2005).
41 V. S. L'vov, S. V. Nazarenko, G. E. Volovik, Energy spectra of developed superfluid turbulence. *JETP Lett.* **80**, 479 (2004).
42 R. J. Donnelly, C. F. Barenghi, The observed properties of liquid helium at saturated vapor pressure. *J. Phys. Chem. Ref. Data* **27**, 1217 (1998).
43 F. Milliken, K. Schwarz, C. Smith, Free decay of superfluid turbulence. *Phys. Rev. Lett.* **48**, 1204 (1982).
44 L. Boue *et al.*, Enhancement of intermittency in superfluid turbulence. *Phys. Rev. Lett.* **110**, 064516 (2013).
45 E. Varga, W. Guo, J. Gao, L. Skrbek, Intermittency enhancement in quantum turbulence in superfluid 4He. *Phys. Rev. Fluids* **3**, 094601 (2018).
46 J. Maurer, P. Tabeling, Local investigation of superfluid turbulence. *Europhys. Lett.* **43**, 29 (1998).
47 J. Salort *et al.*, Turbulent velocity spectra in superfluid flows. *Phys. Fluids* **22**, 125102 (2010).
48 J. Salort, B. Chabaud, E. Leveque, P. E. Roche, Energy cascade and the four-fifths law in superfluid turbulence. *Europhys. Lett.* **97**, 34006 (2012).
49 A. Marakov *et al.*, Visualization of the normal-fluid turbulence in counterflowing superfluid He-4. *Phys. Rev. B* **91**, 094503 (2015).
50 S. Babuin, E. Varga, L. Skrbek, The decay of forced turbulent coflow of He II past a grid. *J. Low Temp. Phys.* **175**, 324–330 (2014).
51 D. E. Zmeev *et al.*, Dissipation of quasiclassical turbulence in superfluid 4He. *Phys. Rev. Lett.* **115**, 155303 (2015).
52 J. Gao, W. Guo, W. F. Vinen, Dissipation in quantum turbulence in superfluid He-4 above 1 K. *Phys. Rev. B* **97**, 184518 (2018).
53 J. Gao, W. Guo, W. Vinen, Determination of the effective kinematic viscosity for the decay of quasiclassical turbulence in superfluid He-4. *Phys. Rev. B* **94**, 094502 (2016).
54 K. W. Schwarz, Theory of turbulence in superfluid 4He. *Phys. Rev. Lett.* **38**, 551 (1977).
55 K. W. Schwarz, Three-dimensional vortex dynamics in superfluid 4He. Homogeneous superfluid turbulence. *Phys. Rev. B* **38**, 2398 (1988).
56 J. T. Tough, "Superfluid turbulence" in *Progress in Low Temperature Physics*, D. F. Brewer, Ed. (North-Holland, 1982), vol. VIII, chap. 3.
57 J. Gao, E. Varga, W. Guo, W. F. Vinen, Energy spectrum of thermal counterflow turbulence in superfluid helium-4. *Phys. Rev. B* **96**, 094511 (2017).
58 J. Gao *et al.*, Decay of counterflow turbulence in superfluid 4He. *JETP Lett.* **103**, 648 (2016).
59 J. Hosio *et al.*, Superfluid vortex front: Decoupling from the reference frame. *Phys. Rev. Lett.* **107**, 135302 (2011).
60 S. R. Stalp, J. J. Niemela, W. F. Vinen, R. J. Donnelly, Dissipation of grid turbulence in helium II. *Phys. Fluid.* **14**, 1377 (2002).
61 T. V. Chagovets, A. V. Gordeev, L. Skrbek, Effective kinematic viscosity of turbulent He II. *Phys. Rev. E* **76**, 027301 (2007).
62 S. Babuin, V. S. L'vov, A. Pomyalov, L. Skrbek, E. Varga, Coexistence and interplay of quantum and classical turbulence in superfluid 4He: Decay, velocity decoupling, and counterflow energy spectra. *Phys. Rev. B* **94**, 174504 (2016).
63 A. Gordeev, T. Chagovets, F. Soukup, L. Skrbek, Decay of counterflow turbulence in He II. *J. Low Temp. Phys.* **138**, 549 (2005).
64 E. Varga, L. Skrbek, Dynamics of the density of quantized vortex lines in counterflow turbulence: Experimental investigation. *Phys. Rev. B* **97**, 064507 (2018).
65 M. S. Babuin, M.Stammeier, E. Varga, M. Rotter, L. Skrbek, Quantum turbulence of bellows-driven 4He superflow: Steady state. *Phys. Rev. B* **86**, 134515 (2012).
66 S. Babuin, E. Varga, W. F. Vinen, L. Skrbek, Quantum turbulence of bellows-driven 4He superflow: Decay. *Phys. Rev. B* **92**, 184503 (2015).

A.2 D. Schmoranzer, M. J. Jackson, Š. Midlik, M. Skyba, J. Bahyl, T. Skokánková, V. Tsepelin, L. Skrbek, Dynamical similarity and instabilities in high-Stokes-number oscillatory flows of superfluid helium, PRB 99 (2019)

Dynamical similarity and instabilities in high-Stokes-number oscillatory flows of superfluid helium

D. Schmoranzer,[1] M. J. Jackson,[1] Š. Midlik,[1] M. Skyba,[2,*] J. Bahyl,[3] T. Skokánková,[1] V. Tsepelin,[4] and L. Skrbek[1]

[1]*Faculty of Mathematics and Physics, Charles University, Ke Karlovu 3, 121 16, Prague 2, Czech Republic*

[2]*Institute of Physics ASCR, v.v.i., Na Slovance 2, 182 21, Prague 8, Czech Republic*

[3]*Faculty of Mathematics, Physics and Informatics, Comenius University, Mlynská dolina, 842 48, Bratislava, Slovakia*

[4]*Physics Department, Lancaster University, Lancaster, LA1 4YB, United Kingdom*

(Received 7 November 2018; published 19 February 2019)

We present a unified analysis of the drag forces acting on oscillating bodies submerged in superfluid helium such as a vibrating wire resonator, tuning forks, a double-paddle oscillator, and a torsionally oscillating disk. We find that for high-Stokes-number oscillatory flows, the drag force originating from the normal component of superfluid helium exhibits a clearly defined universal scaling. Following classical fluid dynamics, we derive the universal scaling law and define relevant dimensionless parameters such as the Donnelly number. We verify this scaling experimentally using all of our oscillators in superfluid ^{4}He and validate the results by direct comparison with classical fluids. We use this approach to illustrate the transition from laminar to turbulent drag regime in superfluid oscillatory flows and compare the critical velocities associated to the production of quantized vortices in the superfluid component with the critical velocities for the classical instabilities occurring in the normal component. We show that depending on the temperature and geometry of the flow, either type of instability may occur first and we demonstrate their crossover due to the temperature dependence of the viscosity of the normal fluid. Our results have direct bearing on present investigations of superfluids using nanomechanical devices [Bradley *et al.*, Sci. Rep. **7**, 4876 (2017)].

DOI: 10.1103/PhysRevB.99.054511

I. PREFACE

Historically, experiments on oscillatory flows of classical viscous fluids have been studied since the days of Stokes [1], with many notable developments made in the last century [2–5]. Recently, oscillating flows have reemerged thanks to developments in micromechanical and nanomechanical engineering, where access to nano electromechanical systems (NEMS) [6–10] has offered unprecedented sensitivity and resolution in fluid dynamical experiments, allowing the transition from continuum to ballistic (molecular) regime to be probed at easily attainable pressures, directly probe fluid boundary layers [9], or formulate universality relations [6–8] for classical oscillatory flows. This work extends such universality relations to superfluids, concentrating on the hydrodynamic regime; the transitional and ballistic regimes will represent the subject of a later publication.

An extremely broad range of working fluids of well-known physical properties [11–13] may be obtained when traversing the different phases of helium, even limiting ourselves to the common isotope ^{4}He. The normal liquid phase of ^{4}He, known as He I, is a highly interesting working fluid thanks to its extremely low kinematic viscosity ν, which provides very high Reynolds number (Re $\approx 10^7$) flows in controlled laboratory experiments [14,15]. Similarly, cryogenic He gas provides extremely large Rayleigh numbers (Ra $\approx 10^{17}$) in convective flows [16]. Liquid ^{4}He undergoes a superfluid phase transition at $T_\lambda \approx 2.17$ K at saturated vapor pressure. Superfluid ^{4}He, or He II, is a quantum fluid, and its flow properties cannot be described by means of classical fluid dynamics. According to Landau's two-fluid model [17,18], it behaves as if composed of two interpenetrating liquids (the normal and superfluid components) with individual velocity fields and temperature-dependent densities. At the superfluid transition at T_λ, the density of the normal component accounts for 100% of the total density, but drops rapidly with decreasing temperature and vanishes for $T \to 0$ K.

Oscillatory flows of He II have been studied using various oscillators such as disks [19,20], piles of disks [21], spheres [22–24], grids [25–29], tuning forks [30–33], reeds [34], double paddles [35–37], cylinders of rectangular [38] or circular cross-section (wires) [39–42] since the discovery of superfluidity, and have led to important insights to this fundamental physical phenomenon. For reviews, see [43,44]. Despite these efforts, a universal picture is still missing in superfluid hydrodynamics, which motivated us to investigate oscillatory flows of He II due to mechanical oscillators of largely varied geometries (vibrating tuning forks, a microwire loop, a torsionally oscillating disk, and a double-paddle oscillator) and search for universal features.

II. INTRODUCTION

In this section, we introduce the key concepts of superfluid hydrodynamics, and use classical oscillatory flows in

*Present address: Oxford Instruments, Abingdon, Oxfordshire, OX13 5QX, United Kingdom.

the high-Stokes-number regime as a stepping stone to derive the properties of similar flows in superfluids. We limit our discussion of the dynamics of superfluids to the Newtonian-type hydrodynamic description applicable above $\simeq 1$ K, as this corresponds to most of the experiments described here.

A. Superfluid hydrodynamics

On a phenomenological level, superfluid ^{4}He at finite temperatures is described as consisting of two components: a viscous normal component and an inviscid superfluid component [17]. Their temperature-dependent densities ρ_n and ρ_s, respectively, add up to the (nearly temperature-independent) total density of He II, ρ. While the normal component behaves classically, possessing finite viscosity and carrying the entire entropy content of He II, the superfluid component has neither entropy nor viscosity and, due to quantum restrictions, the vorticity is constrained into line singularities called quantized vortices [18]. In He II, each quantized vortex carries one quantum of circulation, given as $\kappa = h/m_4 \approx 0.997 \times 10^{-7}$ m^2 s^{-1}, where h is the Planck constant and m_4 denotes the mass of a ^{4}He atom. Superfluid turbulence [45] therefore takes the form of a dynamic tangle of quantized vortices in the superfluid component.

At temperatures above $\simeq 1$ K, where the fraction of the normal fluid is significant, this tangle of quantized vortices typically coexists with classical-like turbulent flow of the normal component, making up what is usually called quantum turbulence (turbulent flow of a quantum fluid). In the presence of quantized vortices, the otherwise independent normal and superfluid velocity fields become coupled by a mutual friction force which arises due to thermal excitations (responsible for the entropy and viscosity of the normal component) scattering off the cores of quantized vortices. Quantum turbulence can thus be loosely defined as the most general way of motion of quantum fluids displaying superfluidity [45].

Does quantum turbulence always contain quantized vortices? Strictly speaking, quantized vortices are not a necessary ingredient of quantum turbulence, as one can imagine a two-fluid flow of He II consisting of turbulent normal flow and potential superflow. Indeed, in the hypothetical case of a macroscopic sample of He II free of quantized vortices (i.e., without mutual friction coupling the two velocity fields), in an isothermal flow the normal and superfluid components move independently and any instability criteria ought to be applied to them separately. In this hypothetical case, quantized vortices must be nucleated intrinsically; this process requires critical velocities of order 10 m/s or higher [45]. In practice, however, remnant vortices always exist in macroscopic samples of He II and nucleation of quantized vorticity takes place extrinsically, by stretching and reconnections of seed vortex loops. In many types of flow, the critical velocity for extrinsic vortex nucleation is observed to be a few cm/s. As turbulence of the normal component may be possible even below this velocity threshold, it follows that there indeed is a possibility of having a quantum flow displaying (nearly) potential superflow together with a vortical flow of the normal component.

With very few remnant quantized vortices present, the mutual friction force is negligible and, according to the two-fluid model of Landau [17], an isothermal flow of the normal component is described by the Navier-Stokes equations, while that of the superfluid component by the Euler equations for ideal fluids. Under these conditions, any body moving through He II at low velocity below the (generally independent) critical thresholds would experience drag forces originating from the normal component alone, while the drag forces offered by the superfluid component are zero (neglecting any drag due to surface waves and compressibility effects). In this case, the superfluid component can be understood as a physical vacuum, merely renormalizing the effective mass of the oscillating body by means of conservative inertial forces. Therefore, to derive the scaling laws for the drag forces in the Newtonian limit, we must analyze the Navier-Stokes equations governing the motion of the normal component.

B. Classical oscillatory flows: Hydrodynamic limit

To describe a classical oscillatory flow, the governing Navier-Stokes equations (NSE) may be expressed in terms of dimensionless velocity $\boldsymbol{u'} = \boldsymbol{u}/U$, time $t' = t/T$, and positions $\boldsymbol{r'} = \boldsymbol{r}/L_i$ as

$$\omega U \frac{\partial \boldsymbol{u'}}{\partial t'} + \frac{U^2}{L_1}(\boldsymbol{u'} \cdot \boldsymbol{\nabla' u'} + \boldsymbol{\nabla'} p') = \frac{\nu U}{{L_2}^2} \Delta' \boldsymbol{u'}, \qquad (1)$$

where the characteristic length scales $L_{1,2}$ are used together with the characteristic velocity U to estimate the maximum magnitude of the respective velocity derivatives. An independent timescale is introduced, given (in the continuum limit) by the angular frequency of oscillation ω. Generally, the choice of L_1 and L_2 depends on body geometry and flow parameters. Candidates may include the typical body size D, the surface roughness R_q, or the Stokes boundary layer thickness (viscous penetration depth), defined as $\delta = \sqrt{2\eta/(\rho\omega)}$, where η denotes the dynamic viscosity of the working fluid. If, for a given body $\delta \ll D$, one may say that the object oscillates in the high-frequency regime, which is equivalent to the high-Stokes-number limit $\mathrm{St} = D^2/(\pi\delta^2) \gg 1$.

In the high-frequency limit, depending on body geometry (especially surface roughness and the presence of sharp corners), δ or D may take the part of L_1 (related to the largest tangential velocity derivative) in the NSE, but it is always δ that takes the part of L_2 (related to the largest velocity derivative in any direction) (see Fig. 1). When sharp corners are present [case (a) in Fig. 1] or when $R_q \gg \delta$ [case (d) in Fig. 1], one may safely put $L_1 = L_2 = \delta$, and the Navier-Stokes equation may be expressed using only one dimensionless parameter, the boundary-layer-based Reynolds number: $\mathrm{Re}_\delta \equiv (\delta\rho U)/\eta$. Conversely, for a hydrodynamically smooth body ($R_q \ll \delta$) without any sharp corners, such as a cylinder [case (b) in Fig. 1], one would obtain the Navier-Stokes equation with the Keulegan-Carpenter number $\mathrm{K_C} = UT/D$ as the only relevant dimensionless parameter [2]. However, for laminar flows with $\mathrm{K_C} \ll 1$, where the nonlinear term can be neglected, the viscous drag force would still be expected to scale with Re_δ, as for the viscous drag $L_2 = \delta$ is the only relevant length scale even in this case.

Of the oscillators used in this work, only the disk may be considered hydrodynamically smooth. The classification of our oscillators would thus be tuning forks [Figs. 1(a) and 1(d)], vibrating wire [Fig. 1(d)], double paddle [Fig. 1(a)],

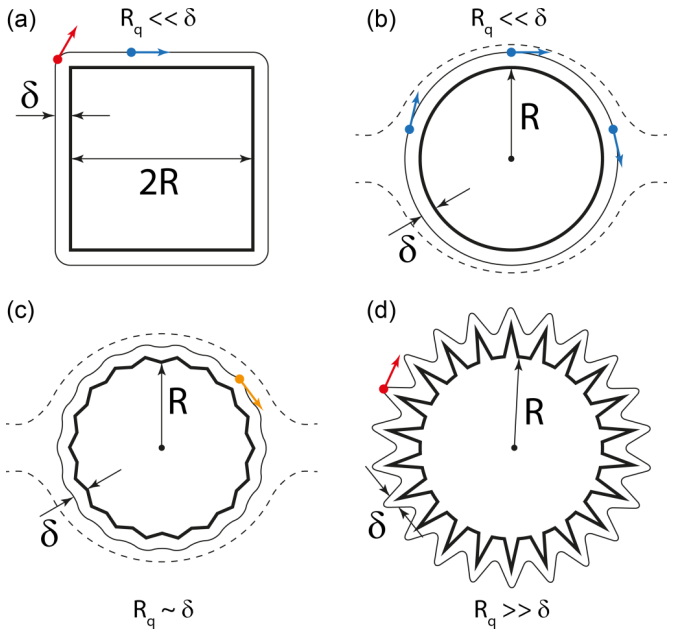

FIG. 1. Illustration of the effects of surface roughness and sharp corners on the estimates of (maximum values of) velocity derivatives in the high-frequency limit, where $\delta \ll R$. In cases (a) and (d), both velocity derivatives present in the NSE are estimated using δ, while in case (b), the tangential velocity derivative is estimated using R and the Laplacian using δ. In case (c), where $R_q \simeq \delta$, reliable estimates of the tangential derivative prove difficult; a smooth crossover between cases (b) and (d) is expected.

disk [Fig. 1(b)]; see Sec. III for details. The tuning forks contain sharp corners and have a surface roughness exceeding the boundary-layer thickness at the same time. We expect the roughness to be more significant for the commercial tuning fork (see Sec. III A).

C. Oscillatory flows of He II

Assuming two independent velocity fields in He II, as is the case at low velocities, where the normal component exhibits laminar flow and the superfluid component remains potential, the above considerations are fully applicable to the oscillatory viscous flow of the normal component. We therefore replace ρ by ρ_n, decompose the pressure into partial pressures of the normal and superfluid components, and replace δ by $\delta_\mathrm{n} = \sqrt{2\eta/(\rho_\mathrm{n}\omega)}$, where η denotes the dynamic viscosity of He II. Again, if, for a given body $\delta_\mathrm{n} \ll D$, and $R_q \gg \delta_\mathrm{n}$ (in our experiments, typically $\delta_\mathrm{n} \approx 1\ \mu$m, except for the disk, where $\delta_\mathrm{n} \approx 0.5$ mm), we may put $L_1 = L_2 = \delta_\mathrm{n}$, and the Navier-Stokes equation may be written using only one dimensionless parameter: $\mathrm{Dn} \equiv (\delta_\mathrm{n}\rho_\mathrm{n}U)/\eta$, which we call the Donnelly number [46]:

$$2\frac{\partial \boldsymbol{u}'}{\partial t'} + \mathrm{Dn}\,(\boldsymbol{u}'\cdot\nabla'\boldsymbol{u}' + \nabla' p_\mathrm{n}') = \Delta'\boldsymbol{u}'. \tag{2}$$

We note that Dn will become equivalent to Re_δ at the superfluid transition temperature T_λ, allowing direct comparison with classical fluids.

If $\delta_\mathrm{n} \ll R$ is satisfied (high-Stokes-number limit), then the flow may be regarded as potential everywhere outside the thin boundary layer of thickness on the scale of δ_n. Moreover, if δ_n is smaller than the typical radius of curvature of the oscillator surface, the surface may be described as consisting of many planar elements, and the velocity profile within the boundary layer is given by the solution to Stokes second problem (an oscillating plane). In *laminar flow* around such a body, the average energy dissipation per unit time is given by [47]

$$\langle \dot{E}\rangle = \frac{1}{2}\frac{\eta}{\delta_\mathrm{n}}\oint |\Delta v_{\mathrm{L}0,\mathrm{t}}|^2 dS = \frac{1}{2}\frac{\eta}{\delta_\mathrm{n}}\oint \alpha_\mathrm{L}^2 u_{\mathrm{L}0}^2 dS, \tag{3}$$

where $\Delta v_{\mathrm{L}0,\mathrm{t}}$ is the difference between two local velocity amplitudes projected tangentially to the surface, that of the potential flow just outside the boundary layer and that of the surface element of the body. Then, α_L is the local flow enhancement factor relating this velocity difference to the (local) velocity amplitude $u_{\mathrm{L}0}$ of the surface element in question: $|\Delta v_{\mathrm{L}0,\mathrm{t}}| = \alpha_\mathrm{L} u_{\mathrm{L}0}$. Integrating over the entire surface of an oscillator, we get

$$\langle \dot{E}\rangle = \frac{\alpha\xi U_\mathrm{p}^2 S_\mathrm{r}}{2}\frac{\eta}{\delta_\mathrm{n}}, \tag{4}$$

where U_p is the maximum velocity amplitude along the surface of the resonator (peak velocity). The dimensionless quantity of order unity $\xi = \oint u_\mathrm{L}^2 dS/(S_\mathrm{r}U_\mathrm{p}^2)$ describes the velocity profile along the resonator, and an effective surface area $S_\mathrm{r} \geqslant S$ may be used to account approximately for surface roughness. The integrated flow enhancement factor α is defined from $\alpha\xi = \oint \alpha_\mathrm{L}^2 u_{\mathrm{L}0}^2 dS/(S_\mathrm{r}U_\mathrm{p}^2)$. We note that for a smooth rigid oscillator this becomes $\alpha = \oint \alpha_\mathrm{L}^2 dS/S$, e.g., for a sphere: $\alpha_\mathrm{L} = 3/2\sin(\theta)$, with the angle θ measured from the direction of the flow, and $\alpha = \frac{3}{2}$. Similarly, for a cylinder oriented normally to flow, $\alpha_\mathrm{L} = 2\sin(\theta)$ and $\alpha = 2$. We emphasize that the above derivation is valid for all the cases described in Fig. 1, as the length scale relevant to viscous drag is always δ_n.

Using the peak velocity U_p, it is possible to model a given mode of the resonator as a one-dimensional (1D) linear harmonic oscillator, as done in Ref. [30] for a tuning fork. This leads to the definition of a (net) dissipative force amplitude:

$$F = \frac{2\langle \dot{E}\rangle}{U_\mathrm{p}} = \frac{\alpha\xi\eta}{\delta_\mathrm{n}} S_\mathrm{r} U_\mathrm{p}. \tag{5}$$

We note that this force is meaningful only in the 1D model of the given resonant mode (or for a rigid oscillator) and does not, generally, offer a direct measure of the total forces experienced by the body. In analogy with steady flow, we define the dimensionless drag coefficient related to the normal component of He II as

$$C_\mathrm{D}^\mathrm{n} = \frac{2F}{A\rho_\mathrm{n}U_\mathrm{p}^2} = \frac{2\alpha\xi S_\mathrm{r}}{A}\frac{\eta}{\rho_\mathrm{n}U_\mathrm{p}\delta_\mathrm{n}} \equiv \Phi/\mathrm{Dn}, \tag{6}$$

where A is the sectional area perpendicular to the direction of flow, and the dimensionless quantity $\Phi = 2\alpha\xi S_\mathrm{r}/A$ is determined purely by the geometry of the oscillator. This scaling law is valid universally for laminar flow around all types of objects shown in Fig. 1.

Additionally, in accordance with the principle of dynamical similarity, for hydrodynamically rough bodies or bodies with sharp corners, the normal fluid drag coefficient may be expressed as a unique function of the Donnelly number

$C_D^n = C_D^n(\mathrm{Dn})$ even in nonlaminar flow. Any departure from this function must then signify either a violation of these assumptions or an instability occurring in the superfluid component. In such a case, if the superfluid component becomes turbulent at some critical velocity U_C, we expect a marked increase in the drag coefficient above the dependence $C_D^n(\mathrm{Dn})$ measured in a classical fluid (substituting the total density ρ for ρ_n and Re_δ for Dn).

The Donnelly-Glaberson (DG) instability leading to the production of quantized vorticity in the superfluid is related to self-reconnections of seed vortex loops. This process has been described in the literature [48,49], and for macroscopic objects, the related critical velocity is expected to scale as $U_C \propto \sqrt{\kappa\omega}$. Hence, it is convenient to define a reduced dimensionless velocity $\hat{U} = U_p/\sqrt{\kappa\omega}$. To facilitate a hydrodynamic description of the drag forces originating in the superfluid component, we also define the superfluid drag coefficient

$$C_D^s = \frac{2F}{A\rho_s U_p^2} = \frac{2F}{A\rho_s \kappa\omega \hat{U}^2}. \tag{7}$$

For laminar/potential flow of normal/superfluid components, this reduces to

$$C_D^s = \frac{\phi}{\hat{U}}; \quad \phi = \Phi\sqrt{\frac{\eta\rho_n}{2\kappa\rho_s^2}}, \tag{8}$$

where Φ is the same as above. If turbulence is triggered in the superfluid component without any significant coupling to the normal component, again a unique function $C_D^s(\hat{U})$ should be observed. However, this scenario seems unlikely except close to the critical velocity, as the action of the mutual friction force would couple the two components when a sufficient density of quantized vortices is produced.

In the turbulent drag regime, at velocities sufficiently above the critical values, the normal and superfluid components are expected to be coupled due to the mutual friction force and contribute to the pressure drag together. In this situation, the classical definition of the drag coefficient is applicable: $C_D = 2F/(A\rho U^2)$, where the total density $\rho = \rho_n + \rho_s$ is used. It is expected that in coupled turbulent flows, C_D will tend towards a temperature-independent constant value of order unity [43,50].

The total energy contained in the oscillatory motion of the resonator and the fluid is given as $E = m_{\mathrm{eff}} U_p^2/2$, defining the effective mass of the resonant mode m_{eff}. For a quasi-one- or two-dimensional resonator oscillating perpendicularly to its large dimension(s), such as a thin cantilever, beam, or membrane, it follows that $m_{\mathrm{eff}} = \xi m + m_{\mathrm{HD}}$, where m is the actual mass of the resonator and m_{HD} represents the hydrodynamic added mass. If the hydrodynamic mass contribution can be neglected, it is convenient to define a fluidic quality factor Q_f:

$$\frac{1}{Q_f} \equiv \frac{\langle \dot{E} \rangle}{\omega E} = \frac{\alpha\xi S_r}{m_{\mathrm{eff}}}\sqrt{\frac{\eta\rho_n}{2\omega}} \approx \frac{\alpha\rho_n S_r \delta_n}{2m}, \tag{9}$$

which can be directly linked to the resonant frequency f and linewidth Δ by $Q_f = f/(\Delta - \Delta_0)$, where Δ_0 is the linewidth in vacuum. Conversely, the effective mass may be expressed from the resonant frequency in vacuum f_0 as $m_{\mathrm{eff}}/(\xi m) = (f_0/f)^2$.

The fluidic quality factor in Eq. (9) differs from the one given in Ref. [7] (in the limit of Newtonian hydrodynamics) by the explicit inclusion of the flow enhancement factor α. We note that this factor is related to the potential flow outside the boundary layer and is necessary not only to recover correctly the analytical solutions obtained for the drag force acting on an oscillating sphere or cylinder, but in fact for all oscillators with nontrivial geometry. The fluidic quality factor Q_f is related to the drag coefficient prefactor Φ by

$$\Phi = \frac{4m_{\mathrm{eff}}}{Q_f A\delta_n\rho_n}. \tag{10}$$

This relation may be used to extract the value of Φ directly from resonant properties of the oscillator, without precise calibration of driving force or peak velocity. In the laminar regime, it can also be used to infer either force or velocity, provided that the other quantity is known, together with m_{eff}, A, and working fluid properties.

The prefactors in the universal scaling law predicted for the oscillators used in this work will be discussed case by case in Sec. III.

D. Multiple critical velocities in the superfluid

Here, we comment briefly on the transition to turbulent drag regime observed in the superfluid at very low temperatures corresponding to the ballistic regime. In oscillatory flows under these conditions, a number of experimental studies using vibrating wires [41], grids [26,27], or tuning forks [31,51] reported observation of more than one critical velocity of hydrodynamic origin. Recently, we have presented convincing evidence for three distinct hydrodynamic critical velocities and proposed an explanation linking all the observations of oscillatory flow in zero-temperature limit into a single framework [33].

The first critical velocity, connected mostly to frequency shifts rather than changes in the drag force, is associated with the formation of a number of quantized vortex loops near the surface of the oscillator, possibly forming a thin layer, which affects the coupling to the fluid and thus the hydrodynamic added mass. This first critical velocity is hardly observable in the two-fluid regime above 1 K. The second critical velocity is related to the quantized vorticity propagating into the bulk of the superfluid, either in the form of emitted vortex loops or, eventually, as a turbulent tangle. It is always accompanied by a marked increase in the drag force and usually hysteresis (detectable with amplitude sweeps). We would like to stress that it is this critical velocity which we will be discussing later in relation to the experiments performed in the hydrodynamic regime above 1 K.

For completeness, there is a third critical velocity of hydrodynamic origin, likely associated with the development of larger vortical structures from bundles of polarized quantized vortices. We note that at finite temperature, such polarized vortex bundles or rings have been studied numerically [52,53]. The mentioned critical velocity (typically above 1 ms^{-1}) might not be relevant in the two-fluid regime at all, as classical features would likely develop in the vortex tangle due to mutual friction even before this mechanism can take effect.

E. Additional dissipation mechanisms

In addition to viscous damping, losses due to sound emission through the surrounding fluid may occur, and may be accounted for approximately [54]. In this work, acoustic losses can be safely neglected for the fundamental mode of both tuning forks used and represent perhaps a very small contribution to the damping the first overtone of the custom-made fork [55]. Based on our previous studies of acoustic emission by oscillating objects in He II [54,55], acoustic losses are negligible for all other oscillators used in this work. In our experiments, no sign of cavitation and associated losses was detected.

We also note that the above description of viscous dissipation is approximate in the sense that it neglects the steady streaming flow that is known to exist in the vicinity of the oscillating objects and has been recently visualized in He II in highly turbulent flow due to vibrating quartz turning fork [38]. However, the streaming flow has negligible effect on the drag forces measured in laminar viscous flow, as the typical length scale associated with streaming is of order of the size of the oscillator, while the boundary-layer thickness is at least an order of magnitude lower in our experiments. Of course, in turbulent flows, the pressure drag is significantly larger than both the viscous friction and any additional drag due to the streaming.

III. EXPERIMENTAL DETAILS

Most of the resonators used in our investigation, the wire, the tuning forks, and the double paddle, were driven by an Agilent A33220 signal generator, and a phase-sensitive Stanford Research SR830 lock-in amplifier was used to measure both the in-phase and out-of-phase components of the induced signals.

The measurements presented here were performed in Prague, mostly in a helium immersion cryostat during a dedicated experimental run for each resonator. The helium bath is brought down to the desired temperature using a rotary pump and a Roots pump and stabilized on the level of few mK either by manually adjusting the pumping speed or using a temperature controller. The lowest attainable temperature of 1.27 K allows access to most of the hydrodynamic (two-fluid) regime.

A. Quartz tuning forks

Quartz tuning forks are piezoelectric oscillators with a calibrated resonant frequency, often used as frequency standards or shear force sensors for scanning optical microscopes [56]. Tuning forks are well-established probes of cryogenic helium flow [30].

The fork is driven by applying an ac voltage V from a function generator to the metallic electrodes deposited on the surface of the quartz. This produces a force proportional to the voltage which sets the two prongs oscillating in antiphase. The distortion of the quartz induces a piezoelectric current I which is proportional to velocity U. The relations between force, velocity, voltage, and current are

$$F = \frac{a_f V}{2} \quad I = a_f U, \tag{11}$$

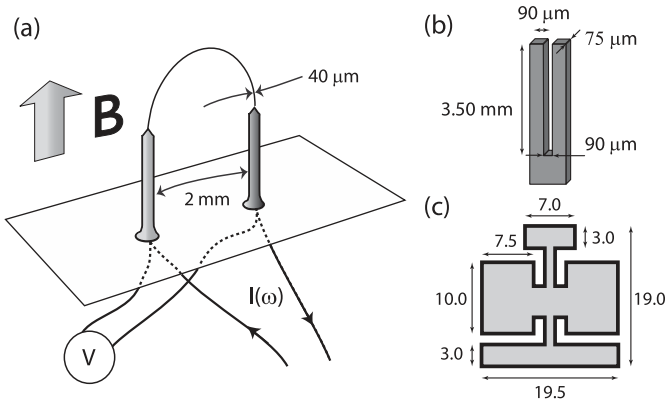

FIG. 2. Schematic diagrams of the vibrating wire resonator (a), of the quartz tuning fork (b), and the double paddle (c). The dimensions of the double paddle are in millimeters. The wafer thickness is 75 μm for the tuning fork and 250 μm for the double paddle.

where a_f is the so-called fork constant, which may be obtained through calibration by deflection measurement or self-calibration in vacuum, in which case it is given as $a_f = \sqrt{4\pi m_{\rm eff}\Delta I/V}$, where $m_{\rm eff}$ is the effective mass of the fork, and Δ is the measured resonant width [30] at half-height of the (Lorentzian) peak. The effective mass [55] of the tuning fork in vacuum is given by $m_{\rm eff} = \xi m = T_f W_f L_f \rho_f/4$, where ρ_f is the density of the fork material (in our case quartz, $\rho_f = 2650$ kgm^{-3}), and the dimensions T_f, W_f, L_f stand for the tine thickness (in the direction of motion), width, and length, respectively. The ac current is measured using an IV converter [57] and a SR-830 lock-in amplifier. The standard measurement scheme used here can be found, e.g., in Fig. 1 of Ref. [33].

We have used two different forks in this work. The first is a commercially produced fork of the following dimensions: $L_{f1} = 2.17$ mm, $T_{f1} = 210$ μm, $W_{f1} = 100$ μm, and the gap between the prongs is $D_{f1} = 120$ μm. Its surface roughness is $\approx$5 μm. The second is a custom-made fork with $L_{f2} = 3.50$ mm, $T_{f2} = 90$ μm, $W_{f2} = 75$ μm (original wafer thickness), and $D_{f2} = 90$ μm, with roughness $\approx$1 μm. A sketch of the fork geometry including the dimensions is shown in Fig. 2. The commercial fork resonates at 32 kHz, while with the custom-made fork, we use two different flexural resonant modes: the fundamental resonance at 6.5 kHz and the first overtone at 40.0 kHz.

To describe the drag force acting on tuning forks in laminar flow, unfortunately, no analytical solutions of NSE can be obtained. However, significant effort has been invested into studying the dynamical response of rectangular beams immersed in viscous fluids [58,59], resorting to numerical integration to obtain the hydrodynamic response function for rectangular beams of arbitrary aspect ratio. These calculations may thus be applicable to tuning forks. Although we consider Φ as a parameter to be determined experimentally for each oscillator due to surface roughness effects, we may use the results of Ref. [59] to obtain the approximate dependence $C_D^n \simeq 4.67/{\rm Dn}$ for the custom-made fork (see Appendix A). For the commercial fork, $C_D^n \simeq 5.55/{\rm Dn}$ is obtained in a similar fashion, if its surface roughness is ignored.

B. Vibrating wire resonator

Vibrating wire resonators are well-established low-temperature probes [60]. They consist of a semicircular loop of wire subjected to a vertical magnetic field B, as shown in Fig. 2. A loop is used to prevent closely spaced or degenerate modes one may observe on a straight wire.

Traditionally, the vibrating wire is described in the following way. Passing an alternating current $I(\omega)$ through the wire forces it to oscillate due to the Lorentz force $F_{\rm L} = BDI$. As the wire moves through the magnetic field, it induces a voltage which can be determined using Faraday's law. For a rigid semicircular wire with leg spacing D, oscillating at a peak velocity $U_{\rm p}$, the area bounded by the loop is $A = \pi D^2/8$ and the rate of change of angle to the field is $2U_{\rm p}/D$. Therefore, the induced Faraday voltage generated by a semicircular vibrating wire loop is traditionally given by

$$V = -\frac{d(\boldsymbol{B}\cdot\boldsymbol{A})}{dt} \simeq \frac{\pi}{4}BDU_{\rm p}. \tag{12}$$

Here, we argue that the traditional model does not describe the behavior at resonance correctly, in the sense that the energy dissipation at resonance is not equivalent in terms of electrical quantities $\dot{E}_{\rm el} = 1/2\,VI$ and within the 1D mechanical model $\dot{E}_{\rm mech} = 1/2\,FU_p$, as they differ by a factor of $\pi/4$. This due to the fact that one cannot take the total Lorentz force $F_{\rm L}$ as the driving force of the resonant mode of the wire, but a projection of this force on the mode shape must be considered. The remaining Lorentz force is driving other resonant modes, as determined by its distribution along the length of the wire, but it does not dissipate any energy, as it is frequency mismatched with respect to those modes (in an off-resonance condition).

A correct definition of the model force may be obtained directly from energy dissipation, as has been done for tuning forks [30]. We use this approach in our proposed model that describes the vibrating wire as a doubly clamped beam. Neglecting for a moment the curvature of the wire (a valid approximation if the wire radius is much smaller than the radius of the loop), the resonant mode shapes may be obtained by solving the Euler-Bernoulli equation. Using the appropriate boundary conditions, one obtains in terms of local velocities

$$u_{\rm L}(x) \propto \left\{\sinh(b_n x) - \sin(b_n x) - \frac{[\cosh(b_n x) - \cos(b_n x)][\sinh(b_n L) - \sin(b_n L)]}{\cosh(b_n L) - \cos(b_n L)}\right\} \tag{13}$$

for $x \in [0, L]$, where L is the length of the semicircular loop, and $b_n = (\mu\omega_n^2/EI)^{1/4}$, with μ representing the mass per unit length, ω_n the angular frequency of the nth mode, E the Young's modulus, and I the second moment of area of the wire cross section. The resonance frequencies are determined from the equation $\cosh(b_n L)\cos(b_n L) = 1$, which has to be solved numerically.

The mode shapes can then be integrated to obtain a *mode-dependent* effective mass. For $n = 1$, we get $m_{\rm eff} \approx 0.396m$. Now taking into account the curvature of the wire to find the changing projected area of the loop on the direction of $\boldsymbol{B}$ using the obtained mode shape, Eq. (12) will be replaced by $V \approx 0.690BDU_{\rm p}$ and the driving force will be given by $F \approx 0.690BDI$. This is the correct projection of the Lorentz force $F_{\rm L}(x) = BI\sin(\pi x/L)$ on the mode shape of the fundamental resonance, as can be verified by direct integration.

To obtain the drag force in laminar flow, we again neglect the curvature of the loop, approximating each segment along the length of the wire as a smooth cylinder oscillating with a local velocity amplitude $u_{\rm L}(x)$. The drag force per unit length acting on such a cylinder is given, e.g., in Ref. [47]. Following the procedure outlined in Sec. II C, for the fundamental mode, the drag coefficient is given as $C_{\rm D}^{\rm n} = 4\pi\xi/{\rm Dn} \approx 4.98/{\rm Dn}$.

The vibrating wire resonator used in this study consists of a semicircular loop of superconducting NbTi wire with a leg spacing of $D = 2$ mm and a diameter of $2R = 40$ μm. The wire was mounted in a brass cell submerged in the bulk superfluid and mounted between a pair of NdFeB permanent magnets in a magnetic field of (170 ± 10) mT at room temperature. We estimate that the field is reduced by approximately 23% at low temperatures [61] due to spin reorientation occurring in NdFeB at 135 K. Given the uncertainty of the magnetic field, we have used Eq. (10) to obtain a self-calibration of the force driving the vibrating wire.

C. Double paddle

Recent studies [36,37] have shown that double-paddle oscillators (DPOs) may serve as promising probes to study superfluid hydrodynamics. They have demonstrated high-quality factors in vacuum compared to other mechanical resonators since any vibrational losses through their base are heavily suppressed.

Here, we reanalyze the results obtained with the silicon DPO etched from a 0.25-mm-thick ⟨110⟩ wafer used by Zemma and Luzuriaga [36], sketched in Fig. 2. The two larger wings are approximately 10 mm × 7.5 mm and the smaller upper paddle is 7 mm × 3 mm. The DPO was driven magnetically by attaching a small magnet located between the wings in the oscillator stem; its displacement was detected capacitively. In order to generate the oscillatory motion, an ac current was applied to a small superconducting coil fixed to the support frame.

The complex geometry of the DPO precludes any analytical solutions of NSE, and we are not aware of any numerical studies detailing the laminar drag experienced by a submerged DPO.

D. Torsionally oscillating disk

The torsional oscillator consists of a 0.05-mm tungsten wire, 32 cm long, with a borosilicate glass disk fixed to the wire at its midpoint using a thin 0.8-mm brass capillary and Stycast 2850 GT. The disk is 1 mm thick with a diameter of 40 mm; a schematic diagram is shown in Fig. 3. When the wire is under tension, the disk is positioned approximately midway between the two copper-coated, polished FR-2 plates placed 10 mm apart (both disk sides are approximately 4.5 mm away from the FR-2 plate facing them). The deflection and angular velocity of the disk are determined from recorded video sequences as detailed in Appendix B.

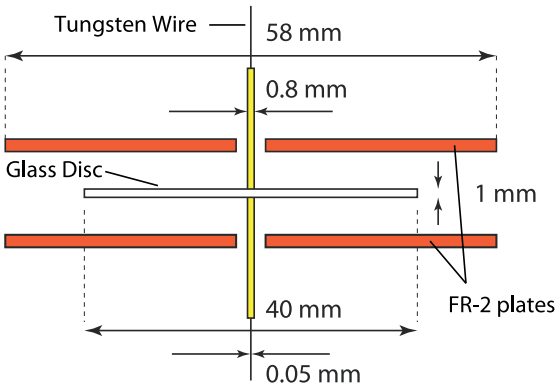

FIG. 3. Schematic diagram of the torsionally oscillating disk.

To facilitate comparison with other oscillators, we define a drag coefficient for a thin disk torsionally oscillating in a viscous fluid of density ρ_n as

$$C_D^n = \frac{2M_F}{A\rho_n\Omega_0^2 R^3}, \tag{14}$$

where M_F is the moment of friction forces, R is the disk's radius, $A = \pi R^2$ is the surface area of one side of the disk, Ω_0 is the amplitude of the angular velocity, and ω is the angular frequency of oscillation. For a rationale of this definition, and for the derivation of the Donnelly number dependence, we refer the reader to Appendix C. In laminar flow, the drag coefficient due to the normal component can be expressed in terms of the Donnelly number as $C_D^n = 2/\mathrm{Dn}$.

IV. EXPERIMENTAL RESULTS AND ANALYSIS

In this section we present our drag force measurements using the resonators introduced above and compare the results against the proposed universal scaling law.

A. Tuning forks

The custom-made tuning forks used in our measurements are fully described and characterized in Ref. [33]. By performing frequency sweeps in vacuum at low temperature, the experimental fork constant is estimated to be $a_f = 3.665 \times 10^{-7}$ C/m and $a_f^o = 1.409 \times 10^{-6}$ C/m for the fundamental mode and first overtone, respectively. We estimate that the fork constant has an uncertainty of 10% since it was shown that the optically measured prong velocity can be 10% lower [62] than that determined from the electromechanical model described in Sec. III A. The details of the commercial fork are given in Ref. [50], where it is labeled "L2."

Figure 4 shows typical results for the drag offered by He II to driven oscillations of the quartz tuning fork and compares them to the numerical results of Ref. [59]. In the left of Fig. 4, we plot the classical drag coefficient as a function of the peak velocity at various temperatures. As expected, the tuning forks exhibit linear damping at low velocities at all temperatures. Upon increasing the velocity, the drag coefficient tends to a temperature-independent constant value of order unity ($C_D \approx 0.6$) as one would expect for fully coupled normal and superfluid components. The flow due to the fork then behaves as a single classical-like fluid in the turbulent drag regime. On decreasing temperature, the drag coefficient drops appreciably over the range of low and intermediate velocities as the density of the normal fluid component decreases. This is in agreement with previous analysis [50].

To characterize the flow of the normal component, we plot the normal fluid drag coefficient as a function of the Donnelly number in the right of Fig. 4. At low Donnelly numbers, the data collapse to a single dependence for each fork, before deviating at some critical value. Note that despite the difference in the velocity profile and the viscous penetration depth, the same prefactor Φ in Eq. (6) is obtained for the two resonant modes of the custom-made fork, supporting the validity of the derived scaling law. This is due to the fact that both modes have the same flow enhancement factor α determined by the rectangular cross section of the prong and practically the same effective mass $m_{\mathrm{eff}} = \xi m + m_{\mathrm{HD}}$ with $\xi = \frac{1}{4}$ (see Appendix A of Ref. [55]). Furthermore, the obtained prefactor Φ agrees almost perfectly ($\approx$2% deviation) with Ref. [59] (see calculation in Appendix A). Careful inspection also reveals differences in the onset of nonlinear drag for the lowest two temperatures (this will be further analyzed in Sec. IV E). The commercial fork shows the same universal scaling, but the obtained prefactor is 1.4× higher than the numerical result. This is likely due to surface roughness effects. Comparison to oscillations in classical liquid helium and helium gas is shown on the commercial fork data, where $\mathrm{Dn} \equiv \mathrm{Re}_\delta$ is used, highlighting the same form of the scaling law in both classical and quantum fluids. As the commercial tuning fork is hydrodynamically rough, a unique dependence $C_D^n(\mathrm{Dn})$ is expected in classical fluids as well as wherever the superfluid component does not contribute to the drag force appreciably. This is illustrated in the lower right panel of Fig. 4, as the data obtained in He I, He gas, and at $T = 2.16$ K agree quite well over the entire range of Dn. Departures from this dependence mark drag forces originating from the superfluid component, or arising in either component due to their coupling by mutual friction.

B. Vibrating wire resonator

The resonant response of the vibrating wire resonator is obtained by measuring the voltage in phase with the driving current, as a function of frequency. In accord with previous works [41,42,60], for small drive levels, the frequency response is of Lorentzian form. Upon increasing the drive level, the Lorentzian shape becomes distorted and the resonant frequency decreases. The flattening of the peak indicates the onset of nonlinear drag forces typically associated with turbulent instabilities in the generated oscillatory flow.

The classical drag coefficient as a function of velocity for the vibrating wire is plotted in the left of Fig. 5. In order to collapse the contribution of the normal fluid component to the drag forces acting on the wire to a single dependence, we again plot the drag coefficient for the normal component as a function of the Donnelly number [see Eq. (6)] in the right of Fig. 5. Universal scaling with the Donnelly number is observed for the wire, up to critical value, which is now, however, temperature dependent, in striking difference with the custom-made tuning fork. We also note that the prefactor

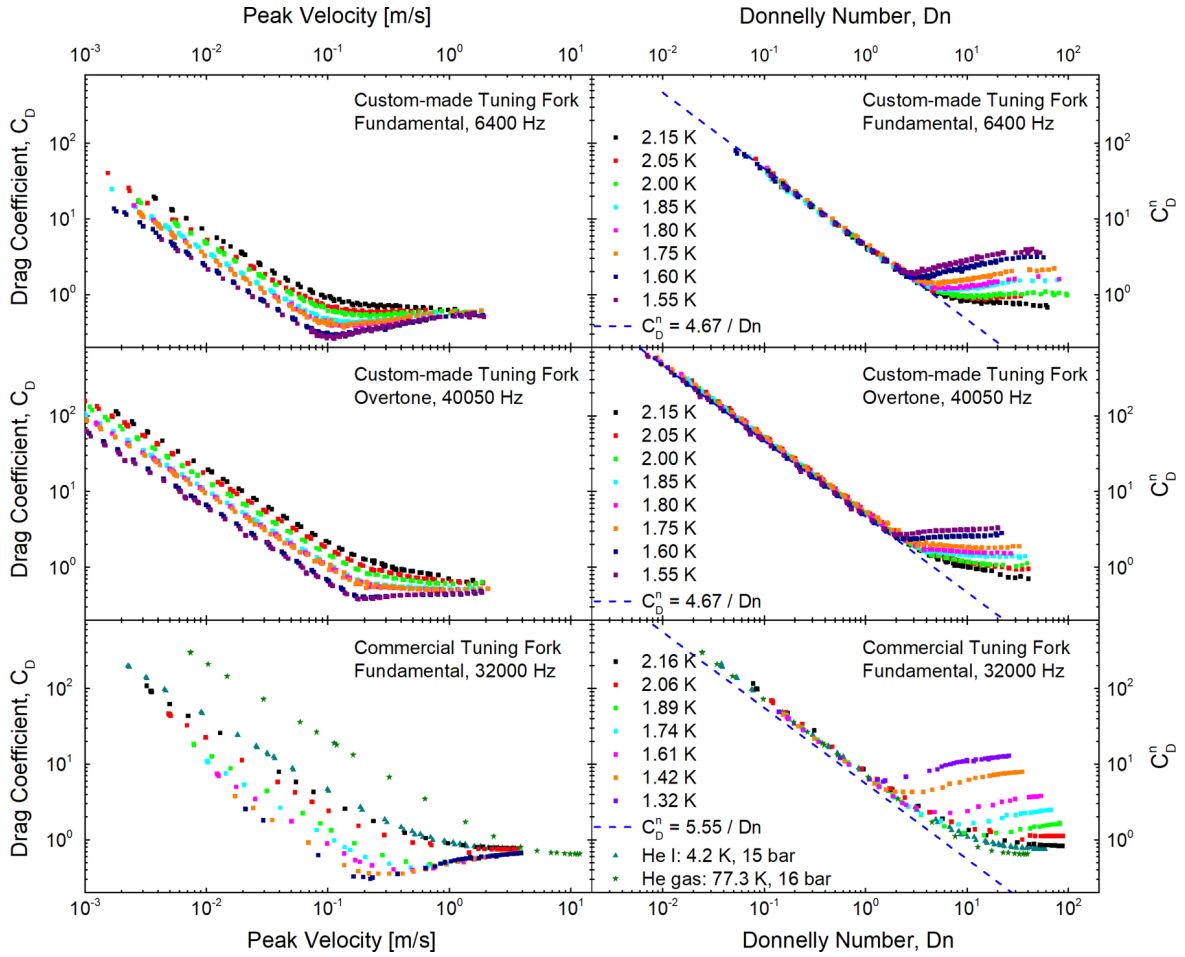

FIG. 4. Left: drag coefficient as function of velocity for the quartz tuning forks. Right: the corresponding normal fluid drag coefficient as a function of the Donnelly number. Note that (i) the same prefactor for the laminar scaling is displayed for the fundamental mode and overtone of the custom-made tuning fork, in near perfect agreement with the calculation described in the text and that (ii) for commercial fork, the same scaling is observed in classical (He I, He gas) and quantum (He II) fluids. A slight disagreement in the prefactor with respect to the numerical calculations is observed: the experimental data can be recovered by applying a multiplicative factor of 1.4, which we associate with the surface roughness of the commercial fork.

for the laminar drag is by 10% to 15% smaller than calculated. This is most likely due to the uncertainty in the wire radius and hence in its effective mass, which enters Eq. (10) that was used to obtain the driving force from resonant properties. While the 2-mm wire loop was located in a cylindrical cavity of diameter 4 mm, we do not expect a significant effect of the container walls on the measured drag, as the viscous penetration depth δ_n is of order 1 μm.

C. Double paddle

We now apply the same analysis to results obtained using a silicon DPO by Zemma and Luzuriaga [36]. Specifically, we

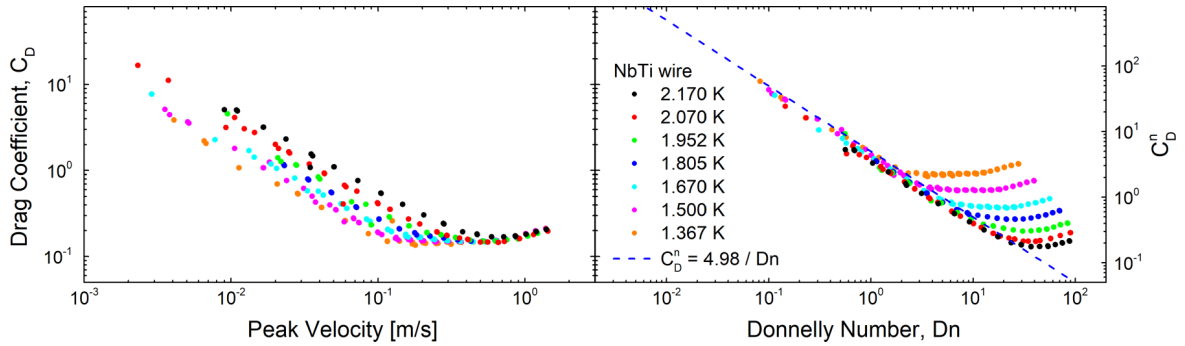

FIG. 5. Drag coefficients as functions of the peak velocity or Donnelly number obtained for the vibrating wire.

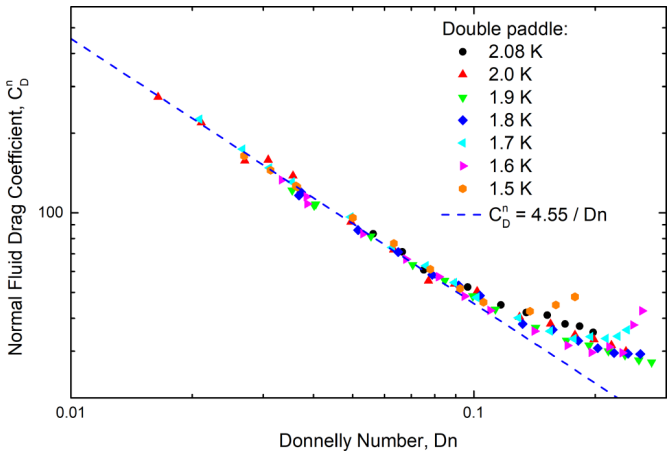

FIG. 6. Normal fluid drag coefficient as a function of the Donnelly number calculated for the silicon double paddle of Zemma and Luzuriaga [36].

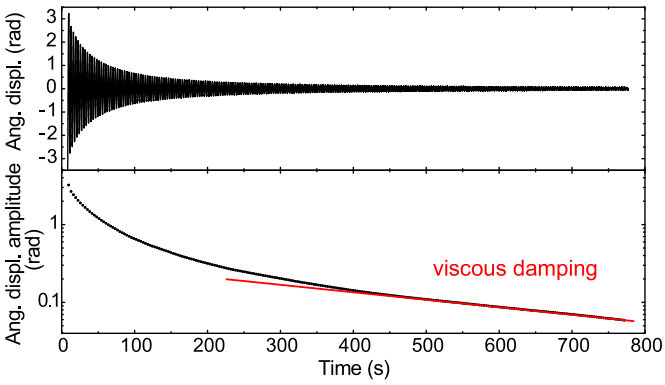

FIG. 7. Typical measurement of angular displacement of the torsionally oscillating disk in He II as a function of time. (Top) The signal extrema were evaluated to obtain the angular displacement amplitude ϕ_0. The logarithmic plot (bottom) clearly shows two distinct regions: exponential (viscous) decay due to laminar flow of the normal component for $t \gtrsim 500$ s and a faster nonlinear decay at earlier times, related to turbulent drag. The position of the disk oscillating with a period of $T \simeq 3.17$ s is sampled at 240 Hz (see Appendix B). The turbulent decay is typically observed on timescales of order 100 s, whereas decays of coflow or counterflow turbulence in He II typically in a few seconds.

analyze the symmetric torsion mode data [35]. In vacuum at ≈4.2 K, the resonant frequency of the paddle is 520 Hz, in liquid helium at 4.2 K it is 358 Hz. The viscous penetration depth is ≈3 μm. Since the lateral characteristic length scale of the paddle is $D \simeq 7$ mm, and the thickness is 250 μm, the paddle is operating in the high-Stokes-number limit, justifying our analysis.

In Fig. 6, we present the normal fluid drag coefficient plotted against the Donnelly number. The viscous drag force again collapses to a single dependence within an uncertainty of ±15%, demonstrating that the paddle is indeed in the high-Stokes-number limit. The drag force offered by the normal fluid is again described by the same universal scaling law, even for an oscillator of significantly different shape than a wire or tuning fork, in this case following approximately $C_d^n = 4.55/\mathrm{Dn}$. To the best of our knowledge, no theoretical or computational works exist that would allow a quantitative comparison of the prefactor.

D. Torsionally oscillating disk

The torsionally oscillating disk differs from the previous oscillators in three fundamental ways. First, as the disk oscillates around its axis, it does not displace any fluid, hence, there is no potential flow outside the boundary layer. Second, in this case we are not able to perform measurements in a steady state and we have to deal with slowly decaying oscillations of the disk and of the flow due to its motion. Third, we cannot directly measure the drag force and have to infer the damping from the decaying amplitude of oscillation. Despite these important differences, we seek to analyze the flow in a manner similar to the above oscillators.

First, we have established that the intrinsic damping of the disk is negligible compared to that due to the surrounding helium. This was done by measurements in vacuum at room temperature and 78 K, and already at 78 K the intrinsic damping was far below any measured in superfluid helium. We note, however, that the entire tungsten filament had to be submerged in helium in order to ensure that its temperature is sufficiently low, as it was connected to the driving mechanism at the top flange by a thin-walled stainless steel tube with no special regards for thermal isolation.

As the moment of frictional forces M_F cannot be obtained directly from the experiment, we have to infer the drag coefficient from other measurable quantities, such as the extremal displacements of the disk during its damped oscillations as shown in Fig. 7. If the series of extremal angular displacements occurring at times t_n is labeled φ_n (interleaving maxima and minima in chronological order), the logarithmic decrements of the amplitude of oscillation α_n are determined as $\alpha_n = \ln(\varphi_{n-1}) - \ln(\varphi_{n+1})$ and the immediate angular frequency of oscillation is $\omega_n = 2\pi/(t_{n+1} - t_{n-1})$. This leads to an alternative definition of the drag coefficient:

$$C_D^n = \frac{2I\alpha}{\pi A \rho_n R^3 \varphi_0} \simeq \frac{\rho_d h_d \alpha}{\pi \rho_n R \varphi_0}, \tag{15}$$

where φ_0 denotes the immediate angular displacement amplitude, and $I = I_0 + I_{HD}$ stands for the effective moment of inertia consisting of the moment of inertia of the disk itself I_0, and of its hydrodynamic enhancement I_{HD}. If $I_{HD} \ll I_0$, the simplified expression on the right-hand side of Eq. (15) holds, where ρ_d is the density of the disk material and h_d the height (thickness) of the disk. The derivation can be found in Appendix C.

We plot the drag coefficient C_D^n measured at various temperatures against the Donnelly number $\mathrm{Dn} = \rho_n \delta_n R \omega \varphi_0 / \eta$ in Fig. 8. At small values of Dn, the data collapse to a single dependence illustrating the universal behavior. As the disk is hydrodynamically smooth, we do not expect the turbulent instability to occur at a well-defined critical value of Dn, but we may still be able to distinguish between a classical instability in the normal component and the onset of superfluid turbulence by considering the dependence of the nonlinear drag on the densities ρ_n and ρ_s.

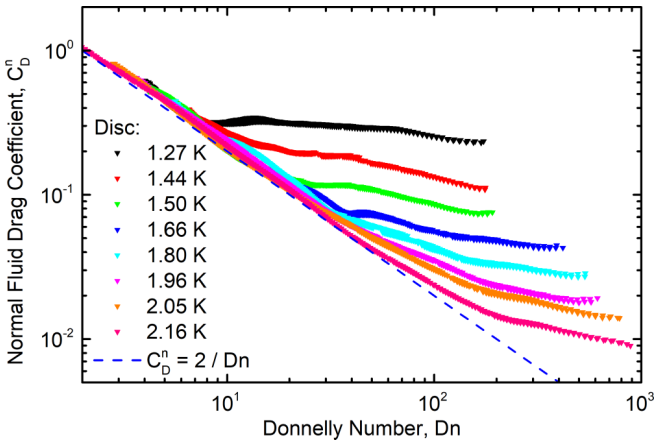

FIG. 8. Normal fluid drag coefficient as a function of the Donnelly number for the torsionally oscillating disk at the various indicated temperatures. The dashed blue line is the predicted dependence for viscous drag $C_D^n = 2/\mathrm{Dn}$. Prior to the calculation of C_D^n, the logarithmic decrements α_n have been smoothed by a 50-point weighted adjacent averaging filter and checked against the original data, showing minimal deviation.

E. Analysis of instabilities

While the drag coefficients shown in the previous sections contain, in principle, all necessary information about the flow properties, it is useful to examine the transition to nonlinear drag in more detail. In particular, we are interested in determining which type of instability occurs upon increasing oscillation amplitude first: a classical instability of the normal component or the multiplication of remnant quantized vortices in the superfluid component?

To tackle this issue, we need to analyze the first departures from laminar drag, hence, we withdraw from the measured drag force the part that is linear with velocity, keeping only the nonlinear contribution. Such a quantity needs to be normalized and plotted against parameters relevant to either component in order to deduce the nature of the first detected instability. It seems particularly advantageous to use the quantity $1 - \Phi/(C_D^n \mathrm{Dn})$ in a plot against Dn to describe the action of the normal component and, analogically, $1 - \phi/(C_D^s \hat{U})$ against $\hat{U}$ for the superfluid component [see Eq. (7)]. These definitions guarantee that the result is always close to zero in laminar flow, and approaches one as the nonlinear drag starts

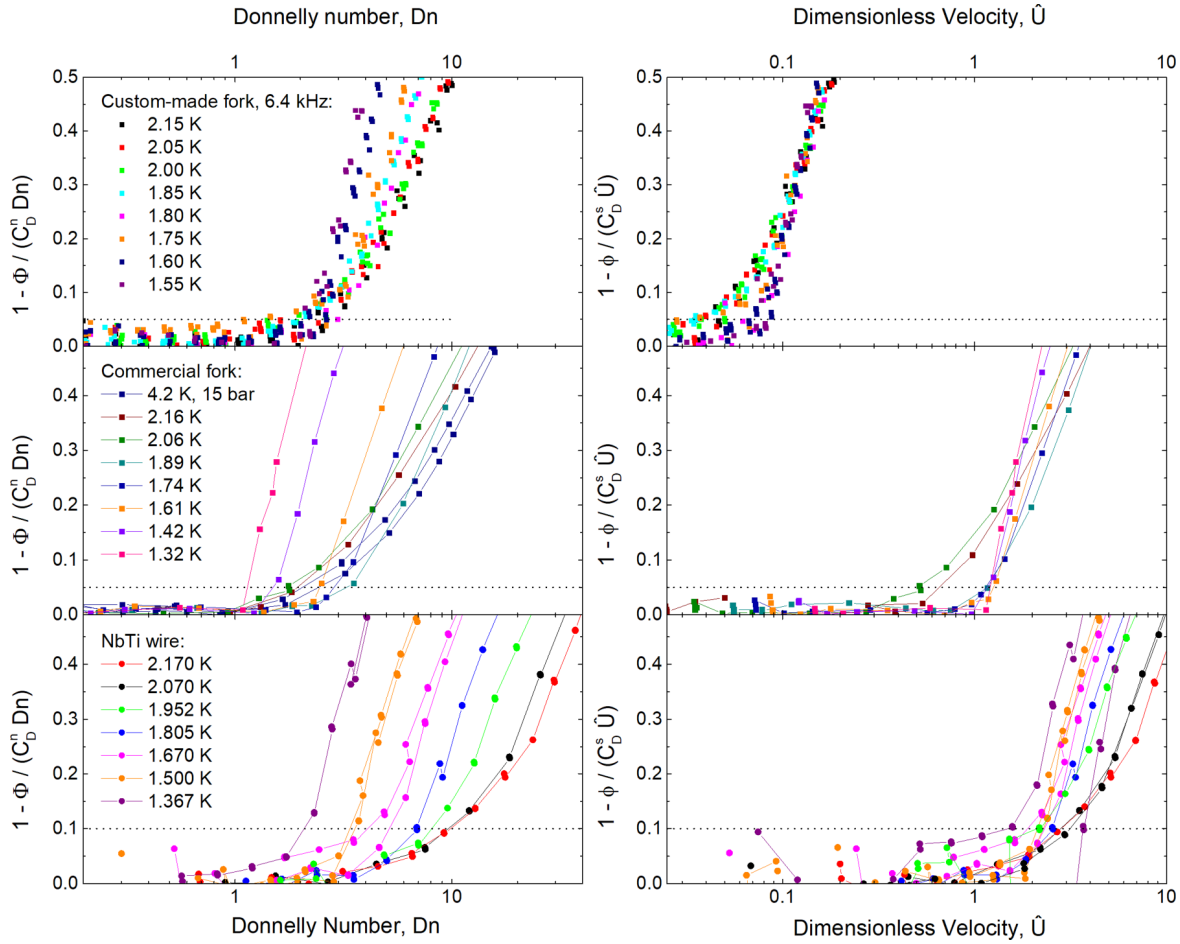

FIG. 9. Turbulent instability analysis for both tuning forks and the vibrating wire resonator. Left: nonlinear drag normalized using normal component properties versus Donnelly number. Right: nonlinear drag normalized using superfluid component properties versus nondimensional velocity $\hat{U}$. We note that the quantities on the ordinate axes are equivalent, as both represent the ratio of the nonlinear drag to the total drag experienced by the oscillator.

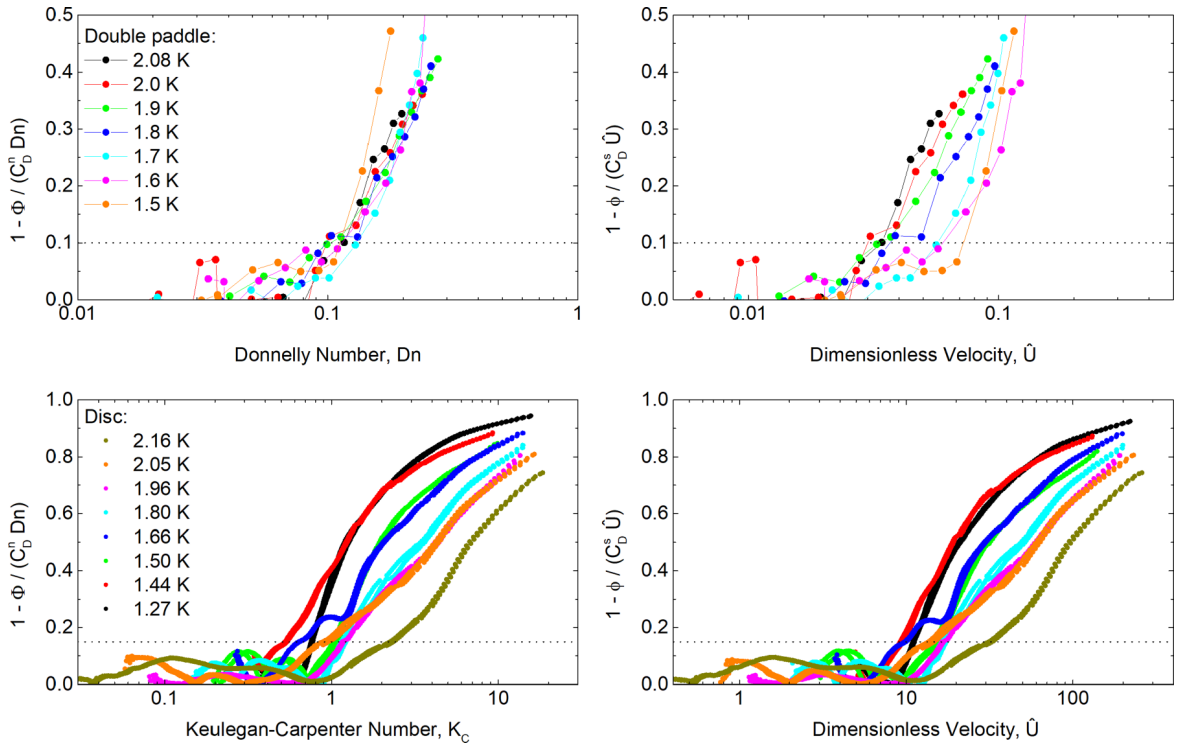

FIG. 10. Turbulent instability analysis for the double paddle and the disk. Left: nonlinear drag normalized using normal component properties versus the Donnelly number or Keulegan-Carpenter number, as applicable. Right: nonlinear drag normalized using superfluid component properties versus nondimensional velocity $\hat{U}$.

to dominate. For the oscillating disk, K_C is used instead of Dn, in agreement with the theory in Sec. II B.

Such plots are shown in Fig. 9 for the two tuning forks and the vibrating wire resonator, with each oscillator displaying different behavior. We consider the instability occurring at a given departure from the linear drag, which must be above the experimental noise level in the data acquired in laminar flow. For the tuning forks, we use a 5% departure criterion, for the wire, 10% seems more appropriate. To understand the results, it is useful to consider two aspects: (i) the magnitude and relative spread of critical values of either Dn or $\hat{U}$ when crossing the given threshold, (ii) the rate at which the nonlinear drag sets in.

In the top two panels of Fig. 9, the custom-made fork shows a notably lower spread in Dn than in $\hat{U}$, signifying that Dn is likely to be the correct parameter governing the (classical) instability in a larger part of the range of temperatures investigated. On the other hand, the vibrating wire resonator (bottom two panels) displays a rather well-defined critical value of $\hat{U}$, while showing significant spread in Dn (except for the two highest temperatures, for which the critical values of Dn coincide), giving evidence of a Donnelly-Glaberson type of instability in the superfluid component. The commercial tuning fork (middle panels) shows a clear crossover: at temperatures below 2.0 K the instability is governed by $\hat{U}$, while at higher temperatures it is determined by Dn. It is interesting to note that whenever the instability is determined by $\hat{U}$, the onset of nonlinear drag is notably sharper. A crossover between a classical and quantum instability might be present in the other two oscillators as well, but is not as pronounced as with the commercial tuning fork.

The presented interpretation is further supported by the observed critical values of the governing parameters. For the commercial fork, the critical dimensionless velocity $\hat{U}_C \approx 1.2$, and for the vibrating wire resonator values between 1.5 and 3 are found. However, the custom-made fork has only $\hat{U} \approx 0.1$ when the nonlinear drag sets in. Hence, the Donnelly-Glaberson instability is very unlikely to occur, and is preceded by the classical instability near $\mathrm{Dn}_C = 2.5$. Furthermore, the (minimum) critical value of Dn characterizing the classical instability can be obtained from measurements in classical fluids, such as He I or He gas, or from experiments very close to T_λ where the drag offered from the very low density superfluid component can be neglected. Hence, for the commercial fork we obtain $\mathrm{Dn}_C \approx 2.5$ and for the wire we get $\mathrm{Dn}_C^{\mathrm{min}} \approx 9$ from the data at 2.07 and 2.17 K. The lower value of Dn_C obtained for the forks is likely related to velocity enhancement in flow past its sharp corners.

In Fig. 10 we analyze the data from the DPO and the torsionally oscillating disk in a similar manner. For the DPO we find a classical instability in the entire temperature range, characterized by a critical value of the Donnelly number $\mathrm{Dn}_C \approx 0.1$, with the rather low value again related to flow enhancement. Indeed, in the symmetric torsion mode of the DPO, the displaced fluid needs to move significantly faster than the oscillator itself to flow from one side of the wings to the other and back during one period of oscillation.

For the disk, the situation is more complex and fundamentally different from the oscillators just discussed, for several reasons. In analyzing the data, we need to bear in mind that contrary to the other oscillators, the disk is hydrodynamically smooth, and hence the instability should be governed by

the Keulegan-Carpenter number K_C. Unfortunately, K_C scales with the fluid properties in a very similar fashion to the dimensionless velocity $\hat{U}$, making our situation complicated. The spread of critical values of both parameters is very similar, and the numerical critical values are in both cases acceptable. For comparison, if the data in the bottom left panel in Fig. 10 were plotted against Dn, the critical values would show a very large spread between 8 and 100 (see Fig. 8). However, since the data taken at 2.16 K (where fluid properties ought to be dominated by the normal component) differ significantly from the all the other series, we are led to believe that except for this highest temperature, the instability has origins in the superfluid component.

Furthermore, since the disk is set into motion at a high amplitude and left to oscillate, we are dealing with a decaying turbulent flow; this has implications for our interpretation, if hysteresis exists at the turbulent transition. Here, we emphasize that temporal decays of quantum turbulence usually observed in both coflow and counterflow geometries are typically much faster than the observed timescale of the decay of torsional oscillations. We thus believe that the intensity of quantum turbulence is, at all times, near its steady-state value determined by the immediate amplitude of oscillations of the disk. Nevertheless, the observed critical values do not signify the first instability occurring in a laminar flow as with the other oscillators, but rather a minimum requirement, a necessary condition for preexisting turbulence to survive, which might generally depend on details of the turbulent flow. Such a requirement seems to be given by $10 < \hat{U}_C < 20$ for all the investigated temperatures except for 2.16 K, where a higher critical velocity is observed.

To the best of our knowledge, there are two possible reasons for this behavior. First, it is likely that most of the nonlinear drag observed at 2.16 K above $\hat{U}_C \approx 30$ is in fact due to the normal component which behaves independently from the superfluid and undergoes its own instability at $K_C \approx 2$, corresponding to $\hat{U}_C \approx 30$. The nonlinear drag from the superfluid component (still present) might then be below our resolution. The second possibility is that at 2.16 K, the significantly enhanced damping of the motion of quantized vortices in He II is responsible for the dissipation of any existing quantum turbulence (the dissipative part of mutual friction force grows steeply with temperature close below the superfluid transition [11]). This seems plausible especially in a situation with no large-scale flow of the superfluid component to provide a supply of energy, as in our case the superfluid is not displaced by the motion of the torsionally oscillating disk.

V. DISCUSSION

Let us summarize the experimental results on the two-fluid He II flows due to several types of mechanical oscillators. In all of them, the normal fluid flow (as well as the corresponding flow of classical viscous normal He I) is characterized by high Stokes number, and for low velocities it is laminar. In this limit, the superflow is either potential or, in the case of the oscillating disk, the superfluid component remains stationary in the laboratory frame of reference (barring a low density of pinned remnant vortices [63]). We therefore have two (almost) independent velocity fields, and flows of the normal and superfluid components can be treated independently. It is therefore natural to treat the normal fluid as classical viscous fluid and it is not surprising that the drag coefficient C_D^n due to the normal fluid displays universal scaling in terms of the Donnelly number Dn. Assuming that the flow of the superfluid component remains potential, upon increasing the Donnelly number the universal scaling holds and, for hydrodynamically rough bodies, describes instabilities in the normal flow leading to gradual transition from laminar to turbulent drag regime in the normal fluid flow. The normal fluid flow is no longer laminar and the overall He II flow can be characterized as quantum turbulence in the sense of a vortical flow occurring in a quantum fluid, despite that there are almost no quantized vortices present.

In some of the investigated oscillatory two-fluid He II flows, the opposite situation appears in that the critical velocity associated with the Donnelly-Glaberson instability in the superfluid component occurs first, before the instability in the normal fluid flow develops. This situation is not new in superfluid hydrodynamics. Indeed, in typical experiments with rotating superfluid ^{3}He-B the thick normal component virtually does not move in the laboratory frame of reference [64]. Still, below about half of the critical temperature T_c the dissipative mutual friction coefficient falls below unity [65] and a tangle of quantized vortices, superfluid turbulence, can exist in the soup of a thick stationary normal fluid.

In He II experiments with oscillators described above, the situation is different in that the quantized vorticity coexists with the laminar boundary layer flow of the normal component. In ^{4}He, this situation is reported and analyzed in this work and is best illustrated for the case of He II flow due to the vibrating wire (see Fig. 9).

Now, as the Donnelly-Glaberson instability occurs upon reaching a critical velocity, but the instability in the normal fluid flow is governed upon reaching a critical Donnelly number, a crossover is possible, thanks to the steep temperature dependence of the kinematic viscosity of the normal fluid. In other words, in the particular example of He II flow due to the commercial tuning fork (see again Fig. 9) at high temperatures, close to the superfluid transition temperature T_λ, the classical instability in the normal fluid is reached first, while at low temperatures the situation is reversed in favor of the Donnelly-Glaberson instability. The existence of this crossover is, remarkably, reported here despite the immense effort in investigating oscillatory flows in He II, especially during the last two decades.

Either instability eventually serves as a trigger for the other one, mediated by the mutual friction force or fluctuating pressure forces, until in the limit of high velocities, both fluids are tightly coupled in the vicinity of the oscillator and He II behaves as a single-component quasiclassical fluid.

VI. CONCLUSIONS

We have performed systematic measurements of high-Stokes-number flows of He II due to oscillatory motion of selected oscillators: vibrating wire resonator, tuning forks, double paddle, and torsionally oscillating disk, over a broad temperature range where our working fluid, He II, displays

the two-fluid behavior. We have shown that in this class of flows the origin of any instability in the normal or superfluid component can be determined by complex drag force analysis, based on which one can separate the drag offered to these oscillators by the normal and superfluid components of He II. For low velocities, we observe *universal viscous drag scaling* in terms of the suitably defined drag coefficient C_D^n and the normal fluid boundary-layer-based Reynolds number which we call the Donnelly number Dn.

The superfluid component does not contribute to the drag until an instability associated with extrinsic production of quantized vorticity occurs, governed by the dimensionless *velocity* $\hat{U} = U/\sqrt{\kappa\omega}$. The underlying physics involves Donnelly-Glaberson instability, i.e., self-reconnections of quantized vortices upon reaching a critical velocity. Until then, the flow of the superfluid component is either potential (excepting pinned remnant vortices) with the superfluid component playing a role of a physical vacuum, renormalizing the hydrodynamic effective mass of the oscillators, or (in the case of the torsionally oscillating disk) the superfluid component remains stationary in the laboratory frame of reference.

Which instability (i.e., classical hydrodynamic instability of laminar flow of the normal component or Donnelly-Glaberson instability in the superfluid component) occurs first depends both on the geometry of the oscillator and temperature. We observe a crossover between these instabilities, thanks to the steep temperature dependence of the kinematic viscosity of the normal fluid. Upon increasing oscillation amplitude, either instability can live on its own until eventually it serves as a trigger for the other one, mediated by the mutual friction force or by pressure forces. At high velocities, both fluids are tightly coupled in the vicinity of the oscillator and He II behaves as a single-component quasiclassical fluid.

We believe that the described approach, i.e., treating the flows of normal and superfluid components of He II independently, can be extended and applied to different two-fluid He II flows, such as different types of coflows (where the normal and superfluid components are forced together) but perhaps also to the more general case of counterflows (where a nonzero difference of mean velocities of normal and superfluid components exists), in particular to special cases known as thermal counterflow and pure superflow. One can find known features of these flows, such as temperature dependence of the onset of quantum turbulence at various geometries, which provide hints that this approach will most likely be useful, however, dedicated detailed experiments are needed to fully resolve the long-standing puzzles of superfluid hydrodynamics such as the existence of experimentally observed [66] turbulent states TI, TII, and TIII in thermal counterflow and pure superflow. We believe that our results will stimulate further research of the fascinating topic of superfluid hydrodynamics and quantum turbulence.

All data used in this paper are available in Ref. [67], including descriptions of the data sets.

ACKNOWLEDGMENTS

We thank E. Zemma and J. Luzuriaga for providing the data of Ref. [36] for further analysis, L. Doležal for skillful manufacturing of various cryogenic parts of the experiments, and E. Collin, V. S. L'vov, M. Rotter, and K. R. Sreenivasan for fruitful discussions. This research is funded by the Czech Science Foundation under Project No. GAČR 17-03572S and UK EPSRC Grants No. EP/P022197/1 and No. EP/L000016/1. M.J.J. acknowledges personal support from Vakuum Praha spol. s r.o. V.T. would like to acknowledge the support of the European Microkelvin Platform EMP.

APPENDIX A: DERIVATION OF TUNING FORK DRAG COEFFICIENT

In Ref. [59], numerical calculations are used to evaluate the inertial and drag forces per unit length acting on uniformly oscillating rectangular cylinders. The cylinders are assumed infinite, with the same cross section everywhere. The drag force amplitude per unit length is expressed in Eq. (2) of Ref. [59] as

$$f_l dl = \frac{\pi}{4}\rho\omega^2 X^2 W_{\mathrm{cyl}}\Gamma(\omega), \tag{A1}$$

where ρ is the fluid density, ω the angular frequency of oscillation, X a dominant length scale which corresponds to the larger dimension of the beam cross section, W_{cyl} is the displacement amplitude, and $\Gamma(\omega)$ is a complex-valued hydrodynamic response function. This function is then evaluated numerically for cylinders of selected aspect ratios at selected values of a modified Stokes number β_d, where $\beta_d = \omega d^2/\nu$, and $d = X/2$. The real and imaginary parts of $\Gamma(\omega)$ correspond to inertial and dissipative forces, respectively; we will thus need to evaluate only the imaginary part $\mathrm{Im}(\Gamma(\omega))$. The local energy dissipation rate is given by $\dot{\epsilon}_l = f_l u_l/2$, where u_l is the local velocity. Integrating the dissipation rate along the length of a tine of a tuning fork, we obtain

$$\dot{E} = \int_0^L \dot{\epsilon}_l dl = \frac{\pi}{8}\rho\omega X^2 L\xi U_p^2 \mathrm{Im}(\Gamma(\omega)), \tag{A2}$$

where ξ again describes the velocity profile along the tine [32]. This leads to the drag force and drag coefficient:

$$F = \frac{\pi}{4}\rho\omega X^2 L\xi U_p \mathrm{Im}(\Gamma(\omega)), \tag{A3}$$

$$C_D = \frac{2F}{\rho W L U_p^2} = \frac{\pi\xi\omega X^2 \mathrm{Im}(\Gamma(\omega))}{2WU_p}. \tag{A4}$$

To estimate the dissipation of a tuning fork of aspect ratio $A_r = T/W$ in the high-Stokes-number limit, we express $\mathrm{Im}(\Gamma(\omega))$ as a function of the modified Stokes number β_d:

$$\lim_{\beta_d\to\infty} \mathrm{Im}(\Gamma(A_r,\omega)) = c(A_r)\beta_d^{-1/2} = \frac{2c(A_r)}{X}\sqrt{\frac{\nu}{\omega}}, \tag{A5}$$

where $c(A_r)$ is a constant coefficient for a given aspect ratio A_r that can be obtained with sufficient accuracy from the numerical data of Ref. [59].

Substituting for $\mathrm{Im}(\Gamma(\omega))$ in Eq. (A4), we get

$$C_D = \frac{\pi\xi X c(A_r)\sqrt{\nu\omega}}{WU_p} = \frac{\sqrt{2}\pi\xi X c(A_r)}{W\mathrm{Re}_\delta}, \tag{A6}$$

where $\mathrm{Re}_\delta = U_p\delta/\nu$ is the boundary-layer-based Reynolds number (equivalent to the Donnelly number in superfluid He).

For both forks discussed here (and indeed for most tuning forks available), we have $T > W$ and therefore $X = T$ or, equivalently, $X/W = A_r$ (in the opposite case we would have used $X = W$). The drag coefficient expressed for the normal component of superfluid helium then becomes $C_D^n = \Phi/\mathrm{Dn}$, where the prefactor $\Phi = \sqrt{2}\pi\xi A_r c(A_r)$ is again determined solely by the geometry of the tuning fork.

To evaluate $c(A_r)$ for the custom-made fork of aspect ratio $A_r = 1.2$ and the commercial fork of aspect ratio $A_r = 2.1$, we analyze the results obtained for the aspect ratios of 1.0, 2.0, 5.0 as given in Ref. [59], obtaining $c(1.0) \approx 3.78$, $c(2.0) \approx 2.41$, and $c(5.0) \approx 1.57$. This gives by linear interpolation $c(1.2) \approx 3.51$ and $c(2.1) \approx 2.38$ for our tuning forks. Using $\xi = \frac{1}{4}$, we finally arrive at $C_D^n \simeq 4.67/\mathrm{Dn}$ for the custom-made fork and $C_D^n \simeq 5.55/\mathrm{Dn}$ for the commercial one.

APPENDIX B: DETERMINATION OF THE POSITION AND VELOCITY OF THE TORSIONALLY OSCILLATING DISK

Sixteen black marks around the circumference of the disk are used to determine the deflection and angular velocity of the disk from recorded video sequences. The motion of the disk is recorded with a Casio EX-10 digital camera. The recordings are acquired at the frame rate of 240 fps with a resolution of 512×384 pixels. A large optical lens is placed between the camera and the cryostat to improve the spatial resolution. Our raw data are in the form of video recordings of the motion of the disk during the experiments. Because the marks on the disk have rather low contrast to the not-entirely-uniform background, standard motion tracking software could not be used to process the videos. Hence, fairly complex postprocessing is required to extract quantitative and interpretable data.

The videos are split into individual frames and de-interlaced. The color images are converted to monochromatic bitmaps by dynamic contrast algorithms implemented in NI VISION software, so that the marks appear as black spots on a white background. These monochromatic bitmaps are then analyzed by a custom-made LABVIEW program. In the first pass, the program localizes the black areas in each image and evaluates their size and center of mass. In the second pass, using only numerical data from the first pass, it then links corresponding images of the same dot between all frames to each other (making special arrangements for those not reproduced in some of the bitmaps) and calculates the angular displacement of the disk in each instant. The program uses a self-calibration obtained from a complete revolution of the disk around its axis. The optical distortion from the lenses and the curved walls of the glass cryostat are negligible, as only a 10-mm central portion of the field of view is used in the processing.

APPENDIX C: HYDRODYNAMIC DESCRIPTION OF THE TORSIONALLY OSCILLATING DISK

Here, we derive the equation of motion of the torsionally oscillating disk and the relevant hydrodynamic quantities. The motion of the harmonic torsional oscillator is given by the equation

$$I_0\ddot{\varphi} + \kappa_f\varphi = M_F, \tag{C1}$$

where φ is the angular displacement, I_0 is the moment of inertia of the disk, κ_f is the moment of torsion of the fiber, and M_F represents the moment of drag forces due to the surrounding fluid.

In laminar flow, with some simplification, the moment of the frictional forces can be calculated on the basis of the analytical solution of the Navier-Stokes equations. First, we assume that the velocity profile $\boldsymbol{u}(\boldsymbol{r}, t)$ locally corresponds to the rotation of the rigid body modulated with the distance from the disk, $\boldsymbol{u}(\boldsymbol{r}, t) = \boldsymbol{\Omega}(z, t) \times \boldsymbol{r}$, where $\boldsymbol{\Omega}(z, t) = (0, 0, \Omega(z, t))$, in which $\Omega(z, t)$ is the instantaneous angular velocity of the fluid at the distance z from the disk surface. Furthermore, we assume that the radius of the disk R is significantly greater than its thickness h_d and all other relevant dimensions. The Navier-Stokes equation is then expressed in the form

$$\frac{\partial\Omega(z, t)}{\partial t} = \nu\frac{\partial^2\Omega(z, t)}{\partial z^2}, \tag{C2}$$

where ν is the kinematic viscosity. Assuming that any temporal changes of the amplitude of oscillation are much slower than one period of oscillation, the solution of this equation meeting the boundary conditions on the surface of the disk ($z = 0$) and at infinity can be expressed in the form

$$\Omega(z, t) = \Omega_0 e^{-z/\delta} e^{i(\omega t - z/\delta)}, \tag{C3}$$

where Ω_0 is the instantaneous amplitude of the disk's angular velocity and $\delta = \sqrt{2\nu/\omega}$ is the viscous penetration depth. The total torque acting on the disk will be determined by integration of drag forces over both surfaces of the disk, neglecting the friction along its edge. The magnitude of the local viscous drag force f_L (per unit area) is given by $f_L(r, t) = \eta\,\partial u(z, t)/\partial z$, where η is the fluid dynamic viscosity. The magnitude of the local contribution to the torque of the viscous forces is then given as $M_L(r, t) = r f_L(r, t)$. The total moment of frictional forces is given as

$$\begin{aligned} M_F(t) &= 2\int_0^R \int_0^{2\pi} M_L(r, t) r\, d\theta\, dr \\ &= -\pi\eta\frac{1 + i}{\delta}\Omega_0 R^4 e^{i\omega t} \\ &= \frac{\pi}{\sqrt{2}}(1 - i)\sqrt{\eta\omega\rho}\ \omega R^4\varphi_0 e^{i\omega t}, \end{aligned} \tag{C4}$$

where $\Omega_0 e^{i\omega t} = i\omega\varphi_0 e^{i\omega t}$ was used, with φ_0 representing the instantaneous amplitude of angular displacement.

The moment of the friction forces is therefore phase shifted with respect to the angular velocity of the disk by $\pi/4$. By defining a hydrodynamically induced moment of inertia $I_{HD} = \pi R^4\sqrt{\eta\rho/2\omega}$ and the coefficient $\Gamma = \pi R^4\sqrt{\eta\rho\omega/2}$, we can rewrite the moment of the frictional forces as

$$M_F(t) = -\Gamma\dot{\varphi}(t) - I_{HD}\ddot{\varphi}(t), \tag{C5}$$

where the two terms on the right-hand side correspond to dissipative and inertial torques, respectively.

The energy dissipated by the viscous forces can be obtained as

$$\dot{E}(t) = -2\int_0^R \int_0^{2\pi} \mathrm{Re}(M_\mathrm{v}(r,t))\mathrm{Re}(\Omega_t) r\, d\theta\, dr$$
$$= -\frac{\pi\eta\Omega_0^2 R^4}{\delta}[\sin(\omega t)\cos(\omega t) - \cos^2(\omega t)]. \quad \text{(C6)}$$

Averaging over one period, we get

$$\langle \dot{E} \rangle = \frac{\pi}{2}\frac{\eta\Omega_0^2 R^4}{\delta}. \quad \text{(C7)}$$

Using the fact that the total energy stored in the motion of the disk is $E = I_0\Omega_0^2/2$, and its moment of inertia is given by $I_0 = mR^2/2$ (neglecting hydrodynamic contributions), we may define a fluidic quality factor

$$\frac{1}{Q_\mathrm{f}} = \frac{\langle \dot{E} \rangle}{\omega E} = \frac{A}{m_\mathrm{d}}\sqrt{\frac{\eta\rho\omega}{2}}, \quad \text{(C8)}$$

where $A = \pi R^2$ is the area of one side of the disk, and m_d is the disk's mass.

To define the drag coefficient, we follow the definition used in classical steady flow: the force F acting on a body in steady flow is given by $F = \frac{1}{2}\mathrm{C_D}A'\rho U^2$, where $\mathrm{C_D}$ is the dimensionless drag coefficient, A' is the cross section of the body perpendicular to the direction of motion, ρ is the density of the fluid, and U is the (homogeneous) velocity of the fluid. In analogy, it is possible to define the drag coefficient for the torsionally oscillating disk from

$$\frac{M_\mathrm{FD}}{R} = \frac{1}{2}\mathrm{C_D}A\rho\Omega_0^2 R^2, \quad \text{(C9)}$$

where $M_\mathrm{FD} = \Gamma\Omega_0$ is the dissipative part of the moment of frictional forces and we again use $A = \pi R^2$.

Finally, to define the dimensionless Donnelly number, we use the peak velocity at the circumference of the disk $U = R\Omega_0$, yielding

$$\mathrm{Dn} = \frac{R\Omega_0\rho_\mathrm{n}\delta_\mathrm{n}}{\eta}. \quad \text{(C10)}$$

Comparing with Eq. (C9), we arrive at $\mathrm{C_D^n} = 2/\mathrm{Dn}$, where the normal component drag coefficient $\mathrm{C_D^n}$ differs from $\mathrm{C_D}$ only by replacing the density ρ with ρ_n.

Substituting (C5) into the dynamic equation (C1) and dividing by the total moment of inertia $I = I_0 + I_\mathrm{HD}$, we get

$$\ddot{\varphi} + 2\gamma\dot{\varphi} + \omega_0^2\varphi = 0, \quad \text{(C11)}$$

where $\gamma = \Gamma/2I$ is the damping coefficient and $\omega_0^2 = \kappa_\mathrm{f}/I$ is the square of the intrinsic angular frequency of the undamped resonator. Thus, we have a standard equation of the damped harmonic oscillator, which is satisfied by the solution

$$\varphi(t) = \varphi_0 e^{-\gamma t}e^{i\omega t}, \quad \text{(C12)}$$

where the angular frequency ω is related to the frequency of a hypothetical undamped oscillator by $\omega^2 = \omega_0^2 - \gamma^2$.

After processing the recorded videos of the disk motion, we obtain data in the form of $\varphi(t)$. From this, we determine the extrema $\varphi_{0,i}$ and the logarithmic decrements $\alpha_i = \ln(\varphi_{0,i-1}) - \ln(\varphi_{0,i+1})$, which are related to the damping coefficient γ in Eq. (C11) by $\gamma_i = \alpha_i\omega/(2\pi)$. The dissipative part of the moment of friction forces, the first term on the right-hand side of Eq. (C5), is then $M_{\mathrm{FD},i} = 2I\omega\gamma_i\varphi_{0,i}$. The drag coefficient obtained from each experimental point may then be expressed as

$$\mathrm{C_{D,}}_i = \frac{2I\alpha_i}{\pi A\rho R^3\varphi_{0,i}}. \quad \text{(C13)}$$

If the hydrodynamic contribution to the moment of inertia is negligible, we may put $I \simeq I_0 = mR^2/2$, where the mass of the disk can be expressed as $m = Ah_\mathrm{d}\rho_\mathrm{d}$, where h_d is the disk height and ρ_d its density. The drag coefficient can then be further simplified to

$$\mathrm{C_{D,}}_i = \frac{1}{\pi}\frac{\rho_\mathrm{d}h_\mathrm{d}\alpha_i}{\rho R\varphi_{0,i}}, \quad \text{(C14)}$$

which no longer requires the precise knowledge of I or I_0.

[1] G. G. Stokes, On some cases of fluid motion, Trans. Cambridge Philos. Soc., Vol. VIII. Part I, 105 (1843), reprinted in: Mathematical and Physical Papers by G. G. Stokes, Vol. I, Cambridge University Press, 1880.

[2] G. H. Keulegan and L. H. Carpenter, J. Res. Natl. Bureau Standards **60**, 423 (1958).

[3] C.-Y. Wang, J. Fluid Mech. **32**, 55 (1968).

[4] T. Sarpkaya, J. Fluid Mech. **165**, 61 (1986).

[5] M. Tatsuno and P. W. Bearman, J. Fluid Mech. **211**, 157 (1990).

[6] K. L. Ekinci, V. Yakhot, S. Rajauria, C. Colosquiac, and D. M. Karabacak, Lab Chip **10**, 3013 (2010).

[7] K. L. Ekinci, D. M. Karabacak, and V. Yakhot, Phys. Rev. Lett. **101**, 264501 (2008).

[8] E. C. Bullard, J. Li, C. R. Lilley, P. Mulvaney, M. L. Roukes, and J. E. Sader, Phys. Rev. Lett. **112**, 015501 (2014).

[9] M. Defoort, K. J. Lulla, T. Crozes, O. V. Maillet, O. Bourgeois, and E. Collin, Phys. Rev. Lett. **113**, 136101 (2014).

[10] D. I. Bradley, R. George, A. M. Guénault, R. P. Haley, S. Kafanov, M. T. Noble, Y. A. Pashkin, G. R. Pickett, M. Poole, J. R. Prance, M. Sarsby, R. Schanen, V. Tsepelin, T. Wilcox, and D. E. Zmeev, Sci. Rep. **7**, 4876 (2017).

[11] R. J. Donnelly and C. F. Barenghi, J. Phys. Chem. Ref. Data **27**, 1217 (1998).

[12] R. D. McCarty, Thermophysical properties of helium-4 from 2 to 1500 K with pressures to 1000 atmospheres, Technical Note No. 631, National Bureau of Standards, 1972 (unpublished), https://nvlpubs.nist.gov/nistpubs/Legacy/TN/nbstechnicalnote631.pdf.

[13] V. D. Arp and R. D. McCarty, The properties of critical helium gas, Technical Note 1334 (revised), National Bureau of

Standards, 1998 (unpublished), https://nvlpubs.nist.gov/nistpubs/Legacy/TN/nbstechnicalnote1334.pdf.
[14] S. Fuzier, B. Baudouy, and S. W. Van Sciver, Cryogenics **41**, 453 (2001).
[15] B. Saint-Michel, E. Herbert, J. Salort, C. Baudet, M. Bon Mardion, P. Bonnay, M. Bourgoin, B. Castaing, L. Chevillard, F. Daviaud, P. Diribarne, B. Dubrulle, Y. Gagne, M. Gibert, A. Girard, B. Hébral, Th. Lehner, and B. Rousset, SHREK Collaboration, Phys. Fluids **26**, 125109 (2014).
[16] J. J. Niemela, L. Skrbek, K. R. Sreenivasan, and R. J. Donnelly, Nature (London) **404**, 837 (2000).
[17] L. D. Landau, J. Phys. (USSR) **5**, 71 (1941); Zh. Eksp. Teor. Fiz. **11**, 592 (1941) [J. Phys. (USSR) **11**, 92 (1947)].
[18] R. J. Donnelly, *Quantized Vortices in Helium II* (Cambridge University Press, Cambridge, 1991).
[19] A. C. Hollis-Hallett, Proc. R. Soc. London, Ser. A **210**, 404 (1952).
[20] R. J. Donnelly and A. C. Hollis-Hallett, Ann. Phys. **3**, 320 (1958).
[21] E. L. Andronikashvili, Zh. Eksp. Teor. Fiz. **16**, 780 (1946) [J. Phys. USSR **10**, 201 (1946)].
[22] J. Jäger, B. Schuderer, and W. Schoepe, Phys. Rev. Lett. **74**, 566 (1995).
[23] M. Niemetz and W. Schoepe, J. Low Temp. Phys. **135**, 447 (2004).
[24] J. Luzuriaga, J. Low Temp. Phys. **108**, 267 (1997).
[25] S. I. Davis, P. C. Hendry, and P. V. E. McClintock, Physica B (Amsterdam) **280**, 43 (2000).
[26] H. A. Nichol, L. Skrbek, P. C. Hendry, and P. V. E. McClintock, Phys. Rev. Lett. **92**, 244501 (2004).
[27] H. A. Nichol, L. Skrbek, P. C. Hendry, and P. V. E. McClintock, Phys. Rev. E **70**, 056307 (2004).
[28] D. Charalambous, L. Skrbek, P. C. Hendry, P. V. E. McClintock, and W. F. Vinen, Phys. Rev. E **74**, 036307 (2006).
[29] P. Švančara and M. La Mantia, J. Fluid Mech. **832**, 578 (2017).
[30] R. Blaauwgeers, M. Blažková, M. Človečko, V. B. Eltsov, R. de Graaf, J. J. Hosio, M. Krusius, D. Schmoranzer, W. Schoepe, L. Skrbek, P. Skyba, R. E. Solntsev, and D. E. Zmeev, J. Low Temp. Phys. **146**, 537 (2007).
[31] D. Garg, V. B. Efimov, M. Giltrow, P. V. E. McClintock, L. Skrbek, and W. F. Vinen, Phys. Rev. B **85**, 144518 (2012).
[32] S. L. Ahlstrom, D. I. Bradley, M. Človečko, S. N. Fisher, A. M. Guénault, E. A. Guise, R. P. Haley, O. Kolosov, P. V. E. McClintock, G. R. Pickett, M. Poole, V. Tsepelin, and A. J. Woods, Phys. Rev. B **89**, 014515 (2014).
[33] D. Schmoranzer, M. J. Jackson, V. Tsepelin, M. Poole, A. J. Woods, M. Človečko, and L. Skrbek, Phys. Rev. B **94**, 214503 (2016).
[34] E. N. Martinez, P. Esquinazi, and J. Luzuriaga, Am. J. Phys. **58**, 1163 (1990).
[35] C. L. Spiel, R. O. Pohl, and A. T. Zehnder, Rev. Sci. Instrum. **72**, 1482 (2001).
[36] E. Zemma and J. Luzuriaga, J. Low Temp. Phys. **166**, 171 (2012).
[37] D. Schmoranzer, M. Jackson, E. Zemma, and J. Luzuriaga, J. Low Temp. Phys. **187**, 482 (2017).
[38] D. Duda, P. Švančara, M. La Mantia, M. Rotter, and L. Skrbek, Phys. Rev. B **92**, 064519 (2015).
[39] W. F. Vinen, Proc. R. Soc. London, Ser. A **181**, 1524 (1961).
[40] M. Morishita, T. Kuroda, A. Sawada, and T. Satoh, J. Low Temp. Phys. **76**, 387 (1989).
[41] D. I. Bradley, D. O. Clubb, S. N. Fisher, A. M. Guénault, R. P. Haley, C. J. Matthews, G. R. Pickett, and K. L. Zaki, J. Low Temp. Phys. **138**, 493 (2005).
[42] R. Goto, S. Fujiyama, H. Yano, Y. Nago, N. Hashimoto, K. Obara, O. Ishikawa, M. Tsubota, and T. Hata, Phys. Rev. Lett. **100**, 045301 (2008).
[43] L. Skrbek and W. F. Vinen, The use of vibrating structures in the study of quantum turbulence, in *Progress in Low Temperature Physics*, edited by M. Tsubota and W. P. Halperin (Elsevier, Amsterdam, 2009), Vol. XVI, Chap. 4.
[44] L. Skrbek and W. F. Vinen, Proc. Natl. Acad. Sci. USA **111**, 4699 (2014).
[45] C. F. Barenghi, L. Skrbek, and K. R. Sreenivasan, Proc. Natl. Acad. Sci. USA **111**, 4647 (2014).
[46] R. J. Donnelly suggested using this dimensionless parameter, a "Reynolds number" based on the viscous penetration depth defined for the normal component of He II only, in his joint publication with A. C. Hollis-Hallett in Ref. [20] (note that such an analysis was not included in previous work of Hollis-Hallett on the subject [19]). Unfortunately, the importance of this parameter was originally discounted, as it failed to describe the onset of turbulence for a sphere torsionally oscillating in He II. Now we know that this was because in the experiment the turbulent transition occurred first in the superfluid component and that the Donnelly number remains to be relevant for description of the normal fluid flow in this seminal boundary layer experiment.
[47] L. D. Landau and E. M. Lifshitz, *Fluid Mechanics* (Pergamon, London, 1959).
[48] W. I. Glaberson, W. W. Johnson, and R. M. Ostermeier, Phys. Rev. Lett. **33**, 1197 (1974).
[49] R. Hänninen and W. Schoepe, J. Low Temp. Phys. **158**, 410 (2010).
[50] M. Blažková, D. Schmoranzer, L. Skrbek, and W. F. Vinen, Phys. Rev. B **79**, 054522 (2009).
[51] D. I. Bradley, M. J. Fear, S. N. Fisher, A. M. Guénault, R. P. Haley, C. R. Lawson, P. V. E. McClintock, G. R. Pickett, R. Schanen, V. Tsepelin, and L. A. Wheatland, J. Low Temp. Phys. **156**, 116 (2009).
[52] A. W. Baggaley, J. Laurie, and C. F. Barenghi, Phys. Rev. Lett. **109**, 205304 (2012).
[53] D. H. Wacks, A. W. Baggaley, and C. F. Barenghi, Phys. Rev. B **90**, 224514 (2014).
[54] D. Schmoranzer, M. La Mantia, G. Sheshin, I. Gritsenko, A. Zadorozhko, M. Rotter, and L. Skrbek, J. Low Temp. Phys. **163**, 317 (2011).
[55] D. I. Bradley, M. Človečko, S. N. Fisher, D. Garg, E. Guise, R. P. Haley, O. Kolosov, G. R. Pickett, V. Tsepelin, D. Schmoranzer, and L. Skrbek, Phys. Rev. B **85**, 014501 (2012).
[56] K. Karrai and R. D. Grober, in *Near-Field Optics*, edited by M. A. Paesler and P. T. Moyer, Proceedings of the SPIE, Vol. 2535 (SPIE, Bellingham, WA, 1995), p. 69.
[57] S. Holt and P. Skyba, Rev. Sci. Instrum. **83**, 064703 (2012).
[58] J. E. Sader, J. Appl. Phys. **84**, 64 (1998).

[59] D. R. Brumley, M. Willcox, and J. E. Sader, Phys. Fluids **22**, 052001 (2010).

[60] A. M. Guénault, C. J. Kennedy, S. G. Mussett, and G. R. Pickett, J. Low Temp. Phys. **62**, 511 (1986).

[61] K. J. Strnat, D. Li, and H. Mildrum, High and low temperature properties of sintered Nd-Fe-B magnets, in 8th International Workshop on Rare-Earth Magnets and their Applications, Dayton, OH, 1985; T. Hara, T. Tanaka, H. Kitamura, T. Bizen, X. Maréchal, T. Seike, T. Kohda, and Y. Matsuura, Phys. Rev. Accel. Beams **7**, 050702 (2004).

[62] D. I. Bradley, P. Crookston, M. J. Fear, S. N. Fisher, G. Foulds, D. Garg, A. M. Guénault, E. Guise, R. P. Haley, O. Kolosov, G. R. Pickett, R. Schanen, and V. Tsepelin, J. Low Temp. Phys. **161**, 536 (2010).

[63] D. D. Awschalom, F. P. Milliken, and K. W. Schwarz, Phys. Rev. Lett. **53**, 1372 (1984).

[64] A. P. Finne, T. Araki, R. Blaauwgeers, V. B. Eltsov, N. B. Kopnin, M. Krusius, L. Skrbek, M. Tsubota, and G. E. Volovik, Nature (London) **424**, 1022 (2003).

[65] T. D. C. Bevan, A. J. Manninen, J. B. Cook, H. Alles, J. R. Hook, and H. E. Hall, J. Low Temp. Phys. **109**, 423 (1997).

[66] J. T. Tough, *Progress in Low Temperature Physics*, Vol. VIII (North-Holland, Amsterdam, 1982).

[67] http://dx.doi.org/10.17635/lancaster/researchdata/264.

A.3 Š. Midlik, D. Schmoranzer, L. Skrbek, Transition to quantum turbulence in oscillatory thermal counterflow of He-4, PRB 103 (2021)

Transition to quantum turbulence in oscillatory thermal counterflow of ^{4}He

Š. Midlik,* D. Schmoranzer, and L. Skrbek
Faculty of Mathematics and Physics, Charles University, Ke Karlovu 3, 121 16 Prague 2, Czech Republic

(Received 23 January 2021; revised 12 April 2021; accepted 13 April 2021; published 27 April 2021)

We report an experimental study of oscillatory thermal counterflow of superfluid ^{4}He and its transition to quantum turbulence inspired by the work of Kotsubo and Swift [Phys. Rev. Lett. **62**, 2604 (1989)]. We use a pair of transversally oriented second-sound sensors to provide direct proof that upon exceeding a critical heat flux, quantized vorticity is generated in the antinodes of the longitudinal resonances of the oscillating counterflow. Building on modern understanding of oscillatory flows of superfluid ^{4}He [D. Schmoranzer *et al.*, Phys. Rev. B **99**, 054511 (2019)], we re-evaluate the original data together with ours and provide grounds for the previously unexplained temperature dependence of critical velocities. Our analysis incorporates a classical flow instability in the normal component described by the dimensionless Donnelly number, which is shown to trigger quantum turbulence at temperatures below ≈ 1.7 K. This contrasts with the original interpretation based on the dynamics of quantized vortices, and we show that for oscillatory counterflow, such an approach is valid only at temperatures above ≈ 1.8 K. Finally, we demonstrate that the instabilities occurring in oscillatory counterflow are governed by the same underlying physics as those in flow due to submerged oscillators and propose a unified description of high Stokes number coflow and counterflow experiments.

DOI: 10.1103/PhysRevB.103.134516

I. INTRODUCTION

Quantum turbulence [1,2] in superfluid ^{4}He (He II) in the temperature range from $\approx$1 K to T_λ, where He II displays the two-fluid behavior, is easy to generate experimentally but challenging to understand in its entirety. In the frame of the two-fluid model, He II consists of two components: the viscous normal component of density ρ_n carrying all the entropy content of He II and the inviscid superfluid component of density ρ_s, with the total density $\rho = \rho_n + \rho_s$. This makes superfluid ^{4}He a complex system: One can expect an interplay of turbulent normal component of very low kinematic viscosity ν_n, obeying in some cases classical laws, and of inviscid superfluid component, behaving under quantum restrictions, with all rotational flow in the form of quantized vortices possessing angstrom-sized cores [3]. These line singularities, usually arranged in a complicated tangle, carry a single quantum of circulation $\kappa \cong 10^{-7}$ m^{2}s^{-1} each. Vortex lines mediate the interaction between the two components via a mutual friction force acting at all relevant length scales; moreover, any thermal gradient in He II generates thermal counterflow.

Various forms of quantum turbulence in He II can be generated using mechanical and thermal drives [4]. Classical-like mechanical forcing (e.g., by towing or oscillating a grid or any bluff body such as a wire or a quartz tuning fork) usually [4] results in a *coflow*, the closest analog to classical viscous flows, in which the normal fluid and superfluid components move, on average, with the same mean velocity in the same direction. By combining mechanical and thermal driving, the two components of He II can also be made to flow, on average, relative to each other [5], a situation called *counterflow*. The special case of counterflow with no net mass flow in the laboratory frame of reference called *thermal counterflow* is probably the most frequently investigated quantum flow since the pioneering experiments of Vinen [6]. In another special case called *pure superflow*, only a net flow of the superfluid component occurs in the experimental frame of reference, while the normal component remains statistically steady [7–9].

Additionally, as first shown by Kotsubo and Swift [10,11] and later by Chagovets [12], quantum turbulence can be generated in He II by applying a high-amplitude second sound in the longitudinal direction of a closed channel acting as a second-sound resonator. Here we present a similar experiment, however, with the addition of direct measurement of vortex line density, L, in the center of the resonator. Based on our results and subsequent analysis, taking into account experiments described in Refs. [10–12], we point out the close similarity of the underlying physics between quantum turbulence generated in an oscillating flow due to a bluff body [13,14] or U-tube oscillations [15] and by second sound, which involves a high Stokes number oscillatory flow of the normal component of He II in the resonator [16].

II. EXPERIMENTAL SETUP AND METHODS

The experimental volume of He II is contained in the 1-cm-wide brass channel of square cross section 3.2-cm long, a second-sound resonator, closed from both ends with brass plugs. We generate two different second-sound signals which we refer to as (i) longitudinal second sound, driven thermally at high amplitude along the longer dimension of the resonator,

*midliks@o365.cuni.cz

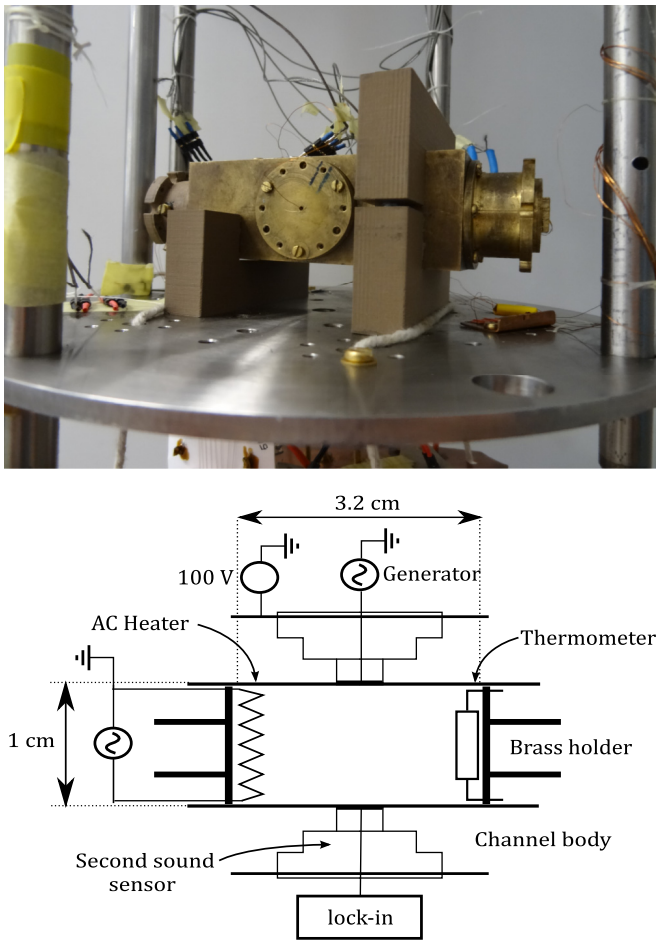

FIG. 1. Top: Photograph of the experimental brass cell with the transversal second-sound sensor holder on its front side and the heater and thermometer on the brass holders inserted from the left and right sides. Bottom: Schematic of the experimental cell arrangement. Longitudinal second-sound signal is generated by the resistive heater, forming a standing wave along the resonator, and probed by the sensitive resistance thermometer placed at the opposite end. Transversal second-sound signal is driven in the middle of the resonator perpendicularly to its length by one of two capacitive sensors acting as a generator with the opposing one used as a detector.

which is used for generation of quantized vorticity; and (ii) transversal (or detection) second sound, driven at low amplitude mechanically across the center of the resonator. A schematic view of the experiment is shown together with a photograph of the setup in Fig. 1.

The longitudinal second sound is driven by a flat heater of resistance $R \approx 50\ \Omega$. It is made of a manganine wire and glued to one of the brass plugs at one end of the resonator. The applied ac voltage $U = U_0 \cos(\omega t)$ of angular frequency ω and amplitude U_0 results in radiation of a heat flux $\dot{q}$ at 2ω. In a channel of constant cross section, A_s, the time-dependent heat flux is formally given as

$$\dot{q} = \dot{q}_{\rm dc} + \dot{q}_{\rm ac}\cos(2\omega t) = \frac{U_0^2}{2RA_s}[1 + \cos(2\omega t)], \qquad (1)$$

resulting in radiation of (i) the ac temperature wave and (ii) the dc heat flux. The net dc heat flux is carried away from the heater by the normal component of He II and causes steady thermal counterflow of some form, which we discuss in Sec. IV.

In a conventional counterflow channel of constant cross section, with one end open to the helium bath, from the conservation of energy, the counterflow velocity is found as

$$v_{\rm CF} = \frac{\dot{q}_{\rm dc}}{ST\rho_s}, \qquad (2)$$

where $\dot{q}_{\rm dc}$ is the applied heat flux (power per unit area) and S and T denote, respectively, the specific entropy and the temperature of He II. The dc heat flux might generate quantized vorticity. This happens above the critical counterflow velocity v_0; the intensity of generated quantized vorticity is characterized by vortex line density, L, which follows the experimentally established [6] power law scaling,

$$L - L_0 = \gamma^2(T)(v_{\rm CF} - v_0)^2, \qquad (3)$$

where L_0 corresponds to the remnant vortex line density [17]. The dimensional coefficient $\gamma(T)$ (for the so-called T II state of thermal counterflow in relatively wide channels) has been experimentally established with about 20% accuracy [7].

The generated longitudinal second sound is detected by a semiconductor-based Ge/GaAs Microsensor TTR − G thermometer [18–20] biased with a constant current of 1 μA, placed on the brass plug closing the opposite side of the resonator. The thermometer signal is measured using a Stanford SR830 lock-in amplifier at the expected frequency ω/π, i.e., at double frequency of the driving voltage. Under the assumption of linear damping of the second-sound wave, the maximum counterflow velocity reached in the antinodes of the second-sound wave is given by a similar equation as for steady counterflow, Eq. (2), enhanced by the quality factor Q of the second-sound resonator.

For the detection of quantum turbulence, we have built and further improved the traditional capacitive sensors; for details of their construction and readout method see Refs. [8,21] and references therein. In short, two identical sensors, serving as a transducer and receiver, are constructed from a 10-μm-thick nuclepore membrane, coated on one side with a 30- to 60-nm-thick layer of gold. It is stretched across a circular Delrin holder 1 cm in diameter and lightly pressed against a brass electrode. Its gold-plated side and the electrode constitute a parallel-plate capacitor of typically 30 to 100 pF. The two sensors face each other across the resonator in the middle of its length (see Fig. 1), one being driven by an ac voltage superimposed on a high dc bias of 100 V, while the voltage signal from the other sensor is read using a lock-in amplifier. Assuming a random vortex tangle, homogeneous across the width of the channel, the vortex line density in the probed volume is then obtained from the level of attenuation of the standing transversal second-sound wave as

$$L = \frac{6\pi\Delta f}{\kappa B}\left(\frac{A}{A_0} - 1\right), \qquad (4)$$

where Δf and A_0 are the full width (FWHM) and the amplitude of the second-sound signal measured without the application of the longitudinal drive, A is the amplitude of the attenuated signal, κ is the circulation quantum, and B is the tabulated [22] mutual friction coefficient. We note that Eq. (4)

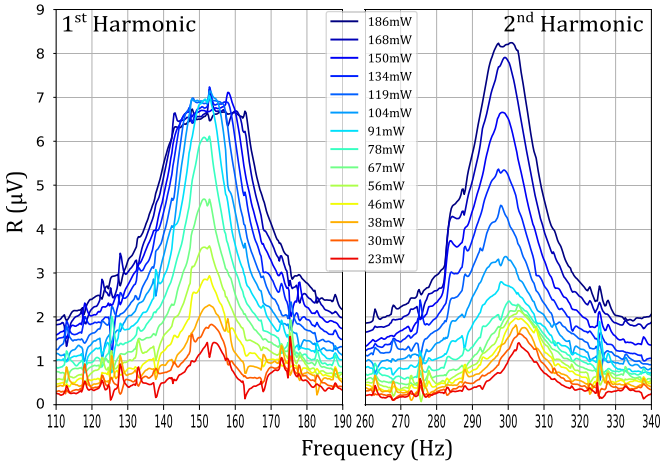

FIG. 2. The amplitudes of first two resonant modes of longitudinal second sound measured at 1.65 K and plotted against the frequency of the ac driving voltage supplied to the heater. The crossover between two different peak shapes is displayed: (i) Lorentzian shape in the linear damping regime and (ii) flattened-top shape caused by the generation of additional quantized vorticity by the high-amplitude second-sound wave.

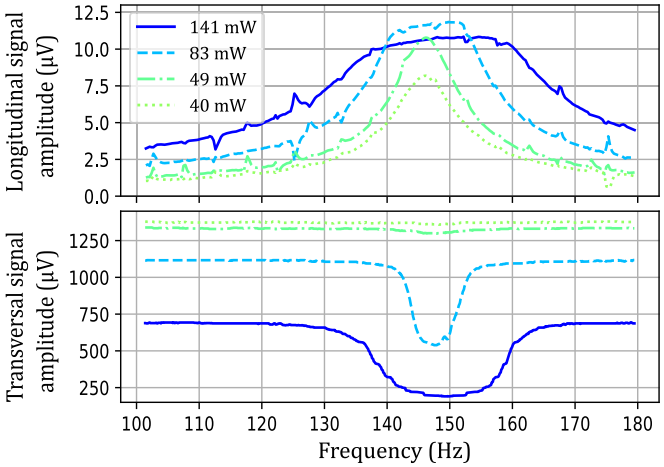

FIG. 3. Top: Selected frequency sweeps of the first harmonic mode at 1.45 K. Bottom: The simultaneously measured resonant amplitude of transversal second-sound wave propagating perpendicularly across the center of the resonator. The attenuation of the transversal signal clearly corresponds to the saturation part of the longitudinal amplitude, proving the generation of quantized vorticity in the superfluid component. In both panels, the horizontal axis represents the frequency of the voltage supplied to the heater.

was derived for moderate values of L not requiring screening corrections (for details, see Refs. [8,21]); the calculated L values may therefore differ from reality by up to ≈30%.

III. EXPERIMENTAL RESULTS

Figure 2 shows the voltage amplitude across the calibrated temperature sensor [18–20] during frequency sweeps across the resonances for the first two longitudinal resonances measured at 1.65 K for various heater powers. In agreement with previous results of Kotsubo and Swift [10,11] and Chagovets [12], we observe a crossover between two distinctly different shapes of the longitudinal second-sound resonances. At low drives, the Lorentzian shape of the resonances with the amplitude directly proportional to the driving power indicates a linear damping regime. Upon increasing the drive, the shape changes, resulting in flat-top peaks above some critical amplitude, as a new, nonlinear dissipation mechanism sets in. In accord with Refs. [10,11], as the power is increased further, the flattened peaks become broader and overall dissipation increases as well, while the level of the flattened top remains approximately constant. This is a signature of turbulent flow in the resonator, as quantized vortices are generated above the critical amplitude, over an increasingly wider frequency range around the resonance. This behavior appears qualitatively similar when measured at 1.45 K and 1.83 K.

Our experimental setup allows us to present direct proof of quantum vortex generation in oscillatory counterflow by simultaneously tracking the in-phase amplitude of a weakly driven transversal resonant second-sound wave. This is shown in Fig. 3 for a few selected heater powers driving the first longitudinal harmonic mode, in both linear and nonlinear damping regimes at 1.45 K. The true tracking of the transversal second-sound resonance is secured via a procedure described in detail in Refs. [21,23]. The attenuation of the transversal wave due to additional quantized vorticity in the resonator clearly corresponds to the amplitude saturation of the longitudinal signal.

Figure 4 compares the evolution of the peak amplitude of the longitudinal signal with the vortex line density L in the center of the resonator calculated using Eq. (4) at 1.45 K as a function of the applied heater power. The top panel shows

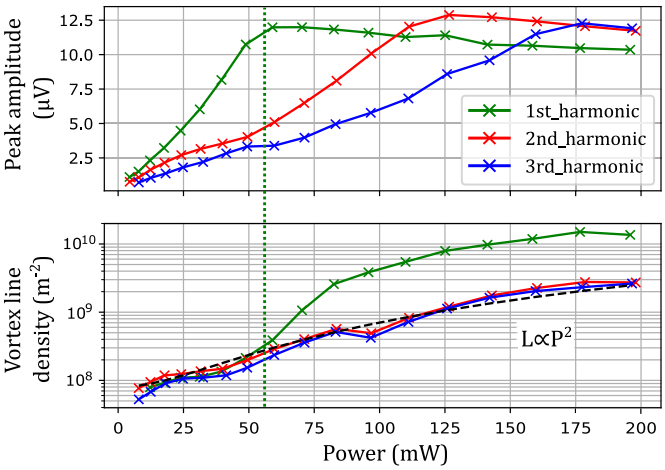

FIG. 4. Top: Power evolution of the peak amplitude of longitudinal second sound for first three modes at 1.45 K. Amplitude saturation implies the generation of quantized vorticity by the ac counterflow. Bottom: The corresponding vortex line density, L, measured in the center of the channel. The black dashed line represents the power law $L \propto P^2$, for vorticity originating from the dc counterflow alone. The green vertical dotted line indicates the critical power for the first mode, where both signals show generation of quantized vortices in the antinode of the longitudinal resonance. The lack of observation of any additional vortex line density for the second mode confirms the antinodal localization of vortex generation.

TABLE I. Critical values of heat flux for turbulent transition in oscillatory counterflow for different harmonic modes, estimated at three temperatures.

Harmonic mode	T K	$\dot{q}_{\mathrm{crit}}$ mW/cm^2
	1.45	55
First	1.65	85
	1.83	115
	1.45	120
Second	1.65	195
	1.83	–
	1.45	175
Third	1.65	–
	1.83	–

similar behavior for all three harmonic modes: the peak amplitude rises approximately linearly with the heating power and then saturates. The critical power values, for which the amplitude saturation occurs, have been found for all presented harmonic modes at 1.45 K. For experimental reasons, it was not possible to reach saturation with all modes at higher temperatures 1.65 K and 1.83 K. The observation is also partially masked by a rather strong background vortex line density due to the dc counterflow carrying the applied power in the resonator to the surrounding helium bath. The frequency dependence of the critical power is clearly seen; we shall discuss it in the next section.

All estimated values of critical heater power determined from the onset of saturation of amplitude of the longitudinal signal are shown in Table I. Note that critical conditions for turbulent transition were not reached for all cases, as the same heating power generates lower counterflow velocity at temperatures of 1.65 K and 1.83 K than at 1.45 K, in accord with Eq. (2).

IV. DISCUSSION

First, let us discuss possible caveats and experimental difficulties. The analysis of our data described above must be treated as semiquantitative for the following reason. While generating the steady-state quantum turbulence, we continuously apply heat typically of order 0.1 W to the He II sample inside the resonator, which must be carried to the surrounding helium bath. Our resonator is made of brass with walls about 1 cm thick. Assuming that the applied heat is conducted via brass walls, a simple estimate would lead to a temperature difference of order 1 K between the He II sample in the resonator and the helium bath, about three orders of magnitude higher than what is experimentally observed. For evidence, see, e.g., Fig. 2 which shows only a slight shift of the resonance frequency of the measured second-sound harmonics with the applied heat flux—the position of resonance would have followed the changes of the second-sound velocity with the increasing temperature of He II inside the resonator. We are therefore led to conclude that the applied heat is carried away from the He II sample in the resonator by a much more efficient mechanism—thermal counterflow, specifically by the normal component carrying the entropy through gaps between the brass plugs, second-sound sensors, and the brass body of the resonator.

It is difficult to characterize the geometry of such counterflow in our experiment as well as in the experiments cited above and to judge how much these thermally driven flows affect our considerations below. We attempted to compensate the steady heat flux supplied by the heater, Eq. (1), by the same steady heat flux from an additional heater placed at the opposite end of the resonator. This, however, resulted in an increase of attenuation of the transverse second sound, indicating an increase of effective vortex line density in the center of the resonator. This suggests that a significant part of the heat exits the resonator via gaps adjacent to the second-sound sensors rather than via gaps between the brass plugs and the body of the resonator at its ends. We therefore treat the vortex line density in the center of the resonator generated at frequencies of longitudinal second-sound resonances simply as a heat flux-dependent background. Bearing in mind this caveat, we now attempt to determine the peak counterflow velocity of the studied oscillatory counterflow that corresponds to the applied ac heat flux.

A. Determination of critical velocity

Two different approaches may be employed. The first one is based on the idea that the peak counterflow velocity $v^I_{ns,\mathrm{ac}}$ (i.e., its antinodal amplitude) is the same as that in the dc case [given by Eq. (2)] but resonantly enhanced by the quality factor Q, found to be of order 10:

$$v^{\mathrm{I}}_{ns,\mathrm{ac}} = Q\frac{\dot{q}_{\mathrm{ac}}}{ST\rho_s}. \tag{5}$$

We stress that this approach is valid only in the linear damping regime, when the observed resonances are of Lorentzian shape. In the turbulent regime, further increase of the peak counterflow velocity is suppressed by the action of the mutual friction force.

The second and perhaps more straightforward way to determine the peak velocity is based on the direct measurement of the magnitude of the temperature variations δT in the resonator. The same approach was used by Kotsubo and Swift [10,11], who assumed a harmonic time dependence and spatial profile of the resonant standing wave. Following the same reasoning that leads to Eq. (13) in Ref. [11], we find the peak oscillatory counterflow velocity as

$$v^{\mathrm{II}}_{ns,\mathrm{ac}} = \frac{\rho S}{u_2\rho_n}\delta T, \tag{6}$$

where u_2 stands for the second-sound velocity. The amplitude of the temperature oscillations δT can be determined from the ac voltage measured across the calibrated resistive thermometer biased by a constant current. The velocity determined in this manner should hold over the entire range of applied heat fluxes, as it is calculated from experimentally observed quantities.

On the other hand, discrepancies between the determined values of $v^{\mathrm{I}}_{ns,\mathrm{ac}}$ and $v^{\mathrm{II}}_{ns,\mathrm{ac}}$ in the subcritical region and observation of an additional phase shift, which both occurred for higher harmonics, suggest that either the thermal inertia together with the Kapitza resistance at the heater or the

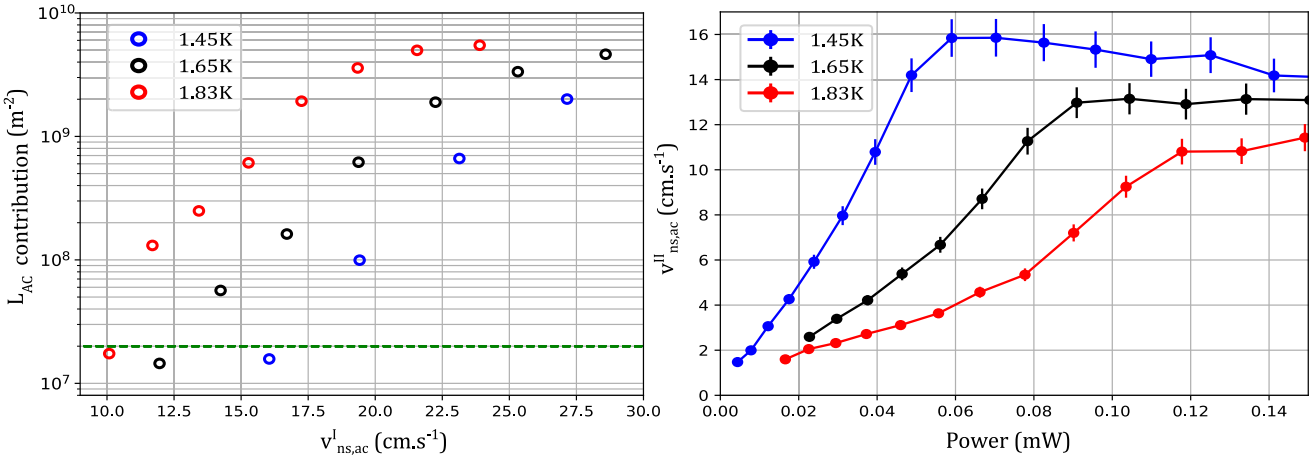

FIG. 5. Left: Contribution to vortex line density due to oscillatory counterflow (difference of values observed for first and second modes), plotted as a function of the velocity $v^{\mathrm{I}}_{ns,\mathrm{ac}}$. The rapid increase of vortex line density above the noise level (highlighted by the green dashed line) indicates the position of the critical velocity. Right: Oscillatory counterflow velocity $v^{\mathrm{II}}_{ns,\mathrm{ac}}$ obtained from the amplitudes of longitudinal resonances via Eq. (6) plotted as a function of heating power. The onset of saturation of $v^{\mathrm{II}}_{ns,\mathrm{ac}}$ determines the critical velocity. The error bars represent the fluctuations of the bias current supplied to the thermometer.

thermalization time constant of the used thermometer may affect the measurements at frequencies higher than the first fundamental mode, and thus may influence the temperature wave amplitude reading as well as the actual, slightly smoothed, heat flux amplitude delivered to the liquid which may be lower than Eq. (1) suggests. Indeed, the values of the critical heat flux amplitude measured at $T = 1.45$ K for first three harmonics, given in Table I, grow somewhat faster than with the square root of frequency, predicted for both classical [24] and quantum [25–27] oscillatory flows. For these reasons, we have limited deduction of critical oscillatory counterflow velocities for further quantitative analysis to the data measured using the first harmonic mode, where good agreement is obtained in the linear damping regime for both methods of determination of the peak counterflow velocity.

Let us now discuss the critical velocities determined by these two different approaches. In the left panel of Fig. 5, we plot the difference of vortex line density measured for the first harmonic mode (containing both ac and dc contributions) and second harmonic mode (giving the dc contribution only) as a function of $v^{\mathrm{I}}_{ns,\mathrm{ac}}$. The critical velocity can be determined from the onset of vortex line density (above the noise level, taken as 10% of the background due to dc counterflow near the critical power) and must be directly connected to a transition in the oscillatory counterflow accompanied by a rapid increase of quantized vortex generation. The second approach, via directly measured temperature oscillations in the channel, leads to the values of $v^{\mathrm{II}}_{ns,\mathrm{ac}}$, see the right panel of Fig. 5 showing the counterflow velocity obtained from the amplitudes of longitudinal resonances as a function of heater power. The saturation of this velocity marks the same transition as above and, moreover, indicates the longitudinal resonance as the energy supply for the additional vorticity, see also Refs. [10–12]. The critical velocities are listed below in Table II, showing quantitative agreement of the two approaches. In both cases, we estimate the uncertainty to be of order 1 cm/s, caused by the subjectivity of noise level determination and/or thermometer bias current fluctuations.

B. Comparison with other experiments

With these data at hand, we may turn to the broader discussion of the transition to quantum turbulence in various oscillatory He II flows generated mechanically, thermally, and by second sound in the frame of the two-fluid model.

Historically, the two-fluid model description of independent and coupled oscillatory flows of the normal and superfluid components was already considered by Donnelly and Penrose [15] in 1956 in an attempt to explain the experimentally observed crossover between two regimes of U-tube oscillations. Although the notion of quantized vortices and their role for the mutual friction force was not yet widely appreciated, their approach was capable of formally explaining the existence of the two observed decay regimes, assuming that at low velocity the two fluids move independently and their motion becomes gradually coupled upon reaching some critical velocity and eventually they move as a single fluid, i.e., in coflow. The length scale relevant to the (uncoupled) normal flow is the viscous penetration depth $\delta_n = \sqrt{2\eta/\rho_n\omega} \approx 70 - 200\ \mu$m, where η is the dynamic viscosity. This scale is significantly smaller than the diameter of the U tubes ($\approx$1 cm); we therefore deal with flows of high Stokes number, defined as $\mathrm{St} = D^2/(\pi\delta_n^2)$, similarly to the counterflow experiments presented here.

TABLE II. Critical oscillatory counterflow velocities and corresponding critical Donnelly numbers obtained by two different approaches for all studied temperatures. See the text for details.

T K	Critical $v^{\mathrm{I}}_{ns,\mathrm{ac}}$ cm/s	$\mathrm{Dn}^{\mathrm{I}}_{\mathrm{cr}}$	Critical $v^{\mathrm{II}}_{ns,\mathrm{ac}}$ cm/s	$\mathrm{Dn}^{\mathrm{II}}_{\mathrm{cr}}$
1.45	17	15.6	16	14.7
1.65	12.5	15.3	13	15.9
1.83	10	13.2	11	14.5

1. Normal fluid critical velocity

Dynamical similarity and instabilities in high-Stokes-number oscillatory flows of He II have recently been studied by Schmoranzer *et al.* [16]. It was shown, based on systematic measurements of oscillatory He II flows due to various oscillators, that an instability leading to the turbulent transition can occur either in the normal or in the superfluid component of He II. For low velocities, only viscous drag is offered by the normal fluid, obeying a universal scaling law in terms of the suitably defined drag coefficient and the Donnelly number (boundary-layer-based Reynolds number), defined as

$$\mathrm{Dn} = \delta_n v_n / \nu_n, \tag{7}$$

where v_n is the amplitude of normal fluid velocity. Upon exceeding a certain critical value of the Donnelly number, $\mathrm{Dn}_{\mathrm{cr}}$, the normal component undergoes a classical-like transition, also subsequently triggering the generation of quantized vortices in the superfluid component. The corresponding critical velocity of the normal component is denoted as $v_{n,\mathrm{cr}}$.

2. Superfluid critical velocity

Even without the classical-like instability occurring as discussed above, quantized vorticity in the superfluid component may become generated via the Donnelly-Glaberson instability [28–30] at a dimensionless critical velocity $\hat{v}_{s,\mathrm{cr}} = v_{s,\mathrm{cr}}/\sqrt{\kappa\omega}$, where $v_{s,\mathrm{cr}}$ is the dimensional superfluid critical velocity. Indeed, Hänninen and Schoepe [26,27] have argued that the onset of quantum turbulence in oscillatory flows of superfluid helium is universal, and can be derived from a general argument based on the "superfluid Reynolds number". The critical velocity scales as $v_{s,\mathrm{cr}} \propto \sqrt{\kappa\omega}$ with only the numerical prefactor depending somewhat on the geometry of the oscillating object because the flow velocity near the surface of the object may differ from the velocity amplitude of the body. A more detailed analysis derived from the dynamics of the turbulent state gives the criterion [27]

$$v_{s,\mathrm{cr}} \approx \sqrt{8\kappa\omega/\beta}, \tag{8}$$

where the numerical factor β is about unity and depends on the mutual friction parameters.

Hänninen and Schoepe [26] evaluated β for several temperatures: $\beta = 1$ below 1 K, $\beta = 0.95$ (at 1.3 K), 0.89 (at 1.6 K), and 0.79 (at 1.9 K); which implies a slow *increase* of v_c by about 10% and gives fair agreement with experimental results obtained over a wide temperature range from below 0.4 K up to 1.9 K with a sphere 100 μm in diameter oscillating at 236 Hz, as displayed in Fig. 3 of Ref. [26].

It must be noted that virtually the same approach was used to analyze the turbulent instability in oscillatory counterflow in Refs. [10–12] without any consideration of a possible classical-like instability in the normal component. This resulted in the observation of a strong and systematic temperature dependence of superfluid critical velocities that the employed dynamical scaling theory could not explain [10,11], as the temperature dependence of β in Eq. (8) is too weak to account for critical velocities differing by a factor of 4 (see, e.g., Fig. 4 in Ref. [10]).

3. Interplay of the two instabilities

Which instability, i.e., either classical hydrodynamic instability of laminar flow of the normal component upon reaching a critical velocity $v_{n,\mathrm{cr}}$ or Donnelly-Glaberson instability in the superfluid component upon reaching $v_{s,\mathrm{cr}}$ occurs first depends both on the geometry of the oscillator and on the temperature, which determines the dynamic viscosity of He II and the densities of the two components. A crossover between the two outlined mechanisms of turbulence generation is possible and has indeed been observed in flows due to mechanical oscillators [16].

A similar approach may be applied to oscillatory counterflow, with one distinction. In experiments on flow due to mechanical resonators, the comparison of the two criteria for the transition is straightforward, as in coflow, the velocities of the normal and superfluid components are practically identical. However, in counterflow $v_n \neq v_s$, hence a common dimensionless parameter must be found for both types of instability to facilitate such a comparison. For this purpose, the superfluid critical velocity $v_{s,\mathrm{cr}}$ may be converted to an effective critical Donnelly number $\mathrm{Dn}_{\mathrm{cr,eff}}$ using

$$\mathrm{Dn}_{cr,\mathrm{eff}} = \frac{\delta_n v_{s,\mathrm{cr}} \rho_s}{\rho_n v_n}. \tag{9}$$

This is the same formal definition of $\mathrm{Dn}_{\mathrm{cr}}$ as given below Eq. (7), with the critical normal fluid velocity formally expressed as $v_{n,\mathrm{cr}} = \rho_s/\rho_n v_{s,\mathrm{cr}}$, i.e., as the peak normal fluid velocity in the oscillating thermal counterflow at the very first occurrence of the Donnelly-Glaberson instability in the superfluid component oscillating with the critical velocity $v_{s,\mathrm{cr}}$.

Unlike the true critical Donnelly number describing the classical instability $\mathrm{Dn}_{\mathrm{cr}}$, the critical value of $\mathrm{Dn}_{\mathrm{cr,eff}}$ is no longer expected to be constant. On the contrary, requiring a constant value of the correct critical parameter, $\hat{v}_{s,\mathrm{cr}}$, also requires $\mathrm{Dn}_{cr,\mathrm{eff}}$ to be a function of temperature. However, $\mathrm{Dn}_{\mathrm{cr,eff}}$ will be independent of the frequency of oscillations, as both $v_{n,\mathrm{cr}}$ and $v_{s,\mathrm{cr}}$ have the same frequency dependence, with either critical velocity $\propto \sqrt{f}$.

We stress that, assuming no or perhaps a very low number of remnant quantized vortices at low flow velocities, this classical-like instability is not affected by the potential flow of the superfluid component; as mutual friction is nearly absent. This allows us to apply the described model to oscillatory coflows as well as counterflows and in particular to the experiments discussed here.

First, using our data, we have described two different approaches to determine critical counterflow velocities $v^{\mathrm{I}}_{ns,\mathrm{ac}}$ and $v^{\mathrm{II}}_{ns,\mathrm{ac}}$. Requiring zero net mass flow, we can calculate the corresponding peak critical velocities of the oscillating normal fluid. Application of a no-slip boundary condition then leads to critical Donnelly numbers $\mathrm{Dn}^{\mathrm{I}}_{\mathrm{cr}}$ and $\mathrm{Dn}^{\mathrm{II}}_{\mathrm{cr}}$, also given in Table II. We note that for this calculation we naturally use the frequency of the longitudinal second sound, i.e., twice the frequency of the applied oscillatory heat flux. Over the temperature range 1.45–1.83 K (where the normal fluid density changes about five times) the critical Donnelly numbers are approximately constant $\mathrm{Dn}^{\mathrm{I}}_{\mathrm{cr}} \cong \mathrm{Dn}^{\mathrm{II}}_{\mathrm{cr}} \cong 15 \pm 2$, providing a good quantitative characterization of the turbulent instability.

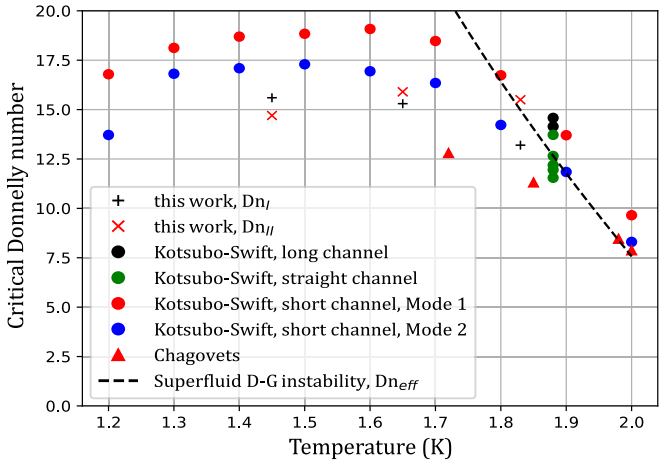

FIG. 6. Temperature dependence of the critical Donnelly number for oscillatory thermal counterflow as determined from this work and the experiments of Kotsubo and Swift [10,11] and Chagovets [12]. The dashed line represents an effective Donnelly number calculated for the instability based on the Hänninen-Schoepe criterion, Eqs. (8) and (9).

Second, we calculate critical Donnelly numbers based on the data measured for mechanically generated ac counterflow of He II at 1.88 K by Kotsubo and Swift, $\mathrm{Dn}_{\mathrm{cr}}^{\mathrm{KS}}$, based on Fig. 5 of Ref. [11], showing critical counterflow velocities from the first two modes in their long resonator and the first five modes in their straight resonator, covering more than a decade of second-sound frequencies. All values of critical Donnelly numbers obtained at this temperature fall within a narrow interval $\mathrm{Dn}_{\mathrm{cr}}^{\mathrm{KS}} = 13 \pm 2$, in fair agreement with our measurements. Furthermore, we have used Fig. 6 of Ref. [11], displaying the scaled temperature dependence of the critical velocities from the first two modes measured in their short resonator. The calculated critical Donnelly numbers are shown in Fig. 6, appearing approximately constant between 1.2 K and 1.7 K, $\mathrm{Dn}_{\mathrm{cr}}^{\mathrm{KS}} \cong 17 \pm 2$, with a pronounced decreasing tendency at higher temperatures.

Finally, we may compare with the critical Donnelly numbers $\mathrm{Dn}_{\mathrm{cr}}^{\mathrm{Ch}}$ for thermally generated ac counterflow of He II estimated using the data measured by Chagovets in an epoxy cylindrical resonator of diameter 7 mm, 3.5 cm long, at four temperatures between 1.72 K and 2.0 K, specifically the data series shown in Fig. 2 of Ref. [12]. For example, at $T = 1.85$ K we estimate the saturated amplitude of the temperature oscillations $\delta T \approx 0.8$ mK that starts to flatten upon reaching about 32 mW/cm^2 of applied heat flux, and the fundamental resonant frequency of second sound $f = 197$ Hz. Similarly, we read the available data for 1.72, 1.98, and 2.0 K and, using the known temperature dependence of the second-sound velocity, we calculate the relevant frequencies of the fundamental mode at these temperatures. These data, together with tabulated values of He II properties [22] allow us to calculate, using Eq. (6), the velocity $v_{ns,\mathrm{ac}}^{\mathrm{II}}$ and, subsequently, the critical Donnelly number $\mathrm{Dn}_{\mathrm{cr}}^{\mathrm{Ch}}$, also shown in Fig. 6.

It is remarkable that, within the experimental accuracy, in the temperature range from 1.2 K to 1.7 K, three different experiments: (i) mechanically driven second sound [10,11], (ii) thermally driven counterflow by Chagovets [12], as well as (iii) our own display the onset of the transition to quantum turbulence characterized by the same critical Donnelly number $\mathrm{Dn}_{\mathrm{cr}} \approx 16 \pm 3$. This strongly suggests that the transition is triggered when the instability in oscillatory laminar flow of the viscous normal component of He II is reached. In the given temperature range, the transition thus cannot be described by the dynamical scaling theory used in Refs. [10,11], which deals solely with superfluid instabilities.

However, the data of Refs. [11,12] show a departure from this value of $\mathrm{Dn}_{\mathrm{cr}}$ as the temperature is increased above ≈ 1.8 K, which is fully explained by the instability in the superfluid component–production of quantized vorticity by means of the Donnelly-Glaberson mechanism. The data are summarized in Fig. 6, where the effective Donnelly number, $\mathrm{Dn}_{\mathrm{eff}}$, for this instability is shown, as calculated based on Eqs. (9) and (8). Hence, we clearly observe a crossover of two different mechanisms of turbulence generation in oscillatory counterflow: one related to a classical instability of the normal fluid dominating at lower temperatures in the two-fluid regime, while the other is purely a consequence of quantized vortex dynamics in the superfluid component and dominates at higher temperatures.

It is interesting to note that oscillating coflow, e.g., due to a quartz tuning fork [16], is similar in that it displays the same general crossover between these two mechanisms. However, the respective temperature intervals are inverted—the classical instability dominates closer to the lambda point and the superfluid one at lower temperatures. It is naturally understood that the behavior of oscillating thermal counterflow is different in this sense, as the equation of continuity requires that $v_s/v_n = \rho_n/\rho_s$, making it likely that the superfluid critical velocity is reached first when the ratio ρ_n/ρ_s is large.

C. Applicability of the obtained results

We have to emphasize that the above hydrodynamic approach is applicable only in the temperature range where superfluid ^{4}He displays the two-fluid behavior. On lowering the temperature below 1 K, the mean-free path of phonons grows and soon becomes greater than the size of the system and, in the $T \to 0$ limit, only the superfluid component exists, hence the very concept of thermal counterflow becomes poorly defined. Still, transition to quantum turbulence occurs in a variety of oscillatory flows, displaying interesting features such as multiple critical velocities [31,32] and hysteretic [33–35] or switching phenomena [36,37]; for reviews, see Refs. [13,14] and references therein. These features fall outside the scope of this paper.

V. CONCLUSIONS

We have presented experimental work on thermally generated oscillatory counterflow in a closed square-cylinder-shaped second-sound resonator, and directly proven generation of quantized vortices in the antinode of the fundamental longitudinal standing wave using the second-sound attenuation technique.

Comparison with studies of oscillatory flows due to mechanical resonators in ^{4}He [16] and previous thermally and mechanically driven second-sound experiments [10–12] reveal that the instabilities marking the turbulent transition in all these flows are of the same type. Namely, (i) a classical-like instability in the flow of the viscous normal component occurring upon reaching the critical Donnelly number $\mathrm{Dn}_{\mathrm{cr}}$ and (ii) the Donnelly-Glaberson instability in the superfluid component leading to vortex multiplication due to self-reconnections.

A crossover between these two mechanisms is observed, while the temperature is varied across the interval corresponding to the two-fluid regime. This strongly suggests, perhaps surprisingly, that transition to turbulence in oscillatory coflow and counterflow is governed by the same underlying physics, although the crossover occurs in the opposite direction for counterflow than for coflow.

We have also shown that the Hänninen and Schoepe criterion for critical superfluid velocity [26,27] (relationship 8) and similar approaches based on quantized vortex dynamics cannot be considered universal in the two-fluid regime, as instabilities of the normal fluid flow are not taken into account. On the other hand, these same criteria remain useful for the description of the superfluid instability and recover universality at very low temperatures, where the two-fluid model is no longer applicable. However, in the two-fluid regime above $\approx$1 K, they must be complemented by a suitable description of the classical-like instabilities of the normal component.

It remains to be seen how the present analysis extends into dc counterflow experiments and how the two described instabilities relate to the T-I and T-II turbulent states observed by Tough [7], and we hope that our work stimulates further research into this area.

ACKNOWLEDGMENTS

The authors appreciate the help of E. Varga at the early stage of the experiments and acknowledge the support by the Czech Science Foundation under Project No. GAČR 20-00918S.

[1] C. F. Barenghi, L. Skrbek, and K. R. Sreenivasan, Introduction to quantum turbulence, Proc. Natl. Acad. Sci. U.S.A. **111**, 4647 (2014).

[2] W. F. Vinen and J. J. Niemela, Quantum turbulence, J. Low Temp. Phys. **128**, 167 (2002).

[3] R. J. Donnelly, *Quantized Vortices in Helium II* (Cambridge University Press, Cambridge, 1991).

[4] L. Skrbek, D. Schmoranzer, Š. Midlik, and K. R. Sreenivasan, Phenomenology of quantum turbulence in superfluid helium, Proc. Natl. Acad. Sci. U.S.A. **118**, e2018406118 (2021).

[5] M. L. Baehr and J. T. Tough, Critical Velocity in Two-Fluid Flow of He II, Phys. Rev. Lett. **53**, 1669 (1984).

[6] W. F. Vinen, Mutual friction in a heat current in liquid helium II, I. Experiments on steady heat currents, Proc. R. Soc. London A **240**, 114 (1957); II. Experiments on transient effects, **240**, 128 (1957); III. Theory of the mutual friction, **242**, 493 (1957); IV. Critical heat currents in wide channels, **243**, 400 (1958).

[7] J. T. Tough, *Superfluid turbulence*, in Progress in low temperature physics (North-Holland Publishing Co., Amsterdam, 1982), Vol. VIII.

[8] S. Babuin, M. Stammeier, E. Varga, M. Rotter, and L. Skrbek, Quantum turbulence of bellows-driven ^{4}He superflow: Steady state, Phys. Rev. B **86**, 134515 (2012).

[9] S. Babuin, E. Varga, W. F. Vinen, and L. Skrbek, Quantum turbulence of bellows-driven ^{4}He superflow: Decay, Phys. Rev. B **92**, 184503 (2015).

[10] V. Kotsubo and G. W. Swift, Vortex Turbulence Generated by Second Sound in Superfluid ^{4}He, Phys. Rev. Lett. **62**, 2604 (1989).

[11] V. Kotsubo and G. W. Swift, Generation of superfluid vortex turbulence by high-amplitude second sound in ^{4}He, J. Low Temp. Phys. **78**, 351 (1990).

[12] T. V. Chagovets, Electric response in superfluid helium, Physica B **488**, 62 (2016).

[13] L. Skrbek and W. F. Vinen, The use of vibrating structures in the study of quantum turbulence, in *Progress in Low Temperature Physics*, edited by M. Tsubota and W. P. Halperin (Elsevier, Amsterdam, 2009), Vol. XVI, Chap. 4.

[14] W. F. Vinen and L. Skrbek, Quantum turbulence generated by oscillating structures, Proc. Natl. Acad. Sci. U.S.A. **111**, 4699 (2014).

[15] R. J. Donnelly and O. Penrose, Oscillations of liquid helium in a U-tube, Phys. Rev. **103**, 1137 (1955).

[16] D. Schmoranzer, M. J. Jackson, Š. Midlik, M. Skyba, J. Bahyl, T. Skoknkov, V. Tsepelin, and L. Skrbek, Dynamical similarity and instabilities in high-Stokes-number oscillatory flows of superfluid helium, Phys. Rev. B **99**, 054511 (2019).

[17] D. D. Awschalom and K. W. Schwarz, Observation of a Remanent Vortex-Line Density in Superfluid Helium, Phys. Rev. Lett. **52**, 49 (1984).

[18] microsensor.com.ua

[19] V. F. Mitin, P. C. McDonald *et al.*, Ge-on-GaAs film resistance thermometers for cryogenic applications, Cryogenics **47**, 474 (2007).

[20] V. F. Mitin, V. V. Kholevchuk, and B. P. Kolodych, Ge-on-GaAs film resistance thermometers: Low-temperature conduction and magnetoresistance, Cryogenics **51**, 68 (2011).

[21] E. Varga, M. J. Jackson, D. Schmoranzer, and L. Skrbek, The use of second sound in investigations of quantum turbulence in He II, J. Low Temp. Phys. **197**, 130 (2019).

[22] R. J. Donnelly and C. F. Barenghi, The observed properties of liquid helium at the saturated vapor pressure, J. Phys. Chem. Ref. Data **27**, 1217 (1998).

[23] E. Varga, S. Babuin, V. S. Lvov, A. Pomyalov, and L. Skrbek, Transition to quantum turbulence and streamwise inhomogeneity of vortex tangle in thermal counterflow, J. Low Temp. Phys. **187**, 531 (2017).

[24] M. Blažková, D. Schmoranzer, and L. Skrbek, Transition from laminar to turbulent drag in flow due to a vibrating quartz fork, Phys. Rev. E **75**, 025302(R) (2007).

[25] M. Blažková, D. Schmoranzer, L. Skrbek, and W. F. Vinen, Generation of turbulence by vibrating forks and

other structures in superfluid ^{4}He, Phys. Rev. B **79**, 054522 (2009).

[26] R. Hänninen and W. Schoepe, Universal critical velocity for the onset of turbulence of oscillatory superfluid flow, J. Low Temp. Phys. **153**, 189 (2008).

[27] R. Hänninen and W. Schoepe, Universal onset of quantum turbulence in oscillating flows and crossover to steady flows, J. Low Temp. Phys. **158**, 410 (2010).

[28] D. K. Cheng, M. W. Cromar, and R. J. Donnelly, Influence of an Axial Heat Current on Negative-Ion Trapping in Rotating Helium II, Phys. Rev. Lett. **31**, 433 (1973).

[29] W. I. Glaberson, W. W. Johnson, and R. M. Ostermeier, Instability of a Vortex Array in He II, Phys. Rev. Lett. **33**, 1197 (1974).

[30] R. M. Ostermeier and W. I. Glaberson, Instability of vortex lines in the presence of axial normal fluid flow, J. Low Temp. Phys. **21**, 191 (1975).

[31] H. A. Nichol, L. Skrbek, P. C. Hendry, and P. V. E. McClintock, Flow of He II Due to an Oscillating Grid in the Low-Temperature Limit, Phys. Rev. Lett. **92**, 244501 (2004).

[32] D. Schmoranzer, M. J. Jackson, V. Tsepelin, M. Poole, A. J. Woods, M. Človečko, and L. Skrbek, Multiple critical velocities in oscillatory flow of superfluid ^{4}He due to quartz tuning forks, Phys. Rev. B **74**, 214503 (2006).

[33] J. Jger, B. Schuderer and W. Schoepe, Turbulent and Laminar Drag of Superfluid Helium on an Oscillating Microsphere, Phys. Rev. Lett. **74**, 566 (1995).

[34] D. Charalambous, L. Skrbek, P. C. Hendry, P. V. E. McClintock and W. F. Vinen, Experimental investigation of the dynamics of a vibrating grid in superfluid ^{4}He over a range of temperatures and pressures, Phys. Rev. E **74**, 036307 (2006).

[35] R. Goto, S. Fujiyama, H. Yano, Y. Nago, N. Hashimoto, K. Obara, O. Ishikawa, M. Tsubota, and T. Hata, Turbulence in Boundary Flow of Superfluid ^{4}He Triggered by Free Vortex Rings, Phys. Rev. Lett. **100**, 045301 (2008).

[36] M. Niemetz and W. Schoepe, Stability of laminar and turbulent flow of superfluid He-4 at mK temperatures around an oscillating microsphere, J. Low Temp. Phys. **135**, 447 (2004).

[37] N. Hashimoto, A. Handa, M. Nakagawa, K. Obara, H. Yano, O. Ishikawa, and T. Hata, Switching phenomena between laminar and turbulent flows of superfluid ^{4}He generated by a vibrating wire, J. Low Temp. Phys. **148**, 299 (2007).

A.4 Š. Midlik, M. Goleňa, M. Talíř, D. Schmoranzer, Vibrating micro-wire resonators used as local probes of quantum turbulence in superfluid 4He, Accepted for publication in JLTP, (2023)

Vibrating micro-wire resonators used as local probes of quantum turbulence in superfluid ^{4}He.

Šimon Midlik[1], Maximilián Goleňa[1], Marek Talíř[1] and David Schmoranzer[1*]

[1]Charles University, Faculty of Mathematics and Physics, Ke Karlovu 3, Prague, 121 16, Czech Republic.

*Corresponding author(s). E-mail(s): david.schmoranzer@mff.cuni.cz;

Abstract

We report the use of 60 μm thick superconducting NbTi vibrating wire resonator as a local probe of quantum turbulence in superfluid ^{4}He (He II). Wire resonance is driven via magneto-motive force, exclusively in laminar hydrodynamic regime. For the detection of quantized vortices, changes in the probe resonant frequency and peak amplitude are measured in reaction to the applied external counterflow. Calibration of the device response is obtained in thermal counterflow in the temperature range from 1.45 K to 2.1 K against second sound attenuation data. The main motivation of this work is the development of local probes of quantum turbulence suitable for use in non-homogeneous systems such as flows with spherical or cylindrical symmetry. The frequency response of the devices is described with good accuracy at lower temperatures by considering the balance between viscosity and mutual friction and its effect on the boundary layer. Under the experimental conditions, the fluid-structure interaction cannot be modeled reliably by an effective turbulent viscosity and agrees better with a model of the boundary layer modified by mutual friction. The obtained results may be extended to the interaction of nanoscale devices with sufficiently dense vortex tangles.

Keywords: Superfluid helium, Vibrating wire, Local probes, Quantum turbulence

1 Introduction

Following the discovery of superfluidity, this captivating phenomenon akin to superconductivity in solids inspired numerous scientists to devote their time and effort to its deeper study and continues to be an important part of low temperature physics research today. Soon after the first models of superfluid helium formulated by Landau and Tisza were tested experimentally with significant success, it became apparent that superfluids had yet another trick up their sleeve: *quantum turbulence*.

The existence of quantized vortices in superfluid helium, first suggested by Onsager and confirmed experimentally by Vinen [1] using vibrating wires in the superfluid phase of ^{4}He (He II), changed the situation dramatically. It became clear that new and more advanced models of superfluidity were required, while continually improved experimental techniques provided new insights. Today, the range of theoretical, numerical and experimental methods is quite certainly beyond the hopes of the founders of this field, yet many questions remain unanswered, and with more detailed understanding, new ones frequently emerge.

It is then perhaps no surprise that more than 60 years after Vinen's famous experiment [1], vibrating structures such as superconducting wires or their nanomechanical counterparts are still used in the research of quantum turbulence (QT). In this work, we return to some of the original questions – how do solid structures interact with a quantum-turbulent flow? Can a small vibrating device be used for local detection of a tangle of quantized vortices in He II?

Due to the two fluid character of He II, which consists of a normal viscous fluid and an inviscid superfluid component, we have to account for two types of turbulence rather than one: classical-like turbulent flow of normal component; and a very specific turbulent flow of superfluid component which consists only of quantized vortices — topological line defects with circulation $\kappa \approx 10^{-7}$ m^{2}s^{-1}. At temperatures between $\approx$1 K and 2.17 K, where the superfluid transition occurs, both types of turbulent flow may exist based on which flow experiences the first instability [2, 3], but typically soon after the transition, both forms of turbulence are present, as energy and momentum transfer between the two components is mediated by pressure or the mutual friction force.

While experimental detection of quantized vortices is generally quite challenging, many different techniques exist today. It is possible to directly visualize them with the use of frozen hydrogen particles illuminated by a laser sheet [4, 5, 6] or by helium excimers [7]. Second sound attenuation [8] represents a thoroughly tested technique allowing indirect quantification of the amount of quantized vortices, giving the average vortex line density, L, i.e., total length of vortex line per unit volume in the probed region. To allow the conversion of the second sound signal to L, typically, homogeneity and isotropy of the probed flows are assumed.

Recent numerical and experimental works discussing non-homogeneous tangles of quantized vortices generated in thermal counterflow in various

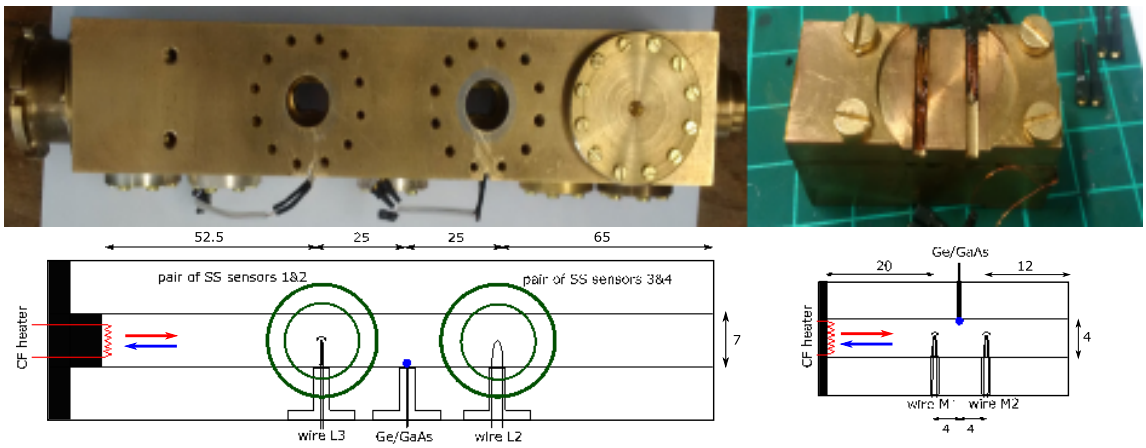

Fig. 1 Photographs of long and short channel assemblies together with their schematics. Left: Second sound ports in the long channel are displayed facing the viewer, while oscillators are installed from the bottom side. Permanent magnets are placed over the long channel assembly using separate plastic holders. Right: The circular cut-out in the short channel body serves for direct installation of permanent magnets with grooves provided for gluing vibrating wire leads.

geometries (oscillatory counterflow, cylindrically or spherically symmetric counterflow) [9, 10, 11, 3] showcased the need for new local detectors of QT. Local probes using second sound [12] represent a highly interesting choice, offering excellent spatial resolution and little or no parasitic effects, but limits are imposed on their sensitivity by the relatively lower resonance quality factor that can be obtained in an open geometry.

Vibrating wire resonators, in the form of superconducting NbTi loops, already proved as useful QT detectors close to 1 K and at sub-kelvin temperatures [13, 14], where the density of normal component of superfluid helium is negligible. Here, we report the use of 60 μm thick superconducting NbTi vibrating wire resonator, driven via the magneto-motive scheme exclusively in its laminar hydrodynamic regime. For the detection of quantized vortices, changes in its resonant frequency and amplitude in reaction to the applied external flow are analysed. The probes are tested and evaluated in well-understood system represented by thermal counterflow turbulence [15], with a pair of second sound sensors placed at the position of each probe, allowing their *in situ* characterization.

2 Experimental Method

All experiments were conducted in a helium bath cryostat with thermal PID temperature stabilization to the level of 1 mK. Bath temperature was measured with Microsensor TTR-G type [16] of Ge on GaAs film thermometer calibrated to saturated vapor pressure. Two brass channels were employed, each with a manganine resistive heater at its closed end, open to the bath on the other side, see Figure 1.

The first channel with inner square cross-section 7 mm $\times$ 7 mm and length of 167.5 mm included slots for both types of used QT detectors: second sound

Fig. 2 Photographs of the vibrating wire detectors installed on custom holders compatible with "long" channel (left) and "narrow" channel (right). The middle photograph shows a close-up view of a sample vibrating wire resonator.

capacitive sensors [8]; and vibrating wires. Vibrating wires were constructed from $d = 60$ μm thick bare NbTi wire in the shape of semicircular loop with leg spacing D of 3 mm (varnish and Cu matrix were stripped in HNO_3), and glued with 2850FT Stycast to a brass holder, see Figure 2. The wire holders were constructed in a way that the top of the loop was positioned close to the center of the flow channel, with 0.5 mm uncertainty. Pairs of sensors were installed at two different positions, 65 mm (for wire "L2" and sensors 3,4) and 115 mm (wire "L3" and sensors 1,2) from the channel inlet in such a manner that each vibrating wire was placed in a volume probed by the second sound sensors, see Figure 1. The wire L2 was oriented so that its plane was perpendicular to the counterflow direction while L3 was parallel. The resonant frequencies of the wires L2, L3 when immersed in superfluid helium were 6314 Hz and 5365 Hz, respectively, with a very small temperature-dependent variation of order 1 Hz. An additional TTR-G thermometer was installed 90 mm from the inlet, exactly midway between the positions of the two wires and close to the channel wall, for direct measurement of the thermal gradient inside the counterflow channel.

The second channel with inner square cross-section 4 mm $\times$ 4 mm and length of 40 mm included two vibrating wires, both oriented perpendicularly to the counterflow direction, at positions 12 mm (wire M2) and 20 mm (wire M1) from the channel inlet, see Fig. 1. A Ge thermometer was mounted at the distance of 16 mm, exactly midway between the wires. In this channel, no second sound sensors were installed. This channel was used to generate more intense vortex tangles at higher counterflow velocities obtained with the same heater power. The resonant frequencies of the wires M1 and M2 were 5830 Hz and 7250 Hz, respectively.

Driving static magnetic field B of order of 100 mT was applied for each wire by the pair of FeNdB permanent magnets. Relations between the driving force F and the driving alternating current I as well as between the induced Faraday voltage U and the wire velocity V that satisfy the conservation of energy are given for semicircular geometry [2] as:

$$F(\omega) = 0.690\, I(\omega) DB;\ V(\omega) = \frac{U(\omega)}{0.690\, DB}. \tag{1}$$

Minor discrepancies may result from deviations of the real geometry from a perfect semi-circle.

Due to a universal scaling of drag forces by normal component acting on oscillators operated in high Stokes number regime [2], one can calibrate the real low-temperature value of the magnetic field from resonance measurements in laminar flow using:

$$B = \sqrt{\frac{\xi \rho_w \Delta f \pi^3 d^2 U_p}{A \times 0.690^2 \, D I_p}}, \tag{2}$$

where $\xi = 0.396$ represents an effective mass prefactor for the fundamental resonant mode [2], ρ_w is the density of the wire material, and Δf, U_p, I_p are the resonant width, the measured peak amplitude of the Faraday voltage and the peak amplitude of the applied driving current, respectively. Both numerical prefactors 0.690 for the force-current relationship and 0.396 for the effective mass, are obtained by integration along the length of the wire, of the driving force projected onto the resonant mode profile, or of the squares of the local amplitudes of motion, respectively, see Ref. [2].

We have performed experiments at temperatures ranging from 1.45 K to 2.1 K, covering a wide range of normal-to-superfluid component ratios of He II. QT was generated by thermally driven counterflow in a slow pulse sequence at various powers ranging between 1 mW and 500 mW in ascending order. Resulting counterflow velocity v_{ns} for the applied heat flux $\dot{q}$ is given as:

$$v_{ns} = \frac{\dot{q}}{sT\rho_s}, \tag{3}$$

where s and ρ_s are the specific entropy and the density of superfluid component, respectively, taken at temperature T. One heater-power step consisted of two repetitions of heater-ON and heater-OFF states with a duration of order 100 s for each state. During the power series, time evolution of the resonant amplitude and frequency of both second sound and vibrating wire signals was measured for all detectors. For this purpose, resonance was tracked with the use of a PID algorithm stabilizing the quadrature signal component to zero (after background correction obtained from a full frequency sweep). In Figure 3, we show a representative measurement of rescaled amplitudes for one pair of detectors during the power series. The decrease of both signal amplitudes is caused by additional damping due to the generation of QT in counterflow and its interaction with the wires and the second sound wave.

The data show that the vibrating wire detects successfully only the highest applied powers and its sensitivity is less than that of second sound. Data such as those in Fig. 3 can be used for calibration of the wire response to a given vortex line density. The resonant frequency of the wires also shifts, as shown in the right panel of Fig. 3. In the following, we analyse the wire response in more detail, estimate its magnitude from HVBK equations [17] and evaluate the response that could be expected for finer (nano-)mechanical structures.

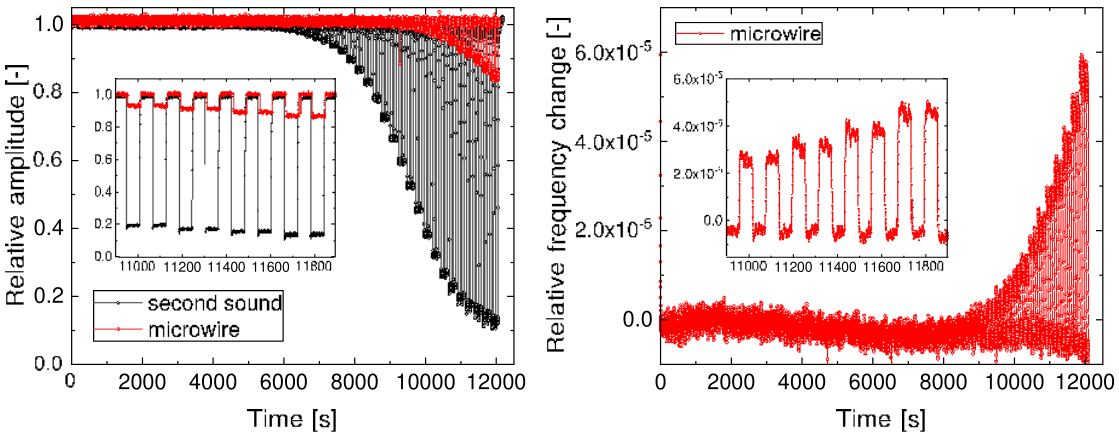

Fig. 3 Left: Measured time series of second sound and vibrating wire L3 amplitude at 1.65 K as the heater power is gradually stepped up. The heater is switched on/off twice at each given power. The microwire is visibly less sensitive than the second sound technique, as expected for a local, but fairly large, mechanical probe. Right: Changes in the resonant frequency of the microwire L3 at 1.65 K. For comparison, changes in second sound frequency reach units of percent at the highest applied powers despite operating near the local maximum in the dependence of second sound velocity on temperature. The insets show details of the individual heater switching events.

3 Results and Discussion

First of all, it is useful to convert the observed resonance frequency shifts to changes in the resonator effective mass, $\Delta m_{\rm eff}$, and then express the extra damping due to counterflow as an inverse quality factor $Q_{\rm cf}^{-1}$ using

$$\frac{\Delta m_{\rm eff}}{m_{\rm eff}} = \left(\frac{f_0^2}{f^2} - 1\right) \; ; \; Q_{\rm cf}^{-1} = \frac{\Delta f_0}{f_0}\left(\frac{A_0}{A} - 1\right), \tag{4}$$

where f_0 and f denote resonance frequencies without and with the counterflow applied, respectively, and similarly A_0 and A represent the amplitudes of the resonant peak, with Δf_0 standing for the resonant linewidth in the absence of counterflow. The obtained values of $\Delta m_{\rm eff}$ are much lower than the effective mass of the resonator, comparable to the mass of the viscous boundary layer of the normal fluid attached to its surface. Similarly, the excess damping is usually lower than the combined background damping due to viscosity and intrinsic dissipation in the device. For these reasons, it is important to provide suitable corrections for parasitic effects. These include most notably variations of local temperature when the counterflow is applied, as the viscous damping scales with $\sqrt{\rho_{\rm n}(T)\eta(T)}$, where $\eta(T)$ is the dynamic viscosity and $\rho_{\rm n}(T)$ the density of the normal component. At the same time, the effect of overheating by about 10 mK (see below) on the observed resonance frequency is negligible except very close to the lambda point.

The temperature gradient in the channel was measured using sensitive TTR-G thermometers and follows the prediction of Eq. (5) below, derived from the HVBK equations [17] assuming that the mutual friction force dominates in thermal counterflow over both turbulent and viscous drag and that the vortex

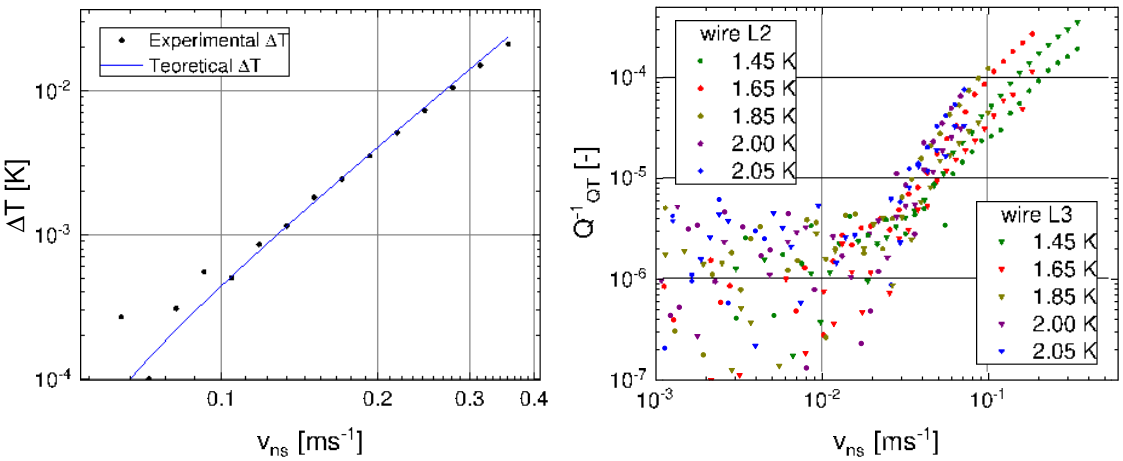

Fig. 4 Left: Temperature rise inside the channel when the heater driving the counterflow is switched on. Right: Corrected microwire excess damping Q_{QT}^{-1} vs. counterflow velocity.

line density is given by $L = \gamma^2 \left({v_{ns}}^2 - {v_{crit}}^2\right)$, which in our case fits the data slightly better than $L = \gamma^2 \left(v_{ns} - v_{crit}\right)^2$. The leading role of mutual friction among dissipative phenomena in counterflow experiments is expected from simple estimates and is found to be in agreement with a more detailed analysis performed for spherical geometry in Ref. [18]. For the purposes of comparison, the gradient ∇T given by

$$\nabla T = \frac{B_{\mathrm{mf}} \kappa \rho_n \gamma^2 \left({v_{ns}}^2 - {v_{crit}}^2\right)}{2 s \rho} v_{ns}, \tag{5}$$

with B_{mf} being the dissipative mutual friction coefficient and ρ being total helium density, is converted to a finite temperature difference using the distance of the thermometer from the open bath, see Fig. 4, left panel. The agreement is quite remarkable, considering the simplifications involved in the derivation.

Subsequently, we can account for thermally induced changes of the viscous damping Q_{th}^{-1} at the positions of the wires using

$$Q_{\mathrm{th}}^{-1} = Q_{\mathrm{hd}}^{-1} \left(\sqrt{\frac{\rho_{\mathrm{n}}(T)\eta(T)}{\rho_{\mathrm{n}}(T_0)\eta(T_0)}} - 1 \right) \tag{6}$$

where, Q_{hd}^{-1} is total hydrodynamic viscous damping in the absence of external counterflow and the temperature T_0 is that of the helium bath, while T is the inferred temperature at the wire locations using the gradient obtained from Eq. (5). The damping due to quantum turbulence may thus be expressed as $Q_{\mathrm{QT}}^{-1} = Q_{\mathrm{cf}}^{-1} - Q_{\mathrm{th}}^{-1}$. We note that at all heater powers where the wire detects an excess damping, the thermally induced contribution is always at least an order of magnitude lower than the one due to quantum turbulence, for both counterflow channels used. The resulting values of Q_{QT}^{-1} are shown in the right panel of Fig. 4.

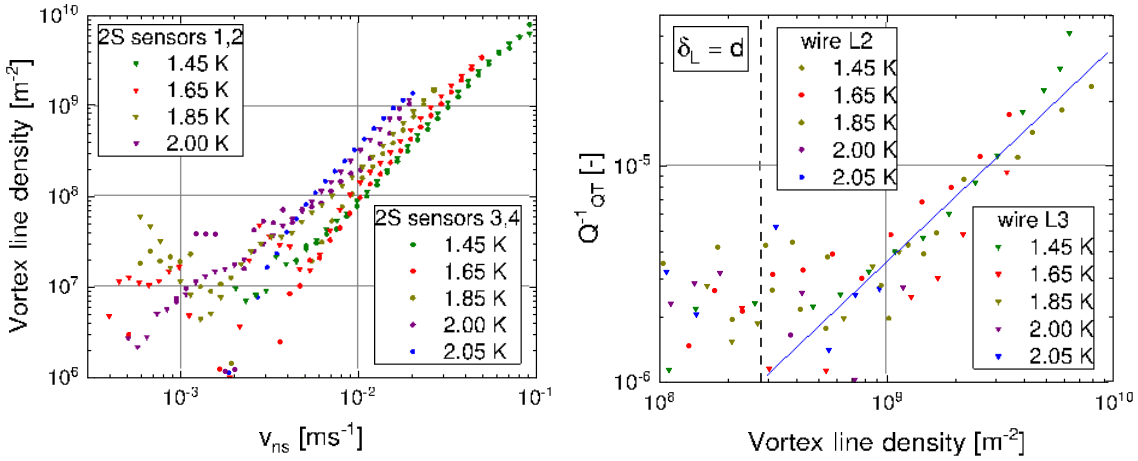

Fig. 5 Left: Vortex line density obtained from second sound measurement in the long channel. The observed γ factors in Eq. (5) are consistent with earlier work [19, 20], see also Table 1. Right: Calibration of microwire response against the vortex line density L. The solid blue line shows a linear relationship which is observed only in the upper decade of L. The mean inter-vortex distance $\delta_L = L^{-1/2}$ is becomes equal to the diameter of the wire at $L = 2.78 \times 10^8$ m^{-2}, indicated by the vertical dashed line.

Additionally, second sound measurements were performed in the same channel, allowing us to establish an approximately linear calibration between the wire response and vortex line density, as is summarily shown in Fig. 5. It is evident that the wire sensitivity is a limiting factor here and that mechanical probes of this size are useful only in highly turbulent tangles. The wires detect no (measurable) additional damping at vortex line densities lower than the threshold given by the comparison of the mean inter-vortex distance with the characteristic dimension – wire diameter $d = 60$ μm.

To test the linearity of the calibration relationship at higher L, we repeated the experiment in the second channel of smaller cross-section, where tangles of higher density could be easily produced. The γ factors from the above measurements were used to deduce vortex line density here, as direct measurement was not available. The γ values are summarized in Table 1 and the results are shown in Fig. 6. The plot shows two regimes which differ by the temperature dependence of the observed damping. At lower L, the proportionality constant c, in the relation $Q_{\mathrm{QT}}^{-1} = cL$ depends systematically on temperature and appears to scale approximately with the superfluid density, ρ_s (showing a notable deviation only at 1.45 K), while at higher L the temperature dependence is mostly suppressed, see also Table 1.

3.1 Interpretation

When the heater is switched on and thermal counterflow is generated, the oscillating wire changes its resonant frequency as well as the damping, as discussed above. Importantly, the frequency increases in all observed instances.

The resonant frequency $\omega_0 = 2\pi f_0$ is determined by the effective hydrodynamic mass, m_{eff}, of the device and by its spring constant, k_s. The resonant frequency defined as the frequency at which maximum power is absorbed from

Table 1 Values of γ used for calculation of vortex line density in the small channel, together with the parameter c relating the inverse quality factor and the vortex line density by $Q_{\mathrm{QT}}^{-1} = cL$. The last column contains a theoretical value for c/ρ_{s} based on Eq. (23) below for wire M1.

T [K]	γ [10^6 s m^{-2}]	c [10^{-15} m^2]	c/ρ_{s} [10^{-17} m^{5}kg^{-1}]	$c_{\mathrm{th}}/\rho_{\mathrm{s}}$ [10^{-17} m^{5}kg^{-1}]
1.45	0.98	4.0	3.0	0.61
1.65	1.22	1.6	1.4	0.59
1.85	1.49	1.1	1.2	0.60
2.00	1.81	0.9	1.4	0.71
2.05	2.05	0.8	1.5	0.90

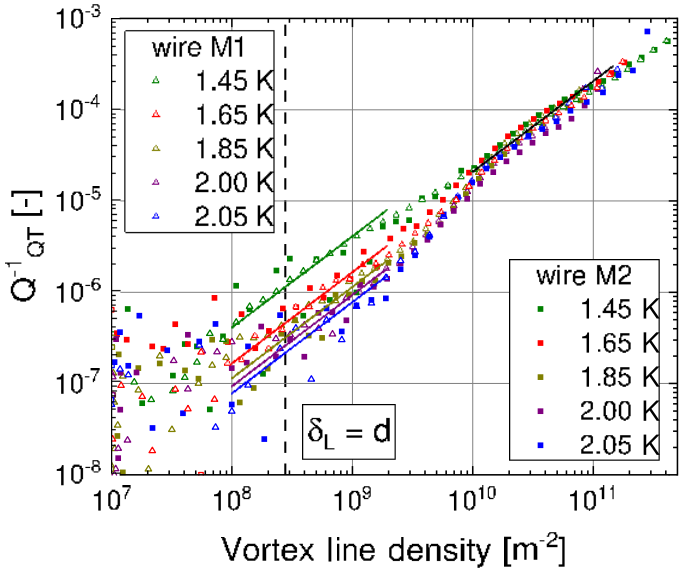

Fig. 6 Microwire damping vs. vortex line density L in the narrow channel. The solid lines depict linear relationships $Q_{\mathrm{QT}}^{-1} = cL$. Two distinct regimes are observed. First, at lower L, the damping is temperature dependent. For the values of the prefactors c, see Table 1. At higher L, the temperature dependence is suppressed; the linear relationship between damping and vortex line density appears with $c \approx 2 \times 10^{15}$ m^2.

a drive mechanism, or equivalently, maximum velocity (rather than displacement) amplitude is reached, is given by $\omega_0^2 = k_{\mathrm{s}}/m_{\mathrm{eff}}$, irrespective of the magnitude of the linear damping. Generally speaking, the observations in the right panel of Fig. 3 may be explained either by an increase in the spring constant, or by a decrease of the effective mass.

The spring constant could change, e.g., due to vortices pinned between the loop of the wire and its base, as long as they are not directed exactly parallel to the direction of motion, in which case only a constant vortex tension would act on the wire. For straight vortices attached to the wire going directly towards a pinning site at its base, the total force projected on the direction of motion would be given by:

$$F_{\mathrm{QV}} = fNF_1\, 2x/D, \tag{7}$$

$$F_{\mathrm{l}} = \frac{\rho_{\mathrm{s}}\kappa^2}{4\pi}\ln\frac{b}{a_0}, \tag{8}$$

$$N = LdD, \tag{9}$$

where F_{l} stands for the force acting due to one quantized vortex (vortex tension), a_0 is the vortex core size, b being a cut-off distance (intervortex spacing in the case of many vortex problem), N denotes the estimated number of attached vortices, x is the immediate displacement of the wire and f is a geometric factor of order unity. This would yield an enhancement to the spring constant due to quantized vortices k_{QV} and its relative magnitude can be estimated as:

$$\frac{k_{\mathrm{QV}}}{k_{\mathrm{s}}} = \frac{\rho_{\mathrm{s}}\kappa^2 Ld}{2\pi m_{\mathrm{eff}}\omega_0^2}\ln(b/a_0). \tag{10}$$

For $T = 1.65$ K and $L = 3\times10^9$ m^{-2} this gives $k_{\mathrm{QV}}/k_{\mathrm{s}} \simeq 10^{-8}$, i.e., three orders of magnitude too small to explain the frequency shift observed in Fig. 3.

Similarly, following Ref. [26], one may consider quantized circulation around the NbTi wire itself interacting with its mirror image reflected through the plane of the base (as per boundary conditions). This interaction produces a static Magnus force, attracting the wire towards its base and changing its tension. However, a semicircular loop with diameter significantly exceeding that of the wire is under tension only due to its curvature. In a situation without vortices, from the neutral line passing through the center of the wire inside, the tension felt by the wire material is negative, while towards the outside it is positive. An integral of the tension taken over the full cross-section of the wire in equilibrium position would yield zero. Circulation trapped around the wire may, in principle, affect this balance of tension forces, but in effect, such a tiny change[1] of the tension due to curvature could not contribute significantly towards the spring constant, which is determined mostly by the elastic modulus of the material itself, seeing as the curved half-loop behaves essentially like a cantilever. We therefore consider it a valid approximation to neglect these effects for our device.

As we cannot justify the observed frequency shift by considering elastic effects, in the following, we analyse the results under the assumption that it is the effective mass that is changing rather than the spring constant. This requires that at high counterflow velocities, the effective mass of the device, or rather, its hydrodynamic enhancement, decreases appreciably. In an ideal fluid (superfluid component), the hydrodynamic mass enhancement of an oscillating object is given in terms of the potential backflow. In a viscous fluid, the same effect exists and additionally, the mass of the viscous boundary layer moving with the object [28, 29] must be considered. For an oscillating body, the backflow contribution is constant regardless of any externally applied stationary flow, we are thus most likely seeing effects related to the viscous boundary

[1] For a nanobeam displaced 2 μm from the substrate, the attractive force was estimated to be of order 10 pN in Ref. [26]. For a microwire loop of diameter 3 mm, this is expected to be roughly three orders of magnitude lower

layer in the normal component. Generally, for an oscillating body in an external stationary viscous flow, two types of boundary layers need to be considered: (i) a stationary Blasius-type boundary layer, and (ii) a periodically changing Stokes-type boundary layer. The interaction of these two types of boundary layers is presently not understood in its entirety and represents a challenging topic with relevance, e.g., in the treatment of waves in shallow water[27] or to some extent in aeronautics, via Interacting Boundary Layer models.

At zero counterflow, the effective mass of the device is given by[2, 29]:

$$m_{\mathrm{eff}} = \xi m + \beta \rho V + \beta' S \rho_{\mathrm{n}} \delta_{\mathrm{n}}, \tag{11}$$

where the first term expresses the effective mass of the device in vacuum (differing from its gravitational mass due to the profile of the resonant mode), the second term represents the ideal backflow and the last term the boundary layer mass, with V and S the volume and surface area of the body, respectively, $\delta_{\mathrm{n}} = \sqrt{2\eta/\rho_{\mathrm{n}}\omega}$ is the Stokes boundary layer thickness and the β and β' are constants of order unity determined by the exact geometry of the body.

In the following, we consider only the Stokes boundary layer, as it is relevant to the oscillating motion of the device which we are measuring, whereas the Blasius-type boundary layer would only affect its steady state characteristics, which are not probed experimentally. Specifically, for an oscillating cylinder, the mass of the Stokes boundary layer, m_{bl}, given by the last term on the RHS of Eq. (11) can be expressed as:

$$m_{\mathrm{bl}} = \frac{\pi^2}{2} \rho_{\mathrm{n}} D \delta_{\mathrm{n}} \left(d + \delta_{\mathrm{n}}\right), \tag{12}$$

and may be used to normalize the observed change of the effective mass. Naively, one might expect that once the counterflow is switched on and turbulence is created in the main flow, vortices will interact with the Stokes boundary layer and cause mixing. This would, in turn lead to partial boundary layer separation, reducing its contribution to the effective mass. The left panel of Fig. 7 shows the mass decrease obtained from the resonant frequency change plotted as a fraction of m_{bl} against L. First of all, we find that the mass change is lower than (but comparable to) the boundary layer mass, making this effect a likely explanation of the experimental data and deserving a closer analysis.

Before proceeding further, let us turn for a moment to the origin of the additional damping. First, let us consider this excess damping due to turbulent motion of both fluids for a moment as if it were a manifestation of some effective dynamic viscosity, η_{eff}, mediating an excess force acting on the oscillator. To begin with, let us state that this notion of an effective viscosity is conceptually different from the usual definition based on turbulent energy dissipation given by $\epsilon = \nu_{\mathrm{eff}}(\kappa L)^2$, as the latter relates to dissipation of the kinetic energy of the externally driven turbulent flow, whereas in our case we are interested in the dissipation of the kinetic energy of the mechanical resonator via fluid-structure

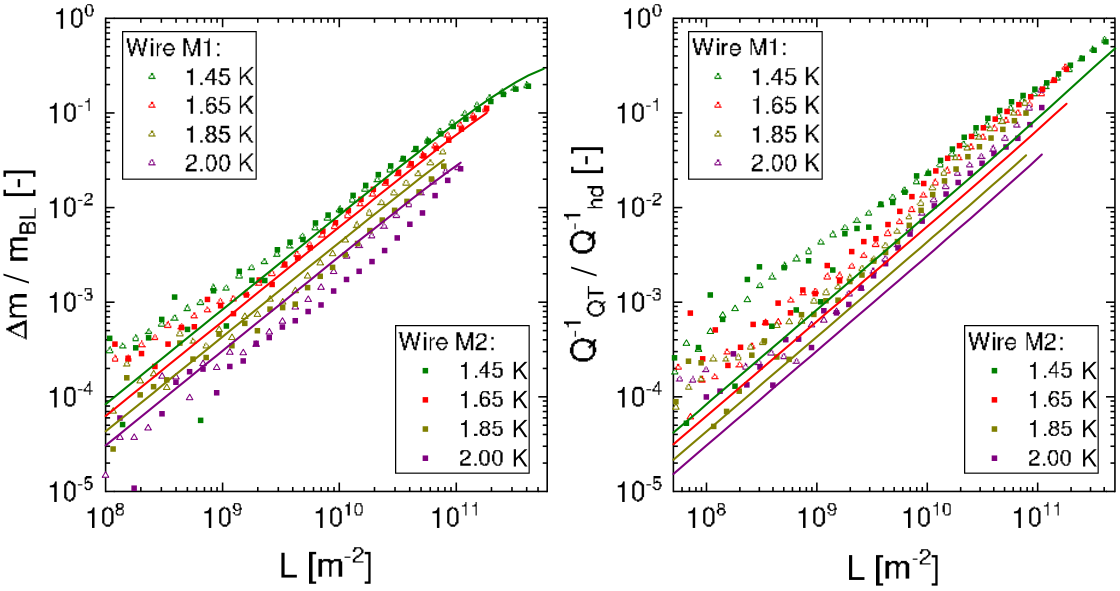

Fig. 7 Left: Change in effective mass normalized by the mass of the Stokes boundary layer plotted against counterflow velocity. The solid lines are calculated using the ratio of effective masses $(a - b)$ as obtained from Eq. (22), showing remarkable agreement with the data. Right: Ratio of extra drag due to quantum turbulence, $Q_{\rm QT}^{-1}$, to the hydrodynamic viscous drag in zero counterflow, $Q_{\rm hd}^{-1}$. The solid lines are obtained using the ratios $(a + b)$ from Eq. (22). The data show higher damping than predicted, see text.

interaction. A viscous-like behaviour would correspond to a situation, where quantized vortices exist in sufficient density to effectively exchange momentum between layers of fluid adjacent to the body. This requires vortex spacing lower than the boundary layer thickness, which may be estimated from Ref. [2], Eq. (9) in the high Stokes number limit, reprinted here for convenience using the present notation:

$$Q_{\rm QT}^{-1} = \frac{\alpha \rho S_r \delta_{\rm eff}}{2m}, \tag{13}$$

where $\alpha = 2$ is the flow enhancement factor for a cylinder, S_r is the effective surface area incorporating roughness, $\delta_{\rm eff} = \sqrt{2\eta_{\rm eff}/\rho\omega}$ is the effective viscous penetration depth and m stands for the (full, not effective) mass of the resonator. The surface area can be approximated by that of a smooth semicircular loop of wire giving $S_r \simeq \pi^2 dD/2$, while the mass of the NbTi wire is given by $m = \rho_{\rm w}\pi^2 d^2 D/8$ with $\rho_{\rm w} = 6550$ kg m^{-3}. Finally, we arrive at:

$$Q_{\rm QT}^{-1} = \frac{4\rho\delta_{\rm eff}}{\rho_{\rm w} d}, \tag{14}$$

which could be used to extract the experimental effective penetration depth $\delta_{\rm eff}$ and hence the effective dynamic viscosity $\eta_{\rm eff}$. The high Stokes number limit manifests by the requirement $\delta_{\rm eff} \ll d$ here, with the wire diameter $d = 60$ μm. The values of $\delta_{\rm eff}$ obtained from our data always fall below 1 μm, requiring $L > 10^{12}$ m^{-2} in order for this scenario to work, which is *not satisfied in our experiments*. In view of this evidence, we rule out dissipation by an effective viscous-like transfer of momentum via interactions with quantized

vortices, although the possibility remains that at higher drives beyond those investigated here, this mechanism may yet come into play.

Here we must consider that while quantized vortices cannot mediate a viscous-like dissipation directly (and should be treated either ballistically, or better, within detailed numerical simulations of the vortex filament model), they may still have a non-zero net effect on the viscous boundary layer via the mutual friction force. As the vortex spacing exceeds the boundary layer thickness, vortices interact with the BL only sporadically. Thus, in a similar fashion to Reynolds decomposition in classical fluids, one may define an mean vortex line density in the boundary layer $\langle L \rangle$, and separate the HVBK equations of motion into steady and fluctuating parts. As the experimental data obtained using the lock-in technique are in any case averaged over thousands periods of oscillation of the device, we must assume that the measurements, in fact, correspond to the mean value $\langle L \rangle$. The question arises: How is the Stokes boundary layer effectively modified in the presence of mutual friction? In the following, we re-derive its properties, extending Stokes' second problem – in-plane oscillations of a planar infinite boundary – to superfluid helium.

3.2 Stokes boundary layer with mean mutual friction

Setting the pressure and temperature gradients to zero and neglecting the vortex tension in the HVBK equations [17], we start from

$$\rho_{\mathrm{n}} \frac{\partial v_{\mathrm{n}}}{\partial t} = -\frac{\rho_{\mathrm{n}}\rho_{\mathrm{s}}}{2\rho} B\kappa L v_{\mathrm{ns}} + \eta \Delta v_{\mathrm{n}}, \tag{15}$$

$$\rho_{\mathrm{s}} \frac{\partial v_{\mathrm{s}}}{\partial t} = +\frac{\rho_{\mathrm{n}}\rho_{\mathrm{s}}}{2\rho} B\kappa L v_{\mathrm{ns}}, \tag{16}$$

where $v_{\mathrm{ns}} = v_{\mathrm{n}} - v_{\mathrm{s}}$. We seek solution in the form

$$v_{\mathrm{n}} = v_{\mathrm{n0}} + v_{\mathrm{n1}} e^{i(kz-\omega t)}, \tag{17}$$

$$v_{\mathrm{s}} = v_{\mathrm{s0}} + v_{\mathrm{s1}} e^{i(kz-\omega t)}, \tag{18}$$

where z is the distance from the plane, and we require $\Im(k) > 0$ to obtain vanishing solutions at infinity. Both velocities oscillate in the same direction as the plane, i.e., we are dealing with a 2D flow, see, e.g., Ref. [28] for a classical hydrodynamical treatment. It follows that the non-linear terms are identically zero due to symmetry of the problem. The superfluid component is expected to be set in motion by the mean mutual friction force and the relation between v_{n} and v_{s} is obtained from the second equation in Eqs. (16). The vortex line density may be expressed as $L = \langle L \rangle + \tilde{L}$, where $\tilde{L}$ represents both random fluctuations in the turbulent flow and oscillations at the frequency of the resonator, ω. Focusing only on terms that oscillate with the frequency ω, neglecting the product $(v_{\mathrm{n0}} - v_{\mathrm{s0}})\tilde{L}$ in comparison to $(v_{\mathrm{n1}} - v_{\mathrm{s1}})\langle L \rangle$ as the oscillator is not expected to generate turbulence of its own at low drive, we

arrive at the condition for the wavenumber k

$$(k\delta_{\rm n})^2 = 2i\,\frac{(2\rho\omega)^2 + \rho_{\rm n}\rho(B\kappa\,\langle L\rangle)^2 + 2i\rho\rho_{\rm s}\omega B\kappa\,\langle L\rangle}{(2\rho\omega)^2 + (\rho_{\rm n}B\kappa\,\langle L\rangle)^2}, \tag{19}$$

where we use the usual viscous penetration depth of the normal component $\delta_{\rm n}^2 = 2\eta/(\rho_{\rm n}\omega)$. Note that the expression $B\kappa\,\langle L\rangle\,/2 \equiv \tau_{\rm mf}^{-1}$ represents a mean inverse relaxation time associated with mutual friction. For $\langle L\rangle = 10^{10}$ m^{-2}, the relaxation time is $\tau_{\rm mf} \approx 2$ ms, meaning that mutual friction is sufficiently fast to act in the experimental window given by the lock-in time constant typically of order 100 ms, but certainly cannot follow each oscillation of the device with a characteristic time given by $\omega^{-1} \approx 30$ μs; hence observation of a "mean-field effect" on the boundary layer is indeed expected. Introducing a dimensionless quantity $w = (\omega\tau_{\rm mf})^{-1}$ analogical to the Weissenberg number used for dilute classical gases, the above expression may be simplified to

$$(k\delta_{\rm n})^2 = 2i\,\frac{1 + x_{\rm n}w^2 + ix_{\rm s}w}{1 + (x_{\rm n}w)^2}, \tag{20}$$

where $x_{\rm n} = \rho_{\rm n}/\rho$ and $x_{\rm s} = \rho_{\rm s}/\rho$. The argument of the complex quantity in the fraction is always between 0 and $\pi/2$ and one may take the positive square root in Eq. (19) to obtain

$$k\delta_{\rm n} = (1+i)(a+ib) = a - b + i(a+b), \tag{21}$$

with $a \geq 1 \geq b \geq 0$, satisfying the requirement that $\Im(k) > 0$. The wavenumber k may be substituted in Eq. (18) to obtain the exact velocity profiles satisfying the boundary condition that the normal fluid moves together with the oscillating plane at $z = 0$. The viscous stress at the boundary will be then given by

$$\sigma = \eta\frac{\partial v_{\rm n}}{\partial z}\bigg|_{z=0} = \left[-(a+b) + i\,(a-b)\right]\frac{\eta v_{\rm p}}{\delta_{\rm n}}e^{\ i\omega t}, \tag{22}$$

where $v_{\rm p}\exp(-i\omega t)$ is the velocity of the planar surface. Comparison of this result with the classical treatment in Ref. [28] shows that the viscous dissipation will be re-scaled by the factor $a + b > 1$ compared to the case without counterflow (and thus without mutual friction) while the added mass will be re-scaled by $a - b$, in agreement with the observations of increased damping and decreased effective mass ($a - b < 1$ for our experimental conditions). We also note specifically that the phase shift between the viscous force and the plane velocity generally differs from $\pi/4$ that is obtained in the case without mutual friction [28], and is restored here in the limit $L \to 0$. It may be also noted that in order for an effective viscosity to describe this problem correctly, the two prefactors $a+b$ and $a-b$ would have to be identical, contrary to both this simple model and experimental observations.

In linear approximation, the prefactors may be expanded in terms of L with

$$a \approx 1; \quad b \approx \frac{1}{2} w x_{\mathrm{s}} = \frac{\rho_{\mathrm{s}}}{\rho} \frac{B \kappa L}{4\omega}. \tag{23}$$

In the case of flow past a circular cylinder, a similar treatment holds as for the planar surface if $\delta_{\mathrm{n}} << d$ and we may approximate its surface by planar elements. Both terms in the stress tensor in Eq. (22) would further contain the flow enhancement factor $\alpha = 2$ expressing the ratio between the velocity of the cylinder surface and that of the potential flow around it, but the comparison to the case without counterflow would yield the same ratios $a + b$, and $a - b$ for the dissipation and the effective mass, respectively.

The modification of the Stokes boundary layer by mutual friction is not the only mechanism responsible for additional dissipation in our experiment. Additionally, one should consider direct momentum transfer from collisions with quantized vortices impacting on the device. While a rough estimate may be obtained from a simplistic model of ballistic vortex ring propagation that agrees in order of magnitude with the observed additional damping, it cannot be formulated precisely without a detailed knowledge of the distribution of sizes of vortex rings, and a thorough analysis would require running numerical simulations that would be heavily influenced by the boundary conditions at the device surface. The experimental data follow the same temperature dependence as given by Eq. (22), which exhibits scaling with ρ_{s} in linear approximation, see the right panel of Fig. 7, but the data are consistently higher than the theoretical prediction. Thus we expect that direct momentum transfer from impacting vortex rings will also contribute to the dissipation significantly. The results indicate that the frequency shift is indeed a safer way to measure the vortex line density with similar devices.

Although we cannot ascertain that the presented crude model is fundamentally correct and further studies using different techniques are certainly required, let us, for a moment, consider its implications for measurements with nanoscale devices. The sensitivity of the nanodevice would be again given by the prefactors expressed in Eqs. (22,23), which will be to some extent influenced by the detailed geometry of the device and its density, but for a wire-like geometry, it will be always inversely proportional to the resonance frequency. This result may be be used to design the approximate dimensions and frequencies of devices with a given sensitivity to quantized vortices present in flows of superfluid helium. For example, one may expect nanomechanical beams resonating at MHz frequencies to display a lower *relative* change in frequency, while the *absolute* frequency shift would be approximately the same. Thus if suitable demodulation techniques are used in the high frequency measurements, the nanoscale devices would operate equally well as far as sensitivity to the average vortex line density L is concerned. However, due to their reduced size, they would perform two or three orders of magnitude better in terms of spatial resolution, or equivalently, the total length of vortex line that they can detect *locally* in comparison to the current, rather large, superconducting

wire. Finally, we note that detection of quantized vortices *stably attached* to nanodevices will behave differently from the model presented here, as both the dissipation and the frequency shifts will be dominated by different mechanisms than discussed here.

4 Conclusion

We have tested several NbTi superconducting microwires as probes of quantum turbulence in thermal counterflow of He II generated in the two-fluid regime above 1 K. The devices respond to the counterflow, displaying changes in damping and resonant frequency. In both cases, the effect is proportional to the vortex line density and the observations can be approximately described by considering a net effect of quantized vortices modifying the Stokes boundary layer due to mutual friction. The observed dissipation displays two regimes differing by their temperature dependence and agrees within an order of magnitude with that given by the above model, but exceeds it systematically, leaving momentum transfer by collisions with vortex rings as a likely additional dissipative mechanism. On the other hand, the observed frequency shift corresponds quite well to the modified Stokes boundary layer model, allowing a *local* quantification of the mean vortex line density, especially after device calibration in a well-characterised flow. This is a promising advance in view of studies of inhomogeneous flows such as cylindrically or spherically symmetrical thermal counterflow and may be extended to modern nanomechanical devices. We hope that our results will stimulate further work both theoretical and experimental and that the simple model presented will help to provide a basic understanding of fluid-structure interactions in turbulent superfluids.

Acknowledgments. We gratefully acknowledge numerous fruitful discussions with L. Skrbek. This research is supported by the Czech Science Foundation project GAČR20-13001Y and by the Charles University under GAUK Project No. 343721.

References

[1] Vinen W. F., The detection of single quanta of circulation in liquid helium II, Proc. R. Soc. Lond. A **260**, 218–236 (1961).

[2] D. Schmoranzer, M. J. Jackson, Š. Midlik, M. Skyba, J. Bahyl, T. Skokánková, V. Tsepelin, L. Skrbek, Dynamical similarity and instabilities in high-Stokes-number oscillatory flows of superfluid helium, Phys. Rev. B **99**, 054511 (2019).

[3] Midlik Š.; Schmoranzer, D.; Skrbek, L., Transition to quantum turbulence in oscillatory thermal counterflow of He-4. Phys. Rev. B **103**, 134516 (2021).

[4] Bewley, G., Lathrop, D., Sreenivasan, K., Visualization of quantized vortices. Nature **441**, 588 (2006).

[5] La Mantia, M., Duda, D., Rotter, M., Skrbek, L., Lagrangian accelerations of particles in superfluid turbulence. J. Fluid Mech. **717**, (2013).

[6] La Mantia, M., Chagovets, T. V., Rotter, M., Skrbek, L., Testing the performance of a cryogenic visualization system on thermal counterflow by using hydrogen and deuterium solid tracers, Rev. Sci. Instrum. **83**, 055109 (2012).

[7] Guo, W., Cahn, S. B., Nikkel, J. A., Vinen, W. F., McKinsey, D. N., Visualization study of counterflow in superfluid 4 He using metastable helium molecules, Phys. Rev. Lett. **105**, 045301 (2010).

[8] Varga, E.; Jackson, M. J.; Schmoranzer, D.; Skrbek, L., The Use of Second Sound in Investigations of Quantum Turbulence in He II. J. Low Temp. Phys. **197**, 130–148 (2019).

[9] Varga, E., Peculiarities of spherically symmetric counterflow, J. Low Temp. Phys. **196**, 28–34 (2019).

[10] Sergeev, Y. A.; Barenghi, C. F., Turbulent radial thermal counterflow in the framework of the HVBK model, Europhys. Lett. **128**, 26001 (2019).

[11] Inui, S.; Tsubota, M., Spherically symmetric formation of localized vortex tangle around a heat source in superfluid 4He. Phys. Rev. B **101**, 214511 (2020).

[12] Woillez, E., Valentin, J., Roche, P. E., Local measurement of vortex statistics in quantum turbulence, EPL **134**, 46002 (2021).

[13] Nago, Y.; Nishijima, A., et al., Vortex emission from quantum turbulence in superfluid 4He. Phys. Rev. B **87**, 024511 (2013).

[14] Wakasa, Y.; Oda, S., et al., Vortex emissions from quantum turbulence generated by vibrating wire in superfluid 4He at finite temperature. Journal of Physics: Conference Series **568**, 012027 (2014).

[15] Varga, E., Babuin, S., Skrbek, L., Second-sound studies of coflow and counterflow of superfluid 4He in channels, Phys. Fluids **27**, 065101 (2015).

[16] http://microsensor.com.ua/products/ge-on-gaas-film-resistance-thermometers/

[17] Holm, D. D. Introduction to HVBK Dynamics. In: Barenghi, C.F., Donnelly, R.J., Vinen, W.F. (eds) Quantized Vortex Dynamics and Superfluid Turbulence. Lecture Notes in Physics, vol 571. Springer, Berlin, Heidelberg (2001).

[18] Xie, Z., Huang, Yu., Novotný, F., Midlik, Š., Schmoranzer, D., Skrbek, L., Spherical Thermal Counterflow of He II, J. Low Temp. Phys. **208**, 426-434 (2022).

[19] Martin, K. P., Tough, J. T., Evolution of superfluid turbulence in thermal counterflow, Phys. Rev. B **27**, 2788 (1983)

[20] S. Babuin, M. Stammeier, E. Varga, M. Rotter, L. Skrbek, Quantum turbulence of bellows-driven ^{4}He superflow: Steady state, Phys. Rev. B **86**, 134515 (2012).

[21] Wang, R. T., Swanson, C. E., Donnelly, R. J., Anisotropy and drift of a quantum vortex tangle, Phys. Rev. B **36**, 5240 (1987).

[22] Adachi, H., Fujiyama, S., Tsubota M., Steady-state counterflow quantum

turbulence: Simulation of vortex filaments using the full Biot-Savart law, Phys. Rev. B **81**, 104511 (2010).

[23] Childers, R. K., Tough, J. T., Helium II thermal counterflow: Temperature- and pressure-difference data and analysis in terms of the Vinen theory, Phys. Rev. B **13**, 1040 (1976).

[24] Baggaley, A. W., Sherwin, L. K., Barenghi, C. F., Sergeev, Y. A., Thermally and mechanically driven quantum turbulence in helium II, Phys. Rev. B **86**, 104501 (2012).

[25] Baggaley, A.W., Laurie, J. Thermal Counterflow in a Periodic Channel with Solid Boundaries. J. Low Temp. Phys. **178**, 35–52 (2015).

[26] Guthrie, A., Kafanov, S., Noble, M.T. et al., Nanoscale real-time detection of quantum vortices at millikelvin temperatures, Nat Commun **12**, 2645 (2021).

[27] James, F., Lagrée, P.-Y., Le, M. H., Legrand, M., Towards a new friction model for shallow water equations through an interactive viscous layer. ESAIM: Mathematical Modelling and Numerical Analysis 53, 269–299 (2019).

[28] Landau L. D., Lifshitz, E. M., Fluid Mechanics (Pergamon, London, 1959).

[29] Blaauwgeers, R., Blažková, M., Človečko, M., Eltsov, V. B., de Graaf, R. , Hosio, J. J., Krusius, M., Schmoranzer, D., Schoepe, W., Skrbek, L., Skyba, P., Solntsev, R. E., Zmeev, D. E., J. Low Temp. Phys. **146**, 537 (2007).

A.5 M. T. Noble, Š. Midlik, L. Colman, D. Schmoranzer, V. Tsepelin, Acoustic emission in bulk normal and superfluid He-3, APL, 122 (2023)

Applied Physics Letters ARTICLE scitation.org/journal/apl

Acoustic emission in bulk normal and superfluid ^{3}He

Cite as: Appl. Phys. Lett. **122**, 163502 (2023); doi: 10.1063/5.0148457
Submitted: 1 March 2023 · Accepted: 23 March 2023 ·
Published Online: 21 April 2023

View Online Export Citation CrossMark

M. T. Noble,[1,a)] Š. Midlik,[2] L. Colman,[1] D. Schmoranzer,[2] and V. Tsepelin[1]

AFFILIATIONS

[1]Department of Physics, Lancaster University, Lancaster LA1 4YB, United Kingdom
[2]Faculty of Mathematics and Physics, Charles University, Prague, Czech Republic

[a)]Author to whom correspondence should be addressed: t.noble@lancaster.ac.uk

ABSTRACT

We present measurements of the damping experienced by custom-made quartz tuning forks submerged in ^{3}He covering frequencies from 20 to 600 kHz. Measurements were conducted in the bulk of normal liquid ^{3}He at temperatures from 1.5 K down to 12 mK and in superfluid ^{3}He-B well below the critical temperature. The presented results complement earlier work on tuning fork damping in ^{3}He, removing possible ambiguities associated with acoustic emission within partially enclosed volumes and extend the probed range of frequencies, leading to a clearly established frequency dependence of the acoustic losses. Our results validate existing models of damping and point toward the same mechanism of wave emission of first sound in normal ^{3}He and liquid ^{4}He and zero sound in superfluid ^{3}He. We observe a steep frequency dependence of the damping $\approx f^{5.5}$, which starts to dominate around 100 kHz and restricts the use of tuning forks as efficient sensors in quantum fluids. The acoustic emission model can predict the limiting frequencies for various devices, including micro-electromechanical and nano-electromechanical structures developed for quantum turbulence and single vortex dynamics research.

The general form of motion of quantum fluids such as superfluid phases of helium isotopes ^{4}He and ^{3}He, quantum turbulence, has sparked scientific interest since its discovery in the middle of the last century. Close analogies to turbulence in classical fluids have been formulated, focusing on large flow structures, while fundamental differences exist that highlight the unique nature of such flow.[1] A significant part of experimental research of quantum turbulence focuses today on the use of submerged electro-mechanical resonators of micrometer and sub-micron dimensions. The goal here is to manufacture devices with the ability to interact with a single quantized vortex,[2] providing experimental access to probing its dynamics, which holds the key to some of the most important outstanding questions, such as how vortices interact with solid structures and how kinetic energy is dissipated in a fluid with zero viscosity. Single vortex sensing can be achieved by lowering the dimensions and mass of a mechanical resonator (beam, wire, tuning fork, etc.) and probing the energy dissipation at the lowest attainable length scales.[3–5] Recently, this development has been made possible by the improved accessibility of nanofabrication facilities allowing for custom production of devices of various shapes and dimensions[2,6–11] based on materials, such as monocrystalline silicon, silicon nitride, quartz glass, or thin layers of superconducting metals.

When designing such a detector, it is crucial to understand the behavior of the device itself and its interaction with the fluid in the relevant dynamical regimes, especially with numerous dissipative mechanisms affecting its sensitivity. First, it is necessary to evaluate the intrinsic damping of the device, as measured in a low temperature vacuum. Defects in the crystal lattice, such as two-level systems,[12] present at grain boundaries or interfaces can contribute to this damping as well as any clamping losses due to finite acoustic transmission through supports. Submerged devices additionally experience a generally temperature dependent "background" damping in the hydrodynamic[13] and ballistic regimes[14,15] of the working fluid. Finally, any submerged oscillating body emits sound waves in the fluid, and acoustic damping[16,17] becomes especially important at high frequencies, imposing a severe practical limit on the design and usability of such devices.

All the mentioned regimes were recently explored systematically using quartz tuning forks[18] in ^{4}He and to a lesser extent[19] in ^{3}He. The results for ^{4}He provide a robust validation of the models for both normal liquid and superfluid phases. Here, we provide bulk measurements of acoustic damping of quartz tuning forks in ^{3}He, covering the frequency range from 20 to 600 kHz, and remove any ambiguities associated with acoustic emission inside a partially enclosed volume

present in the earlier study.[19] Furthermore, the data shown validate the applicability of a single acoustic emission model for both ^{4}He and ^{3}He liquids, including the superfluid phases He-II and ^{3}He-B. Considering the differences in the behavior of the two helium isotopes due to their bosonic (^{4}He) vs fermionic (^{3}He) nature, this finding points toward similar mechanisms of acoustic wave emission in the mentioned classical and quantum fluids.

The measurements were conducted using a custom-made[20] array of quartz tuning forks[18,19,21,22] consisting of five devices connected in parallel, sharing electrical leads. The fundamental and the first overtone resonant frequencies of each fork were determined by varying the fork length from 1.9 to 0.9 mm in order to cover a wide range of frequencies while ensuring sufficient frequency spacing between the resonances to avoid any crosstalk. All of the remaining dimensions, see Fig. 1, were common for all of the forks, namely, prong width $T = 90\ \mu$m, thickness $W = 75\ \mu$m given by wafer thickness, and prong spacing $D = 90\ \mu$m.

For mechanical rigidity and easy manipulation, the fork array was glued between two Stycast 1266 impregnated papers, and an electrical connection was realized via soldering device contacts to copper leads representing also the only thermal link in the case of measurements under vacuum. All vacuum measurements characterizing the device intrinsic damping were performed using a dipstick submerged directly into a ^{4}He transport Dewar at 4.2 K. The intrinsic damping varied within an order of magnitude depending on the position of the fork in the array, pointing toward the importance of the base rigidity. For liquid ^{3}He measurements, the fork array was enclosed inside a Stycast cell[23] shown in Fig. 2, containing also 80 silver-sintered copper plates of the nuclear demagnetization stage, mounted on the Lancaster advanced dilution refrigerator,[24] allowing us to reach temperatures down to 100 μK. The cell was kept at nearly zero pressure and included vibrating wires used for thermometry.[25]

The basic principle of the measurements relies on the piezoelectric properties of quartz,[26] and the connection scheme is illustrated in Fig. 1. Oscillatory movement of the fork prongs, in anti-phase with respect to each other, is induced by the driving voltage, using an Agilent 33521A function generator with output attenuated by 60 dB. The device response results in an ac current proportional to the velocity amplitude of the prong tip. The resulting current signal is first amplified and converted to a voltage using a custom I–V converter[27] with gain 10^6 V/A and then detected by phase-sensitive lock-in amplifiers SR830 or SR844, depending on the measured frequency.

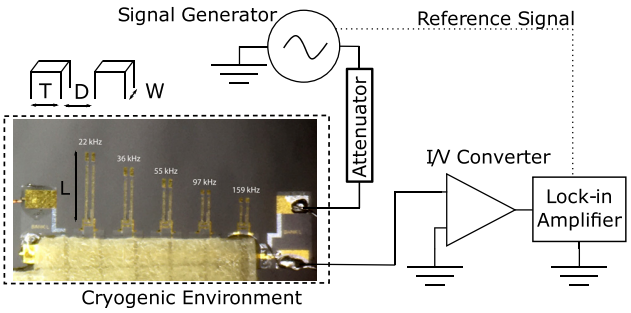

FIG. 1. Photograph of the tuning fork array and a schematic connection diagram.

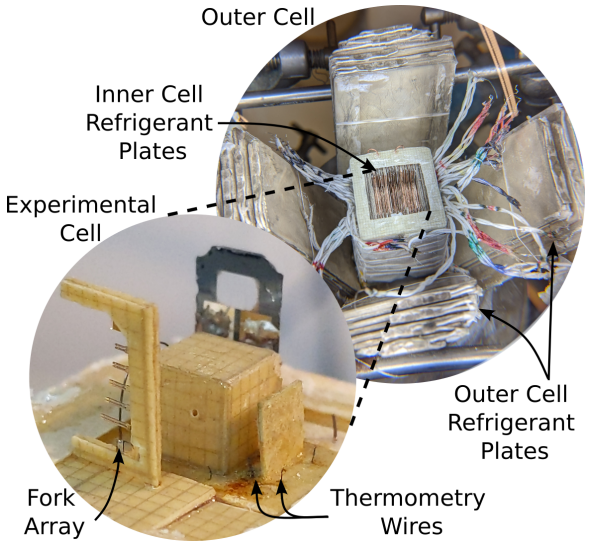

FIG. 2. Photograph of the open double-wall demagnetization cell. The inner cell contains the tuning fork array and thermometry. Copper plates, the refrigerant of the demagnetization stage, covered with silver sinter present in the inner and outer cells are visible.

In order to describe the behavior of an oscillating structure submerged in a liquid, it is necessary to introduce theoretical models of its damping for all relevant flow regimes. First, it is needed to characterize the intrinsic damping, measured in vacuum at low temperatures, caused solely by the mechanical structure of the oscillator. Additional temperature and frequency-independent contributions to the damping may be considered, such as magnetic losses and eddy current heating if using a magneto-motive driving scheme.[28]

In the presence of a working fluid, additional dissipation of hydrodynamic origin appears. The intrinsic damping Δf_0 being well below or at most comparable to the hydrodynamic damping Δf_H is typically considered a necessary condition for the device to be used as a detector. The temperature- or frequency-dependent hydrodynamic contributions to the total damping originate from multiple effects and must be considered separately. In this work, we describe only the laminar/potential flow regime of the normal/superfluid components at velocities below any turbulent instability. It is known that losses due to acoustic emission dominate at high frequencies.[16,17] Damping of the submerged oscillator at frequencies well below this point is well understood and described either by viscous drag in the normal liquid phase or the two-fluid regime of the superfluid phase or at even lower temperatures (for ^{3}He below $\simeq 0.25T_C$) by the frequency-independent ballistic drag.

Although modeling the ballistic drag in superfluid ^{3}He is generally a nontrivial task due to the effects of Andreev reflection[29] reducing the resulting damping force on a moving object, it may be derived for the case of simplified geometries and low velocities.[19] In the viscous drag regime, both the width (corresponds to the damping) and resonant frequency (linked to the mass) of the oscillator's resonance are affected by the fluid. The decrease in the resonant frequency f_H with respect to its vacuum value f_0 is caused by the fluid back-flow and by the mass enhancement due to the creation of a Stokes boundary

layer.[13] For boundary layer thicknesses well below the oscillator dimensions,[22] the solution for an incompressible liquid leads to the square-root frequency dependence of the viscous contribution to the resonance width,[30]

$$\Delta f_{\mathrm{H}} = C\frac{S}{2m_{\mathrm{eff}}}\sqrt{\frac{\rho_{\mathrm{nf}}\eta f_0}{\pi}}\left(\frac{f_{\mathrm{H}}}{f_0}\right)^2, \tag{1}$$

where C denotes a geometrical factor of the order of unity, S is the prong surface area, m_{eff} is the effective mass of the oscillator, and ρ_{nf} and η are temperature dependent density of the normal fluid component and helium viscosity, respectively. The model describes the system accurately when considering the high-frequency limit, i.e., when oscillator characteristic dimensions greatly exceed the viscous penetration depth δ_n given by $\sqrt{\eta/\rho_{\mathrm{nf}}f_0\pi}$. Further corrections accounting for large δ_n are needed when approaching the superfluid transition in ^{3}He due to a steep rise of helium viscosity,[14,30] and slip effects need to be considered in transitional flow between the hydrodynamic and ballistic regimes.

At high frequencies, however, the above-mentioned damping will be negligible compared to energy losses due to the emission of acoustic waves. In order to describe the behavior of the resonator correctly, a suitable model of acoustic emission must be considered.[16] For acoustic emission by a tuning fork in liquid ^{4}He, a "3D" model presented in Ref. 16 is the most successful in describing the experimental data. The tuning fork is modeled as a linear quadrupole of planar sources with effective strength based on the mode-dependent velocity distribution. In the model, emission of spherical waves is considered, leading to the following solution in form of spherical Bessel functions j_m:

$$\Delta f^{3D} = C_{3D}\frac{\rho_{\mathrm{H}}}{c}\frac{W^2L_{\mathrm{eff}}^2}{m_{\mathrm{eff}}}\frac{f_{\mathrm{H}}^4}{f_0^2}\sum_{\substack{m=0,\\ \text{even}}}^{\infty}(2m+1)$$
$$\times\left[j_m\left(\frac{\pi f_{\mathrm{H}}(2T+D)}{c}\right)-j_m\left(\frac{\pi f_{\mathrm{H}}D}{c}\right)\right]^2 \tag{2}$$

with the total helium density ρ_{H}, sound velocity c, a geometrical factor of the order of unity C_{3D}, and an effective prong length L_{eff}. In the long wavelength limit, using Taylor expansion, Eq. (2) yields the steep $\approx f^6$ dependence of the acoustic drag, which starts to dominate around 100 kHz for typical tuning forks[18] in ^{4}He.

To correctly account for the velocity distribution along the prong, it is necessary to introduce the mode-dependent prefactors ξ_{eff} and μ_{eff}, giving the effective mass $m_{\mathrm{eff}} = \xi_{\mathrm{eff}}m$ and effective length $L_{\mathrm{eff}} = \mu_{\mathrm{eff}}L$. Their values for a cantilever may be derived based on Refs. 16 and 18, giving $\mu_{\mathrm{eff}} = 0.3915$ for the fundamental resonance and $\mu_{\mathrm{eff}} = 0.2169$ for the first overtone, while $\xi_{\mathrm{eff}} = 1/4$ for both modes.

In order to describe the sound emission in liquid ^{3}He, the previous work of the Lancaster group[19] gives a strong hint toward the applicability of the introduced model for both quantum liquids, albeit the results clearly show an effect of the resonator confinement resulting in the suppression of the sound emission for the part of the frequency range coinciding with the cavity dimensions.

Finally, when discussing acoustic emission in quantum fluids, it is necessary to distinguish between different sound modes. In bulk liquid ^{4}He, the first sound is a pressure wave, and the second sound[31] is a temperature wave, which must be considered. Due to the driving mechanism being a moving rigid wall, first sound emission is stronger than second sound emission by several orders of magnitude in the described experiments, and second sound is not discussed further. Considering the fermionic nature of ^{3}He, sound waves may be regarded as deformations of the Fermi sphere, with first sound corresponding to a symmetric "breathing" mode and the so-called Landau zero sound mode[32] being described as asymmetric deformations. Second sound mode is strongly suppressed due to the very high viscosity of the normal component. The preference for first sound or zero sound depends on the frequency of oscillation ω and on the temperature, which affects the fluid relaxation time τ. The emission of zero sound is relevant only in the collisionless limit[33] $\omega\tau \gg 1$, and values of $\omega\tau$ for the forks at $0.16T_c$ are given in Table I. In normal ^{3}He, $\omega\tau$ remains below 0.04 even for the highest frequency at all investigated temperatures. Two types of zero sound are known to propagate in superfluid ^{3}He-B: a longitudinal mode and a transverse mode. The transverse mode is not expected to propagate at low pressures.[33] The speed of the longitudinal mode here is 190 m s^{-1}, increased from that of first sound by 6 m s^{-1}.

All measurements presented in this work were conducted in bulk liquid ^{3}He. Prior to the experiments on the demagnetization refrigerator, we characterized the intrinsic damping of each fork in vacuum at ≈4.2 K. The vacuum widths of individual forks differed by up to one order of magnitude, see Table I, which was caused most likely by the differences in the rigidity of the base at each tuning fork site. The obtained vacuum widths, with values comparable to the measurements in ballistic regime on superfluid ^{3}He at the lowest temperature, were subtracted from all datasets presented below. The differences in intrinsic damping between 4.2 K and low temperatures are negligible in comparison with the dominant acoustic or viscous losses.

In Fig. 3, we summarize the experimentally obtained resonant widths using the fork's fundamental and first overtone modes. Each point in the graph results from the resonant peak fit for the resonant frequency and full width at half height. Presented data were obtained from the measurements at five temperatures in normal liquid ^{3}He ranging from 1.5 K down to 12.4 mK and $0.16\,T_C$ in the ballistic regime of superfluid ^{3}He.

TABLE I. Vacuum properties of fundamental and overtone resonant modes of used tuning forks measured at 4.2 K. The last column shows the product of the angular frequency ω and the estimated relaxation time τ in superfluid ^{3}He-B at $0.16\,T_C$. This relaxation time represents the thermalization of individual quasiparticles to the walls of the cell and is obtained by dividing the mean free path of order 1 cm by the root mean square group velocity determined from $\langle v_g^2\rangle \simeq 2v_F^2k_BT/\Delta$, where v_F is the Fermi velocity and Δ is the energy gap.

Fork-mode	Frequency (Hz)	Width (Hz)	$\omega\tau$ ($T = 0.16T_C$)
L1-fund	22 403	0.05	56.1
L2-fund	35 770	5.15	89.7
L3-fund	55 276	0.29	139
L4-fund	97 055	3.58	243
L5-fund	159 316	0.55	399
L1-over	138 689	0.44	348
L2-over	220 110	32	552
L3-over	337 514	3.90	846
L4-over	579 000	159	1450

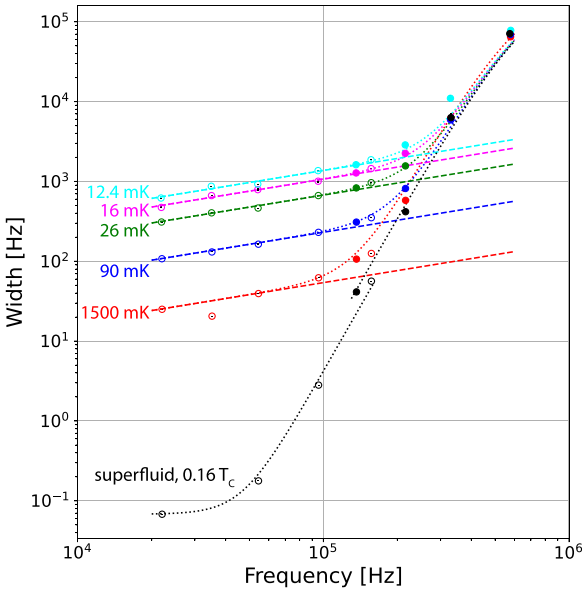

FIG. 3. Measured damping width minus the intrinsic contribution Δf_0 as a function of tuning fork frequency at five temperatures in normal liquid ^{3}He and one temperature in superfluid ^{3}He-B. Empty and filled circles represent fundamental and overtone resonant modes, respectively. Dashed lines correspond to the viscous drag contribution using fitted value of the geometrical parameter $C = 0.65$. The dotted lines represent fits of total resonance width as a sum of viscous drag and acoustic emission contributions. For the superfluid ^{3}He data, we obtained different geometrical coefficients describing acoustic emission by fundamental resonant mode $C_{3D}^{\mathrm{fund}} = 3.3$ and overtone resonant mode $C_{3D}^{\mathrm{ovt}} = 8.5$.

For measurements in normal ^{3}He, we have evaluated the viscous hydrodynamic drag contribution by fitting the data to Eq. (1), shown in Fig. 3 as dashed lines. The fits exclude points at frequencies above 100 kHz, where the acoustic damping becomes significant. Using experimental values of resonant frequency shift in liquid f_H/f_0, known values[30,34] of ρ_{nf} and η for ^{3}He, and dimensions of the used tuning forks, we can evaluate a corresponding geometric C coefficient for each tuning fork for both resonant modes separately and at each temperature. The obtained values of C coefficients vary by less than 1% for different forks considering both their modes and by less than 3% across all the measured temperatures. The resulting temperature and frequency independent value $C = 0.65$ are in reasonable agreement with previous experiments[19] using tuning forks in partially enclosed volumes of normal liquid ^{3}He. The constant C is determined by the fork geometry and may be affected by the ratio of the viscous penetration depth to the tine dimensions, usually falling between 0.5 and 0.65, with higher values possible for short, high-frequency forks.[18,22]

Subtracting the viscous drag contribution, we have performed the fits of the acoustic contribution based on Eq. (2), for all measured temperatures in normal and superfluid ^{3}He states. We have used known ^{3}He properties with first sound and zero sound velocities taken from Refs. 33 and 35 and measured properties of the tuning forks, leaving the geometric prefactor C_{3D} as the only fitting parameter. As the two resonant modes used have different velocity distributions along the prong length, we consider fundamental and overtone datasets separately. For normal liquid ^{3}He, practically, all experimental points usable for the acoustic contribution evaluation come from the overtone mode. Only for the superfluid ^{3}He data can we distinguish the two modes using the derived values of μ_{eff}.

The model describes the observed damping with good accuracy, with values of geometrical coefficients for overtone and fundamental resonant modes $C_{3D}^{\mathrm{ovt}} = 8.5$, with deviation of 20% between the measured temperatures and $C_{3D}^{\mathrm{fund}} = 3.3$. In Fig. 3, we show resulting curves (dotted lines) describing the total measured widths as a sum of viscous/ballistic and acoustic contributions based on the performed fits. The value obtained for the fundamental mode agrees quite well with results from superfluid ^{4}He,[18] where $C_{3D} = 2.17$ was obtained. We note that the analysis in Ref. 18 uses the same effective prong length $\mu_{\mathrm{eff}} = 0.3915$ for both the fundamental resonance and the first overtone, while the data dominated by acoustic damping come mostly from overtone measurements. After adjustment for the correct effective prong length $\mu_{\mathrm{eff}} = 0.2169$, a prefactor of $C_{3D} = 7.1$ is obtained in ^{4}He, in good agreement with the present value $C_{3D}^{\mathrm{ovt}} = 8.5$.

The results confirm the validity of the model of acoustic emission by quartz tuning forks presented in Ref. 16 for the bulk normal liquid ^{3}He and superfluid ^{3}He-B in addition to the previous results in liquid ^{4}He. The values of geometrical coefficients representing the only fitting parameters in the viscous drag and acoustic emission models are in good agreement with previous results. It is important to point out that the single value of the geometrical coefficient can describe acoustic emission in the whole range of temperatures in both quantum liquids. Our results, therefore, point toward the same mechanism of wave emission of the first sound in normal ^{3}He and liquid ^{4}He and longitudinal zero sound in superfluid ^{3}He-B, expected to dominate at the temperature and frequencies used. In addition, we showed that resonant modes with different velocity profiles along the tuning fork prong must be considered separately. Complementing previous experiments, this work brings together proof of the general validity of acoustic emission models, derivable for resonators of various shapes and sizes. Predictions of ballistic, viscous, and acoustic damping obtained from the models can be expected to hold across a wide frequency range in all classical fluids and in quantum fluids as long as the coherence length is lower than the size of the oscillator.

The research leading to these results has received funding from the Czech Science Foundation under Project No. GAČR 20-13001Y, the European Union's Horizon 2020 Research and Innovation Programme under Grant Agreement No. 824109, the European Microkelvin Platform (EMP), and the United Kingdom Science and Technology Funding Council under Grant No. ST/T006773/1.

AUTHOR DECLARATIONS

Conflict of Interest

The authors have no conflicts to disclose.

Author Contributions

Mark Theodore Noble: Conceptualization (equal); Data curation (lead); Investigation (equal); Project administration (lead); Writing – review & editing (equal). **Šimon Midlik:** Conceptualization (equal); Data curation (supporting); Formal analysis (lead); Investigation (equal); Methodology (equal); Writing – original draft (equal);

Writing – review & editing (equal). **Liam Colman:** Conceptualization (equal); Data curation (supporting); Formal analysis (equal); Investigation (equal). **David Schmoranzer:** Conceptualization (equal); Formal analysis (equal); Funding acquisition (lead); Methodology (equal); Project administration (equal); Supervision (equal); Writing – original draft (equal); Writing – review & editing (equal). **Viktor Tsepelin:** Conceptualization (equal); Investigation (equal); Project administration (equal); Supervision (equal); Writing – review & editing (equal).

DATA AVAILABILITY

The data that support the findings of this study are openly available in Lancaster University at the Lancaster University Data Repository https://doi.org/10.17635/lancaster/researchdata/607, Ref. 36.

REFERENCES

[1]L. Skrbek, D. Schmoranzer, Š. Midlik, and K. R. Sreenivasan, "Phenomenology of quantum turbulence in superfluid helium," Proc. Natl. Acad. Sci. U. S. A. **118**, e2018406118 (2021).

[2]A. Guthrie, S. Kafanov, M. T. Noble, Y. A. Pashkin, G. R. Pickett, V. Tsepelin, A. A. Dorofeev, V. A. Krupenin, and D. E. Presnov, "Nanoscale real-time detection of quantum vortices at millikelvin temperatures," Nat. Commun. **12**, 2645 (2021).

[3]M. Leadbeater, D. C. Samuels, C. F. Barenghi, and C. S. Adams, "Decay of superfluid turbulence via Kelvin-wave radiation," Phys. Rev. A **67**, 015601 (2003).

[4]T. P. Simula, T. Mizushima, and K. Machida, "Kelvin waves of quantized vortex lines in trapped Bose-Einstein condensates," Phys. Rev. Lett. **101**, 020402 (2008).

[5]E. B. Sonin, "Symmetry of Kelvin-wave dynamics and the Kelvin-wave cascade in the T = 0 superfluid turbulence," Phys. Rev. B **85**, 104516 (2012).

[6]A. Kraus, A. Erbe, and R. H. Blick, "Nanomechanical vibrating wire resonator for phonon spectroscopy in liquid helium," Nanotechnology **11**, 165 (2000).

[7]M. Defoort, K. J. Lulla, T. Crozes, O. Maillet, O. Bourgeois, and E. Collin, "Slippage and boundary layer probed in an almost ideal gas by a nanomechanical oscillator," Phys. Rev. Lett. **113**, 136101 (2014).

[8]T. Kamppinen and V. B. Eltsov, "Nanomechanical resonators for cryogenic research," J. Low Temp. Phys. **196**, 283–292 (2019).

[9]I. Golokolenov, B. Alperin, B. Fernandez, A. Fefferman, and E. Collin, "Fully suspended nano-beams for quantum fluids," J. Low Temp. Phys. **210**, 550–561 (2023).

[10]E. Collin, L. Filleau, T. Fournier, Y. M. Bunkov, and H. Godfrin, "Silicon vibrating wires at low temperatures," J. Low Temp. Phys. **150**, 739–790 (2008).

[11]Š. Midlik, J. Sadílek, Z. Xie, Y. Huang, and D. Schmoranzer, "Silicon vibrating micro-wire resonators for study of quantum turbulence in superfluid ^{4}He," J. Low Temp. Phys. **208**, 475–481 (2022).

[12]T. Kamppinen, J. T. Mäkinen, and V. B. Eltsov, "Dimensional control of tunneling two-level systems in nanoelectromechanical resonators," Phys. Rev. B **105**, 035409 (2022).

[13]R. Blaauwgeers, M. Blazkova, M. Človečko, V. B. Eltsov, R. de Graaf, J. Hosio, M. Krusius, D. Schmoranzer, W. Schoepe, L. Skrbek, P. Skyba, R. E. Solntsev, and D. E. Zmeev, "Quartz tuning fork: Thermometer, pressure- and viscometer for helium liquids," J. Low Temp. Phys. **146**, 537–562 (2007).

[14]M. Morishita, T. Kuroda, A. Sawada, and T. Satoh, "Mean free path effects in superfluid ^{4}He," J. Low Temp. Phys. **76**, 387–415 (1989).

[15]D. I. Bradley, P. Crookston, S. N. Fisher, A. Ganshin, A. M. Guénault, R. P. Haley, M. J. Jackson, G. R. Pickett, R. Schanen, and V. Tsepelin, "The damping of a quartz tuning fork in superfluid ^{3}He-B at low temperatures," J. Low Temp. Phys. **157**, 476–501 (2009).

[16]D. Schmoranzer, M. La Mantia, G. Sheshin, I. Gritsenko, A. Zadorozhko, M. Rotter, and L. Skrbek, "Acoustic emission by quartz tuning forks and other oscillating structures in cryogenic ^{4}He fluids," J. Low Temp. Phys. **163**, 317–344 (2011).

[17]J. Rysti and J. Tuoriniemi, "Quartz tuning forks and acoustic phenomena: Application to superfluid helium," J. Low Temp. Phys. **177**, 133–150 (2014).

[18]D. I. Bradley, M. Človečko, S. N. Fisher, D. Garg, E. Guise, R. P. Haley, O. Kolosov, G. R. Pickett, V. Tsepelin, D. Schmoranzer, and L. Skrbek, "Crossover from hydrodynamic to acoustic drag on quartz tuning forks in normal and superfluid ^{4}He," Phys. Rev. B **85**, 014501 (2012).

[19]A. M. Guénault, R. P. Haley, S. Kafanov, M. T. Noble, G. R. Pickett, M. Poole, R. Schanen, V. Tsepelin, J. Vonka, T. Wilcox, and D. E. Zmeev, "Acoustic damping of quartz tuning forks in normal and superfluid ^{3}He," Phys. Rev. B **100**, 104526 (2019).

[20]Manufactured by the Statek Corporation, 512, N. Main Street, Orange, CA 92868, USA.

[21]S. L. Ahlstrom, D. I. Bradley, M. Človečko, S. N. Fisher, A. M. Guénault, E. A. Guise, R. P. Haley, O. Kolosov, P. V. E. McClintock, G. R. Pickett, M. Poole, V. Tsepelin, and A. J. Woods, "Frequency-dependent drag from quantum turbulence produced by quartz tuning forks in superfluid ^{4}He," Phys. Rev. B **89**, 014515 (2014).

[22]D. Schmoranzer, M. J. Jackson, Š. Midlik, M. Skyba, J. Bahyl, T. Skokánková, V. Tsepelin, and L. Skrbek, "Dynamical similarity and instabilities in high-Stokes-number oscillatory flows of superfluid helium," Phys. Rev. B **99**, 054511 (2019).

[23]D. I. Bradley, A. M. Guénault, V. Keith, C. J. Kennedy, I. E. Miller, S. G. Mussett, G. R. Pickett, and W. P. Pratt, Jr., "New methods for nuclear cooling into the microkelvin regime," J. Low Temp. Phys. **57**, 359–390 (1984).

[24]D. J. Cousins, S. N. Fisher, A. M. Guénault, R. P. Haley, I. E. Miller, G. R. Pickett, G. N. Plenderleith, P. Skyba, P. Y. A. Thibault, and M. G. Ward, "An advanced dilution refrigerator designed for the new Lancaster microkelvin facility," J. Low Temp. Phys. **114**, 547–570 (1999).

[25]C. Bäuerle, Y. M. Bunkov, S. N. Fisher, H. Godfrin, and G. R. Pickett, "Laboratory simulation of cosmic string formation in the early Universe using superfluid ^{3}He," Nature **382**, 332–334 (1996).

[26]K. Karrai and R. D. Grober, "Piezo-electric tuning fork tip–sample distance control for near field optical microscopes," Ultramicroscopy **61**, 197–205 (1995).

[27]S. Holt and P. Skyba, "Electrometric direct current I/V converter with wide bandwidth," Rev. Sci. Instrum. **83**, 064703 (2012).

[28]E. Collin, T. Moutonet, J.-S. Heron, O. Bourgeois, Y. M. Bunkov, and H. Godfrin, "A tunable hybrid electro-magnetomotive NEMS device for low temperature physics," J. Low Temp. Phys. **162**, 653–660 (2011).

[29]S. N. Fisher, A. M. Guénault, C. J. Kennedy, and G. R. Pickett, "Beyond the two-fluid model: Transition from linear behavior to a velocity-independent force on a moving object in ^{3}He-B," Phys. Rev. Lett. **63**, 2566 (1989).

[30]D. I. Bradley, M. Človečko, S. N. Fisher, D. Garg, A. M. Guénault, E. Guise, R. P. Haley, G. R. Pickett, M. Poole, and V. Tsepelin, "Thermometry in normal liquid ^{3}He using a quartz tuning fork viscometer," J. Low Temp. Phys. **171**, 750–756 (2013).

[31]E. Varga, M. J. Jackson, D. Schmoranzer, and L. Skrbek, "The use of second sound in investigations of quantum turbulence in He-II," J. Low Temp. Phys. **197**, 130–148 (2019).

[32]W. R. Abel, A. C. Anderson, and J. C. Wheatley, "Propagation of zero sound in liquid He^3 at low temperatures," Phys. Rev. Lett. **17**, 74 (1966).

[33]D. Vollhardt and P. Wolfle, *The Superfluid Phases of Helium 3* (Courier Corporation, 2013).

[34]J. Wilks, *The Properties of Liquid Helium* (Elsevier, 1966).

[35]H. L. Laquer, S. G. Sydoriak, and T. R. Roberts, "Sound velocity and adiabatic compressibility of liquid helium three," Phys. Rev. **113**, 417 (1959).

[36]M. T. Noble, Š. Midlik, L. Colman, D. Schmoranzer, and V. Tsepelin (2023) "Dataset of Publication: Acoustic emission in bulk normal and superfluid 3He," Lancaster University. https://doi.org/10.17635/lancaster/researchdata/607.

A.6 Š. Midlik, J. Sadílek, Z.L. Xie, Y.H. Huang, D. Schmoranzer, Silicon Vibrating Micro-Wire Resonators for Study of Quantum Turbulence in Superfluid He-4, JLTP 208 (2022)

Journal of Low Temperature Physics (2022) 208:475–481
https://doi.org/10.1007/s10909-022-02675-2

Silicon Vibrating Micro-Wire Resonators for Study of Quantum Turbulence in Superfluid ^{4}He

Šimon Midlik[1] · Jakub Sadílek[2] · Zhuolin Xie[1] · Yunhu Huang[1] · David Schmoranzer[1]

Received: 30 September 2021 / Accepted: 15 January 2022 / Published online: 9 February 2022

Abstract

We report a fabrication process and characterization measurements of single crystal silicon micro-wire resonators to be used for study of quantum turbulence in superfluid ^{4}He at millikelvin temperatures. Our devices are single standing goal-post-shaped silicon structures with a width and height of the order of 7 microns. Vapour-deposited superconducting aluminium film of 120 nm thickness is used for magneto-motive drive of the resonators. In the window of each chip, two such devices of different dimensions are placed 30 μm to 1 mm apart, with the intent to study interaction due to pinned quantized vortices. With resonant frequencies below 10 kHz, the devices reach quality factors of $\approx 2 \times 10^4$ in cold helium vapour.

Keywords MEMS · Superfluid ^{4}He · Quantized vortices

1 Introduction

General trend of device miniaturization opens new possibilities in the research of dynamics of quantum fluids. Reaching the nano-scale dimensions of the electro-mechanical resonators would allow detailed characterization of quantum turbulence [1] on a scale of single quantized vortices—the fundamental building blocks of quantum turbulence. Through the coupling of resonating structures with a single quantized vortex it will be possible to study the spectrum of Kelvin waves [2] generated on a quantized vortex, representing the dominant form of dissipation in isotopically pure superfluid ^{4}He in the limit of zero temperature.

✉ Šimon Midlik
midliks@o365.cuni.cz

[1] Faculty of Mathematics and Physics, Charles University, Ke Karlovu 3, 121 16 Prague, Czech Republic

[2] Faculty of electrical engineering and communication, Brno University of Technology, Technická 10, 61600 Brno, Czech Republic

Therefore, various micro- and nano-electromechanical systems (MEMS and NEMS) in the form of wires, tuning forks, or beams are becoming widely used in low temperature research [3–6]. These resonating structures built on silicon wafers or SOI (silicon on insulator) wafers are used to probe a wide range of media; from cold helium gas [7], superfluid ^{4}He down to millikelvin temperatures [5, 6] to superfluid ^{3}He at sub-mK temperatures [6, 8].

One of the most important features of the mentioned sensors is their extremely low intrinsic damping resulting in the desired sensitivity. Quality factors up to 10^6 were reported for nano-devices made from silicon nitride [9]. For operation in quantum liquids, relatively low resonant frequencies are also important due to the steep frequency dependence of acoustic damping [10–12].

The devices reported here satisfy such requirements, with resonant frequencies below 10 kHz and quality factors approaching 2×10^4 already in cold, low pressure helium vapour. The fabrication process is based on multiple optical lithography steps from both sides of the chip, and the resulting structures are goal-post shaped wires (hydrodynamically smooth for the normal component of He II), inspired by those in the work of Collin [13], made from single crystal silicon with thin layer of aluminium deposited on top. We report the step-by-step fabrication process of our MEMS devices together with preliminary characterization measurements of their resonances, at $T \approx 1.3$ K, in cold ^{4}He gas. We also compare the resonant frequencies measured in vacuum with the theoretical values derived from finite element models.

2 Fabrication Process

We fabricated our MEMS devices from 300-µm thick double side polished single crystal 4 inch silicon wafers with <100> orientation and 5–10 Ohm/cm resistivity. Before any further processes, the wafer was cleaned using RCA1 and RCA2 procedure and 75 nm thick Si_3N_4 layer was deposited from both sides using PECVD (plasma enhanced chemical vapour deposition) process. The schematic of the used processes and the final chip structure are illustrated in Fig 1.

First, the windows are opened in the Si_3N_4 layer from the top side using reactive ion etching with CHF_3 gas in Oxford PlasmaPro NGP 80 RIE-fluorine machine. For the lithography, we used a 1.4 µm layer of AZ5214E image reversal spin-coated photoresist (using SÜSS MicroTec RCD8 machine), which was exposed on SÜSS MicroTec MA8 UV light (h-line) lithograph and developed using AZ726MIF/deionized water 1:4 solution (~ 60 s).

Next the 120 nm thick aluminium wires are deposited in the e-beam evaporator (Bestec). The dimensions of the goal-post-shaped wires are varied chip-to-chip with nominal widths 5, 10 or 20 µm, leg spacing from 0.2 to 1 mm and leg length of 1 mm. Aluminium is deposited directly on the silicon in the previously opened windows and partially in the region still covered with Si_3N_4 creating the leads to later deposited electrodes. Lift-off in 80 °C NMP bath is used in this step with double layer resist for optical lithography. We used 0.8 µm of AR-BR 5480 optically non-sensitive resist as bottom layer and 1.4 µm of AZ5214E as top layer, both

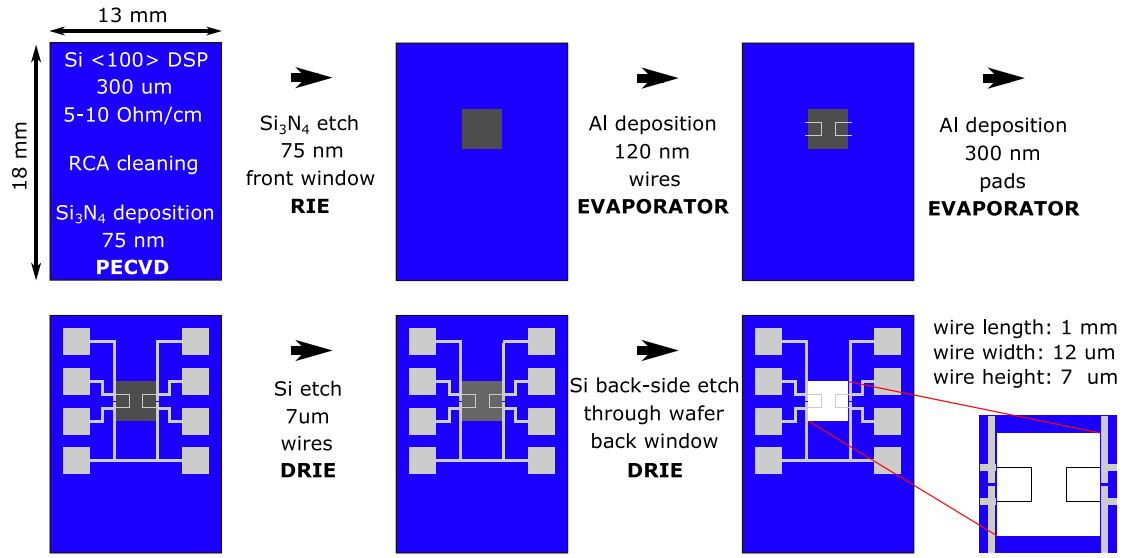

Fig. 1 Schematic of the process workflow, showing the initial state of the wafer and following fabrication steps, which are described in more detail in Sect. 2

spin-coated. For the exposure, direct laser writing was used (Heidelberg DWL 66-fs) with the same developing procedure as in the first step.

In following step, the 300 nm thick aluminium electrodes are deposited on the Si_3N_4 layer, working as a buffer layer for the mechanical strain caused during contacting. The procedure was similar as for the previous deposition, but using SÜSS MicroTec MA8 lithograph and negative tone of the top AZ5214E resist.

Further, the wafer was cut with a laser saw to continue with processes on single chips. In the following step the smooth Bosch process [14] on Oxford Instruments PlasmaPro 100 deep reactive ion etching (DRIE) machine was used to etch 5 to 9 µm high wire structures in the pre-opened window in Si_3N_4 at a temperature of 5 °C. The recipe based on looping the steps with SF_6 (etching and break-through steps) and C_4F_8 (deposition step) gases results in hydrodynamically smooth vertical walls (with scallops) of the silicon wires. The result of this process is shown in the scanning electron microscope (SEM) picture, see Fig. 2. We estimate, that the horizontal depth of the scallops is of the order of 10 nm. We again used the AZ5214E photoresist in positive tone exposed with DWL. The width of the silicon wires was chosen to be overlapping the aluminium lines by 1 µm at each side to ensure no metal is exposed during the process, leaving the final width of the device to be 7, 12 or 22 µm.

The final step was the DRIE Bosch process etching the window from the back side of the chip in order to release the devices. For this purpose, we used 7-µm thick AZ10XT photoresist exposed via DWL, with the window design enlarged by 300 µm. The bigger size of the back-side window was chosen to overcome the troubles with wall screening effect resulting in non-homogeneous etch rate at higher depths causing rounding of the walls.

Finally, we cleaned the chips in 80 °C hot NMP overnight and finished the cleaning in O_2 plasma using RIE-Fluorine machine. The resulting device is shown in Fig. 2, under the optical microscope, where one free standing wire is shown together

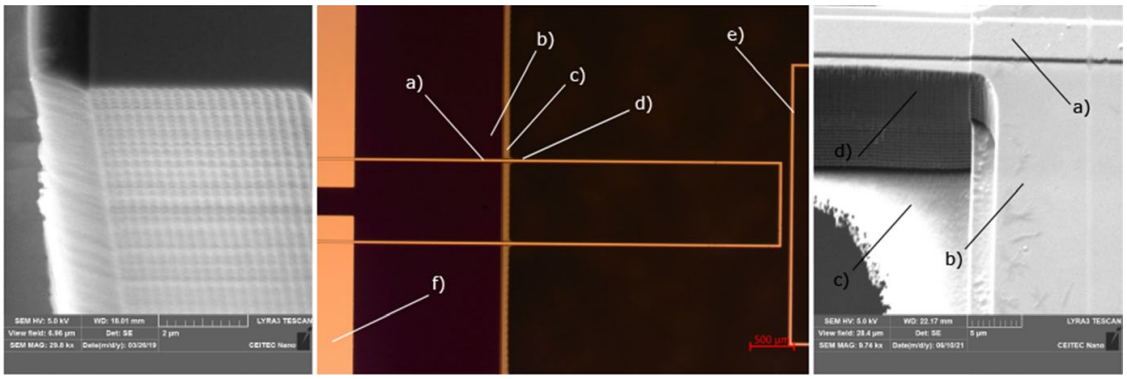

Fig. 2 Left: SEM image of smooth Bosch DRIE process result, showing the scallop structure of the vertical wall of the fabricated silicon wire. Middle: Optical microscope image of the final device in the open window. **a** 120 nm aluminium layer on top of the substrate, **b** substrate, still covered with 75 nm of Si_3N_4, **c** thin Si ledge, as a result of wall screening effect during deep back-side etching, **d** Si wire, with 120 nm of aluminium layer on top, freely standing in the open window **e** the crossbeam of the oppositely standing wire separated by a gap of 30 µm. **f** 300 nm thick aluminium leads. Right: SEM image of the base of the silicon wire showing its structure. Pointers a)->d) correspond with the middle picture

with the top part of the opposing wire separated by 30 µm. In Fig. 2 we show the SEM image with a detailed view of the base of the wire, were slight leftover ledge originating from the wall rounding during back-side etch is visible. From the analysis of SEM pictures we can deduce that the variation of wire height over the length of its leg is less than 0.5 µm.

3 Measurement Scheme and Device Characterization

To drive the oscillatory motion of the silicon wires, we use the magneto-motive method (same as in [4]), where alternating current $I(\omega) = I_0\cos(\omega t)$ is passed through the aluminium layer on top of the silicon. The resonator is placed in static magnetic field B 100 mT, pointing in direction along the wire‘s legs, which results in alternating Lorentz force $F(\omega)$ acting on the wire’s crossbar. The motion of the current biased wire in a magnetic field results in the induction of Faraday voltage $U(\omega)$ proportional to the velocity $V(\omega)$. In this geometry, see Fig 4, following equations between the mechanical and electrical properties of MEMS hold:

$$F(\omega) = I(\omega)LB; V(\omega) = U(\omega)/LB, \tag{1}$$

with L being the leg spacing.

We performed the characterization measurements of three fabricated devices. Table 1 contains device dimensions, along with a comparison of resonant frequencies measured in vacuum at room temperature to those resulting from FEM models. These experiments were performed in a simple glass desiccator connected to a rotary pump. A sinusoidal voltage signal was supplied by an Agilent 33220A function generator. A 10 kΩ resistor was connected in series to the wire to regulate the current. Using a current of 1 µA , we observed the resonance amplitude about 0.25 µV. Induced voltage signal was measured using a Stanford Research Systems SR830

Table 1 Dimensions of the three wires that were tested at room temperature, and comparison between the modeled and the measured resonant frequencies

Name	L (μm)	h (μm)	w (μm)	t (μm)	d (μm)	f_{calc} (kHz)	f_{meas} (kHz)	Q-factor
G1–1	1000	1000	22	6.8	1080	4.80	4.88	388
G1–2	1000	900	22	6.8	1080	5.72	5.50	340
H3	300	1000	12	7.3	30	7.08	7.62	417

In this table L denotes the bar length, h the leg length, w the width, t the thickness, and d the spacing between the two wires on the same chip. The frequencies f_{calc} were calculated from the design geometry using the finite element technique, while f_{meas} was measured experimentally. We note that the uncertainty in the thickness t of up to 0.5 μm due to uneven etching is sufficient to explain the discrepancies in the resonant frequencies

lock-in amplifier. A detection scheme using two lock-in amplifiers will be used to measure two wires on a single chip simultaneously, using the separation of their resonance frequencies to filter out cross-talk.

To construct the finite element models, the geometry of the entire chip was used, with fixed boundaries imposed on all surfaces of the chip except for the wires. To model anisotropic elasticity of <100> Si, values of elastic constants $c_{11} = 165.7$ GPa, $c_{12} = 63.9$ GPa, $c_{44} = 79.6$ GPa were used [15]. An adaptive mesh was applied to the wire geometry and the first few resonant modes were obtained using frequency domain analysis, see Fig. 3.

For the H3 device we also performed cryogenic measurements in low pressure ^{4}He gas at 1.3 K in a glass cryostat, with the aim of estimating the resonance quality factors. For mounting and heat-sinking the chips, custom-made copper plates were used, shown in Fig. 4. Superconducting NbTi leads were anchored to the Cu plates by GE varnish and glued to the aluminum pads using MG Chemicals 8330S silver conductive epoxy enriched by silver powder, with resulting low temperature contact resistance 10 mΩ. The copper plate was then mounted onto a 3D-printed holder made from colorFabb copperFill, a copper-doped PLA filament. The static magnetic field was supplied by two permanent NdFeB magnets placed in the holder.

To estimate the intrinsic damping of the device, a series of low-drive frequency sweeps was performed in cold helium vapour, just as liquid helium ($T \approx 1.3$ K) was used up in the cryostat, see Fig. 5. The device showed to be very sensitive to the vapour

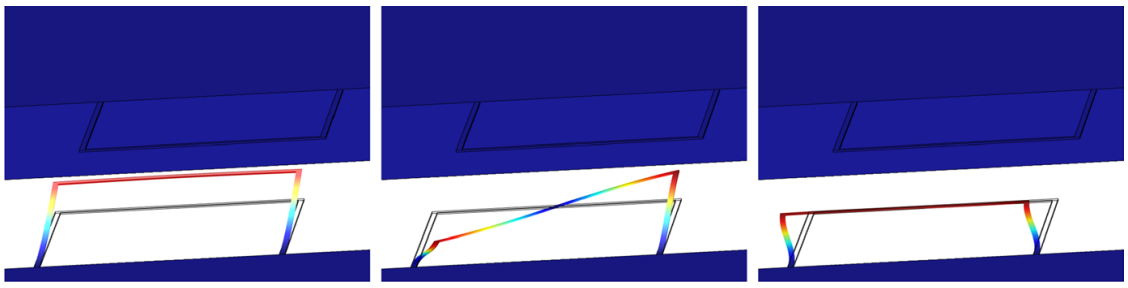

Fig. 3 First three resonant modes of the G1–1 silicon device (see Table 1). The left and middle panels show flexural modes at 4.8 kHz and 12.6 kHz, while the rightmost panel illustrates the "windscreen wiper" mode at 25 kHz. The deformation amplitudes are enhanced for clarity

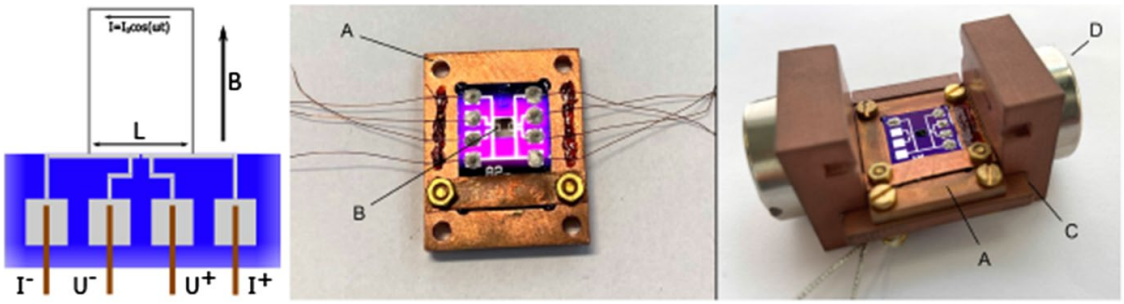

Fig. 4 Measurement scheme and the construction of the chip holder. Left: geometrical sketch of the measurement scheme. Center: micro-wire chip mounted onto a copper backing plate. Right: the backing plated mounted onto a 3D-printed holder, along with magnets. The letters are: A—copper backing plate; B—micro-wire; C—3D-printed holder; D—one of the two magnets

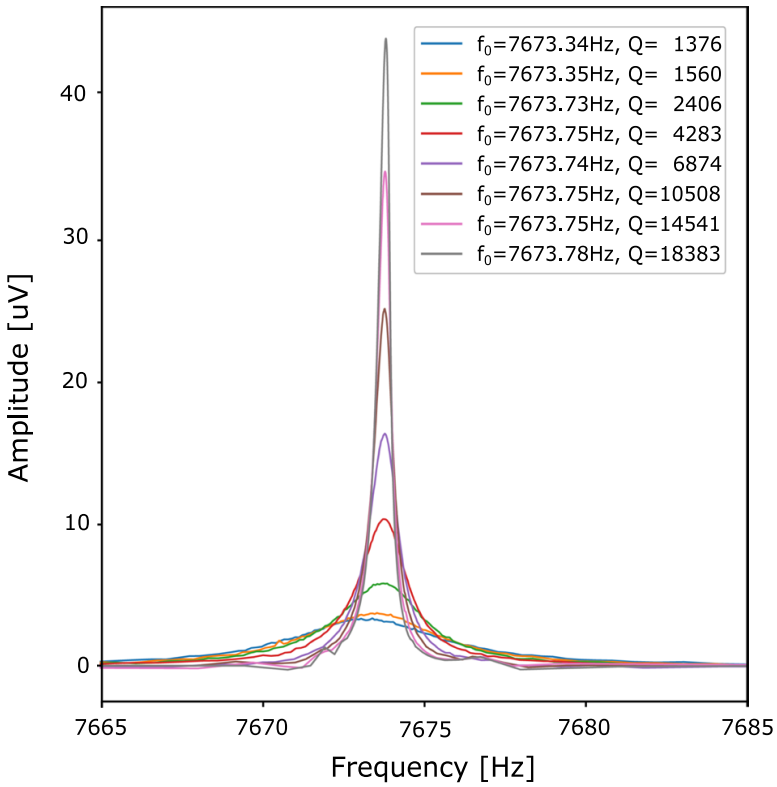

Fig. 5 Resonance curves measured with the H3 device in a glass cryostat under cryogenic conditions as the helium pressure was gradually decreasing after all superfluid helium was evaporated. The tallest curve corresponds to the pressure of ≈0.1 Torr. Subsequent measurements showed even higher quality factors, but were affected by frequency drift due to increasing temperature. We note that at $T > 1.3$ K, the aluminium layer was in normal state—the curves were offset to suppress the background (resistive) contribution (Color figure online)

pressure, which is evident from the rapid rise of the Q factor during pumping. The resonance with the highest measured Q factor in the experiment $\approx 5 \times 10^4$ is not shown, as the temperature of the device was already unstable at that point and caused frequency drifts. Nevertheless, a simple estimate suggests that under true cryogenic vacuum, at temperatures below 1 K, quality factors $> 10^5$ will be reached. Finally, we note that measurements with these devices in superfluid helium on a dilution refrigerator are currently under way, with more results to appear in the near future.

4 Conclusion

Novel micromechanical devices were manufactured based on the adaptation of existing designs, allowing to study the interaction of two closely spaced resonators mediated by quantized vortices in superfluid helium. A detailed description of the fabrication process is presented, along with preliminary characterisation measurements of said devices. The MEMS devices show potential for further use in quantum turbulence research.

Acknowledgements This research is supported by the Czech Science Foundation project GAČR20-13001Y. CzechNanoLab project LM2018110 funded by MEYS CR is gratefully acknowledged for the financial support of the sample fabrication at CEITEC Nano Research Infrastructure.

References

1. L. Skrbek, D. Schmoranzer, Š Midlik, K.R. Sreenivasan, Phenomenology of quantum turbulence in superfluid helium. PNAS **118**, 16 (2021)
2. W.F. Vinen, M. Tsubota, A. Mitani, Kelvin-wave cascade on a vortex in superfluid He-4 at a very low temperature. PRL **91**(13), 135301 (2003)
3. D.I. Bradley, R. George, A.M. Guenault et al., Operating Nanobeams in a Quantum Fluid. Sci. Rep. **7**, 4876 (2017)
4. T. Kamppinen, V.B. Eltsov, Nanomechanical resonators for cryogenic research. JLTP **196**, 283–292 (2019)
5. C.S. Barquist, W.G. Jiang, K. Gunther et al., Damping of a microelectromechanical oscillator in turbulent superfluid 4He: a probe of quantized vorticity in the ultralow temperature regime. PRB **101**, 174513 (2020)
6. A. Guthrie, S. Kafanov, M.T. Noble et al., Nanoscale real-time detection of quantum vortices at millikelvin temperatures. Nat. Commun. **12**, 1 (2021)
7. M. Defoort, K.J. Lulla, T. Crozes et al., Slippage and boundary layer probed in an almost ideal gas by a nanomechanical oscillator. PRL **113**, 136101 (2014)
8. M. Defoort, S. Dufresnes, S.L. Ahlstrom et al., Probing bogoliubov quasiparticles in superfluid 3He with a 'vibrating-wire like' MEMS device. JLTP **183**, 284–291 (2016)
9. M. Defoort, K.J. Lulla, C. Blanc et al., Modal "self-coupling'' as a sensitive probe for nanomechanical detection. Appl. Phys. Lett. **103**(1), 013104 (2013)
10. D. Schmoranzer, M. La Mantia, G. Sheshin et al., Acoustic emission by quartz tuning forks and other oscillating structures in cryogenic 4He fluids. JLTP **163**, 317–344 (2011)
11. D.I. Bradley, M. Človečko, S.N. Fisher et al., Crossover from hydrodynamic to acoustic drag on quartz tuning forks in normal and superfluid 4He. PRB **85**, 014501 (2012)
12. A.M. Guénault, R.P. Haley, S. Kafanov et al., Acoustic damping of quartz tuning forks in normal and superfluid 3He. PRB **100**, 104526 (2019)
13. E. Collin, L. Filleau, T. Fournier, Y.M. Bunkov, H. Godfrin, Silicon vibrating wires at low temperatures. JLTP **150**, 739–790 (2008)
14. F. Laerme, A. Schilp, K. Funk, M. Offenberg, Technical digest, in *IEEE International MEMS 99 Conference. Twelfth IEEE International Conference on Micro Electro Mechanical Systems* (1999) 211–216. https://doi.org/10.1109/MEMSYS.1999.746812.
15. M.A. Hopcroft, W.D. Nix, T.W. Kenny, Systems. J. Microelectromech. **19**, 229 (2010)